
This item was submitted to [Loughborough's Research Repository](#) by the author.
Items in Figshare are protected by copyright, with all rights reserved, unless otherwise indicated.

The performance evaluation of lithium thionyl chloride batteries for long-life meter applications

PLEASE CITE THE PUBLISHED VERSION

PUBLISHER

© Tim G. Saunders

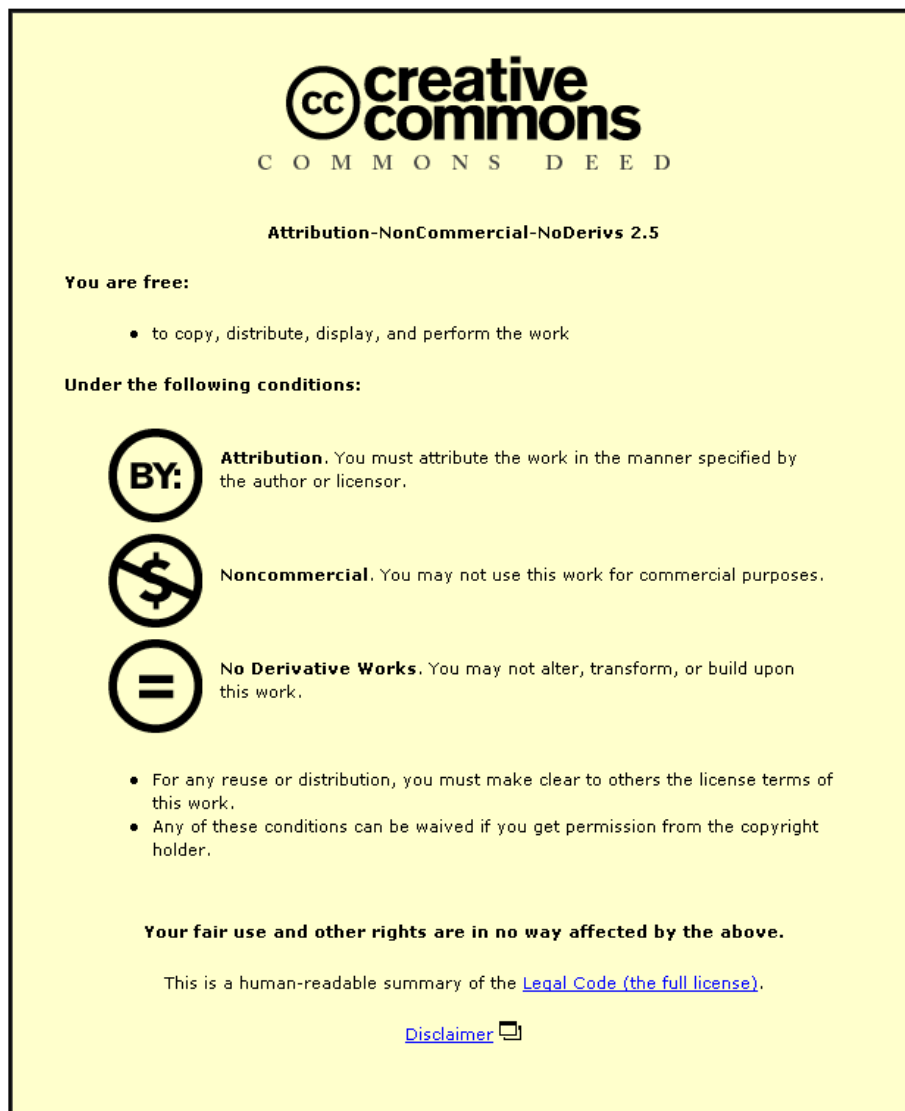
LICENCE

CC BY-NC-ND 4.0

REPOSITORY RECORD

Saunders, Tim G.. 2019. "The Performance Evaluation of Lithium Thionyl Chloride Batteries for Long-life Meter Applications". figshare. <https://hdl.handle.net/2134/13855>.

This item was submitted to Loughborough University as a PhD thesis by the author and is made available in the Institutional Repository (<https://dspace.lboro.ac.uk/>) under the following Creative Commons Licence conditions.



For the full text of this licence, please go to:
<http://creativecommons.org/licenses/by-nc-nd/2.5/>

Pilkington Library

Author/Filing Title SAUNDERS, T.G.

Accession/Copy No.

Vol. No. Class Mark T

Robert G. P.
open shelf copy

FOR REFERENCE ONLY

0401661318



**THE PERFORMANCE EVALUATION
OF LITHIUM THIONYL CHLORIDE BATTERIES
FOR LONG-LIFE METER APPLICATIONS**


by Tim G. Saunders

Supervisor: Dr. Philip J. Mitchell

A Doctoral Thesis

Submitted in partial fulfilment for the award of
Doctor of Philosophy of Loughborough University
March, 1998

© Tim G. Saunders, March, 1998

 Loughborough University Library	
Date	Oct 98
Class	
Acc No.	040166138

K0629488

THE PERFORMANCE EVALUATION OF LITHIUM THIONYL CHLORIDE BATTERIES FOR LONG-LIFE METER APPLICATIONS

Doctoral Thesis by Tim G. Saunders

Dedication

This thesis is dedicated to the memory of my mother and father

Abstract

A research project has been carried out to provide BG plc with service life predictions of lithium primary batteries capable of supplying a continuous pulsed power supply to two new electronic domestic gas meters over a desired design life of 11.5 years, in UK weather conditions. The paper study includes investigations of the range of suitable lithium technologies and test methods, and detailed reviews of the discharge processes, polarisation and self-discharge failure modes of the lithium thionyl chloride system.

A new multi-channel load test rig and a high resolution measurement system, and software analysis tools were designed and constructed, and some 440 accelerated discharge tests were carried out at different stress levels on 4 cell types. The results provide a unique database of the voltage/temperature/load trends through discharge, and generate a ranking order of performance. Basic statistical analyses have been carried out to quantify the variability of performance trends. A hitherto unreported behaviour pattern is characterised. Qualitative models are postulated to account for deviations from normal behaviour exhibited by two cell types. The analysis suggests that catholyte additives could predispose a system to early failure (due to modification of the crystal structure of the reaction products), and that manufacturing tolerances define the degree of failure.

Mathematical models of self-discharge rate for both low and medium rate discharge were developed from laboratory measurements. Meter load profiles were also measured, which together with the self-discharge model enabled prediction of operational energy utilisation rates.

A sample of 50 batteries was extracted from customers homes, after operating in the field for periods of up to 2 years, and the battery capacity loss rates were measured by the residual capacity method. A comparison of predicted and actual capacity utilisation rates yielded a discrepancy of approximately 1.28. Analysis implied that the source of the discrepancy could be adduced to an under estimate of the impact of self-discharge, but that a factor of up to six times the predicted value was required. Evidence was provided to show that self-discharge rate under operational stresses could be significantly higher than that under the steady-state laboratory measurement conditions, but that the amplitude and time constant associated with a self-discharge peak was unknown and not predictable.

Mean service lives of 14 and 10 years for the respective battery types in the two types of meter are predicted, the worst case (probability of 0.13% of the population) being failure within approximately 5.9 years.

THE PERFORMANCE EVALUATION OF LITHIUM THIONYL CHLORIDE BATTERIES FOR LONG-LIFE METER APPLICATIONS

by Tim G. Saunders

Acknowledgements

I would like to acknowledge the assistance of Dr. Philip Mitchell for his expert technical and enthusiastic moral support throughout the project. I would also like to express my particular gratitude to Dr. Herzl Yamin (Tadiran Ltd., Rehovot, Israel) for his invaluable contributions to the study. I also have received valuable support from external colleagues: Dr. Anne Brown (Saft, UK), Drs. Wendy Cieslak and Sally Hoier (Sandia National Laboratories, New Mexico, US), Dr. Mogens Mogensen (Riso National Laboratories, Denmark), Dr. Philippe Chenebault (SAFT, Poitiers, France), and many other workers in the field, who have given to me the benefit of their experience of specialist aspects of lithium battery technology and processes. Mr. Nathan Grange (Loughborough University) wrote the rig control and data handling software, which added significantly to the quality of the data analysis. Mr. Chandra Tailor (BG plc, Gas Research Centre, Loughborough) gave his technical expertise to optimising equipment design and performance. Finally I wish to thank BG plc, who sponsored the PhD. study and who provided the training funds and most of the financial support for the project.

CONTENTS

CHAPTER 1	1
INTRODUCTION.....	1
1.1. METER POWER SOURCE.....	4
1.2. PRELIMINARY TECHNICAL RESEARCH.....	5
1.2.1. <i>Safety performance</i>	6
1.2.2. <i>Electrical performance</i>	6
1.3. PHD. RESEARCH PROGRAMME	7
 CHAPTER 2	 9
METER LOAD AND BATTERY OPERATING REQUIREMENTS	9
2.1. METER POWER REQUIREMENTS.....	9
2.2. OPERATING STRESSES	11
2.3. BATTERY SERVICE-LIFE AND REPLACEMENT PROTOCOL.....	12
2.4. DIMENSIONS.....	12
2.5. ORIENTATION.....	12
2.6. TOLERANCES ON THE LOAD AND SERVICE REQUIREMENT	12
2.7. GENERAL SPECIFICATION FOR THE METER BATTERY	13
 CHAPTER 3	 14
BASIC BATTERY OPERATING PRINCIPLES.....	14
3.1. THERMODYNAMICS.....	14
3.2. KINETICS.....	15
3.2.1. <i>Chemical kinetics</i>	15
3.2.2. <i>Electrochemical kinetics</i>	16
3.3. POLARISATION	16
3.4. FAILURE MODES.....	17
 CHAPTER 4	 18
LITHIUM BATTERY OPTIONS.....	18
4.1. ELECTRODE MATERIALS.....	18
4.2. LITHIUM CELL COUPLES	19
4.3. PRACTICAL ENERGY CAPACITY AND VOLTAGE	20
4.4. DISCHARGE CURVE	20
4.5. STORAGE AND SERVICE LIFE.....	21
4.6. ENERGY DENSITY AND PERFORMANCE PARAMETERS	22
4.7. STATUS REVIEW OF MASS PRODUCED LITHIUM PRIMARY CELLS.....	22
4.7.1. <i>Liquid cathode systems</i>	23
4.7.2. <i>Solid cathode systems</i>	24
4.8. BATTERY RELIABILITY AND QA	25
4.9. TOLERANCES	26
4.10. PRACTICAL E6 METER BATTERY OPTIONS	27
 CHAPTER 5	 29
DESIGN OF Li/SOCl_2 BATTERIES	29
5.1. BASIC CELL REACTION	29
5.2. ENGINEERING DESIGN OF THE CANDIDATE CELLS	29
5.2.1. <i>Materials balance</i>	31
5.3. ANODE DESIGN.....	32
5.4. CATHOLYTE FORMULATION.....	33
5.5. POSITIVE CARBON ELECTRODE (PCE) DESIGN	34
5.6. PASSIVE CELL COMPONENTS	35

CHAPTER 6	36
LI/SOCL₂ CELL PROCESSES	36
6.1. POLARISATION	37
6.2. ANODIC OVERPOTENTIAL (η_a)	38
6.3. CATHODIC OVERPOTENTIAL (η_{ca})	39
6.4. OHMIC LOSSES (IR)	40
6.5. DISCHARGE PROCESSES	40
6.6. CATHOLYTE DISCHARGE PROCESSES	41
6.7. ANODIC DISCHARGE PROCESSES	43
6.8. CATHODIC DISCHARGE PROCESSES	44
6.8.1. <i>Open-circuit storage pce processes</i>	45
6.8.2. <i>Cathodic reduction processes</i>	46
6.8.3. <i>The operation and performance of the pce</i>	46
6.8.4. <i>Effect of porous structure on pce performance</i>	48
6.8.5. <i>Effect of load on pce performance</i>	49
6.9. TEMPERATURE AND ORIENTATION	51
6.10. IMPLICATIONS FOR THE METER APPLICATION	53
 CHAPTER 7	 54
THE PASSIVATION LAYER AND SELF-DISCHARGE	54
7.1. MEASUREMENT METHODS OF THE PL GEOMETRY AND SELF-DISCHARGE RATE	56
7.2. THE FORMATION OF THE PASSIVATION LAYER ON OPEN-CIRCUIT	57
7.3. OPEN-CIRCUIT GROWTH RATE OF THE PL	58
7.4. PHYSICAL STRUCTURE OF THE PL	59
7.5. THE ON-LOAD GROWTH RATE OF THE PL	60
7.6. THE EFFECT OF CATHOLYTE COMPOSITION AND LITHIUM PURITY	61
7.7. THE EFFECT OF TEMPERATURE ON PL MORPHOLOGY	62
7.8. THE STABILITY OF THE PL UNDER DISCHARGE	62
7.9. DYNAMIC PROPERTIES OF THE PL	64
7.9.1. <i>Electrical shock</i>	64
7.9.2. <i>Mechanical shock</i>	65
7.9.3. <i>Thermal shock</i>	65
7.10. SELF-DISCHARGE RATE	65
7.11. THE EFFECT OF TEMPERATURE ON SELF-DISCHARGE RATE	68
7.12. THE EFFECT OF LOAD ON SELF-DISCHARGE RATE	68
7.13. EFFECT OF DEPTH OF DISCHARGE ON SELF-DISCHARGE	70
7.14. EFFECT OF DYNAMIC STRESSES ON SELF-DISCHARGE	71
7.15. PRACTICAL IMPLICATIONS	71
 CHAPTER 8	 74
TEST PROGRAMME	74
8.1. EVALUATION METHODS	75
8.2. TEST MATRIX	76
8.3. THERMAL ENVIRONMENT	77
8.4. VOLTAGE MEASUREMENTS	78
8.5. THE DISCHARGE TEST RIG	78
8.6. SOFTWARE	85
8.6.1. <i>Data acquisition software</i>	85
8.6.2. <i>Data processing software</i>	87
8.7. CAPACITY COMPUTATION	91
8.8. CALIBRATION	92
8.9. BATTERY TEST CODE AND TRACKING SYSTEM	92
8.10. SAMPLING METHODOLOGY	92
8.11. EXPERIMENTAL SAFETY	93

CHAPTER 9	94
DISCHARGE TEST METHODOLOGY	94
9.1. TEST VARIABLES	95
9.1.1. Thermal environment	95
9.1.2. Passive resistive load	96
9.1.3. Discharge Load levels	96
9.1.4. Battery Orientation	97
9.1.5. Battery Storage time	97
9.2. TREATMENT OF THE DISCHARGE TEST DATA	97
9.3. PRESENTATION OF DISCHARGE TEST RESULTS	97
9.4. RIG MALFUNCTIONS	99
9.5. PRE-DISCHARGE TESTING	101
 CHAPTER 10	 102
DISCHARGE TEST RESULTS FOR CELL TYPE TE	102
10.1. CHARACTERISTICS OF DISCHARGE UNDER THERMAL CYCLE	103
10.1.1. High states of charge (C100% to C60%)	104
10.1.2. Mid states of charge (C60% to C20%)	105
10.1.3. Final states of charge (C20% to C0%)	106
10.2. ROOM TEMPERATURE DISCHARGE	107
10.3. PULSED DISCHARGE	107
10.4. IMPLICATIONS FOR THE METER APPLICATION	108
 CHAPTER 11	 109
DISCHARGE TEST RESULTS FOR BATTERY TYPE TD	109
11.1. CAPACITY TO 2.5 V	110
11.2. CAPACITY TO 0 V	113
11.3. DISCHARGE PROFILES	114
11.3.1. R_L of 100 Ω	114
11.3.2. R_L of 200 Ω	115
11.3.3. R_L of 360 Ω	116
11.3.4. R_L of 560 Ω	116
11.3.5. R_L of 1200 Ω	117
11.4. CAPACITY DISTRIBUTIONS	118
11.5. EFFECT OF TEST PARAMETER	120
11.5.1. Production lot	120
11.5.2. Storage duration	120
11.5.3. Orientation	121
11.5.4. Room-temperature	121
11.5.5. Pulsed discharge	122
11.6. THE PREMATURE FAILURE MODE	123
11.7. THE SADDLE-BACK FAILURE MODE	125
11.7.1. Physical characteristics of the voltage perturbations	127
11.7.2. A speculative model for the saddle-back premature failure mode	128
11.8. EXPLANATION OF 'SADDLE-BACK FAILURE' MODE	130
11.8.1. Positive electrode and separator	130
11.8.2. Negative electrode	131
11.8.3. Statistical distribution of the failure mode	132
11.8.4. Susceptibility of the Td cell type to premature failure	133
11.9. IMPLICATIONS FOR THE METER APPLICATION	134
 CHAPTER 12	 135
DISCHARGE TEST RESULTS FOR CELL TYPE TA AND TB	135
12.1. BATTERY TYPE TA	135
12.2. BATTERY TYPE TB	137
12.3. INTERPRETATION OF THE TA AND TB TEST RESULTS	139

CHAPTER 13	142
REVIEW OF DISCHARGE TEST RESULTS.....	142
13.1. $R_L = 360 \Omega$ RESULTS	142
13.2. THE $Q_{2.5}$ RESULTS	144
13.3. Q_0 RESULTS	146
13.4. IMPLICATIONS FOR THE METER APPLICATION.	148
13.5. GENERAL COMMENTS ON THE EXPERIMENTAL TECHNIQUES	150
 CHAPTER 14	 152
SELF DISCHARGE MEASUREMENTS	152
14.1. SNL TESTS.....	152
14.2. RESULTS IN THE LITERATURE	155
14.3. SELF-DISCHARGE MEASUREMENTS FROM THE MANUFACTURERS	158
14.4. CORRELATION OF DISCHARGE-TEST CAPACITY LOSSES.....	159
14.5. SELF DISCHARGE MODEL FOR THE ACCELERATED TEST RANGE	160
14.6. BATTERY MANUFACTURERS' SELF-DISCHARGE DATA	162
14.7. IMPLICATIONS FOR THE METER APPLICATION	164
 CHAPTER 15	 166
OPERATIONAL CAPACITY LOSSES OF THE METER BATTERY	166
15.1. OPERATIONAL CAPACITY LOSS MEASUREMENT PRINCIPLES.....	166
15.2. METER AND CONTROL BATTERY CAPACITY MEASUREMENTS	169
15.3. CONTROL CELLS - CAPACITY MEASUREMENTS	169
15.4. METER BATTERIES - CAPACITY MEASUREMENTS.....	170
15.5. IN-SERVICE CAPACITY LOSS RATES.....	171
15.6. METER DRAIN RATE MEASUREMENTS.....	173
15.7. COMPARISON OF THE MEASURED AND PREDICTED MODELS.....	174
15.8. PREDICTED SERVICE LIFE DISTRIBUTIONS	177
15.9. PRACTICAL IMPLICATIONS.....	177
15.9.1. <i>Clustered capacity loss data</i>	179
15.9.2. <i>Outlier capacity loss data</i>	180
15.10. COMMENT ON ELEVATED SELF-DISCHARGE.....	181
 CHAPTER 16	 182
PREDICTED BATTERY SERVICE LIFE DISTRIBUTIONS	182
16.1. BATTERY SERVICE LIFE	183
16.2. IMPLICATIONS FOR THE METER APPLICATION	184
 CHAPTER 17	 186
FINAL SUMMARY AND CONCLUSIONS	186
 CHAPTER 18	 190
FUTURE WORK.....	190
18.1. MONITORING EXERCISE	190
18.2. SELF-DISCHARGE.....	190
18.3. END-OF-LIFE POLARISATION AND DISCHARGE PROFILE	191
18.4. PREMATURE FAILURE	191
18.5. NOISE.....	192
 CHAPTER 19	 193
REFERENCES.....	193

PRINCIPAL SYMBOLS AND DESIGNATIONS

a	Effective radius of an ion in solution.
$A_{a,c}$	Area, A_a and A_c represent active anode and cathode electrode surface areas.
C	Concentration.
$Cx\%$	State of charge (depth of discharge) where C100%, C50% and C0% designate a fully charged, half discharged and a completely discharged battery respectively.
D	Diffusion coefficient.
E°	Open-circuit voltage potential; this can be influenced by impurities and surface conditions at the electrode, $E^\circ = \Delta G/zF$.
E	Potential difference.
E^θ	Open-circuit voltage at standard conditions.
E_H	Thermoneutral potential, $E_H = \Delta H/zF$.
E_L	Load voltage of a battery.
E_{th}	Theoretical open-circuit voltage calculated from thermodynamic parameters.
F	Faraday constant (96487 C/mol).
ΔG	Gibbs free energy of a reaction.
ΔH	Enthalpy change of a reaction.
I	Current.
I_L	Load current.
I_{SD}	Rate of self discharge expressed in terms of current.
j	Current density.
j_0	Exchange current density.
j_{SD}	Rate of self discharge (I_{SD}/cm^2).
k	Boltzmann constant.
l	Length.
L	Thickness of the passivation layer.
M_r	Relative molecular mass.
m	Mass.
P	Duty cycle of a pulsed discharge, $P = \text{on-time}/(\text{on-time} + \text{off-time})$
q	Measured heat output given off by a cell.
Q	Cell capacity (Ah).
Q_P	Capacity unavailable due to polarisation.
Q_L	Electrical capacity delivered to the load.

- Q_{SD} Capacity lost due to self-discharge.
- Q_0 Stoichiometric capacity of the cell (given by the stoichiometric capacity of the capacity limiting electrode¹).
- Q_V Energy dissipated electrochemically, through e.g. an external load, measured under the specified conditions and to a cut-off voltage, V_X . $Q_{2.5}$ and Q_0 are the measured battery capacities to 2.5 and 0 V. For $Q_{2.5}$, capacity is measured to the first incursion through 2.5 V. For Q_0 , capacity is measured to complete depletion of the reactants, i.e. to the 'final' value of 0 V (i.e. it includes temporary cell recovery), and gives the upper limit of available electrochemical capacity.
- $^{max}Q_V$ Maximum measured capacity recorded for a given test of n cells. Gives the maximum value of Q_V .
- $^{min}Q_V$ Minimum measured capacity recorded for a given test of n cells.
- R Gas constant (8.314 J/K/mol).
- R^2 The index of determination to indicate the quality of fit of a regression curve (on a scale of 0 to 1, with 0 indicating a poor fit, and 1 a good fit and a meaningful regression line)².
- T Temperature (K)
- R_L Load resistance.
- t Duration.
- V_L Load voltage.
- V_X Cut-off voltage, e.g. 2.5 V.
- T Temperature, period.
- W_V Volumetric energy density (i.e. power density \times hours of service, $W/cm^3 \times h$).
- Z Battery impedance. Generally: d.c. resistance.
- z Change in charge number for the electrode reaction.

Greek symbols:

- α Charge transfer coefficient (α for the cathode is taken as 0.5 (Ref. ³).
- ϵ_c Coulombic efficiency = (Q_V/Q_0) , Ref. ⁴.
- ϵ_F Faradaic efficiency = $(Q_V)/(Q_V + Q_{SD})$, Ref. ⁵.
- σ Standard deviation of a specified characteristic of members of a parent population.
- $\sigma(Q_V)$ Standard deviation of the measured capacity (Q_V) for a set of cells in a specified test.
- μ Mean value of a specified characteristic of members of a parent population.
- $\mu(Q_V)$ Mean value of the measured capacity (Q_V) for a set of cells in a specified test.

τ_p Time for the concentration of products at the electrode surface to change to a value to cause a concentration overpotential.

Common subscripts:

L Load resistance.

v Cut-off voltage.

Conventions:

The term *cell* refers to an energy producing unit, and the term *battery* refers to an assembly of one or more cells connected to form a single unit.

Catholyte refers to the mixture of liquid electrolyte, liquid cathode and other liquid additives in liquid cathode cells.

CHAPTER 1

INTRODUCTION

The familiar mechanical positive-displacement 'diaphragm' meter shown in Figure 1.2a on page 3 is currently the predominant domestic gas billing meter throughout the world. The design originated in the 19th century, and the technology has evolved to a state where little further improvement in cost, size and performance can be made. During the early 1980s changes in market needs and new technical developments encouraged the reappraisal of gas metering options in the domestic sector. Much of the stimulus arose from a need for a more compact and aesthetically appealing meter, and a desire to take advantage of advances in electronic systems and communications technology.

Following initial feasibility studies, in 1987 British Gas plc (BG) launched an international competition to aid its search for novel domestic gas meter designs¹. BG's aim was to identify an electronic meter concept which would offer the potential of (a) a technical performance and unit cost to match or better that of the mechanical gas meter, (b) providing the industry with a micro-processor based device which would be capable of both utilising the new automatic meter reading and communication data transfer technologies, and (c) meeting the technical and aesthetic aspirations of customers in the twenty first century.

Later in 1987, some 4 meter concepts were selected from 21 submissions for collaborative development through to 'proof-of-concept' models. In 1990 these, and two other independently developed designs, were subjected to a range of 'Proof of Concept' laboratory tests to compare performance with the diaphragm meter.

Two meter designs were found to offer superior performance and commercial potential. Both measure gas flow rate directly by means of an ultrasonic 'time-of-flight' measuring technique shown schematically in Figure 1.1, but differences in the measurement systems employed in the two meters and the commercial advantage of competitive double sourcing justified the decision to continue with both meter types. The designs were further developed to a field trial version, and some 120 of each meter type were manufactured. The operational performance and reliability of these was tested by means of an initial field trial of some hundred units, which were installed in customers' homes spread throughout the UK in 1991. The two types of

ultrasonic meter and a conventional meter were mounted in series, to provide triplicated gas consumption measurements which were logged continuously and analysed at frequent intervals over a three year period².

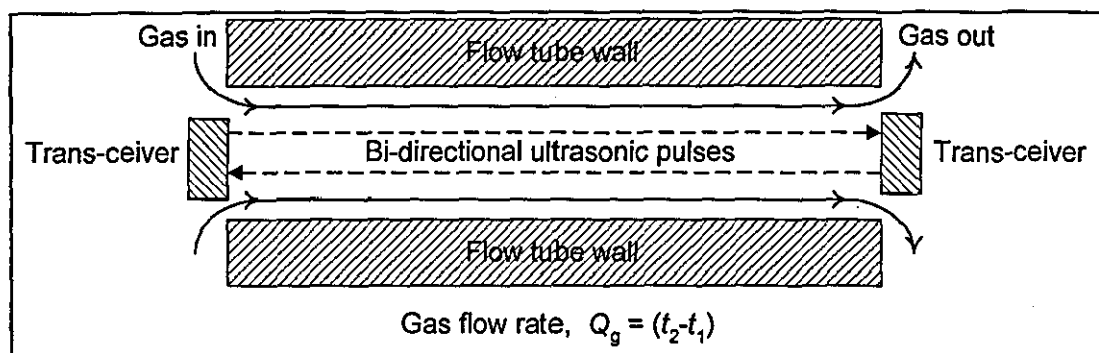


Figure 1.1 Ultrasonic meter - cross-sectional schematic of flow tube - the gas flow rate is given by $Q_g = (t_2 - t_1)$ where t_2 and t_1 are the upstream and downstream times of flight of the ultrasonic pulse.

Following successful results from the field, approval was sought and received from the Technical Directorate of the Office of Gas Trading (Ofgas) to use both meters for billing in the UK. The meters are designated the E6 meter (electronic, 6 m³/h maximum flow rating), and both types are now being manufactured under licence by several companies in the UK, whilst licences to manufacture have been procured by several overseas agencies. The domestic customer base in the UK is about 19 m, implying a very large market. Since 1993, some 500,000 E6 meters have been installed, with fresh contracts in place for 1997. For information, photographs of each of the meters are given in Figure 1.2b.

The development and commercialisation of a competitively priced ultrasonic gas meter represents a very significant achievement. The meter measures gas consumption to an accuracy of $\pm 2\%$ over an extended flow range (0.08 to 6 m³/h), gas composition (four main constituents: CH₄, H₂, C_nH_{2n+2}, and N₂), temperature (-10 to $+40$ °C), and containing quantities of liquid and solid contaminants. Additionally the meter is compact, and provides a suitable platform and interface for electronic communication systems. In recognition of the achievement marked by the successful development of the BG meter from concept through to manufacture, BG and its design contractor, Gill Research and Development, were jointly awarded the Prince of Wales Award for Innovation in 1994 and the Royal Academy of Engineering McRobert Award in 1995. (As the second meter was developed abroad by Siemens Measurements Limited (SML) in Germany, it was not eligible for either award).



Figure 1.2(a) The existing U6 diaphragm meter and the smaller BG design of ultrasonic meter.



Figure 1.2(b) The two types of ultrasonic gas meter: the BG design is on the left, the battery module and compartment are in front of the meter. The SML design is on the right, and the 'D' size battery, flying lead and compartment are located in front of the meter.

1.1. Meter power source

Unlike the mechanical meter, which draws its power from the positive pressure in the gas supply line (20 mbar above atmospheric pressure), the E6 meter requires an electrical power source, ideally with sufficient capacity to power the meter for the whole of its twenty year design life. At an early stage in the project, BG made a policy decision to use an integrated power source in order to avoid the complexities of wiring and billing associated with connection to distributed mains or other external electricity supply systems. Effectively this decision discounted the use of rechargeable power supplies, and restricted the range of options to either a primary battery or some novel form of power source, (for example, a micro-generator fuelled by natural gas from the household supply).

A minimum service life of 10 years was a basic performance requirement included in the original meter specification, and early in the meter development it was realised that this represented a major technical challenge. A search for suitable power source technologies was carried out at a low activity level during the initial development of the E6 through the 1980s. This involved feasibility studies which were based on three initial battery candidates, which were undertaken by means of simple discharge tests to establish energy capacity, and investigations through discussions with the meter designers and interested battery manufacturers. In parallel with these studies, a survey of current and novel power source options was also carried out by PA Consultants Ltd. The results implied that (lithium) primary batteries offered the greatest potential in terms of cost, energy density, performance, physical size, and the manufacturing capability required to meet the tight deadlines imposed by BG's planned meter installation programme. Thus, a decision was made to adopt lithium primary cell technology as the preferred power source.

By 1991, it became clear that the battery was a critical factor in defining the future commercial and technical viability of the meter in the competitive arena. The battery accounts for up to one third of the total cost of the meter. Reliability of the E6 is a crucial requirement for BG, the gas suppliers, and the customer, as it is effectively the industry 'cash till'. A credit domestic gas meter has no shut-off valve, and in the event of loss of power, gas flow will continue but gas consumption will not be registered. Thus unexpected or premature failure of the power source in service will

lead to significant financial penalties in terms of lost billing revenue and the costs of unscheduled service call-outs and battery replacement.

At this time BG had no dedicated battery test facilities or equipment, and very little expertise in the field of long-life batteries. The project management team recognised that battery evaluations were required but that the technology is complex. Approval was given to generate a specific Deliverable with the objective of developing a 'Centre of Excellence' within the company in order to provide the necessary technical expertise to support BG's commercial and operational business needs. Funding was to be reviewed annually, but amounted to the equivalent of half a man-year of effort and £20-30k direct expenditure for equipment purchases.

1.2. Preliminary technical research

Preliminary investigations had identified three potentially suitable primary lithium battery technologies: lithium polycarbon monofluoride ($\text{Li}/(\text{CF})_x$), lithium manganese dioxide (Li/MnO_2), and lithium thionyl chloride (Li/SOCl_2). A parallel investigation of novel power sources had identified fuel cells as the alternative technology with the greatest potential for this application, and a miniature solid polymer electrolyte fuel cell and fuel pack was successfully developed and tested at Loughborough University under a BG contract in the early 90s. Reductions in funding caused the work to be discontinued in 1995.

Technical fitness for purpose of a battery is mainly determined by its ability to satisfy the basic engineering requirements and to power a given device both safely and reliably for the required service life. Early battery investigations involved reviews of product literature and discussions with the manufacturers, users such as the Defence Research Agency (DRA), and independent battery experts. It became evident that there was a general agreement that lithium batteries represented the best power source option for the application. However, no independent performance database was available in the literature, and little consensus and even conflicting reports existed regarding safety, electrical performance and product reliability. It is now realised that this uncertainty was due, and still is in no small part, to the fact that lithium primary batteries are a still evolving technology³. This general lack of reliable information prompted the need for BG to undertake a research study to build an appropriate knowledge base.

1.2.1. Safety performance

Clearly, the domestic utilisation of such a device is dependent on a satisfactory safety performance, and hazard assessments of candidate batteries were among the first tasks to be undertaken. In 1991, the safety of lithium primary battery technology was subject to controversy⁴. In 1992, the author formulated a safety test specification designed to evaluate the safety performance of the range of candidate lithium primary batteries over both the normal and extreme abuse ranges of electrical, mechanical and thermal stresses. The test programme was carried out under contract at the Defence Research Agency safety test laboratories at GEC Marconi in Wembley, (latterly at Borehamwood). The results demonstrated that all of the candidate batteries were stable under the range of operating conditions to be encountered in service in the UK, and that the batteries vented violently only under extreme thermal, mechanical or electrical abuse conditions. A paper describing the programme and the favourable results was presented by the author at the Power Sources Symposium in 1995⁵. On the basis of this work, three battery technologies were recommended and adopted for use in the first series of production meters. The meters were manufactured and installed in customers' homes from 1994 onwards.

1.2.2. Electrical performance

The initial electrical performance feasibility studies had suggested that a 'D' size battery possessed the electrical capacity to power an E6 meter for just greater than half of the 20 year design life of the meter. Thus a limit of one battery change per meter life was adopted as a preliminary target. The battery manufacturers were confident of achieving an 11.5 year life. By contrast, experienced users such as the Defence Research Agency, Her Majesty's Government Communications Centre, and SML all reported that the service life and performance repeatability of systems they had tested and used varied widely. The general view amongst users was that a ten year service life represented the extreme end of the known operating range. It was clear that significant disagreement existed between users, manufacturers and independent experts. The lack of clarity regarding reliability, service life and failure mechanisms signalled the need for an in-depth study.

During the 1980s, the Chemistry Department at Loughborough University had carried out research into a range of power sources, including Li/SOCl₂ and other primary battery technologies (in particular using complex impedance spectroscopy^{6,7,8,9,10,11}).

As an established and leading authority of battery technology, the Department offered a source of operational and intellectual expertise to support the Deliverable. In 1993, BG opened the new Gas Research Centre sited adjacent to the University campus, presenting an ideal opportunity for a collaboration between industry and academia. The collaboration was formalised by the author's registration for a post graduate research degree with Dr. P.J. Mitchell, lecturer in Electrochemistry in the Chemistry Department as supervisor. The project was entitled 'The performance evaluation of lithium thionyl chloride batteries for long-life meter applications'.

1.3. PhD. research programme

The main aims of the investigation of electrical performance were (a) to characterise the performance of a range of lithium battery options in the operating domain of the electronic meters, and (b) to predict service life distributions. This would involve (a) the collation of information from the external sources, (b) laboratory tests, and (c) measurement of actual in-service losses of batteries removed from the field after periods of operation.

In this application, battery failure is defined as the (lower) voltage at which the meter electronic systems cease functioning effectively. The criteria used to define the basic electrical performance of a primary battery system are voltage, energy capacity, rate capability, internal corrosion rates and operating life, all of which are interrelated¹². The actual discharge profile of a battery and the associated time to failure in a particular application depends on these parameters, and is also heavily dependent on the type of applied load (i.e. pulse/constant, constant voltage, current energy, etc.) and on the operating conditions (particularly temperature).

To investigate these factors, the research programme was conceived as several parallel investigations as listed below.

1. Identification and procurement of suitable candidate batteries from manufacturers.
2. Literature study of the basic cell processes and failure modes.
3. Identification of relevant accelerated test techniques.
4. Design and construction of a dedicated laboratory test rig.
5. Implementation of a laboratory test programme to characterise electrical performance as a function of operating parameters such as load, temperature, depth of discharge.
6. Investigation of the kinetics of corrosion related capacity loss (self-discharge).

7. Measurement of capacity loss rates of batteries in actual operation in the field.
8. Integration of the laboratory and field results into a unified battery replacement strategy.

In practice, the Li/SOCl_2 battery is the only system available in the commercial marketplace that can satisfy the basic technical specifications of both meter types and the research topics listed from Chapter 4. onwards below focus solely on this battery type.

The four Li/SOCl_2 candidate cells and the test codes used for tracking the battery types used in the thesis are listed in Table 1.1.

Table 1.1 Li/SOCl_2 primary cell candidates for the electronic meter application.

Li/SOCl_2 cell manufacturer	Project Test Code
Crompton Eternacell	Ta
Eagle Picher	Tb
Saft	Td
Tadiran	Te

CHAPTER 2

METER LOAD AND BATTERY OPERATING REQUIREMENTS

Battery selection is dependent on the load and service life requirements, which for a given battery system will be dependent on the operating conditions experienced during storage and service¹. The meter load requirements and operating stresses define a performance spectrum that candidate batteries must meet, and supply the information necessary to assess the susceptibility of a given battery candidate to its intrinsic failure modes (e.g. polarisation, passivation and self-discharge).

2.1. Meter power requirements

In order to minimise demands on the power source and to optimise service life, the meter designers focus on reducing the load and low-voltage operating threshold presented by the meters. It is envisaged that meter drain rates and pulse amplitudes should reduce as meter designs are improved, and the data given below represent the best information available at the beginning of the project.

The meter battery is installed and 'switched-on' during the meter manufacturing process (to allow calibration), and it then discharges continuously until replaced or exhausted. In normal measuring mode, the load presented by the meter is relatively constant, and varies slightly according to the composition of the gas being measured - some gas compositions attenuate the ultrasonic measuring pulse, and the meter compensates by increasing the gain of the signal amplifier, thereby increasing load fractionally. Additionally, the meter may be interrogated via an optical port involving a load of ~12 mA for about 150 ms. Such an event equates to a battery capacity utilisation of 1.8 mAs (a charge of 1.8 mC). Apart from its usage during first-time calibration, this diagnostic activity is expected to be of extremely low incidence and will only occur to investigate cases of suspected meter malfunction or fraud. The 1.8 mC charge is insignificant by comparison with the 11.5 year operational capacity requirement of 10-16 Ah.

To minimise power consumption, both meters utilise a discrete (rather than continuous) measurement process; gas flow rate is sampled at random points within successive 2 second time windows. The cumulative volumetric consumption is computed by integrating each individual rate measurement with respect to time and adding it to the existing total. Data is transferred from volatile memory to EEPROM

at 6 h intervals, but this activity is relatively low in energy usage. This measurement strategy translates into three main levels of power consumption: microprocessor 'sleep' state, transducer firing, and thirdly data processing. As an example, Table 2.1 lists assumed values of amplitude and duration for these three functions and the total charge per 2000 ms measurement window. The bottom line of the Table gives the time-averaged mean current.

Table 2.1 Meter load functions

Operating mode	Load amplitude (μA)	Duration per 2000 ms 'window' (ms)	Charge (μC)
Microprocessor 'sleep' state.	20	1970	~40
Microprocessor active (control, DP & storage tasks)	1000	27	27
Transducer firings	10000 - 20000	15	150-300
Total per 2 s timing 'window'			217-370
Mean load current	108-185		

The average discharge current ranges from approximately 100 and 185 μA, presenting a cumulative battery capacity requirement over ten years of 9.5 and 16 Ah respectively. These illustrative values are slightly greater than those reported by the manufacturers.

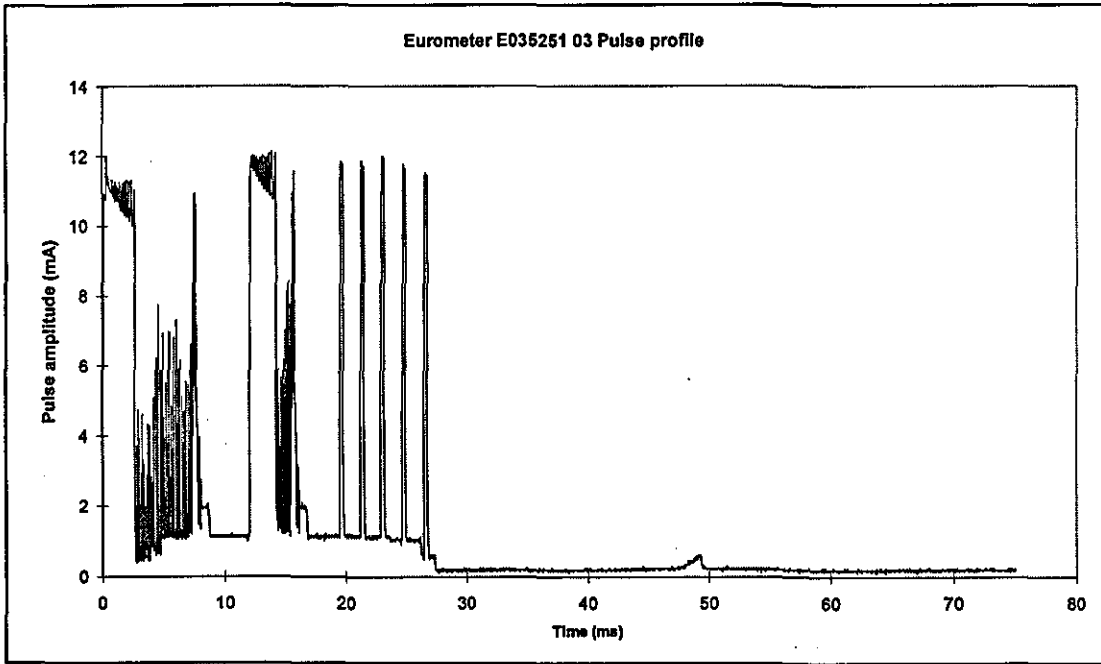


Figure 2.1 Load profile of active phase of Meter Type A

The active operating phase of Meter A is shown in Figure 2.1. The profile comprises a sequence of rectangular pulses that are defined by firing of the ultrasonic transducers and the signal processing and calculation functions of the micro-processor. In the 'sleep' mode the processor presents a 10 μA load, and the active phase accounts for

about 50% of the mean consumption. The mean drain has been measured at approximately 90 μA and the low voltage threshold (cut-off point) is 2.5 V.

Meter B shown in Figure 2.2 exhibits a different load characteristic, in that the high amplitude pulsed load associated with transducer firing is smoothed by means of a capacitor. The microprocessor sleep load is approximately 10 μA . The mean drain lies between 120 and 200 μA (manufacturing tolerances) and the cut-off voltage is approximately 3.0 V.

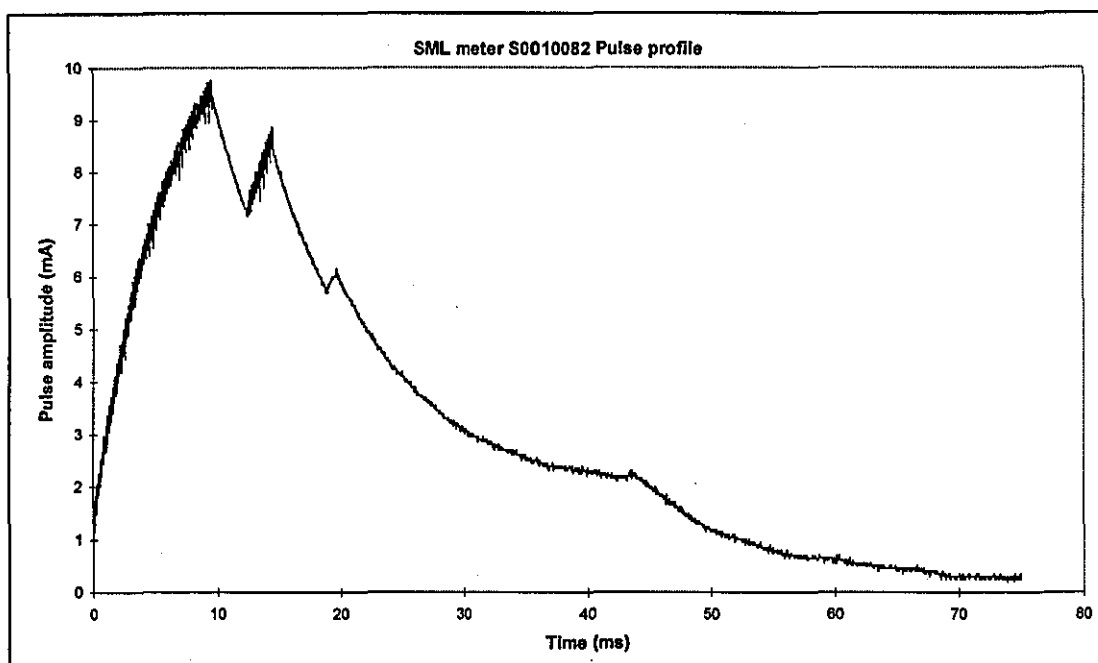


Figure 2.2 Load profile of active phase of Meter Type B.

Empirical tests on the meters have shown that very short time-scale (i.e. 1 kHz), voltage perturbations below the cut-off limit do not adversely affect the meter operation. However, the meters will power down and reset as these approach 10 Hz. At specified 'alarm' voltage levels, the microprocessor is programmed to carry out an ordered power-down sequence before critical power loss occurs. This enables the integrity of the internal meter memory registers to be maintained.

2.2. Operating stresses

Meters are installed both internally and externally in the UK. Internal batteries will experience a relatively stable room temperature environment with a small proportion experiencing temperatures of up to say 45/50 $^{\circ}\text{C}$. External meters are subject to diurnal and seasonal thermal cycling, and operating temperatures of between -20 to +45 $^{\circ}\text{C}$ have been measured in the UK during field trials.

In transit the batteries are subject to the normal mechanical stresses associated with meter transportation and handling (vibration and bumping). However once installed the battery will be static, and not normally subject to any movement or vibrations. However, exceptions to this rule will invariably occur, and some meters may experience enhanced physical stresses such as mechanical and thermal shocks.

2.3. Battery service-life and replacement protocol

The battery specification stipulates storage durations for new and replacement batteries of up to 6 months.

The specified battery service life is nominally 10 years, which is half of the design life of the meter. To accommodate delays associated with battery replacement in the field and up to 6 months in store, a tolerance band of 1.5 year is included, giving an on-load service-life requirement of 11.5 years.

2.4. Dimensions

The meter battery compartment is designed to accommodate either one 'D' size or two 'C' size cells. A single cell battery is desirable as it minimises cost and should be more reliable than a multi-cell pack with its associated inter-cell connections. However, it imposes the need for high voltage couples to satisfy the meter low-voltage operating threshold of 2.5 or 3 V (which is defined by the microprocessor design). The meter compartment and battery connections are visible in Figure 1.2b.

2.5. Orientation

The battery mounting is horizontal for Meter Type A and vertical for Meter Type B.

2.6. Tolerances on the load and service requirement

The electronic circuit design, load and operating parameters are controlled by the meter manufacturer, and the form of the discharge load profile will vary according to the production tolerances of the individual components. Because of the random variability of the characteristics of the electrical components in the meter, the actual capacity requirement of the population of meters of a given design will be subject to a distribution. However no effective statistical information is available regarding the distribution of loads presented by the manufactured meters.

Batteries experience significant change in their operating characteristics with temperature and other applied stresses where long-life is required and self-discharge makes a significant impact. Again, at present it is not possible to identify suitable models of these characteristics.

To obtain reliable operation in the meter, the battery application specification should take account of the worst-case limits of the meter load and environmental stresses, and the service-life requirement should correlate with a level which is well within the capabilities of the power source. Here we are dealing with a largely unknown set of tolerances, and the initial service requirement is defined on the basis of assumed battery performance information and the commercial imperative of a single battery change per meter life.

2.7. General Specification for the meter battery

The battery requirements for the two meters are summarised in the outline meter battery specifications and environmental conditions given in Table 2.2 and Table 2.3, respectively:

Table 2.2 Battery specification for the two meters

Performance parameter	Meter A	Meter B
Cut-off voltage	2.5 V	3.2 V
Mean current	90 μ A	150 μ A
Target service life	11.5 y	8 y
Capacity requirement	10 Ah	14 Ah
Pulse parameters:		
Interval (mean)	2 s	2 s
Active period	30 ms	30 ms
Peak current	18 mA	12 mA
Pulse shape	Rectangular	Smoothed (capacitive)
Cell size equivalent	1 X 'D', 2 X 'C'.	1 X 'D', 2 X 'C'.
Cell orientation	Horizontal	Vertical

Table 2.3 Environmental operating conditions

Environmental stress	Operating range/condition
Temperature	
Internal meter installation	+15 to +45 °C
External meter installation	-20 to +50 °C
Max.dT rate (estimated)	10 °C/h
Mechanical	
Installed	Static
Transportation	N/A

CHAPTER 3

BASIC BATTERY OPERATING PRINCIPLES

In primary batteries the basic operating parameters and the characteristic failure modes are defined by both the thermodynamic properties of the chemical and electrochemical reactants and their reactions, and the kinetics of these reactions and discharge processes that occur during the life of the battery.

3.1. Thermodynamics

From the practical viewpoint, a study of the thermodynamics of electrochemical systems yields the maximum electrical energy and the theoretical open-circuit voltage available from a system, and the likelihood of parasitic chemical reactions. The maximum energy available from a particular electrochemical couple can be calculated from their free energies. Each substance has a unique free energy, and the difference in the free energy of the starting materials from the end materials resulting from the battery discharge process gives the net free energy of the process, that is the net driving force for electron flow.

The theoretical capacity is expressed as the total quantity of electricity available from the reaction, and is defined in terms of coulombs or ampere hours. Theoretically 1 gram equivalent weight of material will deliver one Faraday of electricity (96487 C or 26.8 Ah). The theoretical capacity of a system, based only on the active materials participating in the electrochemical reaction, is calculated from the equivalent weight or volume of the reactants. The capacity of batteries is also considered on an energy basis by taking voltage as well as the quantity of electricity into consideration. A battery system having a high specific energy depends on a large difference in the standard electrode potentials of the anode and cathode reactants. The theoretical specific energy density can be expressed on a volume W_v basis through the relationship:

$$W_v = -\Delta G / \Sigma_v \quad \text{Equation 3.1}$$

where ΔG is the Gibbs free energy for the reaction and Σ_v is the sum of the volume of reactants (based on the number of moles of each reactant involved in the overall process).

The standard potential of a cell is determined by its active materials and can be calculated from free energy data or obtained experimentally. The thermodynamic

reversible cell potential E° is related to the Gibbs free energy change ΔG by the equation:

$$E^\circ = -\Delta G/zF \quad \text{Equation 3.2}$$

where z is the number of electrons involved in the reaction, and F is the Faraday constant.

The theoretical open-circuit voltage, E° , is also dependent on the concentration of materials and temperature as expressed in the Nernst equation:

$$E^\circ = E^\ominus + (RT/nF)\ln(\mu C^c \mu D^d / \mu A^a \mu B^b) \quad \text{Equation 3.3}$$

where the overall cell reaction is:



and E^\ominus is the emf under standard conditions, μ is the activity of the relevant species, R is the gas constant, and T is the absolute temperature. a , b , c and d are the number of moles of A, B, C and D reactants which take up z electrons to complete the reaction.

3.2. Kinetics

Two main classes of kinetics need to be considered in connection with primary batteries: chemical and electrochemical kinetics.

3.2.1. Chemical kinetics

The chemical kinetics are expressed in terms of the capacity loss rates due to 'parasitic' chemical reactions involving reactants which result in a loss of electrochemical capacity, which are generally termed 'self-discharge' reactions. The probability of chemical reactions occurring between battery materials and reactants is given by calculating the net free energy change associated with resulting reactions. Often these reactions are between the chemical anode and cathode, although other elements may be involved, such as the electrolyte, the solvent or the can material. In all of these cases, the reactions are detrimental because they utilise battery components in competition with the Faradaic reaction, and can lead to a significant reduction in practical battery discharge capacity.

The self-discharge rate has a significant effect on battery reliability and service life for long-term and high-stress applications. The rate is a complicated function of all the factors associated with the battery design and quality of manufacture, the application, temperature and other environmental stresses, and their past usage, and it can be determined by experiment alone¹.

3.2.2. Electrochemical kinetics

Electrochemical kinetics are associated with the mass transfer and electron-exchange processes that occur in the cell during discharge across a load, which cause the voltage to fall from its equilibrium value, and contribute to the overall polarisation (see Section 3.3) of a battery. Their effects are implicitly accounted for in the discharge profiles of the batteries and their change with time. Kinetic analyses show that polarisation for a given battery design is influenced by operating conditions and may be expected to increase with an increase in current, depth of discharge, and decrease in temperature².

3.3. Polarisation

When the cell is producing current, the terminal voltage varies from its zero current (open-circuit) value E^0 to its working value due to several internal resistance phenomena. The cell load voltage, E_L , can be expressed in the form:

$$E_L = E^0 - \eta_a - \eta_c - IR \quad \text{Equation 3.5}$$

where η_a and η_c are the overpotentials associated with polarisations at the anode and cathode respectively, and IR represents the voltage losses due to electrical connections and the catholyte resistance.

The IR polarisation is ohmic. An ideal battery system would have no internal resistance and thus there would be no energy loss within the battery other than that predicted by thermodynamics. However, the conductivity of any battery is not infinite, and in some practical cases the conductivity may be quite low. Because of this, the current flowing through the battery will cause some voltage drop that will be proportional to Ohm's Law.

The η_a and η_c polarisations are non-ohmic and are not linearly proportional to the amount of current flowing. In fact, voltage drop from non-ohmic polarisation usually increases exponentially with current because one or more kinetic processes cannot operate quickly enough to keep up with the demand placed on the battery by the external load. Two common causes are slow diffusion of a reactant species to or from an electrode surface and the slow transfer of an electron to or from a reactant at the electrode surface. Other types of non-ohmic polarisation exist such as the initiation of crystal growth.

The magnitude of the polarisation is dependent on a range of factors, including cell design and history, and tends to increase with discharge due to deposition of reaction

products. Its effect is also influenced by operating factors such as temperature, and the interrelationship between the various non-ohmic polarisation processes can become very significant towards end-of-life when the rates of mass transport of reactive species between the electrodes can become restricted.

3.4. Failure modes

On the basis of the thermodynamic and kinetic theory discussed above, the service life of a given battery will be governed by the degree of impact of polarisation and self-discharge. The exponential relationship between polarisation processes and discharge current implies that mass transport effects limit battery capacity at high rates, whereas the proportion of capacity lost due to self-discharge increases with operating and storage life.

CHAPTER 4

LITHIUM BATTERY OPTIONS

The key battery performance requirements for this application are:

1. High voltage and flat discharge curve (to give maximum energy capacity above the 2.5/3.2 V cut off voltage).
2. Compactness.
3. Long storage and service life.

In terms of battery selection, these requirements call for a high performance galvanic couple having a high volumetric energy density, high thermodynamic reversible cell potential, low polarisation through discharge, and low self-discharge rate (i.e. high Faradaic efficiency).

4.1. Electrode materials

The electrode materials should therefore have a high electrochemical equivalence (high coulombic output for a given volume of material) and a high electrode potential.

Table 4.1 Characteristics of some anode materials (from Ref. 1)

Material	Atomic weight g	E° (20 °C) V	Density g/cm ³	Valence change	Electrochemical equivalence	
					Ah/g	Ah/cm ³
Li	6.94	-3.05	0.54	1	3.86	2.08
Mg	24.3	-2.4	1.74	2	2.20	1.12
Al	26.9	-1.7	2.7	3	2.98	8.1
Ca	40.1	-2.87	1.54	2	1.34	2.06
Fe	55.8	-0.44	7.85	2	0.96	7.5
Zn	65.4	-0.76	7.1	2	0.82	5.8
Cd	112	-0.40	8.65	2	0.48	2.10

The main requirements of an anode material are efficiency as a reducing agent, and working voltage; also conductivity, stability and ease of fabrication and cost. The properties of selected anode materials are given in Table 4.1, and it is apparent that the electrochemical properties of lithium make it an outstanding candidate for high performance cell designs. It possesses the lowest standard electrode potential of all existing metals; it is the anode material that gives up its electrons most easily to form positive ions², and possesses the highest reduction potential of all anode materials. Associated with very oxidising species such as sulphuryl chloride (SO₂Cl₂), voltages as high as 3.92 V can be obtained³.

It is inferior only to aluminium and magnesium on a volumetric energy density (Wh/cm^3) basis, and its gravimetric electrochemical equivalence is the highest of the metals. Aluminium however, has not been used successfully as an anode material because of its poor electrochemical behaviour, and magnesium has a low operating voltage. The engineering properties of lithium are also favourable: it is one of the lightest of all elements; it is soft and malleable, can easily be extruded and is a good conductor of electricity.

A number of inorganic and organic materials have been examined for use as the cathode in primary lithium batteries. The critical requirements for the cathode material to achieve high performance are high battery voltage, a high energy density, and compatibility with the electrolyte. Elements of high standard electrode potential, such as halogens and more generally, all oxidisers can be used as cathode material because of their strong affinity for electrons. The electronegativity difference is reflected by the reversible cell voltage, which is maximised by the Li-F system selected from the upper rows of the periodic table. There are many choices of cathode material, including both liquid and solid depolarisers. A list of selected cathode materials used in lithium cells and their properties is given in Table 4.2.

Table 4.2 Cathode materials used in lithium batteries

Material	Molecular weight g	Density g/cm^3	Valence change	Theoretical faradaic capacity (cathode only)	
				Ah/g	Ah/ cm^3
SO ₂	64	1.37	1	0.419	0.30
SOCl ₂	119	1.63	2	0.450	0.27
SO ₂ Cl ₂	135	1.66	2	0.397	0.23
(CF) _x	(31) _x	2.7	1	0.86	1.16
MnO ₂	86.9	5.0	1	0.31	3.22
CuO	79.6	6.4	2	0.67	1.49

4.2. Lithium cell couples

Gabano⁴ lists the theoretical values of energy density and reversible cell potential (E°) of a range of lithium battery systems - for this application only couples having E° significantly greater than the lower operating voltage thresholds of the Meter A and Meter B (2.5 V and 3.2 V respectively) are of interest. The reversible cell potentials and volumetric energy densities of several lithium couples and their cell reactions are shown in Table 4.3.

Table 4.3 Cell reactions and theoretical energy densities and reversible cell potential of some lithium primary battery systems (Taken from Ref. 2).

Cell reaction	E° (V)	W_v (Wh/dm ³)
$2\text{Li} + \text{F}_2 \rightarrow 2\text{LiF}$	4.5*	6443
$4\text{Li} + 2\text{SOCl}_2 \rightarrow 4\text{LiCl} + \text{SO}_2 + \text{S}$	3.66	2005
$\text{Li} + \text{MnO}_2 \rightarrow \text{MnO}_2\text{Li}$	3.50	3097
$2\text{Li} + 2\text{SO}_2 \rightarrow \text{Li}_2\text{S}_2\text{O}_4$	2.91	1353
$2\text{Li} + \text{I}_2 \rightarrow 2\text{LiI}$	2.77	1920
$2\text{Li} + \text{CuO} \rightarrow 2\text{Li}_2\text{O} + \text{Cu}$	2.24	3140

* See Section 4.3.

4.3. Practical energy capacity and voltage

The LiF system would appear to offer the greatest potential for the application in terms of voltage and energy density. In practice however, the theoretical values of both E° and W_v function only as approximate indicators, and the measured values differ from theoretical values. Many factors influence these parameters, including design, storage, discharge rates, polarisation, etc. The Li/(CF)_x cell presents a notable and relevant example here. The measured value of the open-circuit voltage is 3.2~3.5 V. However, the theoretical value of E° calculated from the free energy of formation of LiF (-583 kJ/mol) and the heat of formation of (CF)_x (-195 kJ/mol) is around 4.5 V. Fukuda⁵ suggests that the difference derives either from E° being a mixed potential resulting from anodic reaction of the solvent with the cathodic reaction of (CF)_x, or by an intermediate ternary reaction.

The volumetric energy density of cell or battery is affected by non-active components (separator, current collector, etc.), and must also take account of factors that reduce the cell's faradaic efficiency, such as corrosion of the reactants (self-discharge) and polarisation below the application cut-off voltage. The effective energy density will therefore depend on the efficiency of the packaging of the various components. Liquid depolarisers can also act as the electrolyte, thus reducing required space and enhancing the volumetric energy density. The effective values of E° and W_v for a range of commercially available practical couples are given in Table 4.4 below.

4.4. Discharge curve

A flat discharge curve (constant voltage and impedance through most of the discharge) is typical for most lithium systems. Discharge curve profiles are influenced by the location and resistivity of the discharge products that generally accumulate

between the electrodes and lead to increases in cell polarisation and impedance through discharge.

The discharge profiles of a range of battery systems reproduced from Linden's Battery handbook⁶ are given in Figure 4.1. Liquid cathode systems (e.g. Li/SO₂, Li/SOCl₂ and Li/SO₂Cl₂) offer the flattest discharge curves, because the cell impedance remains virtually constant until either the carbon cathode becomes passivated, or the anode and cathode materials are depleted,. Thus they are of particular interest here. Solid cathode systems such as Li/MnO₂ and Li/(CF)_x exhibit relatively flat profiles, although polarisation becomes more significant in the final third of discharge.

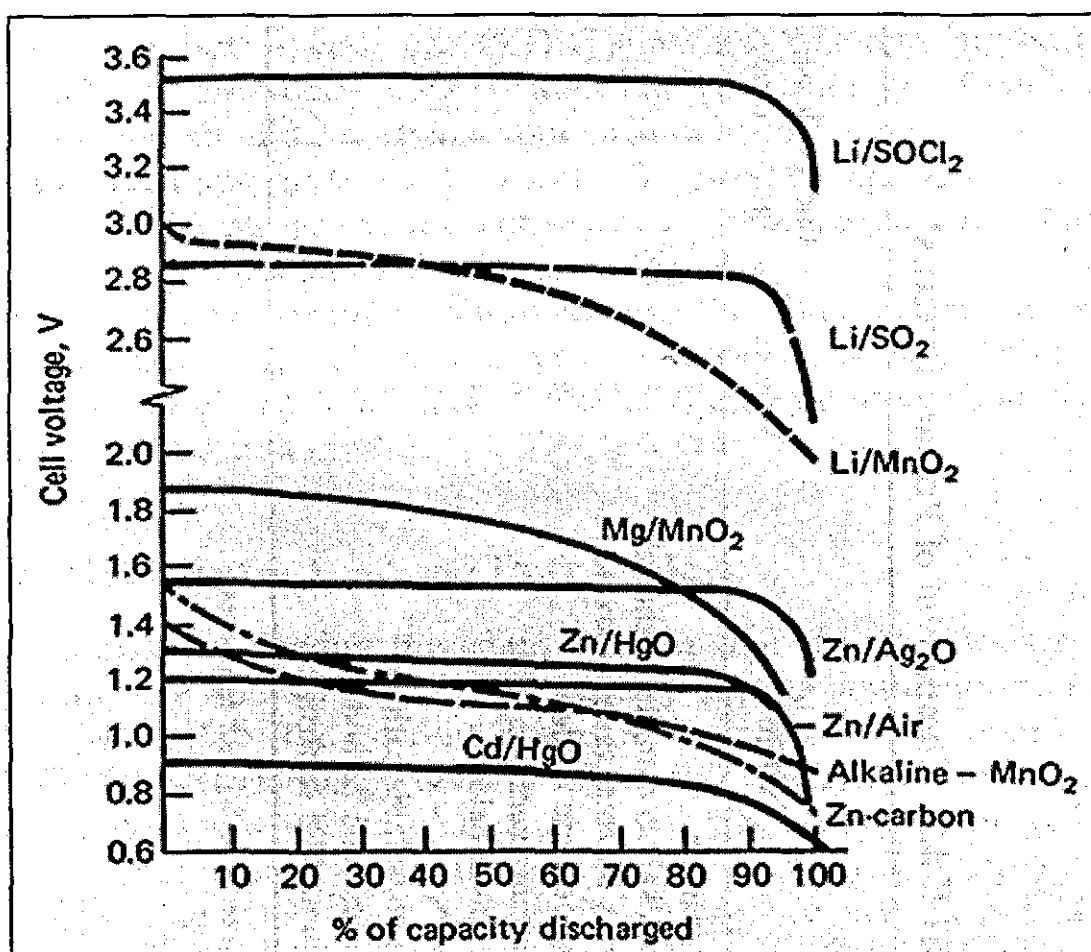


Figure 4.1 Discharge profiles of primary battery systems (from Ref. 6).

4.5. Storage and service life

Lithium is (unexpectedly) stable in non-aqueous electrolytes. This is due to the formation of an insoluble salt film which is created on the metal by reaction with the electrolyte during the first moments of contact⁷. This film selectively passes lithium ions, but is (almost) impermeable to solvent and anions, and possesses an exceedingly low electronic conductivity. While this layer remains intact, the corrosion reactions

are minimised and self-discharge occurs at the lowest rate of all battery systems, implying that the lithium non-aqueous electrolyte system offers the greatest potential in terms of service life.

4.6. Energy density and performance parameters

Table 4.4 Comparative design and performance parameters of primary batteries (taken from Ref. 8)

System	Load Voltage (V)	Energy density (Wh/l)	Power density	Flat discharge profile?	Operating temperature (°C)	S.D. rate % p.a.
Li/SOCl ₂	3.3	650	Low	V. flat	-40 to >70	2
Li/MnO ₂	2.7	450	Mod.	Flat	-20 to 55	3
Li/(CF) _x	2.6	450	Mod.	Flat	-20 to 55	3
Zn/alkaline	1.2	220	Mod.	Mod. slope	-20 to 55	7
Zn/carbon	1.2	100	Low	Sloping	-5 to 45	15
Mg/MnO ₂	1.7	195	Mod.	Mod. slope	-20 to 60	3

The properties of commercially available cell designs are summarised in Table 4.4. As can be seen, the lithium primary cell technologies possess the highest performance spectrum in terms of voltage, energy density, temperature and discharge characteristics, and also present the lowest self-discharge rates. These properties make them the outstanding option for the present meter application.

The Li/SOCl₂ couple offers the highest practical volumetric energy density. This is mainly due to the fact that the SOCl₂ serves a dual role: as an electrolyte carrier for ions and as the active cathode depolariser on the catalytic surface. This dual role provides a significant energy density advantage over solid cathode systems which require a separate electrolyte.

However, the Li/MnO₂ and Li/(CF)_x systems are useful alternative technologies. Both offer similarly high energy densities, but operate at a load voltage which is significantly lower than that of the Li/SOCl₂, and in a single cell or parallel format they can only be of interest to Meter Type A, whose lower voltage threshold is 2.5 V

4.7. Status review of mass produced lithium primary cells

Having identified potential systems, it is instructive to review the historical development and present status of available manufactured systems, and the accepted knowledge regarding reliability, safety and electrical performance. This is because battery quality and reliability tend to be linked to production methods and quality systems, which are in turn influenced by product maturity and volume sales.

Interest in the use of lithium as an anode material in high energy density batteries was rekindled in 1958 after it had been demonstrated that metallic lithium could be deposited from organic electrolytes comprising lithium salts dissolved in organic solvents such as propylene carbonate^{9,10}. In the 1960s, NASA pioneered the serious development of lithium high energy density systems as a power source for space development projects, when their perceived advantages of very high energy density, high operating voltage, and ultra-long service life potential were first demonstrated. Over the past thirty years technological progress (particularly initially in the space and military fields) has substantially increased the demand for high voltage, compact and long-life electrical power sources. Lithium cells were first used in applications in the early 1970s for selected military and later space roles. However, their range of use was limited because suitable cell structures, formulations and safety considerations had to be resolved¹¹.

Subsequent progress made in battery developments, particularly in resolving the safety and reliability problems of mass produced lithium technologies, has made such systems viable for use in Original Equipment Manufacturer (OEM) applications such as utility metering. By the early 1980's a range of lithium primary battery technologies had emerged, stimulated by advances in the miniaturisation of electronic technologies, and the attendant need for compact long-life power sources (e.g. in biomedical devices), and progress in resolving the above problems.

In terms of their general usage, mass produced primary lithium batteries can be classified according to the phase of the cathode material:

1. Liquid cathode systems developed originally for military and specialist high-power applications, which possess a very high effective energy density and high and stable voltage through discharge.
2. Solid cathode systems developed for consumer applications (cameras, watches, etc.), which have a lower effective energy density and slightly sloping operating voltage characteristic but which are generally considered as presenting a lower hazard profile.

4.7.1. Liquid cathode systems

The Li/SOCl₂ cell belongs to a family of liquid oxidant cell systems in which the reductant component (lithium) and the oxidant component (SOCl₂) are initially placed in direct contact with one another. Other members of the family include

lithium/sulphur dioxide, lithium thionyl chloride with bromine chloride dissolved in the catholyte, lithium sulphuryl chloride, and lithium sulphuryl chloride with chlorine dissolved in the catholyte. Of these only the Li/SOCl₂ based system have seen any significant usage in OEM applications.

In 1969, Gabano¹² patented the liquid cathode system, using SOCl₂ as a solvent for chlorine (or bromine), in a rechargeable lithium cell with 1.0 M LiAlCl₄ added as electrolyte. E° was measured at 3.67 V. In 1973, a Li/SOCl₂ cell which incorporated a carbon cathodic current collector resulted in the technology becoming generally accepted when Auburn¹³ and Behl¹⁴ described such a system. In the 1980s, Li/SOCl₂ cells began to be utilised in OEM applications, although in relatively low volumes when compared with the solid cathode systems¹⁵ discussed below. SOCl₂ is corrosive and volatile, creating engineering and safety problems that required special solutions (e.g. SOCl₂ corrosion resistant materials, hermetic sealing and special glass formulations in the glass to metal seal, development and incorporation of a purpose designed pressure vent).

The safety hazard is a particular concern with spiral wound designs, because fault conditions such as external and internal short-circuit may generate extremely high discharge currents. This renders the cell susceptible to thermal run-away and explosion. This hazard has been virtually eliminated by the introduction of low-rate Li/SOCl₂ designs; these were first introduced 17 years or so ago, and the annual production rate of all sizes is now millions per annum. The author has recently completed a detailed review of the safety record and performance of lithium batteries used in consumer and OEM applications¹⁶. The combination of (a) several years of incident free operation¹⁶, particularly recently in metering applications, and (b) the positive BG safety test results have now demonstrated that the low-rate cell design is stable under all reasonable levels of stress. The Li/SOCl₂ system is therefore deemed to be acceptable for the meter application. The development of solutions to the corrosion problems also retarded the rate of introduction of Li/SOCl₂ cells into the civil marketplace. But larger cell sizes in the E6 meter range of interest ('C', 'D') are now available from European and US manufacturers.

4.7.2. Solid cathode systems

Solid cathode systems can be classified in two groups: low operating voltage systems, 1-1.8 V (Li/CuO and Li/FeS₂); and medium voltage systems, 2.5-3 V (Li/MnO₂ and

$\text{Li}/(\text{CF})_x$. Li/MnO_2 and $\text{Li}/(\text{CF})_x$ are the only two of the solid cathode types of battery that generate a load voltage above 2.5 V and are suitable to the meter application in a single cell format. Both have high volumetric energy densities of between 400 and 600 Wh/l, and were among the first lithium/solid cathode systems to be used commercially for low to medium discharge rate applications.

The Li/MnO_2 system became viable in 1975 when Sanyo¹⁷ solved a number of basic performance problems by developing an improved heat treatment of synthetic active forms of MnO_2 . The $\text{Li}/(\text{CF})_x$ system was first developed by Matsushita in the early 1970s; mass production started in 1976¹⁸. The latter part of the 1970s saw the introduction of both of these systems, particularly by Japanese manufacturers who targeted the systems for huge volume consumer applications such as cameras, shavers, etc. The majority of production output is in small cell sizes suitable for the consumer applications, however $\text{Li}/(\text{CF})_x$ cells are manufactured by Panasonic in Japan in sizes up to 'C'. US designers are researching the system, but are not known to have produced any products of interest to this application. Li/MnO_2 cells are manufactured in high-rate spiral configurations in sizes up to 'D', by Fuji in Japan, in Europe, and in the US.

4.8. Battery reliability and QA

Battery reliability is defined as the probability that a group of batteries will deliver the required electrical service to the lower voltage limit, the cut-off voltage¹⁹. After 30 or so years of development, it could be thought that lithium primary cell design has now matured, and that reliability is well established (as for other electronic components). However, lithium primary batteries are a still evolving technology²⁰. In comparison with consumer types of battery (e.g. alkaline cells and watch batteries) which are mass produced in billions, lithium battery production is several orders of magnitude lower, and details of cell design are much more likely to vary with time. Experience has demonstrated that ongoing changes in the component design, manufacturing processes and procedures represent the rule rather than the exception²⁰, and that the quality and performance of lithium cells can vary from lot to lot and from manufacturer to manufacturer. No database of the performance of the range of lithium technologies is available, so expectations for good reliability should be addressed with caution.

Unfortunately, no reliability standard has ever been formally established for conventional primary batteries²¹. The goal is zero defects for the present application,

and the manufacturers of candidate batteries were generally confident of the ability of their systems to meet the required service life. The manufacturers based their estimates of service life on the difference between battery starting capacity and capacity lost by (a) self-discharge, assuming an annual temperature cycle of 6 months each at 30 °C and 0 °C, and (b) powering the meter. However, the meter application sits at the extreme end of the known performance spectrum, and although data is available from certain of the manufacturers, this is of limited value as no analogous application appears to exist.

4.9. Tolerances

Statistics play a significant role in battery modelling, since even batteries free of gross defects often show statistical variations of performance²². These are a reflection of variations associated with cell construction, electrolyte composition, separator homogeneity, and reproducibility of assembly operations.

Wide variations in reliability of different cell designs were still being reported in the literature²³ in 1997. In 1996 the author was consulted regarding premature failures that were occurring with two battery applications involving standard production Li/SOCl₂ cells (supplied by candidate manufacturers). In one application²⁴, a simple pulse load static device operating at room temperature with a 5 year battery service life expectancy, the pack of 4 AA cells suffered a high incidence rate of failure after less than 1 year. The second application involved a pair of double 'D' cells powering externally located gas pressure telemetry equipment, which suffered a high incidence of failure during the first cold spell of winter after some months in the field. In both cases, the manufacturer was unable to explain the failures, in the first the problem was solved by procuring Li/SOCl₂ cells from another manufacturer, and in the second the battery design was modified (the upright/upside-down configuration was changed in favour of both cells mounted upright).

Quality Assurance (QA) should play an important role in defining the uniformity of cell construction and the eventual capacity distributions in service. The manufacturers all claim adequate QA procedures, but qualitative information gained through visits to the manufacturing plants and discussions with the various manufactures strongly suggests that considerable differences in standards exist in practice. All manufacturers include 100% quality tests during manufacture (OCV and CCV,

weight, continuity, etc.), however none of these tests provide an accurate and effective predictor of future battery performance and capacity.

4.10. Practical E6 meter battery options

The range of lithium primary batteries that comply with the basic commercial and performance requirements of the E6 meter specification are listed in Table 4.5, together with some of their basic design and performance characteristics.

It is evident that all three technologies satisfy the 2.5 V cut-off voltage requirement of the Meter A design. It is of interest to note that rated capacity of the solid cathode batteries is limited to approximately 10 Ah in the recommended battery pack configurations (1×D, 2×C). The specified capacity requirement for meter A is ~9 Ah; providing minimal allowance for manufacturing, operating tolerances and self-discharge.

Because of its intrinsic high electrical performance characteristics, the Li/SOCl₂ system stands out as the best option for the meter application, and is the only candidate having a working voltage high enough to satisfy the power requirement of Meter B design. At an early stage two manufacturers of Li/SOCl₂ cells, Saft and Tadiran Ltd., and one Li/(CF)_x manufacturer (Panasonic), expressed keen interest in the application, appeared to offer mature designs and good manufacturing quality. On the basis of acceptable safety performance, cells from these manufacturers were approved for use in the meters.

Table 4.5 Practical E6 meter lithium battery options and basic details

System	Manufacturer	Country of origin	E_L (V)	Cell size for meter appln. (ANSI)	Rated Capacity (Ah)
Li/SOCl ₂	Tadiran	Israel	3.65	1 off 'D' cell	19
	Saft	France	3.65	1 off 'D' cell	16
	Eagle Picher	US	3.65	1 off 'D' cell	16
	Crompton Eternacell	UK	3.65	1 off 'D' cell	14
Li/(CF) _x	Panasonic	Japan	2.7	2 off 'C' cells	10
Li/MnO ₂	Hoppecke	Germany	2.7	1 off 'D' cell	10
	Dowty (Ultralife)	UK	2.7	1 off 'D' cell	10
	Sanyo	Japan	2.7	2 off 'C' cells	10

As the study evolved, the additional manufacturers also listed in Table 4.5 expressed interest in the application, and submitted batteries for evaluation. Tests were carried out on this range of technologies, however as the key project aim is to identify a general solution that can be used to power both types of meter, the research reported

in this thesis is restricted to the Li/SOCl_2 technology, and specifically to cells submitted by the four manufacturers listed. It is of interest to note that both the Hoppecke and Ultralife plants were destroyed by fire during the course of these evaluations. This event, and the relatively higher cost of Li/MnO_2 spiral wound cell designs, effectively discounted this technology from the list of practical options for the meter application.

CHAPTER 5

DESIGN OF Li/SOCl₂ BATTERIES

The volumetric energy density of Li/SOCl₂ cells is among the highest of all battery systems. The effective open-circuit voltage is 3.67 V. The load voltage at the E6 meter drain rates is significantly higher than the respective 3.2 and 2.5 V cut-off thresholds for the two meters, and the voltage profile during discharge is almost flat. The storage characteristics of the system are outstanding, low rate cells stored for 5 years have demonstrated 97% of their original capacity¹, and the operating temperature range is exceptionally wide: -55 °C to >150 °C. The system is the only one available in the commercial marketplace that can satisfy the power requirements of Meter type B, and which is available at a competitive price and in volume production. In addition, it potentially offers the longest service life to both meters.

5.1. Basic cell reaction

The mechanism for the discharge at the anode is the oxidation of lithium to form lithium ions with the release of an electron. The lithium ion moves across the cell to the porous carbon cathode (pce) where it reacts with SOCl₂ to form lithium chloride (LiCl). The electron moves through the external circuit to the cathode where it reacts with SOCl₂, which is reduced. The overall cell reaction is given in Equation 5.1.



5.2. Engineering design of the candidate cells

The Li/SOCl₂ cell comprises a lithium foil anode, a porous carbon electrode which acts as the positive electrode, a separator, and a non-aqueous thionyl chloride/lithium tetrachloroaluminate (SOCl₂:LiAlCl₄) mixture. SOCl₂ serves as both the electrolyte and active cathode material; LiAlCl₄ is added to enhance conductivity, and the composition is termed the catholyte.

Two geometric designs of Li/SOCl₂ cells exist which are of specific interest to this application, namely: the bobbin cell that is utilised in cell types Ta, Td and Te, and the 'squat spiral' configuration utilised in the Tb design. The cells are cylindrical in shape, and conform to ANSI standard D size cylindrical configuration, approximately 63 mm high and 33 mm in diameter.

The 'bobbin' geometry is configured with a relatively low surface area of lithium, A_a , and is designed for low current applications. A low A_a minimises self-discharge and

as the bobbin design typically requires a lower volume of internal components it also lends itself to maximised energy density. The engineering design of a typical bobbin construction Li/SOCl₂ cell is shown in cross-section in Figure 5.1, with the main components identified.

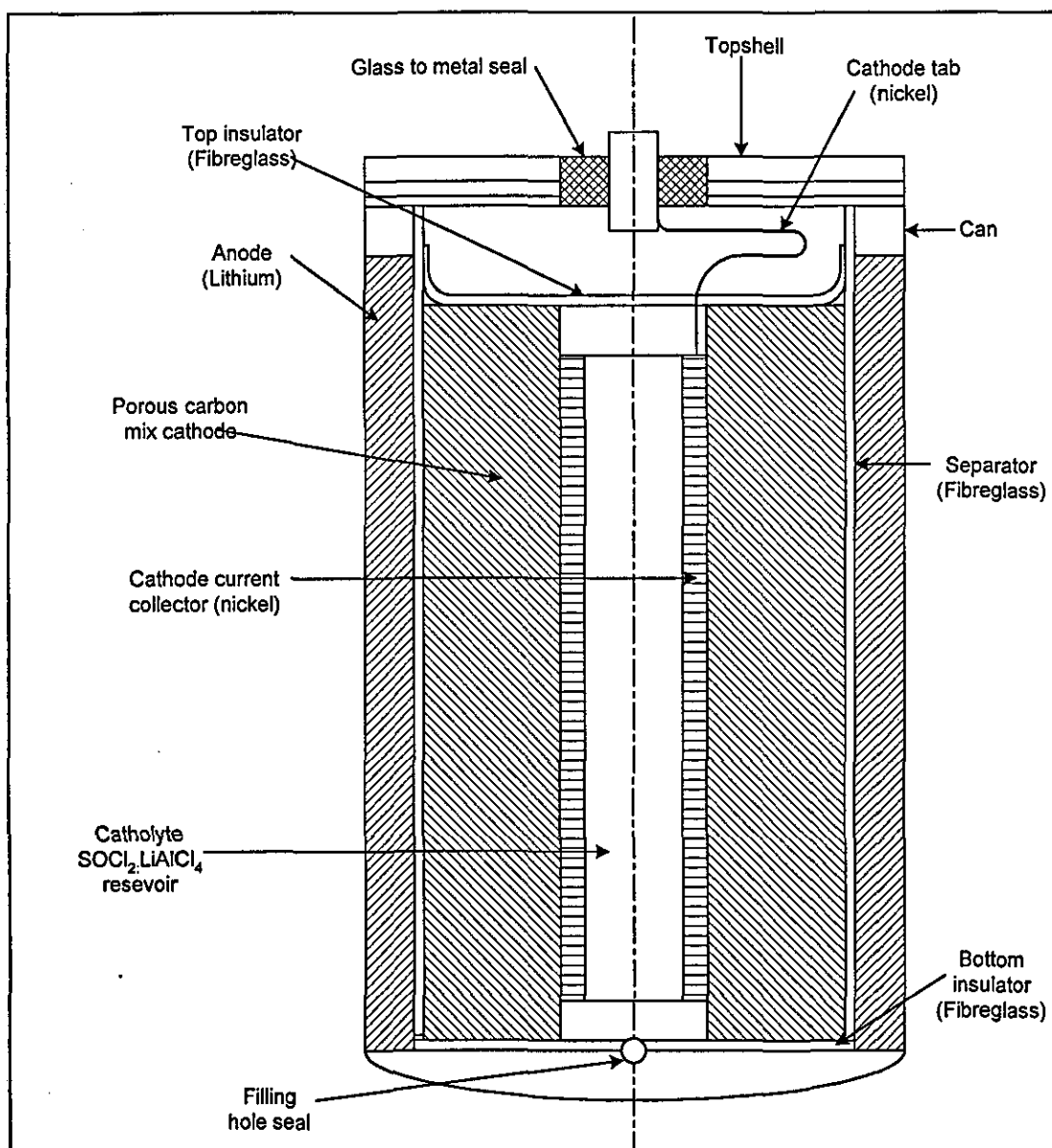


Figure 5.1 Cross-sectional view of a bobbin cell.

Typically, the electrodes of a bobbin cell comprise a lithium strip which is cold-welded onto the inner surface of the can to form an annular anode, and a hollow cylinder of porous carbon at the centre which forms the positive electrode. To prevent electronic contact between the two electrodes and to ensure electrolyte distribution over their surfaces, a separator is located around the carbon electrode. A cathodic current collector is placed in the central hole of the carbon and welded to the centre

pin of a glass to metal (GTM) seal, which also insulates the positive and negative battery connections. Because of the high oxidising properties of thionyl chloride, only very stable materials are used internally. The separators are made from glass fibre and the can is made of stainless steel, or nickel-plated rolled steel. Cell filling is carried out under vacuum, and the cell is closed by welding a steel ball onto the filling hole.

The 'squat-spiral' design is optimised for operation at low to medium discharge rates. Cieslak has published some details of this design². It is known that the electrode assembly comprises a strip of negative current collector, lithium anode, separator, carbon cathode and positive current collector, which is wound through 1.5 turns. Both the anode and cathode are pressed onto metal current collectors which are connected to the positive and negative battery terminals. The laminated strip is wound into a spiral whose centre is mounted on the central axis of the can.

All of the Li/SOCl₂ cells tested here incorporate a pressure relief vent, whose function is to evacuate the liquid SOCl₂ in the event of thermal runaway caused by an abuse condition, such as short circuit. Various designs of vent are utilised; their function is to open at 100-120 °C, giving a safety margin of approximately 60 °C below the melting point of lithium (180.5 °C).

In types Ta, Td and Te the can is negative, in Tb it is positive.

5.2.1. Materials balance

Marincic³ showed that cells made for low rate application must include extra electrolyte stored outside the electrode structure, in order to compensate for volume reduction, avoid bubble formation within the pce, and to provide sufficient catholyte to allow complete utilisation of lithium. By empirical analysis, Eichinger and Gabriel⁴ found that capacity optimisation of a bobbin type cell discharged at low to medium rates involved a trade-off between lithium thickness and the amount of catholyte, and that the carbon cathode was not the limiting factor.

The amounts of reactants, compositions of electroactive components and polarity of the can of these four battery types are given in Table 5.1. Manufacturers classify much of the relevant information as proprietary (for example the formulation of the catholyte); for this reason the database is incomplete in several areas. The Te design is SOCl₂ limited, whereas the other three designs incorporate a slight excess of SOCl₂.

Table 5.1 Summary of manufacturers' declared Li/SOCl₂ cell design parameters.

Manufacturers' declared cell design capacities and parameters					
Cell Test Code	Anode Surface Area cm ²	Anode Stoich. Cap. Ah	Catholyte composition	Catholyte Stoich. Capacity Ah	Carbon electrode materials
Ta	37.4	17.4	Li/SOCl ₂ + LiAlCl ₄ + SO ₂	17.8	Blended Ac. Black + PTFE
Tb	145	17.6	Li/SOCl ₂ + LiAlCl ₄ + ?	19.3	(50/50) Shawingian Ac. black + Cabot black pearls
Td	42.5	17.5	Li/SOCl ₂ + LiAlCl ₄ + anti delay adds.	17.7	Ac. Black + PTFE
Te	45	>19.6	Li/SOCl ₂ + LiAlCl ₄ + ?	19.6	Carbon + PTFE

Abbreviations: Ac. = Acetylene, Stoich. = Stoichiometric.

The manufacturers' declared values of the stoichiometric capacity, Q_0 , of the four Li/SOCl₂ 'D' size cell types are given in Table 5.2, below. It may be seen that Q_0 for type Te is significantly greater than that for any of the other batteries, and that there is very little difference between the values of Q_0 for types the Ta, Tb, and Td.

Table 5.2 Manufacturers' declared stoichiometric capacities of Li/SOCl₂ 'D' size cell types

Battery type	Te	Tb	Td	Ta
Q_0 (Ah)	19	17.6	17.5	17.4

5.3. Anode design

Lithium is ductile and mechanically strong, and has a melting point of 180.5 °C. Two anode geometries are utilised in the designs of the cells tested here.

The general anode arrangement for the bobbin geometry used in battery types Ta, Td and Te is as shown in Figure 5.1, and comprises a strip of lithium foil that is swaged onto the inner surface of the can wall. The values of A_a for the different cells are given Table 5.1, generally the area is approximately 45 cm² for a 'D' size cell of the bobbin geometry. The direct connection of the lithium to the can gives the case its negative polarity.

In the squat spiral design utilised in type Tb, the lithium foil is pressed onto an expanded nickel screen anode. A laminate is formed of the separator, cathode and nickel mesh current collector, which are pressed together and wound through one and

a half turns to form a squat spiral. The value of A_a for this geometry is 145 cm^2 , and the cell is case positive.

In both types of design, the anode faces the carbon cathode from which it is isolated by the separator. The packing of these three components is fairly tight (a separation in bobbin cells of 0.5 mm has been quoted⁵).

Both the maximum power output and corrosion rate are proportional to A_a . For low rate, long-term pulsed applications, it is desirable to minimise the magnitude of A_a exposed to the SOCl_2 in order to minimise self discharge. The limiting area is defined by the need to achieve a current density sufficient to service the high amplitude part of a pulsed load. The relatively low value of A_a of these designs (by comparison with high rate spiral wound configurations) restricts both the maximum electrical discharge and self-discharge rates of the reactants, and enhances the volumetric energy density and safety performance.

5.4. Catholyte formulation

The liquid SOCl_2 serves a triple role: as an electrolyte carrier for ions; as the active cathode depolariser (oxidant) on the carbon cathode surface; and thirdly as a solvent to which an electrolyte is added to increase the conductivity and facilitate the transport of Li^+ ions dissolved in the solution. LiAlCl_4 is employed as the electrolyte in all of the cells included in this programme. The liquid $\text{SOCl}_2\text{:LiAlCl}_4$ mixture comprises both cathode and electrolyte materials and is conventionally termed the catholyte (to distinguish it from a simple electrolyte).

The catholyte must have a high electrical conductivity to minimise ohmic losses in the battery, must facilitate the anode reaction with low overpotential, and must be capable of being reduced on the cathode with low overpotential. Ideally it should also act to minimise self-discharge rates and polarisation effects resulting from the anodic film.

Catholyte composition is based on compromises between characteristics such as viscosity, conductivity, surface tension, vapour pressure and discharge rate, all of which affect overall cell performance. Catholyte conductivity varies with concentration, temperature and the above solvent properties⁶, and electrical performance is also affected by transport properties. Dey⁷ found that cell capacity is a function of catholyte concentration, with 1.0 LiAlCl_4 being optimum. He later found that higher concentrations improved (high) rate capability, with 1.8 M being the

optimum⁸, and this is still the general view⁹, the high concentration being necessary to minimise Li^+ concentration polarisation effects¹⁰.

It is important to note that manufacturers commonly incorporate so-called catholyte additives to modify and optimise cell performance. Much attention has been applied to minimising voltage delay. However, an additive designed to improve performance at one end of the spectrum may reduce performance at the opposite end. The manufacturers are unwilling to supply the formulation details of the catholyte. The available data on the catholytes of the cells under test here is given in Table 5.1, however the absence of compositional details precludes the estimation of their effects on performance.

The catholyte volume must be great enough to provide for complete flooding of the porous carbon electrode and the anode working surfaces. During discharge, the lithium and catholyte volumes reduce as they are utilised; the free volume also reduces as the solid reaction product is precipitated, but inter-electrode separation increases.

5.5. Positive carbon electrode (pce) design

The positive carbon electrode (pce) has several functions:

1. The carbon substrate provides a conductive path between the current connector and the site of electro-reduction.
2. Reduction of the SOCl_2 takes place at the surface of the carbon.
3. The pores form a space for the accumulation of the insoluble reaction products (S and LiCl).
4. The pores contain a certain amount of catholyte solution to promote the reaction and the necessary transport processes.

The pce is usually made from amorphous carbon powder with a (~10%) PTFE binder, the filamentary nature of which minimises blockage of the active carbon surface¹¹. It is known that cathode performance is dependent on porosity, pore size distribution, pre-treatment processing, impurity content, PTFE/C balance, as well as being inter-related with other design factors (catholyte composition, packing pressure, provision for cathode swelling), and operational variables such as temperature and discharge rate. In practice, manufacturers use blends of different carbons, as can be seen in the summary of design parameters in Table 5.1. Unfortunately the details of the compositions are proprietary information.

As can be seen in Figure 5.1, in the low-rate bobbin cell (Ta, Td and Te designs), the pce is an annular bobbin in shape. A pre-formed cylinder of expanded nickel is inserted into the annulus to act as the current collector. Sometimes it is inserted under compression so that it expands against the pce to maintain a positive contact throughout discharge. The sprung assembly maintains a minimum separation between anode and cathode as the anode contracts and the pce expands. The carbon bobbin is either pre-formed (by extrusion) as a single unit, or as in the case of battery type Td, it is formed of carbon/PTFE granules which are poured into a pre-formed cavity on manufacture and pressed to obtain the required shape.

In the spiral wound design (Tb) the pce is made up of two 0.9 mm thick parts lying together and acting as a single electrode².

5.6. Passive cell components

The passive cell components comprise: the anode/cathode separator, the case/anode/cathode insulators (top and bottom), the can, the current collector(s), the glass to metal seal, the vent (if a separate component), and the internal connectors. The separator must be thin, highly porous, and an electronic insulator. Its function is to provide an ionically conductive path between the electrodes, but to prevent direct electrical contact. In common with the other internal components it must be inert to all of the materials with which it is contact, both under normal and abuse conditions. The most commonly used insulating material is non-woven glass, which is compatible with the catholyte¹², highly porous and inexpensive, but which lacks strength¹³. Nickel and stainless steel are stable in contact with $\text{SOCl}_2\text{:LiAlCl}_4$ catholyte; the can is normally made either of stainless steel, or nickel-plated rolled steel, while the current collector and connectors are commonly fabricated from nickel. Corrosion of glass in glass to metal seal was a problem in early liquid cathode cells and considerable research has been carried out to identify a resistant glass¹⁴. This research was successful, and a range of glass materials is employed by the manufacturers.

CHAPTER 6

LI/SOCl₂ CELL PROCESSES

Although initially considerable uncertainty regarding the exact cell reaction existed¹, the currently accepted half cell and complete reactions giving the open-circuit cell voltage of 3.67 V are as follows.

The mechanism for the discharge at the anode (negative electrode) is the oxidation of lithium to form lithium ions with the release of an electron:



The lithium ion, which is small (0.06 nm in radius)² and mobile in both the liquid and solid state electrolytes, moves across the cell to the pce where it reacts with SOCl₂ to form lithium chloride (LiCl); the electron moves through the external circuit to the pce where it reacts with SOCl₂, which is reduced. The detailed mechanism for the reduction of thionyl chloride at the pce is complicated and still subject to uncertainty, but it is generally agreed that the reaction at the cathode is as follows:



These two electrode reactions combine to give the overall cell reaction:



Hill et al³ showed that under low rate discharge conditions (7.5 to 45 μA), Li/SOCl₂ cells showed evidence of a perturbation of reaction mechanism below -30 °C (outside our range of interest), and that there was no unambiguous evidence for changes through discharge. It is unlikely that cell performance will be significantly affected by temperature related changes in reaction mechanism here.

The electrochemical discharge products are formed at the surface of the carbon. Sulphur is soluble up to about 1 mol/m³ and is distributed throughout the cell once its saturation limit is reached⁴. Sulphur dioxide is soluble in the catholyte and forms a complex with LiAlCl₄ ($\sim\text{Li}^+(\text{SOCl}_2)(\text{SO}_2)_2\text{AlCl}_4$), which restricts the formation of gaseous SO₂ and minimises the vapour pressure in the cell⁵. LiCl is almost insoluble and precipitates throughout the cell as it is formed⁶.

Although the discharge products of the Li/SOCl₂ reaction consist in part of the highly resistive solids LiCl and S, the salient operating characteristic of the system is its uniformly low impedance and high load voltage through the majority of the discharge life of the battery. This is in marked contrast to many electrochemical systems where

the impedance increases in approximately linear proportion to the degree of discharge. The critical difference lies in the disposition of the electrochemical discharge product, which is deposited within the high-surface-area carbon depolariser. Because of the high cathode surface area of the pce, A_c , the overall impedance generally remains low until the active sites approach full utilisation. The site of formation is related to the manner in which charge is passed through the conductive cathode medium. In Li/SOCl₂ cells the steady-state discharge current is passed through the SOCl₂:LiAlCl₄ catholyte via electro-migration of the Li⁺ ions dissolved in solution. Reduction occurs near the surface of an electrochemically active part of the porous carbon element, and the insoluble LiCl discharge product is deposited at that point⁶.

The low freezing point of the electrolyte of -105 °C, and its relatively high boiling point of 78.8 °C enable the cell to operate over a wide range of temperature.

The electrochemical cell capacity decreases markedly both at low temperature and high rate, due to mass transport limitations which cause the reduction of SOCl₂ to occur primarily near the surface of the carbon cathode. The LiCl precipitate then forms on the outer surface layers of the pce, thereby blocking access to active surfaces within the pore structure. The maximum capacity of the cathode is attained under conditions of moderate to high temperature and low current, i.e. conditions which promote a uniform current density throughout the cathode.

6.1. Polarisation

When the cell is producing current, the terminal voltage varies from its zero current (open-circuit) value E^0 to its working value, E_L , due to internal resistance phenomena, which generate overpotentials at the positive and negative electrodes and IR losses in the catholyte, as follows:

$$E_L = E^0 - \eta_a - \eta_c - IR \quad \text{Equation 6.4}$$

where η_a and η_c are the polarisations at the anode and cathode respectively, and IR represents the voltage losses due to electrical connections and the catholyte resistance. Polarisation at the anode and cathode include contributions from several processes, the magnitudes of which vary according to the cell history, depth of discharge and operating conditions. By systematically examining the contributions of each of these processes through discharge, it is possible to identify and characterise the processes most likely to induce premature failure during accelerated discharge, and which will govern the long-term performance and reliability of cells in the meter application.

6.2. Anodic overpotential (η_a)

The anodic overpotential comprises the components given in Equation 6.5:

$$\eta_a = \eta_{CTa} + \eta_{PL} + \eta_{DIFFa} \quad \text{Equation 6.5}$$

where:

η_{CTa} = Charge transfer at the anode ($\text{Li} - e^- \rightarrow \text{Li}^+$).

η_{PL} = Ion transport through the passivation layer (PL), ($\text{Li}^+_{PL} \rightarrow \text{Li}^+_{\text{SOCl}_2}$).

η_{DIFFa} = Concentration polarisation of non-charged species in the catholyte, primarily SOCl_2 .

The charge transfer overpotential (η_{CT}) at an electrode under load is given by the high overpotential limit approximation of the Butler-Volmer equation⁷:

$$\eta = -RT \ln(j/j_o) / z \alpha F \quad \text{Equation 6.6}$$

where z is the number of electrons involved in the rate determining step, α is the charge transfer coefficient, and j and j_o are respectively the load and exchange current densities at the electrode.

At the lithium metal catholyte interface, j_o for the formation of the Li^+ ion is very high (45 mA/cm^2), and η_{CTa} for the values of j utilised in the accelerated tests and in the meter is very low, and may be neglected here.

η_{PL} and η_{DIFFa} are the overpotentials due to the passivation layer (PL), and are functions of its effective thickness and morphology as described in detail in Chapter 7.

η_{PL} is the ionic resistance of the PL matrix, it is linear and increases with current in accordance with Ohm's law. η_{DIFFa} is due to concentration polarisation within the PL, and is function of time and current, as given by the Sand equation⁸ (Equation 6.7).

$$\tau_p^{-1/2} = 2j / [zFA(\pi D_0)^{1/2} C^b] \quad \text{Equation 6.7}$$

where τ_p is the time for the concentration of products at the electrode surface to a sudden change to a value to cause a concentration overpotential, A is the effective electrode active area, D_0 and C^b are the diffusion coefficient and bulk concentration of the rate determining species, respectively. η_{DIFFa} becomes dominant at high values of current density and pulse duration. D_0 for an ion is related to viscosity η by the equation⁹:

$$D_0 = kT / 6\pi\eta a \quad \text{Equation 6.8}$$

where k is the Boltzmann constant, and a is the effective radius of the ion in solution.

In its simplest form, the conductivity of the catholyte, κ , is given by current density divided by the potential gradient, i.e.

$$\kappa = (I/lE) \quad \text{Equation 6.9}$$

where I , l , and E are respectively the current, length and potential difference of the system. The conductivity of a two phase matrix such as the PL is influenced by the volume fraction of the conducting phases, and the manner in which the phases are interconnected¹⁰. Chenebault et al.¹¹ state that the ionic conductivity of $\text{SOCl}_2\text{:LiAlCl}_4$ is 10^{-2} S/cm, which is much higher than that of LiCl (10^{-10} S/cm). Current flows wherever the ohmic resistance is lowest, which in this case is through the liquid phase, i.e. through voids and cracks in the PL. Thus, for the anode, the LiCl fraction does not contribute to ion transport, and the matrix conductivity of the PL is governed by the dimensions of the active (open-ended) voids and cracks in the PL matrix structure. Chenebault¹¹ gives a matrix conductivity in the region of 10^{-5} S/cm.

6.3. Cathodic overpotential (η_{Ca})

The cathodic overpotential is composed of the following factors:

$$\eta_{\text{Ca}} = \eta_{\text{CTc}} + \eta_{\text{SOLc}} + \eta_{\text{DIFFc}} \quad \text{Equation 6.10}$$

where:

η_{CTc} = overpotential of the charge transfer at the pce,
($2\text{SOCl}_2 + 4\text{e}^- \rightarrow \text{SO}_2 + \text{S} + 4\text{Cl}^-$).

η_{SOLc} = overpotential attributable to ionic mobilities within the porous carbon structure and the bulk catholyte ($\text{Li}^+_{\text{SOCl}_2} \rightarrow \text{pce}$, and $\text{AlCl}_4^- \rightarrow \text{anode}$).

η_{DIFFc} = overpotential due concentration polarisation of non-charged species.

At the SOCl_2/C interface, the exchange current density (j_0) for the reduction of SOCl_2 is low ($\sim 1 \mu\text{A}/\text{cm}^2$), which is four orders of magnitude below that for the lithium electrode, implying that the area required to achieve a given current density is 10^4 times greater at the pce than at the anode. To overcome this potential kinetic limitation and maximise the effective volumetric capacity of the cell, designers select a carbon mixture whose porous structure offers maximum surface area (in practice the true active surface area can amount to several square meters). This strategy results in a very low overpotential at the porous cathode of a practical Li/SOCl_2 cell, which may be contrasted with non-porous glassy or platinum electrodes, where η_{CTc} for the reduction of SOCl_2 is units of $\mu\text{A}/\text{cm}^2$ of geometric surface area.

η_{SOLc} and η_{DIFFc} are defined by the sum of the transport properties of reactants across the bulk catholyte, and through the liquid phase of the carbon pore structure to the reduction sites within the matrix. Transport through the pores is governed by the same transport mechanisms as for the PL layer given in 6.2.

6.4. Ohmic losses (IR)

If we ignore the ohmic losses associated with the electrodes and their connectors, η_{SOLb} is effectively defined by the resistance of the bulk electrolyte between the anode and the pce, R_{SOLb} , which is give by Ohm's law:

$$\eta_{\text{SOLb}} = I_L R_{\text{SOLb}} \quad \text{Equation 6.11}$$

where I_L is the load current. In principle the separator is inert and should play no part in the chemical and electrochemical processes. However, there is evidence to suggest that it can operate as a nucleation and growth site for the LiCl crystals. Popov et al.¹² used impedance spectroscopy to study the open-circuit growth of the passivation layer in lithium-BCX cells; they were able to isolate elements of the cell, and showed that the solution resistance increases due to blocking of the separator pores with LiCl. Mogensen^{13, 14} has used scanning electron microscopy (SEM) to illustrate the presence of cubic LiCl crystals which have formed around individual fibres of the glass separator used in his experiments, but did not quantify the overall effect of this phenomenon on cell impedance.

6.5. Discharge processes

As discharge progresses, the geometries, and the relative concentrations and phases of the active components and discharge products will change, and the various overpotentials discussed above will also be subject to continuous change. The reaction product, LiCl, is of crucial importance to the operation of the cell. It is a very poor ionic conductor that will increase cell impedance when deposited in quantities that 'block' the electroactive areas of the electrodes. Hagan et al.¹⁵ demonstrated that the LiCl is completely insoluble in additive free $\text{SOCl}_2\text{:LiAlCl}_4$ catholyte once precipitated in the solid phase. Yamin¹⁶ has also stated that LiCl is almost insoluble in the catholyte and estimated its solubility as 20 mM. As a result of this low solubility, LiCl normally precipitates on the carbon surface close to the reduction site; any subsequent solution/dissolution processes which occur in the LiCl crystal structure are considered to be extremely local and would not be expected to change the overall structure significantly once precipitated on the PL and in the pce.

To understand and predict the variation of cell voltage under discharge in the meter operating environment, it is necessary to consider the contributions of the various polarisation processes through discharge.

6.6. Catholyte discharge processes

For the Li/SOCl₂ cell, the basic catholyte can be regarded as a concentrated mixture of LiAlCl₄ and SOCl₂, lithium cations (Li⁺), and chloroaluminate anions (AlCl₄⁻). The discharge process produces significant changes of state and composition of the catholyte. A liquid state is necessary for the inter-electrode mass transfer processes, and the kinetic rates will also be affected by changes in the relative concentrations of the catholyte.

The catholyte composition changes from the binary mixture, SOCl₂:LiAlCl₄, of the 'fresh' cell, to a second binary mixture LiAlCl₄:SO₂ at the end of discharge¹⁷. In the mid-discharge phase the catholyte becomes a ternary mixture, SOCl₂:LiAlCl₄:SO₂. The consumption of one mole of SOCl₂ produces one mole of SO₂. Bedford et al.¹⁸ found that fresh catholyte contains the solvated cationic species Li(SOCl₂)₂, and that the SO₂ that is produced during discharge displaces the SOCl₂ to produce first, [Li(SOCl₂, SO₂)⁺, and then Li(SO₂)₃⁺. The presence of the solvated cation is the reason why the pressure above the catholyte of a discharging Li/SOCl₂ cell remains so low until near the end of discharge¹⁹. Various complexes of the form Li(SOCl₂)(SO₂)⁺(AlCl₄)⁻, are formed²⁰ which may play a part in a solution/dissolution process of LiCl.

Table 6.1 LiAlCl₄ solubility in SOCl₂ catholyte versus state of charge for various starting concentrations of LiAlCl₄ (from Ref. 21). Cx% is the state of charge where C100%, C50% and C0% infers a charged, half discharged and a completely discharged battery respectively.

Starting concentration of LiAlCl ₄ in SOCl ₂ (M)	State of charge at the solubility limit of 4.65 M (Cx%)
0.5	10
1	24
1.5	35
2	46

SOCl₂ consumption increases the relative concentrations of LiAlCl₄ and SO₂, and LiAlCl₄ will precipitate when its concentration exceeds its solubility in SOCl₂. Dey²¹ has determined the solubility of LiAlCl₄ in SOCl₂ to be approximately 4.65 M at room temperature, and the state of charge at which LiAlCl₄ concentration reaches its

solubility limit is given in Table 6.1 for various starting salt concentrations. The actual compositions of the catholytes used in the candidate cells are not available, but commercial designs are in the range 1.4 to 1.8 M, which would imply that precipitation will commence at a state of charge of approximately C40%.

Temperature has significant effects on the solubility limits under equilibrium conditions, and on the viscosity and ionic conductivity of the catholyte. These properties have been investigated by Demakhin²² who showed that the $\text{SOCl}_2\text{:LiAlCl}_4$ system remains in a homogenous liquid state at temperatures above -20°C for a LiAlCl_4 salt concentration range up to approximately 3 M. The liquid polytherm of the mixture then rises to a peritectic point of 0°C at the maximum LiAlCl_4 solubility limit of approximately 5 M. This implies that the LiAlCl_4 will show an increasing tendency to solidify at a given temperature in the operating range of -20 to 40°C as the discharge progresses and the relative concentration of LiAlCl_4 increases. Thus, LiAlCl_4 precipitation may occur at relatively high levels of charge at sub zero temperatures, depending on the starting concentrations. A solid crystalline solvate of composition $\text{SOCl}_2\text{:LiAlCl}_4$ was isolated at temperatures below -10°C for high LiAlCl_4 concentrations.

Raising the concentration of the salt leads to an increase in the viscosity of the catholyte, indicating an increasing impediment to viscous flow during discharge. For a salt concentration of 3 M, viscosity was found to vary from between approximately 17.5 g/m/s at -10°C , to 1 g/m/s at $+40^\circ\text{C}$, showing that a change of at least an order of magnitude can occur over this temperature range.

Demakhin²² also measured the variation in specific electrical conductance of the catholyte with salt concentration and temperature. He found the isotherms of conductance to be 'classical in nature' - a rise in conductance due to the increase in the number of charged species in solution, up to a maximum, followed by steady fall due to their aggregation. The position of the maximum on the isotherm varies with temperature. Over the 0.5 to 3 M range of salt concentration measured, the conductivity was found to vary from 2.10^{-3} to $2.6.10^{-2}$ S/cm. Conductance decreases with increasing salt concentration above 3 M. Deligiannis et al.²³ observed that the optimum concentration corresponding to peak conductivity decreases with decrease in temperature, which they attributed to the dominant nature of viscosity effects at low

temperatures. This characteristic was utilised in the design of the 1998 Mars Mission Microprobe cells to optimise performance at very low temperatures²³.

The inter-electrode separation of a fresh cell is minimal, however this may increase during discharge. For example, an increase from 0.1 to 1 cm at 30 mA (the highest current applied here) would result in a change from in η_{SOL} of 6 to 60 mV (R_{SOL} from 0.2 to 2 Ω). Klinedinst²⁴ has measured the effect of a range of 5 inter-electrode separations of 0.068 to 0.45 mm (at high discharge rates), and found no effect on discharge capacity. Thus variations in inter-electrode separation are unlikely to affect load voltage in a fully flooded cell under the accelerated test and meter load levels.

6.7. Anodic discharge processes

The dominant overpotentials at the anode, η_{PL} and η_{DIFFa} , are effectively defined by mass transport across the PL. They generally become dominant under conditions which allow the PL thickness to maximise and the inter-crystalline channels to narrow or close down. For a well managed discharge process, lithium utilisation at the surface of the anode leads to continuous processes of breakdown and repair which systematically give birth to cracks and defects through the PL. In principle, a low discharge current should lead to even utilisation of the lithium and the maintenance of an adequate volume fraction of open-ended catholyte channels for the transfer of active species from C100% up to approximately C15% of cell utilisation²⁵.

During discharge, the amount of LiCl in the PL layer grows in proportion to the self-discharge rate as discussed in Section 7.5. No quantitative model for the evolution of the transport properties of the PL through discharge is known to exist and species mobility will probably vary according to cell design and discharge history. In their models of the kinetics of the PL, Evans et al.²⁶, and Tsaur and Pollard²⁷ chose to neglect the effects of factors such as temperature, current density, and PL growth and crystal morphology because of their mechanistic complexity.

In qualitative terms, the exchange current density at the Li/SOCl₂ interface, and the mobility of the Li⁺ ion in the PL and SOCl₂ are both very high. Thus, at normal ambient conditions and low loads, a relatively small volume fraction of open channels through the PL should be sufficient to allow the charge and mass transfer processes of electroactive species from the anode surface to the bulk electrolyte to operate at very low overpotentials.

η_{DIFFa} is a function of time and current, in accordance with the Sand proportionality, $\eta_{\text{DIFFa}} \propto I.t^{0.5}$ which is derived from Equation 6.8. Yamin has found²⁸ that η_{DIFFa} becomes dominant at high current and at pulse widths exceeding 2 min, and that the limiting current density at the anode is around 6 mA/cm².

The limiting conditions for effective anode kinetics are defined by factors which impair the exchange of active species across the PL. In physical terms, this includes the attenuation of access between the PL and the bulk catholyte through open-ended cracks in the PL. The physical growth kinetics of the PL under open-circuit and load conditions are discussed in detail in Chapter 7. As the volume of SOCl₂ solvent is utilised through discharge the relative concentration of LiAlCl₄ increases and the catholyte conductivity will also reduce. In their study of the anodic discharge, Chenebault et al.²⁹ suggested that temporary precipitation of LiAlCl₄ can occur in cases where the natural transport processes reduce beyond the level required to homogenise the concentrations of these species at the bottom of cracks. Chenebault³⁰ reports the conductivity of solid phase LiAlCl₄ as 10⁻⁴ S/cm, which is two orders of magnitude below that of the catholyte, and the transition from liquid to solid phase would be expected to be accompanied by a sudden reduction in cell voltage.

These processes are exacerbated at lower temperatures. Hu et al.³¹ used impedance spectroscopy to show that a temperature of -10 °C caused a significant impedance increase in the secondary layer of the PL, which was attributed to a viscosity increase within the porous structure.

6.8. Cathodic discharge processes

The pce has several functions:

1. The carbon substrate provides an electronic conductive path between the current connector and the site of electro-reduction.
2. The open pore structure provides channels for mass transport of active species between the bulk catholyte reservoir and the inner sections of the pce.
3. The pores form a space for the accumulation of the insoluble reaction products (S and LiCl).
4. The pores contain a certain amount of catholyte solution to promote the reaction and the necessary transport processes.
5. The surface promotes reduction of the SOCl₂.

The pce matrix comprises two conducting phases, namely electronic and ionic. Electronic conductivity depends on the electrical continuity of the inter-connecting

carbon grains. Ionic and active species conductivities depend on the volume fraction and the degree of inter-pore continuity of the liquid phase in the porous structure.

To achieve 100% pce utilisation efficiency, LiCl must be deposited uniformly throughout the pce, which requires the exchange of electroactive species from the bulk catholyte through a tortuous porous matrix of up to 5 mm thick to an electroactive site. As there are no external forces contributing to the mass transfer processes (other than fluctuations in ambient temperature), it is evident that η_{SOLc} and η_{DIFFc} will be particularly sensitive to the conductivity of the liquid phase of the pce matrix during discharge. Thus, two basic mechanisms can contribute to pce failure:

1. Hindered mass-transfer in the pores (liquid phase) due to some decrease in real free porosity.
2. Deterioration of electrical contact between carbon particles (solid phase).

6.8.1. Open-circuit storage pce processes

Chakov et al.³² and Madou et al.³³ reported the existence of a primary film on carbon when immersed into SOCl_2 . Hansen and Frank³⁴ showed that a carbon electrode is subject to heat output for about 5 days after immersion in SOCl_2 , but that this amounts to only a few percent of the total heat output from the cell. Mogensen³⁵ found that the pce passivates, but that its resistance remains quite low: he applied a load of $35 \mu\text{A}/\text{cm}^2$ and reduced the pce resistance from 9 to 1Ω in a few seconds. Cieslak and Street³⁶ reported that Ketjenblack blended cathode mixture aged poorly. Hughes et al.³⁷ have used impedance spectroscopy to show that only a small fraction of the pce is active at high states of charge, but that the whole porous mass becomes involved as discharge proceeds, although these effects proceed without noticeable effect on cell voltage.

Zhang and Cha³⁸ used a.c. impedance spectroscopy and SEM to study the surface behaviour and composition of porous and glassy carbon electrodes in $\text{SOCl}_2\text{:LiAlCl}_4$ and demonstrated the existence of a primary 'passive' film 10 minutes after catholyte filling. They adduced the film to the combined interaction of SOCl_2 , LiAlCl_4 and the catalytic surface of the carbon electrode. Using X-ray energy dispersion analysis they showed that the film contains sulphur, aluminium and possibly elements of atomic number less than 11 (lithium and oxygen). It would appear that this layer is an analogue of the PL, and supports electron conduction through defects in the crystal layer. Physically, the film was found to remain unchanged with time providing that

the cathodic overpotential does not exceed 500 mV, implying that storage duration will not be a factor in the discharge performance of the pce.

6.8.2. Cathodic reduction processes

The cathodic reduction of SOCl_2 is complex, because of the superposition of two physical processes: clogging of the pores by insoluble LiCl reaction product which may also be porous, and additional swelling of the electrode due to the growth of the LiCl crystals. In their literature review published in 1993, Zhang and Cha³⁹ concluded that no generally accepted mechanism of the reduction of SOCl_2 had been formulated up to that time, although many studies have been carried out and reduction products and intermediates suggested. However, it is generally agreed that reduction of the SOCl_2 is catalysed at an active site on the carbon surface to yield the reaction products given in Equation 6.2, and that chloride and lithium ions combine to form pure LiCl , as given in Equation 6.3. Because of its low solubility in neutral $\text{SOCl}_2\text{:LiAlCl}_4$, the LiCl precipitates instantaneously on the carbon surface close to the reduction site, and passivates that surface fraction permanently. As stated on page 36, sulphur is distributed throughout the cell once its saturation limit in the catholyte is reached. Sulphur dioxide remains in solution in the catholyte until the end-of-life phase is reached.

Limited recovery from pce blocking by LiCl discharge product has been observed in laboratory tests^{40,41}. Bagotsky⁴¹ compared the distributions of LiCl inside the pce immediately after high rate discharge (10 mA/cm^2) at -20°C , and after an eight day storage at room temperature. His results showed that redistribution did take place, albeit at very low rates, and he ascribed the recovery to dissolution and reprecipitation. However, this regeneration took place over time on open-circuit following very short-term high-rate discharge, at LiCl concentrations which may have been below the saturation level in the catholyte, and the effect is not expected to occur in cells under continuous accelerated test or long-term discharge rates.

6.8.3. The operation and performance of the pce

Theoretically, the cathodic reaction rate will be greatest at the front of the electrode, because the electronic conductivity of the carbon solid phase is much greater than the species conductivity of the catholyte in the pores⁴². The measurement of reaction profiles⁴³ has indicated that reduction takes place preferentially within the electrode segment facing the anode at higher rates, inferring that the resistance of the liquid

catholyte phase controls the geometry of the reaction profile. Dey⁴⁴ found that the reaction zone penetrates deeper into the electrode structure with discharge, and that LiCl is distributed more closely to the front surface of the pce with increasing current density and depth of discharge. Sun and Chen⁴⁵ embedded an 8-electrode chloride sensor into a pce to show that LiCl precipitates evenly throughout the depth at a real current density of 10 mA/cm² or below, and that mass transfer limitations of active species come into play at 12.7 mA/cm². Chenebault's chronopotentiometric measurements⁴⁶ showed that the reduction process moves from kinetic to mass transport control at a current density of around 20 mA/cm², and that diffusion control limits the reduction process to a maximum at 40 mA/cm².

Szpak and Venkasetty⁴⁷ have stated that the onset of nucleation and growth of a new phase in a porous medium requires a higher concentration than in the bulk, in accordance with the Gibbs-Thompson relation, which gives the degree of LiCl supersaturation in pores of different radii⁴⁸:

$$c(r) = c(\infty) \ln(2\sigma V_{\text{LiCl}} \cos\beta / RT r) \quad \text{Equation 6.12}$$

where $c(r)$ and $c(\infty)$ are the equilibrium concentrations of LiCl in a pore of radii r and in the bulk. σ is the interfacial surface tension of solid LiCl crystals in the standard catholyte solution saturated with LiCl. V_{LiCl} is the molar volume of solid LiCl, and β is the three-phase 'wetting' angle of the LiCl/pore wall/solution. From this equation, it follows that the degree of supersaturation increases with declining r values and that the probability of crystal deposition is higher in larger pores, where a lower degree of supersaturation is needed, than in narrow ones.

Szpak and Venkasetty⁴⁷ used Equation 6.12 as a basis for a description of the cathodic processes occurring at higher discharge rates. In the first few moments after initiation of discharge, a concentration gradient is established at the electrode/catholyte interface. Because $c(r)$ is greater than $c(\infty)$ and species transport is not inhibited, nucleation and growth of LiCl crystals will take place first at the bulk electrolyte side of the pore. With the growth of precipitate at the pore mouth, species transport becomes restricted and supersaturation builds up, initiating nucleation and growth in the pore interior. Substituting $p = 2\sigma/r$ in Equation 6.12 yields:

$$p = RT/V_{\text{LiCl}} \ln[c(r)/c(\infty)] \quad \text{Equation 6.13}$$

suggesting that crystallites growing within the confines of a pore will exert pressure

and lead to the expansion of the electrode.

Szpak and Driscoll⁴⁹, and Chiu et al.⁵⁰ have shown that pce expansion is a necessary concomitant to achieving peak capacity, and that dimensional constraints on the pce lead to diminished performance. However, even when free to move, the degree of swelling can vary significantly and is not very reproducible⁷. Bagotsky⁵¹ discharged carbon electrodes at room temperature and at -40°C , and at five current densities between 0.5 to 10 mA/cm^2 , and showed that swelling always occurred, due to internal pressure of the insoluble products being formed. The swelling degree (λ_{sw}) varied between 1 to 2.6, and he found that the main factors influencing λ_{sw} were packing tightness of the cell assembly, the elasticity of the electrodes, and the discharge conditions.

It is generally considered that pce utilisation is complete once all of the carbon surface becomes covered with the LiCl discharge product. However, Bagotsky et al.⁵² have observed that the insoluble reaction products which block the macropores do not in practice decrease the active surface area of the electrode. This is due to the fact that the accumulation of products results in the exertion of pressure on the pore walls, as predicted by Equation 6.13, and the subsequent stretching of electrode matrix results in the creation of new active areas and an increase in total pore volume.

6.8.4. Effect of porous structure on pce performance

The relationship between electrode structure and performance was studied theoretically by Marincic⁵³, and experimentally by a number of workers^{54,55,56,57,58}, who showed that pce capacity is determined by its overall porosity and the volume of catholyte in the pores. Danel et al.⁵⁹ studied five carbon materials at high drains and showed that pore size distribution had a significant influence on capacity. He also found that the absorbed volume of catholyte was greater than the calculated porous volume, which he attributed to impregnation of the carbon by the catholyte and swelling.

In 1995, Bagostky⁶⁰ proposed that the functions of pores could be classified according to volume: micropores ($r < 1\text{ nm}$), mesopores ($r > 1 < 10^2\text{ nm}$) and macropores ($r > 10^2\text{ nm}$). He stated that charge transfer takes place mainly in the micropores where the surface to volume ratio is high. Micropores do not play a significant role in the electrochemical reaction, because their radii are comparable to that of the reacting molecules, and they give only a small contribution to the overall capacity of the pce.

The electrochemical reaction occurs mainly in the meso- and macropores, and by means of porosimetric measurements he identified the most important sites as pores with radii in the range 8-30 nm. The macropores with low surface area do not participate significantly in the electrochemical reaction and serve for mass-transfer processes.

6.8.5. Effect of load on pce performance

Figure 6.1 plots current density against the time to failure to a 2.5 V cut-off point. The graph is based on data extracted from Klinedinst's⁶¹ room temperature measurements of the capacity of pce limited cells.

Klinedinst's regression analysis gives the following equation:

$$\ln(t) = 9.6 - \ln(j_c) \tag{Equation 6.14}$$

where t is the time to failure in hours, and j_c is the geometric pce current density.

The pce thickness used in Klinedinst's tests was only 60 μm , and the capacity measurements cannot be related directly to that for a 'D' size cell. Nevertheless, it may be seen that an order of magnitude separates the pce capacity for the two current densities of approximately 500 and 75 $\mu\text{A}/\text{cm}^2$ utilised in the accelerated discharge tests, and by a further order of magnitude for the mean current density of 2.5 $\mu\text{A}/\text{cm}^2$ of the meter load (respective mean discharge currents of 20, 3 mA, and 100 μA).

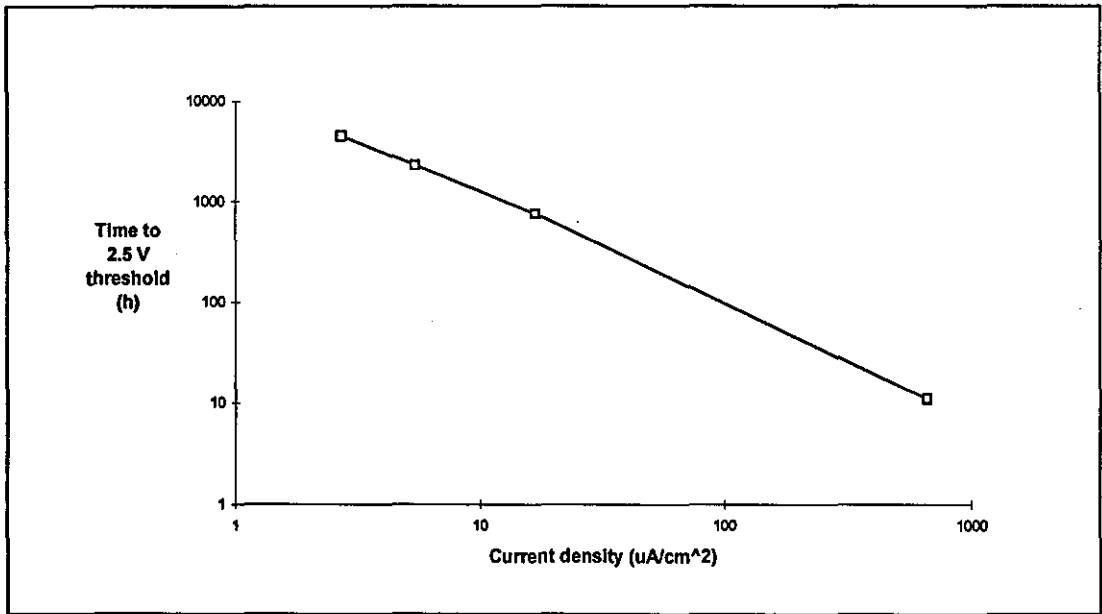


Figure 6.1 Pce capacity versus current density chart (Klinedinst's data⁶¹).

The graph implies that there is no limit to the pce capacity, providing that the drain rate is low enough. This result corresponds with Bagotsky's observation that new

active pores are continuously being generated at low rates as a result of the expansion of pores which accompanies the LiCl deposition process (Section 6.8.3).

The progressive reduction in pce capacity with increasing current density is correlated with diffusion-controlled mass transport limitations, whose effect is to generate a non-uniform ionic current distribution with a maximum within the volume of the pce. The reaction zone is centred about this maximum, and as current density is increased, so the mass transport rates fail to keep up with demand, and the zone is advanced towards the front of the pce (the interface with the bulk catholyte). Precipitation of LiCl in the reaction zone will lead to clogging of the pores within that thickness element. This will tend to block species transport between the anode and the electroactive pce pores behind this zone, leading to isolation and under-utilisation of the interior of the electrode.

From empirical studies, Yamin⁶² has shown that pulsed and constant current loads can induce significant differences in pce performance which are consistent with control of the electrochemical and non-electrochemical processes shifting from kinetic to mass transport with increasing discharge rate. Load performance criteria are summarised in Table 6.2.

Table 6.2 Contributions of cathodic overpotentials and pce utilisation under different load regimes for a 'D' size Li/SOCl₂ cell.

Load condition for D cell	Dominant over-potentials	Pce utilisation
Constant low current, 100 μ A	η_{CTc}	Homogeneous precipitation throughout the pce.
Constant high current, >20mA	η_{SOL} , η_{Diff}	LiCl precipitated in surface layers, the inner pores of pce isolated.
Pulsed load, Pulse width <2min	η_{SOL}	Dependent on pulse width, under short duration high current (e.g. 30 mA), $\eta_{Diff} \rightarrow 0$, $\eta_{CTc} \rightarrow 0$, giving homogeneous precipitation.
Pulse width >2min	η_{SOL} , η_{Diff}	As for constant high current

Mass transport processes keep pace with electrochemical kinetics at current densities in the region of 2 μ A/cm², leading to maximum pce capacity. At current densities greater than 40 μ A/cm², mass transport limitations dominate cell operation, and the utilisation efficiency of the pce decreases. As with the porous PL, the pulse width and current amplitude governs the effective capacity of the pce under pulsed loads, as expressed by the proportionality derived from the Sand equation (Equation 6.7).

$$\eta_{\text{DIFFc}} \propto I.t^{-0.5}$$

Equation 6.15

As the pulse parameters reach the limiting values of either width or current density parameters, η_{DIFFc} becomes the dominant overpotential and can account for as much as 90% of total cell overpotential. The limiting pulse width has been found to be ~2 min; below this limit the concentration overpotential remains low, and is compatible with homogeneous precipitation of LiCl in the pce and maximised utilisation efficiency. Increasing the pulse width beyond this threshold advances the reaction zone to the front of the electrode, causing clogging and reduced capacity.

Yamin reported⁶² that the limiting d.c. current for even precipitation of LiCl through the pce structure for a bobbin type of 'D' cell is ~20 mA (presumably at room temperature), equivalent to a current density of 0.5 mA/cm². The results of the laboratory discharge tests carried out in this study in Section 10.1 give general support to this precept. The capacity yield to 2.5 V for the Te cells was reduced significantly by increasing the load current density from 0.23 to 0.4 mA/cm², implying a reducing capacity of the carbon pce.

6.9. Temperature and Orientation

The only 'environmental' operating factors which are likely to affect cell discharge processes in the meter application are temperature and orientation.

In 1996, Deligiannis et al.⁶³ tested Li/SOCl₂ cells for the 1998 Mars Microprobe on the Mars Surveyor Lander Mission, and demonstrated that they functioned without significant loss of performance in the required operating domain over a range of temperatures from 20 to -85 °C. It is interesting to note that Deligiannis' review of the literature revealed found no published data relevant to these operating conditions.

Yamin and Pallivathikal⁶⁴ found that a reduction in temperature from +20 to -20 °C reduces capacity by a factor of approximately 60% (at a relatively low discharge rate). The manufacturer, Sonnenschein Lithium GmbH⁶⁵, claims an operating temperature range of -40 to +85 °C. Another manufacturer qualifies the performance of samples of production cells by discharge under a temperature cycle from -30 to +70 °C at a current density of 500 µA/cm²; visual inspection of such discharge curves shows that cell voltage remains relatively constant through discharge at temperatures >10 °C, but exhibits a progressive decrease during the low temperature phase of the thermal cycle as discharge approaches approximately C25% of its ambient temperature capacity⁶⁶.

The main effect of temperature is on the viscosity and ionic conductivity of the catholyte. Although the two overpotentials at the pce (η_{SOLc} , and η_{DIFFc}) are transport controlled, these should only become dominant at high current and towards end-of-life. In the present meter application temperature should not affect performance until depletion of reactants is imminent. Under accelerated test loads the effect should be seen earlier in the end-of-life phase.

Doddapaneni et al.⁶⁷ subjected a total of 4 cells, 2 at -2 °C and 2 at 32 °C to low rate discharge, one cell at each temperature being placed horizontally and vertically. High specific pce capacities were achieved in all tests. Product distribution was investigated by SEM, and was found to be affected more by orientation than by temperature. In the cases of both horizontal and vertical orientation, higher cathode utilisation was observed in the lowest part of the pce. This corresponds with the progressive depletion of the liquid catholyte from the upper part of the cell. Sulphur was found mainly on the pce surface and in the pore structure of the separator. It has been reported⁶⁸ that cell performance can vary if the battery is upside down, due to effects such as stratification of the catholyte wetting against the solid reaction surfaces, although it was also stated that the horizontal attitude had no measurable effect.

Orientation has an increasing influence on cell capacity as cell size increases⁶⁹. This is due to unfavourable catholyte distribution at the last stages of discharge when a void or vapour volume may tend to block access of catholyte to remaining electroactive sites in the electrode structure. The capillary effect of the pce and separator pores acts against this tendency. As a result, the orientation effect is smaller for thin cathodes than it is for thick ones, and is stated to be insignificant when discharge currents are very low, i.e. 4 mA for a 'D' size cell, or when wetting is improved by movement of the cell⁷⁰. In smaller cells the capillary action of the pce is sufficient to maintain a uniform electrolyte distribution, even towards the end of discharge. For a 'C' size cell, cell capacity is nearly orientation independent, except at low temperatures (-30 °C) and higher currents⁷¹. At the outset of this study, the manufacturers of 'D' size candidate cells stated that their performance was orientation independent.

6.10. Implications for the meter application

We can summarise the foregoing discussion by stating that the fast electrode kinetics and highly conducting catholyte of the basic Li/SOCl₂ cell design should exclude the onset of polarisation until depletion of reactants is imminent. A 'D' size cell should be capable of supporting operation under the pulsed-load profiles utilised in the meter applications throughout the temperature ranges found in internal and external domestic locations within the UK.

The limiting anode operating condition would appear to be associated with a 'defective' PL layer whose pore structure closes up, and the literature suggests that such an event should not occur under the load and operating conditions utilised in the meter, or under accelerated discharge loads of up to 20 mA/cm².

The pce should perform without problem in the meter application, although blocking of the pce will limit cell capacity as the discharge current is increased. Pce performance should be unaffected at geometric current densities of up to 250 $\mu\text{A}/\text{cm}^2$ at temperatures down -20 °C, but the onset of cathodic polarisation should occur at higher rates. The effect should be observed as a progressive decline in capacity yield as discharge rate is increased. Five current levels are utilised in the accelerated discharge testing performed in this study reported in Chapters 10 and 11, namely: 65, 139, 216, 389 and 778 $\mu\text{A}/\text{cm}^2$. The empirical theory developed above would thus predict that the lower three levels should result in maximised capacity yields, and the highest two should be subject to cathode clogging and reduced cell capacity.

Cell impedance of the cell is largely controlled by concentration polarisation in the porous layers deposited at the electroactive surfaces of both electrodes, whose pore structures, morphologies and geometries are controlled during discharge by the LiCl deposition processes. The literature implies that impedance should remain low through discharge in our operating domains until end-of-life. The limiting cases are presented by reduction of the active liquid phase fractions of the porous structures at the anode (PL) and cathode (pce), causing (a) reductions in mass transport rates, and in the limit, (b) precipitation of LiAlCl₄. These processes are exacerbated by a closed pore structure, and decreasing temperature.

CHAPTER 7

THE PASSIVATION LAYER AND SELF-DISCHARGE

In the Li/SOCl₂ cell, a strong reducing agent, lithium, is immersed in a strong oxidising agent thionyl chloride (SOCl₂). The free energy change of their interaction (ΔG of -1432 kJ/mol) is among the highest encountered in any battery system, and the two are thermodynamically unstable when in contact. On filling the cell with SOCl₂, the two react chemically to form a film on the lithium surface whose main component is LiCl, according to Equation 7.1:



The stoichiometry of the chemical corrosion reaction is identical to that of the electrochemical reaction, but generally takes place at the anode surface, rather than at the carbon cathode, and results in the formation of a layer of insoluble LiCl on the surface of the anode. This layer is protective and its progressive growth markedly slows the corrosion rate of the lithium. The layer gives the system its kinetic stability, allows the reactants to exist together in the battery, and controls the self-discharge rate to one of the lowest of all battery couples. An operating life of 20/30 years is now considered to be feasible^{1,2}. It is the tightness and reparability of this film that gives the cell its long storage and service life, and it is a key determinant of long-term performance. The layer is called the passivation layer (PL), and while contributing to an excellent shelf and operating life, it can cause the well-known problem of voltage delay on start up, particularly at low temperatures. Voltage delay is particularly important in applications where a period of storage is followed by the demand for high-current discharge rate. The amelioration of the problem has been the subject of much research because of its importance in defence and space applications. This parasitic loss of the lithium and SOCl₂ reduces the faradaic efficiency of the cell. At moderate temperatures the corrosion reaction continues both on storage and during discharge. The cumulative loss increases with duration of storage and discharge rate, and in long-term applications its influence on the faradaic efficiency becomes significant.

Metal hardware, such as any exposed anode substrate, leads, tabs and cell container, if attached to the anode and touching the catholyte at the same time, is also coated with the salt film, and contributes to loss of reactants. While the film on the anode is the

direct reaction of the metal with the SOCl_2 solvent, the film on the hardware forms because the attached lithium holds it at a potential well cathodic of the reduction potential of the solvent. The exposed hardware then behaves as a second cathode. Lithium ions from the catholyte combine with chloride ions produced at the hardware surface by the electrochemical reduction of the solvent, and solid LiCl forms on the surface until the bare metal is covered.

An 11.5 year operating life represents the upper extreme of the reported operating life for Li/SOCl_2 technology, and the effect of corrosion of the active cell components (self-discharge) must be factored into any service-life prediction model. At the start of the project no systematic model of the effects of operating conditions on self-discharge existed; here we review the literature in order to determine the potential effects on the meter application.

Self-discharge rate is a function of two design factors:

1. The area of contact between the lithium surface and the catholyte.
2. The composition of the catholyte (salt concentration and additives).

and four operating factors:

1. Time.
2. Temperature.
3. Electrical load.
4. Mechanical stresses.

In the meter application, the battery is subject to an initial period of open-circuit storage, followed by installation in the meter and continuous discharge under pulsed load. The load level is constant through life apart from infrequent data transmissions. However, the meter battery is required to operate under a range of thermal, mechanical stress conditions. Several workers^{3,4,5} have carried out concurrent measurements of the heat flow due to self-discharge and a.c. impedance measurements of the thickness of the PL at low discharge rates. These results showed that the kinetics of the formation of the passivation layer (PL) and self-discharge are exactly complementary, and are dependent on the impedance of the passivation layer. Firstly, we review measurement methods, we then investigate the governing principles of growth and breakdown of the PL, its morphology, and the likely effects of these processes on self discharge rate.

7.1. Measurement methods of the PL geometry and self-discharge rate

Scanning electron microscopy (SEM) and a.c. impedance spectroscopy are two commonly used techniques for observing the geometric and morphological structure of the PL. Both methods yield a measure of PL thickness. SEM gives a visual representation of the PL geometry but involves disassembling the cell and special preparation of the test piece⁶. A.c. impedance data may be converted into layer thickness and conductivity^{7,8,9,10}, assuming that the response of the interface under examination conforms to an idealised parallel plate capacitor¹¹. However, it is now appreciated that this idealised model of the PL is an over-simplification¹². This is due to the fact that the porous structure and irregular surface geometry of the PL distort the capacitive and resistive responses, leading to erroneous thickness measurements. Nevertheless it is a sensitive and non-intrusive method of detecting changes to the PL, and is a useful tool for monitoring the growth of the thickness of the PL with time.

Three techniques are generally used to measure self-discharge rate:

1. Classical - direct measurement of capacity loss after storage - this gives an integrated measure of self-discharge but involves long duration tests¹³.
2. Accelerated storage - correlation of capacity loss with temperature using the Arrhenius relation following storage at elevated temperatures - this is a 1 to 2 year test, but is not effective if the self-discharge mechanism changes with temperature¹⁴.
3. Microcalorimetry - measurement of heat dissipation due to the exothermic self-discharge reaction in the cell - this is the quickest test method, and gives an instantaneous measure^{15,16,17}.

These methods are discussed in detail in the publications cited above. Methods 1 and 2 involve the determination of residual capacity, which is conventionally performed by either accelerated discharge to a selected cut-off voltage or quantitative measurement of anodic lithium metal using acid-base titration¹³. As will be discussed in Section 13.5, with certain cell types the discharge method is subject to gross errors. The sensitivity of the titration method is given as $\pm 2\%$.

Method 3 (microcalorimetry) makes use of the exothermic reaction implied by the negative value of the Gibbs free energy of the corrosion reaction given in Equation 7.1. The heat release from a cell can be related to PL growth, and may be equated to self-discharge rate, I_{SD} , by means of the relation given in Equation 7.2:

$$I_{SD} = q/E_H \quad \text{Equation 7.2}$$

where q the measured heat output measured in joules, and E_H is the thermoneutral potential, which is defined¹⁸ to be equal to $-\Delta H/zF$. Several workers^{19,20,21,22,23} have measured E_H , and their results cover a range. Here we assume a mid value of 3.8 V. Equation 7.2 provides the conversion between energy converted chemically to heat and electrochemically to electricity, and facilitates the use of the microcalorimeter as a tool for measuring PL growth and self-discharge rate in lithium cells.

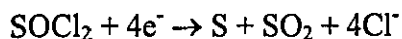
7.2. The formation of the passivation layer on open-circuit

The oxidation and reduction reactions which lead to the formation of the LiCl films are the same as those for the electrochemical reactions given respectively in Equation 6.1 and Equation 6.2. However, in this case the supply of electrons for the reduction process and the formation of chloride ions is by the transport of electronic charge from the lithium surface across the LiCl layers to the Li/SOCl₂ interface (i.e. rather than across the external circuit).

Mogensen²⁴ has presented the following model of the initial growth of the LiCl film. Before exposure, the lithium anode is covered by a thin ~20 Å layer of Li₂O, and impurities such as LiOH. When SOCl₂ comes into first contact with lithium, the two immediately react to form a thin compact layer (~50 Å) of impure LiCl. The impurities are probably lithium sulphur and lithium sulphur oxygen compounds formed by reduction of the SOCl₂ solution at the lithium metal surface. Some LiAlCl₄ may be co-precipitated. It is generally agreed^{25,26,27,28} that these reactions are very fast. Moshtev et al.²⁹ observed the initial phase of growth of the PL in the first 5 μs-5 ms of polarisation, and Kazarinov²⁸ has stated that the thickness is 1-1.5 nm directly after contact with the catholyte.

This primary layer film is predominantly a Li⁺ conductor with high electronic resistivity, and has the properties of a solid electrolyte^{30,31,32,33}. For this reason it is called the solid electrolyte interphase (SEI)³⁴.

After the primary layer is formed, local reactions between Li and SOCl₂ result in electrochemical corrosion of lithium and the production of Li⁺ ions that propagate across the film. The electronic conductivity of the LiCl layer is governed by the existence of energetically favourable defect sites in the crystal structure³⁵, and some electrons continue to tunnel from one defect site in the layer to another by electron diffusion. By this mechanism, SOCl₂ is reduced according to the cathodic reaction:



Equation 7.3

These chloride ions do not precipitate where they are formed, but remain dissolved in the SOCl_2 solution, until the solution is sufficiently saturated to nucleate LiCl crystals on the surface of the primary layer²⁴. After 24 h of storage, the entire lithium electrode surface is covered by a layer of cubic crystals of sizes between 0.1 to $0.5 \mu\text{m}$ ³⁶. The very smooth crystal facets observed by scanning electron microscope (SEM) imply that the LiCl is formed by precipitation from the liquid catholyte³⁷. When the LiCl crystals have grown laterally into one another the primary layer is totally covered with a porous layer of pure LiCl . This is the secondary layer. As the layer grows, the amount of impurities incorporated into the crystal structure is gradually reduced by the process of solution-recrystallisation. This process leads to a reduction in the number of structural defects, a reduction of the electronic conductivity of the layer, and a progressive decay in the growth rate of the layer.

The SEI is always present in a Li/SOCl_2 cell. Any damage is repaired spontaneously, and the secondary layer continues to grow through the life of the cell. The combination of the two layers is called the passivation layer, (PL). As the thickness of the PL grows, the number and size of the solid LiCl grains also increase. The layer continues to grow at a reduced rate because of the continued existence of a low number of defects, and after 25 days the growth of the film reaches a state of dynamic quasi-equilibrium²⁵. The individual crystals are surrounded by cracks³¹, and range in size from a few microns to $\sim 30 \mu\text{m}$.

The low solubility of LiCl in the catholyte implies that the bulk PL experiences very little change once it has been formed. However, dissolution and reprecipitation of the LiCl will occur on a localised scale and cause changes in the open channels in the PL. These processes are driven by differences in the radius of curvature of the crystal facets³⁷.

7.3. Open-circuit growth rate of the PL

It is generally considered that the open-circuit growth rate of the secondary layer of the PL is controlled by the electronic conductance of the SEI³⁸. Peled³⁹ proposed that the open-circuit growth rate obeyed the parabolic relationship given in Equation 7.4, consistent with the decreasing migration rate of electrons through an increasing thickness of LiCl .

$$L = (L_0^2 + 2KV_{OCV}t/\rho_{(e)})^{1/2} \quad \text{Equation 7.4}$$

where L is the film thickness, and $L_0 = 0$ at time, $t = 0$, K is a constant, and V_{OCV} and $\rho_{(e)}$ are the open-circuit voltage of the cell and the electronic resistivity of the SEI respectively³³.

Mogensen⁴⁰ monitored the growth of the PL thickness on open-circuit by measuring the resistance of the PL by impedance spectroscopy at intervals over a period of 3 years and confirmed this basic law, subject to irregularities caused by intermittent breakdown and repair of the PL.

In practice, deviations from this ideal law occur due to: (a) change of $\rho_{(e)}$ with L , (b) variable densities of cracks, holes or grain boundaries in the SEI that provide the electronic leakage path, (c) variability of the processes of breakdown and repair of the PL⁴¹, and (d) the variable surface roughness of the PL⁴². However, as regards the qualitative model required here, the open-circuit growth curve may be described as corresponding to a parabolic-like decay law of uncertain time constant.

From a study of the electronic structure of the PL, Delnick et al.⁴³ proposed that growth is controlled by tunnel emission of electrons to localised states within the SEI. This injection limited film growth extends for a period of up to 10,000 seconds (~7 days), when the film thickness reaches 200 Å, and obeys the power-law expression:

$$I_{SD} = kt^{-n} \quad \text{Equation 7.5}$$

where I_{SD} is the equivalent self-discharge current, t is elapsed time and k and n are empirical constants. After this time, a second mechanism controls film growth, which does not obey linear power law growth kinetics. Delnick postulated that this mechanism is controlled by bulk conduction and/or diffusion in the liquid phase.

7.4. Physical structure of the PL

It is generally accepted that the primary layer is hard and relatively robust, whereas the porous secondary layer resembles a brittle⁴⁴ sinter or compacted powder⁴⁵. It is the amorphous and ill-defined nature of the PL that complicates the assignment of discrete properties to the PL. Using a galvanostatic pulse method, Peled and Yamin³¹ proposed a physical model in which the lithium anode in SOCl_2 is always covered with a compact primary layer capped by a thick, mechanically strong, low porosity polycrystalline secondary layer. Heaps of discrete crystals of varying sizes separated by cracks in the outer region of the PL have been observed in most of the SEM

studies. Independently, other researchers^{46,47} have presented a similar duplex model described as a dense compact film adjacent to the lithium, with a collection of well faceted, loosely connected crystals at the catholyte interface. The dual structure is consistent with a Delnick's two phase growth model given above⁴³.

Deviations from this basic model have been proposed including a triple layer model⁴⁸. Chenebault et al.⁴⁹ also performed SEM studies and found no evidence of a thin compact primary layer or a structure of discrete layers. His model of the morphology of the PL is that of a progressive increase in porosity and crystal size with increasing distance from the lithium/SEI interface⁵⁰.

A discrepancy of about an order of magnitude exists between the PL thickness measured by SEM and galvanostatic pulse. Various workers^{37,51,52,53} have attempted to solve the discrepancy, but it is now generally considered that cracks and holes in the PL can modify its capacitive and resistive responses, and cause a departure from the simple parallel plate model used in impedance spectroscopy. The present consensus³³ is that the thickness of the SEI immediately grows to 1.5 nm on first contact with SOCl_2 , increasing to 5 nm in the following hours. The secondary layer thickness grows to some orders of magnitude greater, and will continue to grow on discharge as self-discharge products are precipitated; an open-circuit thickness of the order of 80,000 nm after one month has been reported⁴⁹.

7.5. The on-load growth rate of the PL

The anodic reaction, through removal of the surface lithium, undercuts and delaminates the PL. By this mechanism, the PL is subjected to continuous breakdown. The repair process utilises both Li and SOCl_2 , and leads to the production of enhanced amounts of LiCl whose precipitation increases the thickness of the PL. In theory, the production rate of LiCl should be proportional to the discharge current. We can determine the amount of LiCl produced during discharge in the low-rate, pulsed load operating domain of the electronic meter, by means of Equation 7.6 which is derived empirically in Section 14.7. The equation relates self discharge rate, j_{SD} , to current density, j , for a bobbin type 'D' cell of anode surface area of $\sim 45 \text{ cm}^2$.

$$j_{\text{SD}} = 0.2817j + 0.2 \quad \mu\text{A} \quad \text{Equation 7.6}$$

For a 'D' cell discharged through a meter at say $100 \mu\text{A}$, the equation predicts a self-discharge rate of approximately $30 \mu\text{A}$, i.e. a ratio of $j:j_{\text{SD}}$ of 3.3:1. The amount of LiCl deposited at the anode can be calculated using Faraday's law:

$$m = I_{SD} t M_{LiCl} / zF \quad \text{Equation 7.7}$$

where M_{LiCl} is the molecular weight of $LiCl = 42.39$, $zF = 96487$ As. For 1 Ah of electrical work, approximately 0.3 Ah is dissipated as self-discharge, and 0.47 g and 1.54 g of $LiCl$ form at the anode and cathode respectively. The density, ρ , of $LiCl$ is 2.068 g/cm^3 , thus a fully dense volume of 0.18 cm^3 of $LiCl$ will be deposited at the anode for each ampere-hour discharged. The equation predicts that the thickness of the PL will increase due to self-discharge by 0.04 mm per ampere-hour of discharge, corresponding to a total of at least 0.6 mm for the complete discharge of a 15 Ah cell. In practice, the physical thickness of the crystal layer is dependent on porosity, discharge rate and temperature; the example given above assumes zero porosity, ambient temperature, and a comparatively low discharge rate. A measured thickness at end-of-life of 5 mm has been quoted for higher discharge rates⁵⁴.

7.6. The effect of catholyte composition and lithium purity

Numerous workers have investigated the effects of the composition and concentration of the $SOCl_2:LiAlCl_4$ catholyte and the presence of organic and inorganic additives on the performance of the PL. In pure $SOCl_2$, only a thin primary layer is formed and the secondary layer is absent^{55,56}. Mogensen⁵⁷ has postulated that in the absence of 'impurities' such as Al^{3+} ions the primary layer operates as a perfect electronic insulator, thus blocking electronic charge transfer and arresting growth of the PL. From their study of the electronic structure of the PL discussed in Section 7.3, Delnick et al.⁴³ suggested that film growth is probably sensitive to SO_2 and Cl_2 in the catholyte.

It was found by Dey⁵⁸ that increasing the concentration of $LiAlCl_4$ in $SOCl_2$ increases the growth rate of the passivating layer, and also causes greater voltage delay in the $Li/SOCl_2$ cell. Peled³² proposed that the increase in electronic leakage current with increased $LiAlCl_4$ concentration was due to: (a) increase in the impurities in the solutions due to $LiAlCl_3$, and/or (b) incorporation of $AlCl_4^-$ into the $LiCl$ crystals or adsorption at the grain boundaries resulting in an increase in the density of crystal defects.

Dey⁵⁹ found that the addition of SO_2 produced a dramatic change in PL morphology, from an irregular open structure to an orderly densely packed structure. This orderly structure has been found to alleviate voltage delay on start up⁶⁰. Chenebault et al.^{61,62,63,64} have described the effects of the additives SO_2 and $LiAl(SO_3Cl)_4$, which

were designed to modify the morphology of the PL and thus alleviate voltage delay of the Td cell, and are presumably present in the current test cells. It is believed that SO_2 is also incorporated in formulation of the catholyte of the Ta cell type to enhance the voltage delay characteristics of the PL. Yamin et al.^{65,66,67,68} described the effects of unnamed additives which are designed to provide both enhanced start-up characteristics and minimised self discharge rate. He reported a nine-fold reduction in self-discharge at open-circuit and fourfold reduction when on-load, following modifications to the basic two component catholyte composition⁶⁹. The Te cells used in these tests do not contain these additives so far as is known.

Hagan et al.⁷⁰ found that the lithium samples from different sources exhibit variable performance at high loads. He showed that voltage and capacity is controlled by the electronic conductivity, permeability and mechanical strength of the PL, and that these factors are in turn controlled by the levels of impurity associated with the lithium material.

Cieslak⁷¹ compared the self-discharge rates of cells fabricated with standard $\text{SOCl}_2\text{:LiAlCl}_4$ catholyte and those containing SO_2 as an additive. Both sets of cells were aged for 63 weeks at a range of temperature levels between 25 and 60 °C. She found that the addition of SO_2 caused a significant increase in the variability of self-discharge capacity losses and capacity utilisation in cells, with some cells exhibiting both higher and lower capacity losses than the standard cells. Cieslak was unable to explain either the increased variability of the results or the actual effect of the SO_2 , but it is highly probable that the effect derives from altered morphology of the PL.

7.7. The effect of temperature on PL morphology

Very little information is available regarding the effect of temperature on the morphology of the PL. However, Dey⁷² carried out a systematic study of the effect of temperature levels of 25, 55, 70, and 85 °C on film growth by SEM to show that the morphology of the PL is dependant upon temperature. The higher the storage temperature, the larger are the LiCl crystals, and the more compact the film.

7.8. The stability of the PL under discharge

Under load, breakdown of the PL is caused by two main processes: (a) local dissolution of the surface of the anode, and (b) stresses in the SEI due to uneven retreat of the anode⁷³. The new anode surface exposed to the SOCl_2 immediately reacts to form a new protective film. By this process, the local thickness of the SEI is

reduced from hundreds of thousands of angstroms under OCV conditions, to 15-50 angstroms under anodic dissolution or corrosion. The continuous breakdown and repair process gives birth to other cracks and defects through the PL⁵⁴.

Ideally, the surface of the lithium will be evenly utilised through discharge, and under optimum conditions this can be achieved through to 85% of cell utilisation⁵⁴. Yamin has stated⁷⁴ that the PL posses no 'memory' effect as such. However, he has observed that the longer term performance can be influenced by an initial de-passivation process designed to seed the PL with 'weaknesses'. This is effected by a short-term discharge at relatively high current which introduces a matrix of channels through the PL. Yamin selects the depassivation process parameters to match the load requirements of the application. The channel structure that is created is semi-permanent, and facilitates species transport through the PL matrix at the required rates, whilst minimising damage to the SEI.

It has been reported that a threshold current density exists below which satisfactory cell operation is maintained without measurable damage to the PL. In 1980, Babai and Gal⁷⁵ showed that a current of $0.07 \mu\text{A}/\text{cm}^2$ causes no change in the passivation layer morphology, whilst a current of $2.2 \mu\text{A}/\text{cm}^2$ causes the formation of 'holes' in the passivation layer. Iwamaru⁷⁶ found a threshold level of $5 \mu\text{A}/\text{cm}^2$, which compares well with the Babai's figure. By measuring cell impedance, Marincic⁷⁷ found that a useful current of 20 to $30 \mu\text{A}/\text{cm}^2$ was consistent with maintaining a passivated lithium surface. Kronenburg⁷⁸ also showed that cells stored at 65°C were protected from increases in cell resistance by continuously discharging cells at $0.01 \text{ mA}/\text{cm}^2$ to maintain channels through the PL. Eichinger⁷⁹ found that a constant load of $10 \mu\text{A}/\text{cm}^2$ and/or a pulse of $1 \text{ mA}/\text{cm}^2$ every 25 h was sufficient to maintain low resistance. The wide variation in these figures makes it difficult to define a clear threshold, and is an example of the problem of assigning a discrete property value to anode behaviour.

The application of a continuous low background current can modify the evolution of PL impedance through discharge. Yamin⁸⁰ discharged cells through d.c. background loads of 10, 20 and $40 \mu\text{A}$ and applied a 1 s, 30 mA rectangular pulse at monthly intervals. He found that the transient minimum voltage (TMV) of the pulses changed gradually over a period of some 15 months. The two higher background loads

promoted an increase of 100 mV in TMV over this period, implying a reduction in impedance of the PL, which in turn implies a gradual reformation of the PL. This effect was attributed to an increase in the availability of charge carriers due to increased porosity of the PL. By contrast, the TMV of the pulse applied over the 10 μ A background load gradually reduced to a lower level over this period, implying a gradual increase in impedance due to closing of the PL channels. Incidentally, Deligiannis et al.⁸¹ reported the same effect using a baseline load of 118 Ω and periodic pulses of 5.1 Ω .

7.9. Dynamic properties of the PL

No systematic studies of the effects of instantaneous stresses on the PL appear to have been reported in the literature⁸². However, a significant body of evidence exists that suggests that the structure of the PL is sensitive to relatively small electrical, mechanical and thermal shocks. Mogensen⁸³ has proposed that the large difference in molar volume of lithium and LiCl (Pilling-Bedworth ratio of 1.58) will cause stresses to accumulate inside the LiCl layer during film growth. In such a situation, small forces may trigger stress relief through cracking of the film. Electrical, thermal and mechanical stresses cause fractures in the PL, however the damage is extremely localised^{84,85}.

7.9.1. Electrical shock

Yamin has stated² that under pulsed load, it is the form of the pulse that controls the amount of damage to the PL, rather than the mean drain rate. This is due to the fact that the degree of disruption at the lithium/SEI interface is a function of pulse width, amplitude and active lithium anode area.

Where the pulse charge density is 1 mC/cm² or less, then the low charge transfer rate allows the lithium ions to diffuse evenly from the lithium surface. Thus for a given pulse, damage at the SEI/lithium metal interface is restricted. Repair only occurs at intervals when the damage to the SEI/metal interface allows the entry of fresh SOCl₂.

When the pulse is greater than 100 mC/cm², lithium utilisation tends to be much less uneven, resulting in the creation of holes in the lithium whose irregular geometry tends to increase the area of exposed surface, and the amounts of reactants required to repair the damage to the PL. A fresh layer of the SEI is formed between the existing SEI and the naked lithium surface, causing a peak in the corrosion rate. For this

charge level the rate of formation of the passivation layer is equivalent to that for a cell which is only a few days or weeks old, and the SEI growth process is restarted.

Kronenberg et al.⁸⁶ observed the surface of partially discharged cells by SEM, and showed that the impact of a short circuit current of 36 mA/cm² of 2 minutes duration is to produce random localised openings in the PL. Eisenmann and Hoier⁸² have demonstrated that short-term, low-amplitude, low-frequency galvanic pulses of 5 mV at 60 mA used in impedance spectroscopy studies are sufficient to cause rupture of the PL.

7.9.2. Mechanical shock

Mogensen⁸⁷ showed that the PL is subject to intermittent breakdown and repair processes even under apparently stable open-circuit conditions where the cell is placed in a mechanically isolated, vibration-free, temperature controlled environment (± 1.5 °C). He monitored the growth of the PL of two nominally identical cells by using impedance spectroscopy to record the increase in resistance of the PL with time, and showed that very small mechanical shocks triggered concurrent reductions in the impedance of both cells. Such coincidences could only be explained by fracturing of the PL induced by the shocks. The breakdown events were followed by a repair phase and a gradual return to the original 'steady state' PL thickness growth trends.

7.9.3. Thermal shock

Mogensen⁸⁷ also showed that the resistance of the lithium electrode drops abruptly on raising the temperature from 20 to 35 °C and above⁸⁸, but that dropping the temperature caused an 'abrupt' increase in impedance. Sonnenschein Lithium GmbH⁸⁹ have reported the usage of shock freezing to break up the PL as a means of depassivating a cell after storage. Eichinger⁷⁹ found that at higher temperatures growth of the PL is not limited, and internal cell resistance builds up to 10⁷ Ω. At 0 °C or lower, film growth is minimised, and the cell resistance remains virtually constant after some 300 h.

From their study of the electronic structure of the PL, Delnick et al.⁴³ showed that growth does not obey linear power law growth kinetics for several weeks following thermal perturbations (from +50 °C to -20 °C).

7.10. Self-discharge rate

From Ohm's law, the theoretical open-circuit self-discharge (corrosion) current, I_{SD} , is given by:

$$I_{SD} = V_{OCV}/L\rho_{(e)} \quad \text{Equation 7.8}$$

substituting for L in Equation 7.4, and assuming $L = 0$ (the thickness of the PL is negligible at time $t = 0$), we get:

$$I_{SD}^2 = V_{OCV}/2K\rho_{(e)}t \quad \text{Equation 7.9}$$

Thus, I_{SD} is inversely proportional to the square root of elapsed time.

In practice, the breakdown and repair process decays to a finite 'steady-state' self-discharge rate after many months on open-circuit. Thus, self-discharge rate is always >0 . If $^{\infty}I_{SD}$ is the steady-state value of I_{SD} , then the instantaneous self-discharge rate is given by Equation 7.10:

$$I_{SD} = ^{\infty}I_{SD} + B(0.5t)^{-0.5} \quad \text{Equation 7.10}$$

where $B = V_{OCV}/L\rho_{(e)}$.

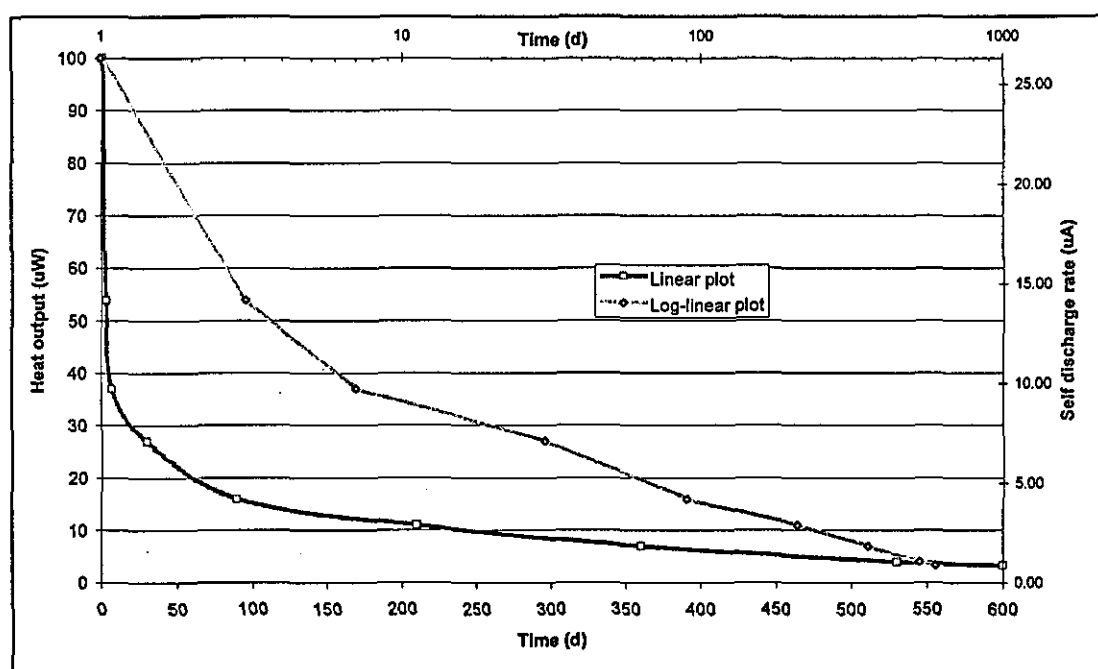


Figure 7.1 Microcalorimetric plot of AA Cell during open-circuit storage at room temperature.

Yamin⁹⁵ has used microcalorimetry to determine the relationship between $^{\infty}I_{SD}$ and t for an AA cell on open-circuit, and his experimental results are reproduced in Figure 7.1. The left hand y-axis is scaled as heat output, and the right hand y-axis in self-discharge rate calculated by means of Equation 7.2.

The heat output is plotted against the linear x-axis time scale, and the self-discharge against the logarithmic x-axis time scale at the top of the graph, in order to detail the first hours of behaviour. The graph demonstrates that I_{SD} decays from the first

measurement of 26 μA at $t=1$ day, to approximately 13 μA after about 4 days; by 600 days corrosion is still evident, but has reduced to approximately 1 μA .

The major point of interest in Figure 7.1 for the meter application is the very large difference in magnitude of self-discharge rate of the newly activated cell, as compared with that of the quasi steady-state value which is approached after some 600 days. In the above example, the difference approaches two orders of between the magnitudes (100 to 4 μW).

Attempts have been made to model the kinetics of open-circuit heat production. However, no consensus exists. In 1982, from preliminary results, Hansen et al.⁹⁰ indicated that growth followed a parabolic law. In 1986, he was reported⁹¹ to have proposed an inverse power law, in qualitative agreement with Iwamaru and Uetani⁹², who measured heat evolution at 20 °C on open-circuit, and developed a relationship between heat output q and time t (h) shown in Equation 7.11

$$q = 7.695/t^{0.931} \quad \text{Equation 7.11}$$

In 1987, Hansen and Frank⁹³ carried out a systematic investigation of the open-circuit evolution of heat over long time scales and determined that the parabolic heat evolution model is inaccurate: (a) the slope of the q versus t curves is not 0.5, (b) the slope changes with temperature, and (c) heat-treated cells generate slopes which differ from those of non-heat treated cells. Their final model is shown in Equation 7.14.

$$q = \Delta U k / t^x \quad \text{Equation 7.12}$$

where ΔU is the heat produced per unit of reaction, and k and x are empirical constants, which are functions of temperature. They concluded⁹³ that the integrity of the PL is more important in determining the corrosion rate than thickness.

Using Microsoft Excel's regression analysis tool-kit, attempts to fit five types of analytic expression were made on Yamin's results given in Figure 7.1, namely: linear, logarithmic, polynomial, power, and exponential. The R^2 value indicates the quality of fit of a regression curve (on a scale of 0 to 1, with 0 indicating a poor fit, and 1 a good fit and a meaningful regression line)⁹⁴. Here the best fit is given by the power law, given in Equation 7.13, with an R^2 value of 0.9535, indicating that the equation gives a reasonably close approximation to the measured data.

$$j_{SD} = 106.17f^{-0.4817} \quad \text{Equation 7.13}$$

7.11. The effect of temperature on self-discharge rate

The theoretical effect of temperature on the open-circuit value of self-discharge rate can be determined by substituting L into Equation 7.8. We assume $L_0=0$ at $t=0$, giving:

$$I_{SD}^2 = V_{OCV}/2K\rho_{(e)}t \quad \text{Equation 7.14}$$

In Equation 7.14, V_{OCV} is only weakly dependent on temperature, and the main dependence of I_{SD} with temperature derives from the SEI electronic resistivity, $\rho_{(e)}$, which can be formulated as follows for a solid electrolyte⁹⁵:

$$\rho_{(e)} = K\exp(-E_a/RT) \quad \text{Equation 7.15}$$

where K is a constant, R is the gas constant (8.314 J/K/mol), T is the absolute temperature, and E_a is the activation energy for the conductance. Yamin⁹⁵ gives $E_a=50$ kJ/mol. From Equation 7.14, $I_{SD} \propto \rho_{(e)}^{-0.5}$, thus a 20 °C increase results in a twofold increase in I_{SD} .

In practice, the equilibrium temperature model is simplistic; changes in temperature introduce thermal stresses in the PL which can cause cracking and lead to sudden increases in I_{SD} . It is also likely that the effect of long-term exposure to different temperatures will be to modify the morphology, properties and porosity of the PL.

7.12. The effect of load on self-discharge rate

Open-circuit self-discharge rates of 1, 0.07 and 0.6 $\mu\text{A}/\text{cm}^2$ at 37 °C, and 0.9 to 1.8 $\mu\text{A}/\text{cm}^2$ at 20 °C have been reported in the literature^{96,97,98,99}, and the manufacturers have reported values of 0.09, 0.25 and 0.70 $\mu\text{A}/\text{cm}^2$. This covers a range of 0.07 to 1.8 $\mu\text{A}/\text{cm}^2$. For the purpose of this study, a mid-value of 0.2 $\mu\text{A}/\text{cm}^2$ is adopted.

Iwamaru and Uetani⁹² measured heat generation at various d.c. current levels, and found that heat output remained at constant level when current density was reduced below a threshold of 1 $\mu\text{A}/\text{cm}^2$, implying that mass transport of active species was maintained without damage to the PL at this rate. However, clearly this must be a temporary situation as the lithium/SEI interface must break down periodically as the surface layer of lithium is dissolved.

In 1991, Levy and Bro stated that no general correlations are available for the extrapolation of battery performance from high rate pulse discharges to low rate pulse discharges¹⁰⁰. Following a literature search, Eisenmann¹⁰¹ concluded in 1996 that no

unified model existed in the public domain. It is clear from the qualitative data available regarding the effects of load on the breakdown and repair processes discussed in Section 7.9, that self-discharge rate generally increases when the cell is discharged under electrical load. However, conflicting data exists, and Yamin et al.¹⁰² have reported a case where discharging a cell at very low rates results in a self-discharge rate which lower than that measured on open-circuit storage.

In a personal communication, Yamin¹⁰³ proposed that the effect of load on self-discharge rate may be classified according to the form of load as shown in Table 7.1. For low direct current loads, the self-discharge rate is approximately proportional to current density. Where the pulse charge is below 0.2 mC/cm^2 , then the availability of charge carriers in the catholyte results in minimal damage to the PL, and self-discharge rate is similar to that for the equivalent mean current. Hoier¹⁰⁴ also supports this relation more generally by observing that the effect of duty cycle disappears as the current density reduces below $1 \text{ } \mu\text{A/cm}^2$, and Takeuchi¹⁰⁷ showed that heat dissipation (and thus self-discharge) remained relatively constant for pulsed loads of average current densities below about $5 \text{ } \mu\text{A/cm}^2$.

Table 7.1 Effect of load type on self-discharge rate.

Type of Discharge	Lithium surface utilisation*	Pulse charge density (mC/cm^2)	Effect on self-discharge rate
Open-circuit			Decreases with storage time
Low d.c. current High d.c. current			Linear relation with current Non-linear relation with current
Pulse	Fraction of a monolayer	<0.2	Similar to average d.c. currents
Pulse	Several monolayers	~1	Up to 20% higher than mean d.c. currents
Pulse	Hundreds of monolayers	>20	As about 1 m old
Pulse	Thousands of monolayers	>200	As fresh ~ 1 week old

1 monolayer = 0.2 mC/cm^2

When the pulse is greater than 1 mC/cm^2 , the self-discharge rate rises to a factor of 20% greater than that for the equivalent average load current. For pulses of between 20 and 200 mC/cm^2 , the self discharge rates revert to those for a cell aged 1 month and 1 week respectively. Even when the mean load is maintained at a low level by extending the interval between pulses, the damage to the surface caused by individual

pulses will cause a cyclic rise and fall of the self-discharge rate as if the passivation layer was repeatedly being stripped off and repaired. Hansen and Frank¹⁰⁵ have shown that the non-faradaic heat output can exceed the external current, where a high amplitude external load is superimposed onto an existing PL repair process.

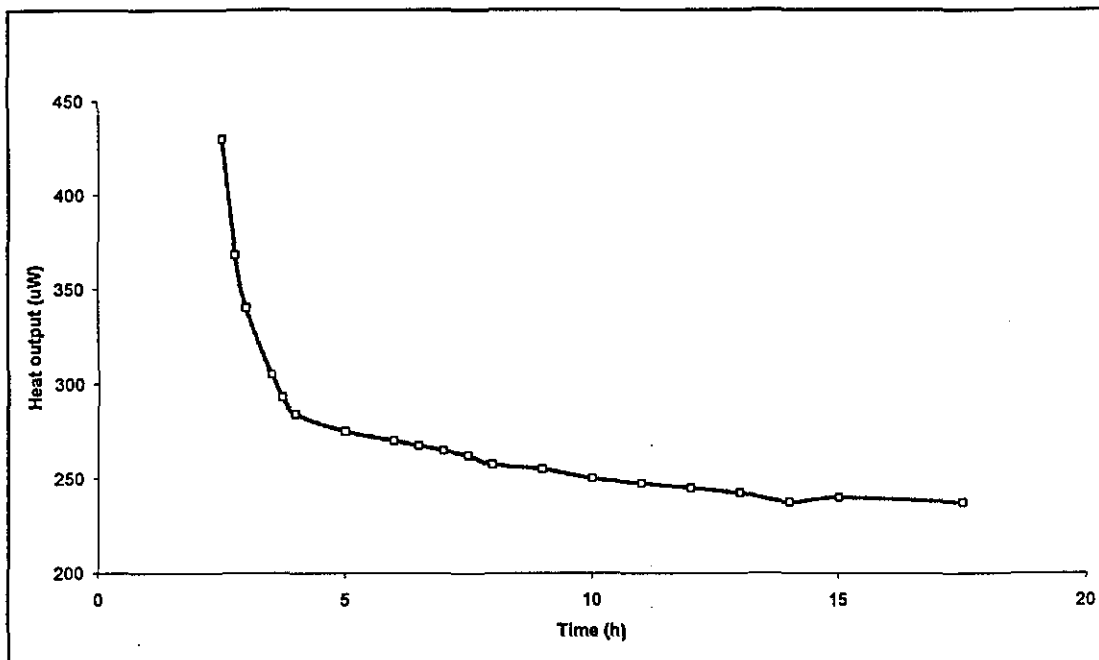


Figure 7.2 Microcalorimetric plot of Te 'D' Cell under Meter A load profile. The profile gives the sum of the heat output dissipated by cell and the 120 kΩ load resistor of mounted within the microcalorimeter cavity.

As indicated in Section 2.1, the meter load comprises a pulse of charge of approximately 0.3 mC, giving a charge density of 0.007 mC/cm². This falls into the category 'similar to d.c. currents', implying a self-discharge rate equivalent to that for a mean current of ~100 μA. Yamin has measured the evolution of heat loss from a Td 'D' size battery subjected to the Meter A load profile and his results are reproduced graphically in Figure 7.2. It is not known whether the high initial rate of heat output at 2 h is due to de-stabilisation of the microcalorimeter, or a true value of the 'activated' discharge rate. The heat output rate decays to approach a steady-state value of 250 μW after some 15 h, equivalent to a self-discharge rate of 65 μA. The curve fitting tests described in Section 7.10 were attempted on the data in Figure 7.2, without success, implying that in this case the self-discharge rate relaxation curve deviates significantly from the power law.

7.13. Effect of depth of discharge on self-discharge

Utilisation of the SOCl₂ by the electrical discharge and self-discharge processes effectively increases the relative concentration of LiAlCl₄ in the cell. Thus the

possibility exists that the compositional changes will modify self-discharge rates during discharge. Skarstad¹⁰⁶ found that the evolution of parasitic heat from Li/SOCl₂ cells varied with depth of discharge. Takeuchi¹⁰⁷ measured self-discharge rate of BRC cells (lithium/bromine chloride in SOCl₂) as a function of depth of discharge at various discharge rates, and showed that self-discharge rate increased by a factor of approximately seven as the cell was discharged from fresh to C50%. The rate then diminished to zero as the discharge process entered the end-of-life phase.

Other workers^{108,109,110,111,112} have carried out static calorimetric measurements of self-discharge rate at various times during discharge. These generally yield curves showing at least one maximum occurring at between 25 and 50% of initial capacity, the heat output then reduces as discharge proceeds. The heat evolution profiles during discharge differed from one experiment to another, and even within a given experiment variations in self-discharge rate of a factor of up to 4 were recorded. In 1996, Hoier¹¹³ stated that nothing is known about the self-discharge behaviour of cells at states of charge of smaller than C50%.

7.14. Effect of dynamic stresses on self-discharge

Damage to the PL will be expected to trigger a rapid rise in self-discharge rate followed by exponential-like decay. Ideally, it should be possible to correlate the magnitude of the peak and the time constant of the decay process of the self-discharge rates with a given stress level. However, no systematic study of such effects has been reported, and there appears to be very little quantitative data in the public domain.

Hoier¹¹⁴ reported an open-circuit heat output of 300 μ W for a Te cell following a temperature change from 5 to 30 °C, equivalent to a self-discharge current of 79 μ A. This is a factor of six greater than the manufacturer's reported steady-state value¹¹⁵. Kronenburg reported a quadrupling of self-discharge rate following a 36 mA/cm² short circuit of 1 minute duration.

7.15. Practical implications

As discussed in Sections 7.6 through to 7.9, it is clear that the morphology and porosity of the PL are affected by a number of design, operating and environmental factors. For example, it is known that both the addition of SO₂ and variation of the temperature change the size of the LiCl crystal and its packing arrangement in the PL. Self-discharge rate may be reduced by reducing the concentrations of LiAlCl₄ and impurities such as Al³⁺ ions. However, no systematic information is available

regarding the effects of the other factors on either self-discharge rate, or the mobilities of active species through the PL.

Discrepancies between the measurements of self-discharge rate and the changes that occur through cell discharge illustrate the difficulty of assigning a discrete value to the Li/SOCl₂ cell. We have shown that the self-discharge rate can vary by at least two orders of magnitude for a given cell design. The rate is dependent on the electronic conductivity of the SEI/PL matrix, which is in turn dependent on cell age, depth of discharge, initial de-passivation process, electrical load, and the external thermal and mechanical stress levels. Neither the peak magnitude of self-discharge rate nor the time constant for the subsequent decay curve following an event which causes breakdown of the PL is known with any accuracy, and their magnitudes will in any case be dependent on recent history of the cell. The available qualitative data suggests that the impact of an applied stress may increase self-discharge by as much as an order of magnitude above the steady-state value for that operating condition. Thus the integrated effect over time for a meter battery which is exposed to background thermal and mechanical shocks may be significantly in excess of that predicted assuming continuous steady-state conditions.

Although it may be possible to prepare mathematical models to account for self-discharge under steady-state open-circuit conditions in the laboratory, no such model exists to accurately predict self-discharge under operation in the field. Calorimetry is effective in determining the instantaneous self-discharge rate, but clearly is less reliable when the time-averaged value of self-discharge rate for a cell operating in a variable environment with variable stress levels is required. Thus any predictions of the effects of self-discharge in the meter application that are made on the sole basis of microcalorimetric measurements would appear to be subject to uncertainty. One means of resolving this uncertainty is to monitor the capacity loss rates of meters in operation in the field; i.e. to analyse the capacity losses of statistically meaningful batch sizes of batteries whose operating and storage history is well defined. From recent discussions with the manufacturers², it would appear that no monitoring of operational self-discharge capacity losses has been reported.

Voltage delay may be an important performance criterion in applications where a high drain rate is required instantaneously from a cell which has been subject to an extended period of storage or operation at low loads. During long periods of off- or

low-load, it is possible that the impedance of the PL layer may grow to such level as to inhibit the immediate voltage response rate to the demand. This phenomenon is known as 'voltage delay', and the effect is widely appreciated as a performance limitation of the Li/SOCl₂ cell type. The voltage/time response curve is dependent on the rate of 'depasivation' of the PL. Generally, voltage delay is not thought to be of significance in low rate applications, however it is not clear whether or not the effect will interfere with the relatively high charge amplitudes associated with a 'meter read' interrogation via the meter's optical port. The activity imposes a peak current in excess of 10 mA, and there is some evidence that voltage delay may present a problem after months of operation in the field at the low normal discharge rate .

CHAPTER 8

TEST PROGRAMME

The main variable that defines performance in the meter application is the service life, which is defined by the time the battery will power the meter until the cut-off voltage, V_X , is reached:

$$dt = dQ/I(t) \quad \text{Equation 8.1}$$

where t is the duration of discharge, I is the discharge current and Q is the delivered charge, normally expressed as the battery capacity. If Equation 8.1 is solved for dQ and integrated over the lifetime of the battery, the final value of charge is the capacity associated with the discharge conditions considered. A classical approach to determining capacity is to obtain capacity for one discharge condition, and assume it will be constant over a wide range of conditions¹. However, for the Li/SOCl₂ battery this approximation becomes inaccurate if extrapolated from medium discharge rates to either high discharge rates. The errors arise from the intrusion of cathodic polarisation at high discharge rate, or losses due to self-discharge which tend to become significant for low-rate, long-duration discharges.

The total charge converted to electricity, heat or unobtainable due to polarisation, Q_T , is given by

$$Q_T = Q_L + Q_{SD} + Q_P \quad \text{Equation 8.2}$$

where Q_L is the electrical charge delivered to the load, and Q_{SD} , and Q_P are the amounts of charge lost through self discharge and polarisation respectively.

To emphasise the charge lost by self-discharge and polarisation effects, Q_L can be written as the difference between the total charge lost, Q_T , and charge lost to internal self-discharge processes, Q_{SD} , and polarisation effects, Q_P . Equation 8.1 now becomes:

$$dt = [dQ_T - dQ_{SD} - dQ_P]/I(t) \quad \text{Equation 8.3}$$

If, as with Li/SOCl₂ cells, the load voltage discharge profile is rectangular, i.e. a uniform voltage to a given state of charge, followed by a perpendicular fall off to the cut-off threshold, then I can be expressed approximately in terms of the load R_L and the battery terminal voltage V_L , and Equation 8.3 becomes:

$$dt = [dQ_T - dQ_{SD} - dQ_P] \times [R_L/V_L(t)] \quad \text{Equation 8.4}$$

The solution to Equation 8.4 is dependent on knowing the relationships between dQ_T and dQ_{SD} and dQ_P , which vary according to battery type and operating condition, and must be determined empirically.

The total capacity lost due to polarisation may be related to the stoichiometric capacity (Q_0):

$$Q_P = Q_0 - Q_{SD} - Q_L \quad \text{Equation 8.5}$$

For Li/SOCl₂ cells discharged at high rate over a short time-scale, Q_{SD} generally becomes an insignificant factor. If Q_0 is known, it is possible to determine the magnitude of the effect of polarisation. dQ_{SD} is relatively small when a low-rate Li/SOCl₂ cell is discharged at a mid-rate, and it is possible to measure Q_T and dQ_P in a relatively short time-scale. The discharge of cells at different rates in this operating domain forms the basis for accelerated testing, and allows the relationship between polarisation and discharge current may be derived. Q_P approaches zero as the discharge rate approaches zero (i.e. long-term discharge), and Q_{SD} may be determined.

8.1. Evaluation methods

Ideally, a single accelerated experimental method would provide measures of the distributions of the electrochemical and self-discharge capacity loss processes (dQ_{SD}/dt and dQ_L/dt). However, because of the complex relationships that exist between the two, which vary through discharge and with operating conditions, the only reliable method of establishing the true rates of capacity loss is by means of real-time observations. Measurement of the residual capacity of batteries removed from service in the field will provide an evolving trend of the real-time capacity loss rates. This measurement technique has been adopted here, and a preliminary batch of cells has been removed from the field after periods of service, as detailed in Chapter 15

The long time-scale involved with such a technique fails to address the needs for (a) immediate and medium term data, and (b) controlled experimentation. Various reviews of laboratory test and evaluation methods that can be applied to determining the electrochemical performance of lithium primary batteries have been published^{2,3,4}. The laboratory investigations of self-discharge are discussed in Chapter 14 of the thesis. However, it was found that accelerated testing can provide accurate measurements of battery capacity, and in principle the mid- to long-term reliability can be estimated from the capacity distributions of statistically meaningful test batches of batteries after allowing for the kinetics of their deterioration.

Fester and Levy³ describe an exploratory technique used where the failure modes are unknown and where the data contains unknown relationships. The technique is suitable for both measuring battery capacity and detecting unforeseen failure modes, and it forms the basis of the experimental methodology used here. This empirical approach regards the battery performance as being based on unknown relationships and operates by generating a data set which enables the characterisation of basic performance trends, inconsistent performance patterns, and unexpected failure modes. The usual approach in accelerated testing is to impose a stress on the battery at higher than normal levels to shorten the time to failure⁵. Elevated temperatures are used to evaluate ageing caused by chemical processes, high-rate discharge assesses basic electrical performance, and increased mechanical stresses are used to assess mechanical properties. Ideally, it is necessary to know what the expected failure modes are in order to apply the appropriate stress factor⁵. However, apart from capacity losses due to self-discharge and polarisation, the manufacturers claim a zero defect rate for this application. The cause(s) of the premature failures and reliability problems observed by users of lithium batteries discussed in the Introduction is not known. By adopting discharge current as the acceleration factor, and scanning through a range of levels, the results should identify any deviations from normal operation, and provide sufficient information to aid in the diagnosis of any malfunction, thus indicating the direction of any further tests that might be necessary.

8.2. Test matrix

The statistical distributions of performance are indicators of reliability, and a minimum number of experiments is required in order to obtain meaningful information. The larger the sample size of the test batch, the greater the confidence level of the statistical parameters. Fester and Levy recommend a minimum batch size of 5 cells to determine trends in performance⁵. Here a sample size of 10 cells was adopted.

Five levels of stress are normally utilised to allow meaningful extrapolations. However, with 7 cell types scheduled for the initial test programme, and other operating variables such as ambient temperature, orientation, storage duration, etc. to characterise, it was evident that a full matrix would require a larger number of test cells and measurement channels than the available resources would allow. Thus the initial test programme involved a reduced test matrix of 5 battery types and 3 levels of

load current. Once the equipment had been commissioned and its scientific effectiveness had been fully demonstrated, two further 3 levels of load current were added.

The initial load levels were selected on the recommendation of the manufacturers, as being in the range that would yield maximum electrical capacity (i.e. minimised polarisation and self-discharge effects). The load levels involved test discharge durations of between 2 and 12 months.

8.3. Thermal environment

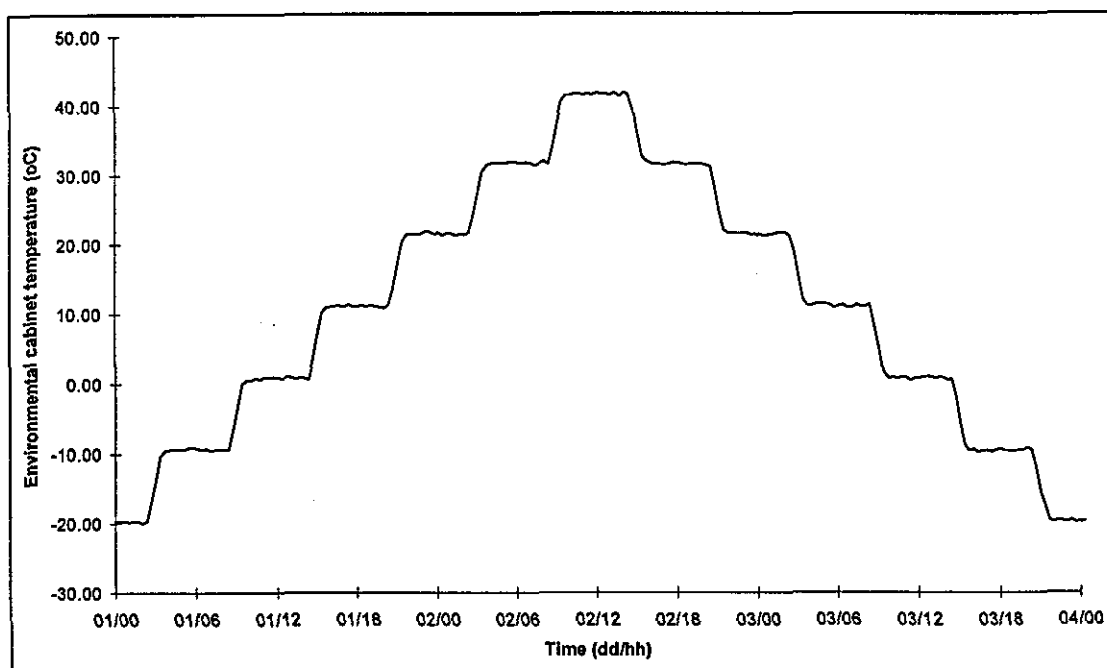


Figure 8.1 Measured temperature trace of the environmental cabinet temperature cycle.

In addition to determining performance under accelerated discharge rates, it was considered important to characterise voltage behaviour under both steady-state and dynamic thermal conditions. To control temperature, the test cells were housed in an environmental chamber which was programmed to give the continuous thermal cycle shown in Figure 8.1. The cycle comprises successive 5 h and 1 h periods of alternate constant and dynamic temperature states, the change rate being 10 °C/h. The constant temperature levels are spaced at 10 °C temperature intervals, giving 7 levels from -20 to +40 °C. The period of the complete cycle is 72 h.

It is important to note that the stress imposed by thermal cycle is relatively benign and is simply designed to be representative of the UK external environment. It is not intended to act as an accelerated stress.

8.4. Voltage measurements

Capacity above the 3.2 and 2.5 V meter operating thresholds represents the key performance criterion in this application. Thus, the battery terminal voltage is the key performance indicator, and an accurate record of voltage during discharge is an important experimental requirement. Transient voltage incursions are known to occur as a result of:

- (a) Electrochemical noise⁶.
- (b) Temperature (and other stress) variations.
- (c) Polarisation.
- (d) Mechanical defects (internal and external).

Voltage incursions below the meter cut-off thresholds will cause the meters to lose data, and it is thus important that the data logger should capture transient voltage events. Ideally the logging system should record voltage continuously to give a complete record of the discharge. However the sheer volume of data associated with multi-channel logging over a period of months makes this an impractical proposition. The optimum solution was to employ a programmable data acquisition system that would sample voltage at discretely, at intervals whose frequency is timed to trap any voltage transients capable of affecting meter operation, and to store the data digitally.

8.5. The discharge test rig

The test requirements outlined in the preceding Sections 8.2 through to 8.4 translate into a basic specification for the discharge test rig as follows:

1. 1000 voltage measurement channels.
2. Programmable temperature environment.
3. PC based automatic control and data acquisition (DAQ) system.
4. Modular battery load system.
5. Unattended operation.

Preliminary investigations showed that no 'off-the-shelf' test rig existed that could be adapted to this specification, and the rig was purpose designed. The hardware was assembled from a mixture of commercially available equipment, and components that were designed and built to specification (e.g. data acquisition modules, software, the load units, cable/connector assemblies, equipment racking, etc.).

The battery performance test rig is shown schematically in Figure 8.2, and illustrated in the photographs given in Figure 8.3 to Figure 8.6. Functionally, the rig measures

the individual terminal voltage, E_L , of test cells that are discharged through resistive loads and exposed to a thermal cycle. Cell voltages are polled at 60 s intervals and the raw data saved to file. Data processing and analysis is carried out under manual control as required (normally at the end of a test).

The control, data acquisition and processing tasks are shared by two dedicated PCs, which are connected by 'thin-wire' Ethernet cables to form a Local Area Network (LAN) as shown schematically in Figure 8.2. The PCs run under Microsoft 'Windows for Workgroups 3.11'. This platform provides built-in networking facilities allowing the mass storage media to be seen as individual drives and accessible from each PC, thus facilitating for easy transfer of data between the two PCs, and pre-programmed back-ups to mass storage media.

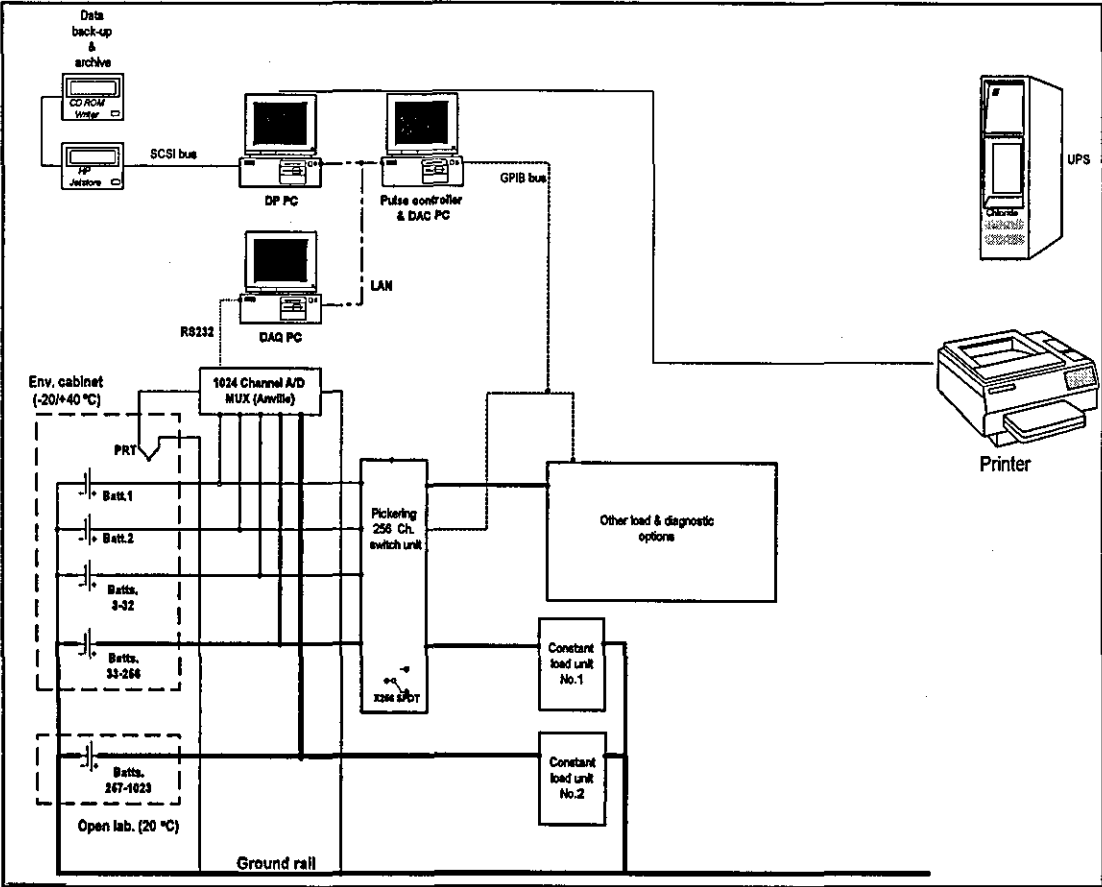


Figure 8.2 Schematic of the test rig.

The main functions of the Data Acquisition (DAQ) PC are: (a) control of the scheduling and execution of the data acquisition processes, (b) display of the status of the data acquisition routines and selected battery voltage values on the PC monitor as shown in Figure 8.4., and (c) storage of the raw data in a specified directory structure and file format. Once activated, this PC operates automatically.



Figure 8.3 Photograph of discharge test rig, showing the environmental chamber (far end), resistance load units (middle distance), wiring interface units, multiplexer and A/D converters, the DAQ PC (atop environmental chamber) and DP PC (at front) and GPIB PC (middle distance). The Uninterruptible Power Supply is just visible beneath the bench.



Figure 8.4 Photograph of discharge test rig. The DAQ PC monitor (far distance) is displaying the 'real time' voltage readings for a block of 100 battery channels and the 'debug' log. The DP PC monitor is displaying an example of a battery discharge profile. The GPIB PC monitor is displaying a battery pulse profile. The DAT recorder and CD-ROM Writer units are situated between the DP and GPIB PCs.

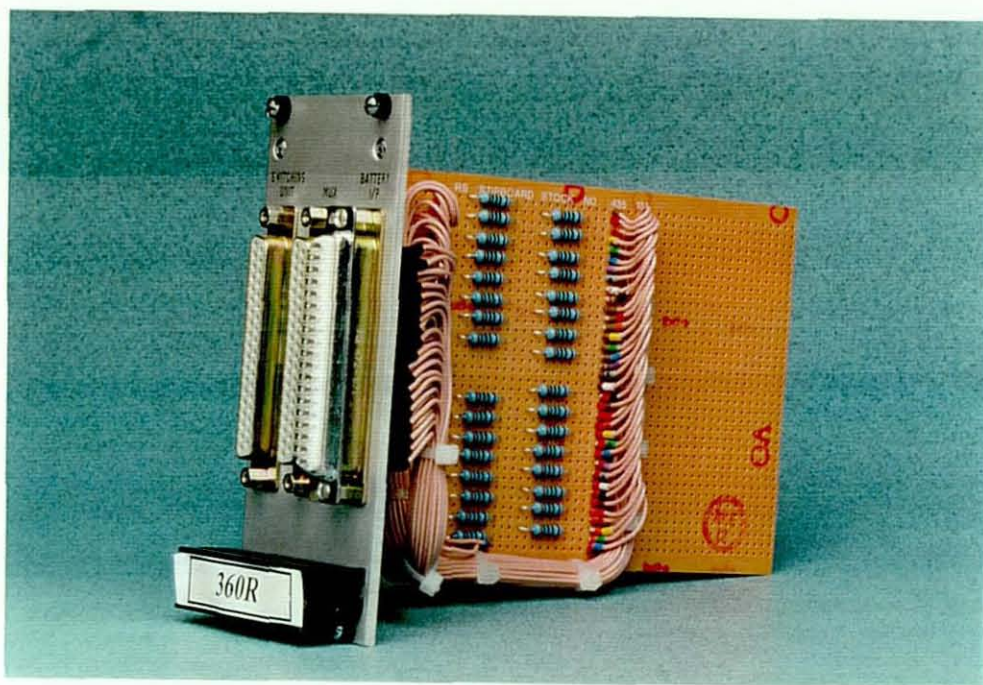


Figure 8.5 Photograph of a 32 channel 360 Ω constant load unit, showing resistors, wiring, and the three D-connectors to batteries, multiplexer unit and remote switch unit respectively.

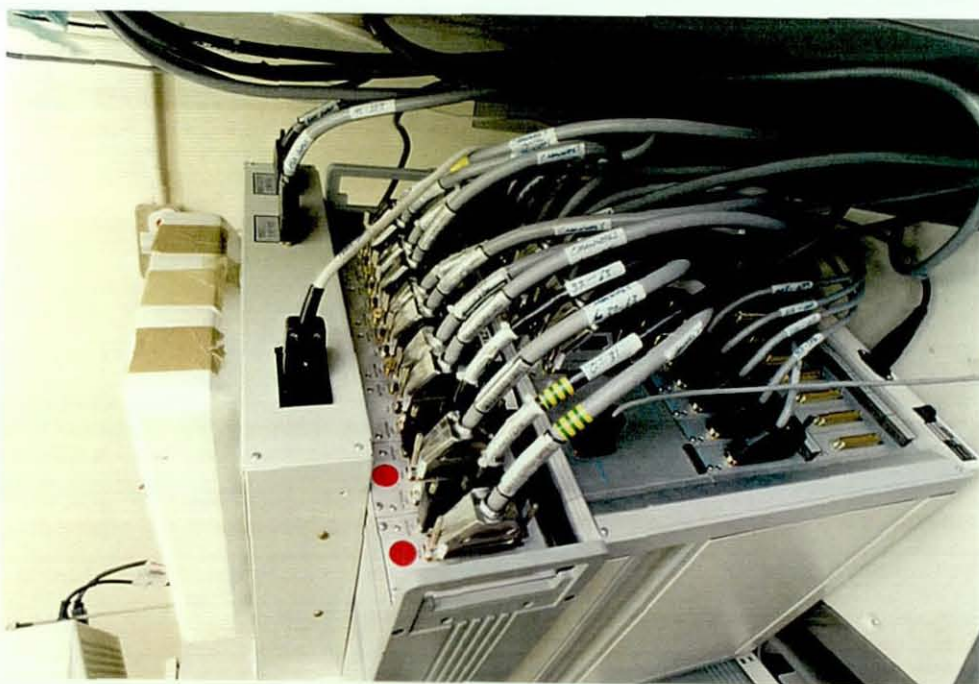


Figure 8.6 Photograph of (a) multiplexer unit and connector plugs (bottom), load module housing unit, (b) cabling to the test batteries and multiplexer unit (middle), (c) 32-channel pulsed load unit, and (d) expanded polystyrene 'egg' box housing test batteries (top). The cables on the right-hand side emanate from the access port of the environmental chamber.

The Data Processing (DP) PC fulfils the following main functions:

- (a) As the 'server' machine on which the main software applications and utilities reside and are utilised.
- (b) Automatic/manual execution of a second back-up of the raw data by means of a programmed scheduler which transfers the raw data from the DAQ PC to the DP PC on a daily basis.
- (c) Processing and analysis of the data.
- (d) It is used as an interface to archive the raw and processed data to mass storage media, and (e) as the manual interface.

The voltage measurements are performed by an Anville Instruments Series 400 Data Acquisition and Control (DAQ) System. The Series 400 is a PC based modular system controlled by a 6809 microcomputer that executes the necessary control, timing, and linearisation tasks. Analogue to digital conversion is provided by a SER400/AD2 unit having a scale length of 16 bits, with the amplifier range set to ± 10 V, giving a voltage resolution of 0.3051 mV and an accuracy of $\pm 0.01\%$. The DAQ system is fitted with 32 multiplexer modules (SER400/MXS-1 units). Each module accommodates 32 single ended voltage inputs, giving a total capacity of 1024 input channels. Connection to the DAQ PC is via an RS423 serial link. The DAQ PC system is programmed to log the voltages of channels 0-999 (i.e. a total of 1000 channels), and each channel is read and recorded at one minute intervals.

Each test battery discharges through an individual load. The 'negative' terminals of the test batteries are connected to the ground rail of the Anville DAQ and MUX system. The positive terminals are connected to the high-polarity lines of the A/D input channels of the DAQ system.

Figure 8.3 shows an example of one of the purpose-designed 32-channel constant load units. The resistors provide each battery with a passive load. The load current 'floats' in relation to terminal voltage, in accordance with Ohm's law, thus replicating the passive nature of the meter load.

Data on the two PCs are backed-up to a Hewlett Packard Jetstore 2000 DAT recorder (2 Gigabyte capacity), and a Plasmon RF4100 CD-ROM Writer. A CD-ROM (CDR) has a maximum data storage capacity of 640 Mb, and provides fast disk access for post-data analysis. Both storage devices are interfaced to the DP PC through an Adaptec 'Small Computer Systems Interfaces' (SCSI) card installed on the DP PC bus. This strategy gives compatibility with 'MS Windows' File Manager and its data

transfer software utilities, and thus provides a standardised platform for data transfer. 32-channel pulsed-load units were also developed and utilised in the latter half of the programme. Two cascaded oscillators are used to programme the timing parameters of a bank of relays (by means of jumpers), which effectively switch the load on and off to give a rectangular load profile. A duty cycle of 50% and a pulse ON + OFF duration of 16.5 ms was utilised. The pulse timing was checked by means of an oscilloscope. The timing of data acquisition and load pulsing was not synchronised. It was assumed and demonstrated that on average the ON and OFF phases of the load cycle would be recorded in approximately equal proportions.

The number of constant load channels was increased during the course of the test programme from an initial 132, covering 3 values of load resistance, to a final total of 388, with the addition of 2 further resistance values. The relatively small number of initial load channels was a considerable constraint on the rate of progress of the test programme, particularly in the initial exploratory stages. The limitation was justified by the need to 'prove' the design and functionality of the equipment before expanding to the full functionality.

A specific battery test normally comprises a batch of 10 batteries. These are coupled to 10 contiguous input channels of a given 32-channel multiplexer module. For identification, the physical 32-channel modules are defined as Blocs. The modules are connected to the physical channels from 1 through to 1023; thus Bloc 1 comprises data Channels 1-32, Bloc 2 comprises Channels 33-64, and so on.

Temperature control of the test batteries is by means of a Sanyo Gallenkamp Model 195 environmental cabinet. The internal dimensions of the battery test chamber are 0.65×0.5×0.6 m. The unit incorporates a Format 500 Series temperature programmer/controller (based on an Intel 386 processor). For these tests the unit was programmed to cycle through a temperature range of -20 to +40 °C (there is no humidity control). Corrugated mesh shelves provided a simple means of retaining cylindrical batteries in the horizontal mode, and approximately 200 'D' size batteries could be accommodated. Polystyrene moulded containers were used to house vertically oriented cells.

To provide a temperature record of the battery temperature, a platinum resistance thermometer (PRT) was installed in the geometric centre of the test chamber. The PRT was connected to a power supply and lineariser, which provides a 4 to 20 mA

loop, which is converted to voltage by a $250\ \Omega$ series resistor. Voltage values of +5, +3 and +1V correspond to temperatures of +50, 0, and -50 °C respectively. On 29/03/95 the PRT signal line was connected to channel 0, subsequently, on 12/3/96, the line was moved to Channel 992 of the DAQ system. The PRT signal is logged at one minute intervals. The algorithm for converting voltage to temperature (°C), is:

$$\text{PRT temperature (°C)} = (V_T - 3)/0.04 \quad \text{Equation 8.6}$$

where V_T is the PRT output voltage.

The electrical connections between the batteries and the load modules are by 32-way wiring 'looms'. The terminals of sets of 32 individual test batteries are connected to JST polarised and hermetically-sealed connectors on the ends of 100 mm flying leads. The JST connectors lead to a 37-way D-connector which plugs into a load resistance unit as shown in Figure 8.6. The ground lines of the batteries are commoned to pins 17-19 and 36-37 of the D-connector. Connection between the 32-channel multiplexer and load modules was via screened 36 way multi-core cable terminated by 37-pin D-connectors, with ground lines commoned as before. The specified⁷ resistance per core is $314\ \text{m}\Omega/\text{m}$, which for a typical load current of 10 mA gives a voltage drop of 6 mV over a two metre cable length. This level of voltage loss is not significant here. (The battery evaluations are based on relative rather than absolute voltage measurements, and 6 mV is 0.24% of the 2.5 V voltage threshold, and is considered to be an acceptable voltage loss that is common to all batteries).

A Chloride 5 kVA 'Lanpower Plus' uninterruptible power supply (UPS) provided power back-up to the DAQ PC and the Anville DAQ System. The UPS operated during several power-cuts that occurred during the course of the test programme!

In the final stages of the project a 256 channel System 10 programmable relay switching system supplied by Pickering Interfaces Ltd. was added to allow remote switching of the batteries from load to open-circuit or to some other load system or diagnostic instrument. The system is provided with low contact resistance ($150\ \text{m}\Omega$) single pole double throw (SPDT) mercury reed switches (giving a voltage drop of 6 mV at 10 mA). The system is controlled by means of a further purpose designed software module residing on a third PC, (the GPIB PC). Communication to the relay unit is via an intelligent GPIB interface, which facilitates independent channel selection and programmable timed and sequenced switching.

8.6. Software

A purpose-designed suite of software modules was designed and written both to automate the data acquisition and control (hardware) tasks, and to facilitate the data processing and analysis tasks. The software was written in Borland 'Turbo Pascal for Windows Version 1.5' and runs seamlessly under Windows for Workgroups. The software is fully compatible with standard PC utilities and provides multi-tasking capability to allow concurrent tasks to be performed (e.g. automatic scheduled backup). The program listing is given in Table 8.1 below:

Table 8.1 Software programme listing

Directory path	File name	Function
i:\winsoft	bgdaq.exe	DAQ controller
c:\bgasplus\bgasapps	bgfile.exe	Daily raw data transfer G:D + error checking/correction
c:\bgasplus\bgasapps	bganal.exe daily.lib	Daily Raw data processor
c:\bgasplus\bgasapps	bganal.exe prt.lib	PRT Raw data processor
c:\bgasplus\bgasapps	bganal.exe x.lib	Genl. Raw data processor
c:\bgasplus\bgasapps	bgconv.exe	1 - Raw Data+PRT to XL
c:\bgasplus\bgasapps	bgview2.exe	2 - Binary DBase Viewer
c:\bgasplus\bgasapps	bgview.exe	3 - DBase Xpt to Excel
c:\bgasplus\bgasapps	exptlib.exe	4 - Expt Library Editor
c:\bgasplus\bgasapps	viewer.txt	Debug database file
c:\bgasplus\bgasapps	analog.txt	Debug database file
c:\bgasplus\bgasapps	bgdaqsim.exe	Simulated data generator
c:\bgasplus\docs	hardware.txt	Debug database file
c:\bgasplus\docs	help.doc	Help utility.
c:\windows	bgas.ini	Configuration file.
c:\windows	timerdll.dll	Library file.
c:\windows	bwcc.dll	Library file.
c:\windows	ngcc.dll	Library file.
c:\msoffice\excel\startup	chrt97.xls	Charting macro

The experimental software modules can be classified into the following main functional groups:

1. Data acquisition.
2. Data transfer.
3. Data reduction and processing.
4. Macros for automated graphing.

8.6.1. Data acquisition software

The data acquisition software comprises two main modules:

1. Data acquisition controller.

2. Raw data viewer.

The data acquisition control programme resides on the DAQ PC, and executes all of the functions associated with the voltage measurements and writing of the raw data to hard disk. In principle, the DAQ PC can operate as a stand-alone machine, and needs no other support. An RS232 command string is transmitted to the Anville DAQ system at pre-programmed time intervals. This command initiates a sequenced voltage measurement of the MUX channels 0-999, and down-loading of the data-set to the DAQ PC. The immediate past record of the cell voltage data is displayed on the screen of the DAQ PC monitor in real time in order to provide a visual status of the logging process (one screen page per 100 channels). Voltage measurements which are less than -1 V are trapped during the data read process and given the value -9.99 V, as a positive identifier of spurious data reads.

In the initial version of the DAQ software, data was collected in blocks of 100 channels. However, with this scheme a fault in one channel causes a data loss across 100 channels (this occurred when two of the 32 channel MUX modules failed). The final software version was modified so that data is written to file in blocks of 32 channels, thus restricting potential data loss to a more reasonable limit.

The duration of a single data-read of all 1000 channels is 32 s (1 s per data read and transfer per 32-channel Group). In order to allow for delays in the rates of any of the sampling routines, the data read command is actuated at 1 minute intervals. To flag any missed readings or power-downs, a history log of the data acquisition activities and an associated error count is displayed in the 'debug window' of the DAQ PC monitor, as shown in Figure 8.4.

The software resolution of the voltage measurements stored to file was set to 1 mV. This resolution level was designed to be consistent both with observing the details of cell voltage noise, and minimising data storage capacity. Effectively, four numeric characters are stored with each voltage measurement. The measurements of all 1000 channels are written to file and stored on the DAQ PC in the directory: c:\bgas\data.

The raw data are 'stamped' with the measurement date and time and channel identification information. Other than these stamps and the normalisation of <-1 V measurements, no changes are made to the raw data. This strategy minimises the risk of introducing of manual or other 'non-measurement' data errors, and restricts the

mass storage requirement to a reasonable size (a complete day's raw data occupies 2.8 Mb of disk space).

The data for all 1000 A/D channels are stored in binary format in 10 data files that are created at the beginning of each logging day. The file-name coding convention is: *yymmdd.rnn*, which identifies the year (*yy*), month (*mm*) and (*dd*), and data block (*rnn*), where *r01* contains data for test Channels 0-99, and *r02* data for 100-199, etc. *r* is an unused variable enabling a further field if required. For each data read operation during a given 24 h period (1440 per day) the files are sequentially reopened, the new data appended, and closed. Defaulting to a normally 'file-closed' status offers maximum data security in the event of a PC 'crash'. At the end of each 24 h 'logging' day the raw data files are finally closed and a new set of files is created with their filenames incremented by one day to *yymmdd+1.rnn*.

The hard discs on both PCs possess storage capacity for about 3 months of data. As a first stage data back-up facility, pre-selected raw data files of active test channels are automatically copied from the DAQ PC to the DP PC at the end of each 'logging day' by programmed execution of the file transfer scheduler, 'bgfile.exe'. Data is then further archived to DAT tape at daily intervals. At the end of each calendar month these files are copied to a CDR to form an additional data archive.

8.6.2. Data processing software

For the data to be analysed, it is necessary to convert the raw data from 'binary code' into 'ASCII' format for importing into a spreadsheet or database. However, the 'row count' of a given set of data for a day's discharge measurements is 1440, which, when multiplied by the number of days of discharge, will exceed the 16384 row limit for normal spreadsheet analysis within 12 days of logging. This constraint implies the need for selective data reduction. The development of a set of software utilities to manage the data reduction process evolved in two main stages:

The first version of the data reduction software was designed to process the raw data automatically on a daily basis. The aim was to provide an easily accessible history of test progress up to the previous day. Two types of file were generated which were written to the DP PC hard disk, namely: (a) a summary of significant events (e.g. transitions of specified voltage thresholds), and (b) a more detailed log of cell voltage events extracted according to a set of criteria specified at the beginning of the test by the user and stored in a Battery Test Database (BTD). However, this approach was

adversely affected by two main problems. First, the rate of growth of the processed files was very large and the process proved to be very difficult to maintain without frequent manual reorganisation of available disk space - as the test rig was manned on a 'part-time' basis, this prerequisite could not be guaranteed. Secondly, the software provided no simple facility for retroactive data processing and any problems such as a PC crash or manual errors in the initial BTd settings required a lot of effort to repair. This method was abandoned in favour of a second approach, in which the raw data is processed retroactively under manual control. The final version of the data reduction software comprises the following main modules:

1. Experiment editor.
2. Binary to ASCII data converter.
3. Experiment database (library).
4. Raw data to Excel processor.

The data processing system is controlled through the 'Experiment Editor' which utilises an 'MS Windows' Graphical User Interface (GUI) screen format. The user can set the range of data processing parameters by means of 'Dialogue Boxes', which give the control over the computer analysis. For information, screen dumps of some of these GUIs are shown in Figure 8.7.

The Experiment Editor allows selected battery discharge data (e.g. a set of 10 channels associated with a given discharge test) to be defined as a 'virtual experiment', so named because the same raw data can be processed as many times as required with different processing parameter settings. The user sets up the required test identification and data processing variables; and the virtual 'experiment' is saved to file as xxxxxxxx.lib as a record in a library of such experiments.

The stored set up is available for future use and editing as required. xxxxxxxx is a user selectable filename. The parameter settings in the '*.lib' file form the basic instructions for the data reduction processing routines.

A virtual experiment may comprise any number of batteries; an exhaustive range of selectable parameters allows complete control of the different types of data processing that may be classified as follows:

1. Computational - the value of the discharge load resistance - to enable the cumulative value of the discharged capacity to be calculated.
2. Descriptive, such as the identification of multiplexer channels, test start and end dates.

3. Identification, for example, input of the battery test code.
4. Data reduction and processing instructions.

Three types of data reduction procedure were developed; these and their functions are listed in Table 8.2, and described below.

Table 8.2 Software data reduction filters and main functions.

Filter	Function
Threshold	A fast method to determine capacity to a given cut-off voltage (e.g. 2.5 V computes electrical discharge capacity to the meter cut-off voltage, 0 V to complete electrochemical exhaustion).
Band-width	To trap voltage transitions across specified bandwidth (e.g. 50 mV).
Time-base	Normally set at 1 m (highest resolution) to view all of the data points, (but other settings such as 24 h are used for fast viewing of discharge trends).

A 'Threshold voltage' analysis generates a Summary File which lists the elapsed times (and other pre-defined parameters) associated with voltage transitions through a 'user defined' set of up to 5 voltage thresholds (e.g. 3.2, 2.5, 0 V, etc.). This analysis method provides a summary of the battery discharge performance, and the computed electrical capacity to each threshold. This is the quickest method of computing the cell capacity to a given voltage threshold.

The 'Voltage bandwidth' processing method filters the data by extracting voltage transitions across a virtual grid of pre-defined voltage bands, whose bandwidth is defined by the user. The method presents a means of trapping voltage changes of set magnitude. For example, a bandwidth setting of 100 mV splits the voltage range into a series of 100 mV steps (3.500, 3.400 V, etc.). A voltage fluctuation that crosses from one band into another is recorded in the database, smaller fluctuations within the 100 mV bandwidths are discarded. A bandwidth of 100 mV has been found to give the resolution necessary to enable visual identification of characteristic levels of voltage noise and incursions in a standard graphical output. A narrower voltage bandwidth enables low amplitude voltage 'noise' to be observed.

The third processing option is to extract the voltage data by adjusting the time-base resolution. For example, selection of 1 data point per day is useful for quickly gaining an overview of a battery discharge profile. A setting of 1/min expands the time-base to its maximum 'zoom' resolution to allow detailed examination of voltage transients.

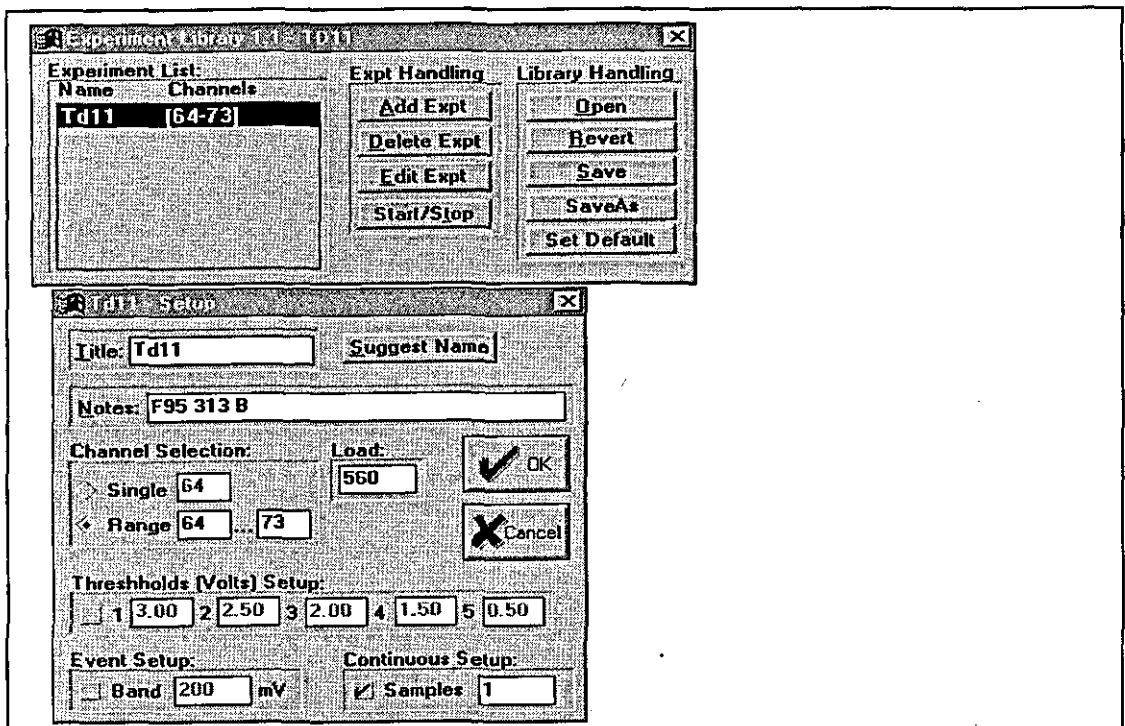


Figure 8.7a Data analysis parameter selection (top) and file handling dialogue boxes.

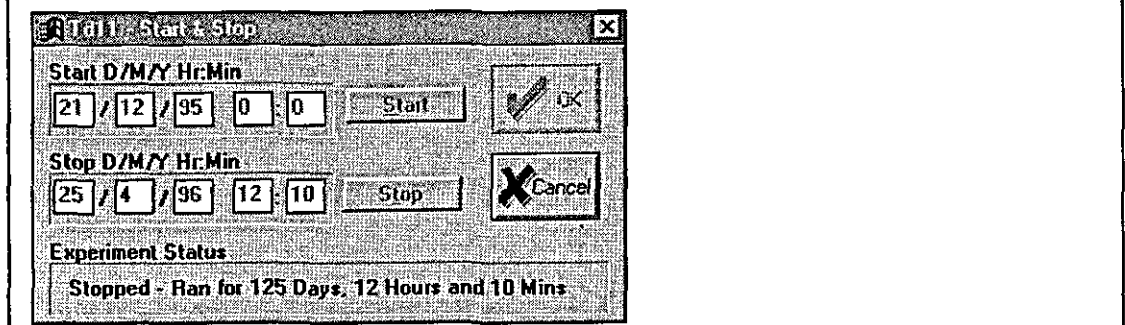


Figure 8.7b Experiment timing and experiment 'start' and 'stop' dialogue box.

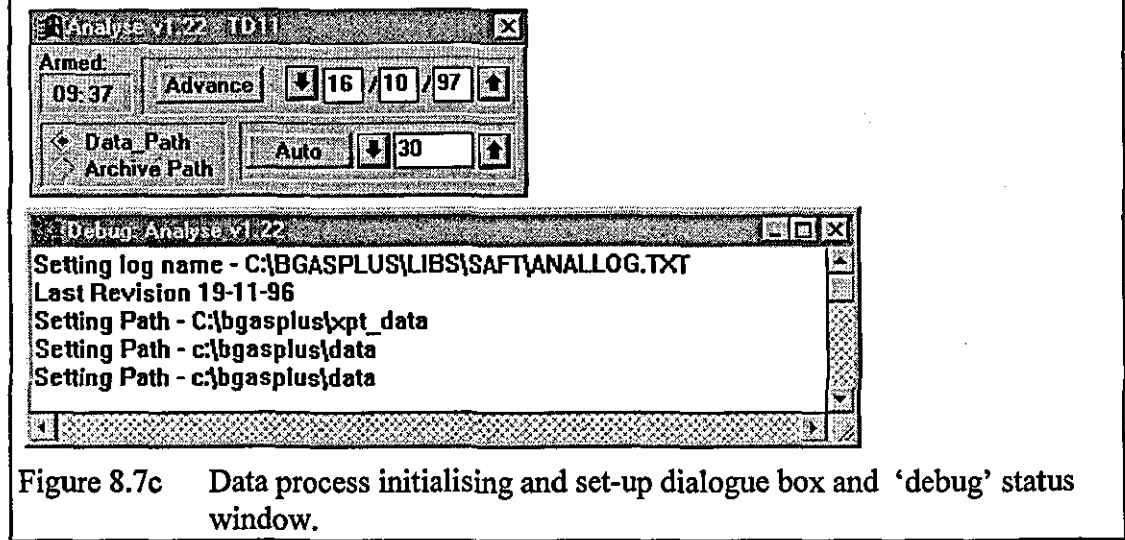


Figure 8.7c Data process initialising and set-up dialogue box and 'debug' status window.

Figure 8.7 Screen dumps of the 'Experiment Editor' data analysis and processing dialogue boxes.

To differentiate between the different types of filtered data, the Threshold Voltage, Voltage Bandwidth, and Time Base types of processed data file are automatically written to sub-directories labelled: \summ, \event, and \cont, respectively.

The 'Raw data to Excel' processor is a utility which provides a fast means of writing a complete set of unfiltered data to MS Excel. It offers a quick means of viewing the day's data for a selected channel (for example, where data corruption may be suspected).

A suite of macro routines was written in Microsoft Excel 4.0 macro language to automate spreadsheet analysis and to translate the processed data into a standardised chart format.

8.7. Capacity computation

Laboratory based capacity and performance measurements conventionally utilise either a fixed end-point voltage in the range 0.5-3 V for Li/SOCl₂ cells^{8,9}. This test criterion is based on the fact that for most applications, the device under power will cease to function at some voltage above zero.

Here, we utilise two thresholds, namely: 2.5 V (the end-point voltage of Meter A), and 0 V which is used to measure the total electrochemical capacity. The capacity to 2.5 V is computed by a macro written in MS Excel, which searches for the first instance of a voltage below the 2.5 V threshold, and then computes the sum of each incremental element of capacity discharged between successive voltage measurements from the start of the on-load discharge to the transition of the voltage threshold, by means of the following equation:

$$Q_{2.5} = \Sigma(V_L dt)/R_L \quad \text{Equation 8.7}$$

where $Q_{2.5}$ is the cumulative capacity to 2.5 V, V_L is the mean load voltage between two successive data points (i, i+1), i.e. $(V_{L(i)} + V_{L(i+1)})/2$, R_L is the value of the load resistance, and dt is the incremental time interval between two successive data points. Q_0 was computed using the same technique, but to an end-point defined by the cessation of electrochemical activity.

The 3.2 V end-point voltage associated with Meter Type B, $V_{3.2}$, is not utilised here, mainly because it was found that the load voltage of Li/SOCl₂ cells at -20 °C tends to level off at 3.2 V during the latter part of a normal discharge. As the test temperature environment and accelerated load conditions are somewhat artificial, it was

considered that to assign a capacity based on a marginal transition would lead to misleading conclusions.

8.8. Calibration

The calibration of the SER400/AD2 analogue to digital converter was checked by supplying a range of constant voltage signals generated by a d.c. power supply to selected MUX channels, and comparing the voltages displayed by the DAQ PC monitor with those measured by a digital voltmeter, which was calibrated to a traceable standard at the Gas Research Centre.

The continuity of the battery channels through the hardware (connections, MUX system) and software (RS232 command, DAQ and data processing stages) was checked using a multimeter and a calibrated d.c. power supply which was manually sequenced through the connections at the battery, through to the processed data output.

The accuracy of the computed capacity was checked (and found to be error free) by importing data into a spreadsheet, and carrying out a manual calculation of discharged capacity.

8.9. Battery test code and tracking system

Table 8.3 Battery test codes and manufacturers' cell type designations

Test Code	Manufacturer	Manufacturer's Designation
Ta	Crompton Eternacell	T20/7
Tb	Eagle Picher	SNL-L (LTC-114)
Td	Saft	LS 33600
Te	Tadiran	TL5940/B

The 4 Li/SOCl₂ candidate cells are encoded as given in Table 8.3. Each test set of (normally) 10 cells is defined as a single test, and is coded xxy-zzz. xx is an arbitrary code that refers to the manufacturer, y is the test series number associated with that manufacturer, and zzz relates to the test Channel number that the battery is connected to.

8.10. Sampling methodology

A standard test batch size of 10 cells is normally used in the discharge tests.

The batteries were obtained directly from the manufacturers and were normally from one production lot. Thus they are not a truly random sample and not necessarily representative of the battery population. The statistical parameters calculated from the test results are thus representative of only a relatively small sample of the population

of production batteries from a given manufacturer. However, in the case of battery type Td, some six production lots were included in the test programme, covering a manufacturing period from October 1993 to April 1996.

8.11. Experimental Safety

All of the batteries included in the test programme have been tested against the British Gas Safety Specification at the specialist laboratories at GEC Hirst, and have been found to be stable over the range of operating loads included here¹⁰. In addition the cells conform to the requirements of the Underwriters Laboratory Standard 1642¹¹. All of the test cells incorporate a vent mechanism; additionally, all of Li/SOCl₂ cells are of low- or medium-rate construction.

High specification, polarised and hermetically sealed JST ELR-02VS and JST ELP-02V male and female connectors are utilised to minimise the possibility of cells being accidentally short-circuited, due to manual error or defective wiring.

The environmental cabinet is fitted with an external over-temperature detector and isolator which is set to shut down the power to the cabinet when the temperature reaches 70 °C or above.

CHAPTER 9

DISCHARGE TEST METHODOLOGY

Four types of 'D' size Li/SOCl₂ battery (coded Ta, Tb, Td and Te) were included in the test programme. The first tests commenced in December 1994, and the main programme continued until December 1996. A total of 63 discharge tests was carried out, normally with 10 batteries per test. Initially, discharge test progress was limited by the relatively small number (132) of load channels and resistance values (3) that were available during the first 12 months or so of the programme. Although their results are not discussed in the thesis, the test programme included Li/MnO₂ and Li/(CF)_x solid cathode cells, because they would provide alternative options in the event of unforeseen problems with Li/SOCl₂ cells. Battery types that were already being fitted to production meters or were close contenders for the application were assigned the highest priority for the initial tests, including cells from Panasonic, Dowty (Ultralife) and Hoppecke.

A total of 46 discharge tests was carried out on Li/SOCl₂ cells; normally under constant load and mostly under the (-20 to +40 °C) thermal cycle, but a small number of tests were carried out in the open laboratory at room temperature (e.g. Td17 and Te4), under a pulsed load regime (Td22p and Te5p), and in different orientations. All but two tests were carried out using a batch size of 10 cells, and in this report a test is defined as a set of 10 nominally identical test cells from the same production lot.

Tests on the Li/SOCl₂ cells fall into two main groups, namely; (a) 13 tests on 3 battery types (Ta, Tb, and Te), and (b) 32 on battery type Td. The large number of tests on the latter was due to the fact that a significant percentage of cells of this battery type was subject to premature failure, with some cells yielding less than 50% of the stoichiometric capacity. The discharge load had been selected from the range recommended by the manufacturer as compatible with achieving maximum capacity, and the failures were very unexpected. The manufacturer was unable to explain the failures, and stated that improvements in design and production methods would be instigated.

The battery was being installed in production meters and it was considered important to resolve the problem as quickly as possible. Repeat tests were carried out both to confirm the original observations and to determine whether the manufacturer's claims

of improvements in design and/or manufacturing quality were having any effect. Gaining an understanding of this failure mode became a major new research objective, however it diverted resources from the programme as originally conceived, resulting in relatively unbalanced experimental test matrix.

9.1. Test variables

The test variables are detailed below. It should be noted that all of the test conditions applied in the experimental programme fall well within the manufacturers' stated ranges of operation.

9.1.1. Thermal environment

Tests were carried out both under the thermal cycle described in 8.3, and under ambient temperature in the open laboratory.

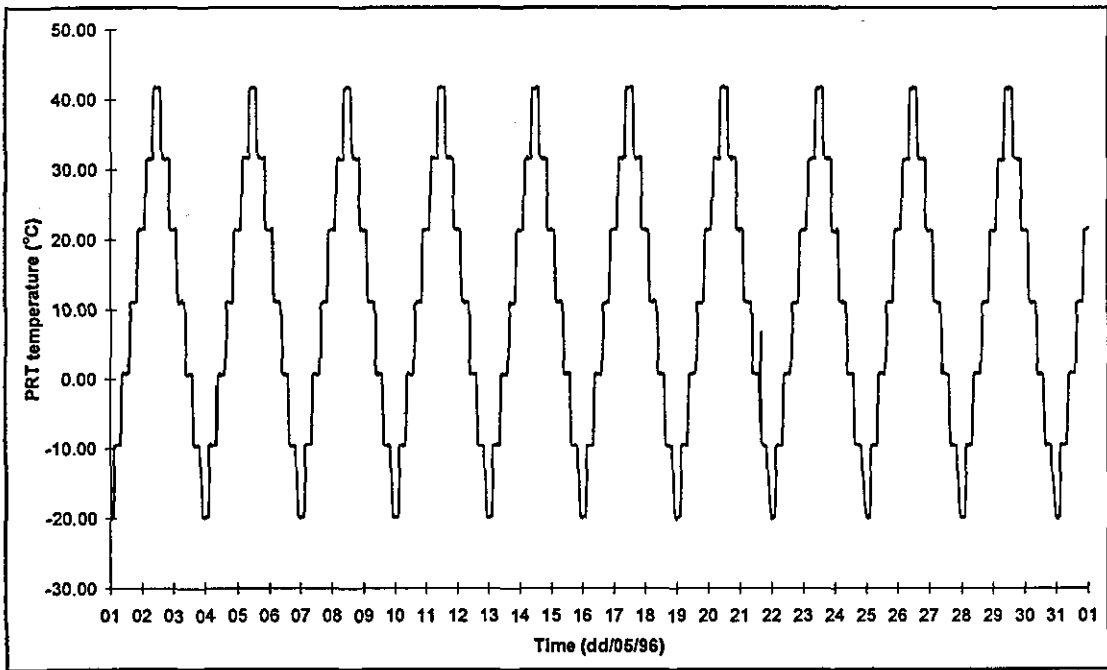


Figure 9.1 PRT temperature trace of the environmental chamber temperature for May 1996.

The temperature record of the environmental cabinet temperature for May 1996 as measured by the PRT is shown in Figure 9.1, and it can be seen that the chamber temperature follows this cycle closely. The temperature profiles within the chamber were not mapped, as it was considered that small temperature variations would not affect performance significantly.

Deviations from the programmed thermal cycle occurred due to power cuts - these are referred to in the text where relevant.

No temperature log of the open laboratory tests was kept - the temperature was assumed to remain constant at 20 °C.

9.1.2. Passive resistive load

The classical techniques used to investigate and evaluate electrochemical systems generally employ feedback controlled power supplies to control the cell potential or discharge current at predetermined levels¹. Here, each test cell is discharged across a resistor, whose passive nature both replicates the form of load employed in the meter application, and provides important information regarding the performance through to the end-of-life phase.

By employing a passive load, battery discharge current, I_L , floats according to Ohm's law, i.e. $I_L = V_L/R_L$, where V_L and R_L are the cell voltage and load resistance respectively. I_L will thus change during discharge as the cell voltage changes due to thermal effects or cell polarisation. Thus, an increase in cell impedance, Z , which occurs at end-of-life, will cause a reduction in the terminal voltage of the cell, which is balanced by a decrease in I_L . The reduction in I_L tends to lead to a reduction in Z , allowing the electrochemical processes to continue through to complete exhaustion of the cell reactants, even where the cell is subject to significant polarisation. By measuring the capacity to zero volts, Q_0 , it is possible to determine the total available electrical capacity of the cell. This value represents a reasonable approximation of the original starting capacity, Q_0 , of the cell, and is a good measure of the practical electrical capacity of the cell.

9.1.3. Discharge Load levels

Initially three resistor values were utilised; these together with their channel assignments () were, namely: 360 Ω (0-63), 560 Ω (64-95), and 1.2 k Ω (96-27). In 1995/6, a further load module was added giving a further 256 load channels, and allowed further resistance values to be incorporated, namely: 100, 200 Ω . Table 9.1 gives values of the battery load current, I_L , for different values of terminal voltage and resistor.

The range of discharge currents (3 to 35 mA) was selected in order to include values close to the maximum pulse amplitudes presented by the meters, namely 10 to 20 mA. The mean load currents presented by the two meters are approximately 80 and 140 μ A, thus the selected discharge loads represent a range of acceleration factors of between 25 and 450, depending on the meter type. The discharge durations covered

by the accelerated tests span an approximate range of 30 to 360 days.

Table 9.1 Initial load current for the range of resistor values for a range of battery terminal voltages.

Load Resistance, R_L , (Ω)	100	200	360	560	1200
I_L (mA) at 3.5 V	35.00	17.50	9.72	6.25	2.92
I_L (mA) at 3.0 V	30.00	15.00	8.33	5.36	2.50
I_L (mA) at 2.5 V	25.00	12.50	6.94	4.46	2.08

The pulse load unit was used in a small number of tests. The load resistance, R_L , was set to 200 Ω , the pulse width and interval was set to approximately 8 ms, i.e. a duty cycle of 50%, giving a mean R_L of 400 Ω .

To avoid any ambiguity, discharge load is referred to by the value of the load resistor, R_L , rather than the discharge current, I_L , or current density, j .

9.1.4. Battery Orientation

Normally, the test batteries were mounted horizontally, however, vertical and upside-down orientations were used in a small number of tests.

9.1.5. Battery Storage time

Storage time varied from between 50 and 500 days. This parameter was not included as a specific variable in the original test programme, but was investigated retroactively in order to determine the effect of self-discharge during storage on long-term capacity.

9.2. Treatment of the discharge test data

The long durations of the discharge test durations generated up to 500k of data points for a single battery. Data sets of this size create problems in the analysis, because the number of data points that can be accommodated in a single series in a chart in an Excel spreadsheet is limited to a maximum of 4000. In addition, the time taken to process a large data set can become excessive, particularly for long-term discharges. As discussed in Section 8.6, the data can be reduced by applying a software filter, however even a tenfold reduction of a 4 week test results in 4000 lines of data. To optimise the analysis process, the compromise strategy was to set a fairly coarse resolution data reduction filter as a first stage, and to carry out a second analysis with increased resolution in cases where further detail was required.

9.3. Presentation of discharge test results

The discharge curve for each of the batteries in a given test was generated and printed as standard practice both for visual analysis, and to provide hard copy backup. A complete set of discharge charts is archived in the laboratory logbooks. In the thesis,

the discharge results are presented in tabulated form in which the basic statistical capacity parameters are summarised. Discharge charts are given to illustrate particular aspects of interest.

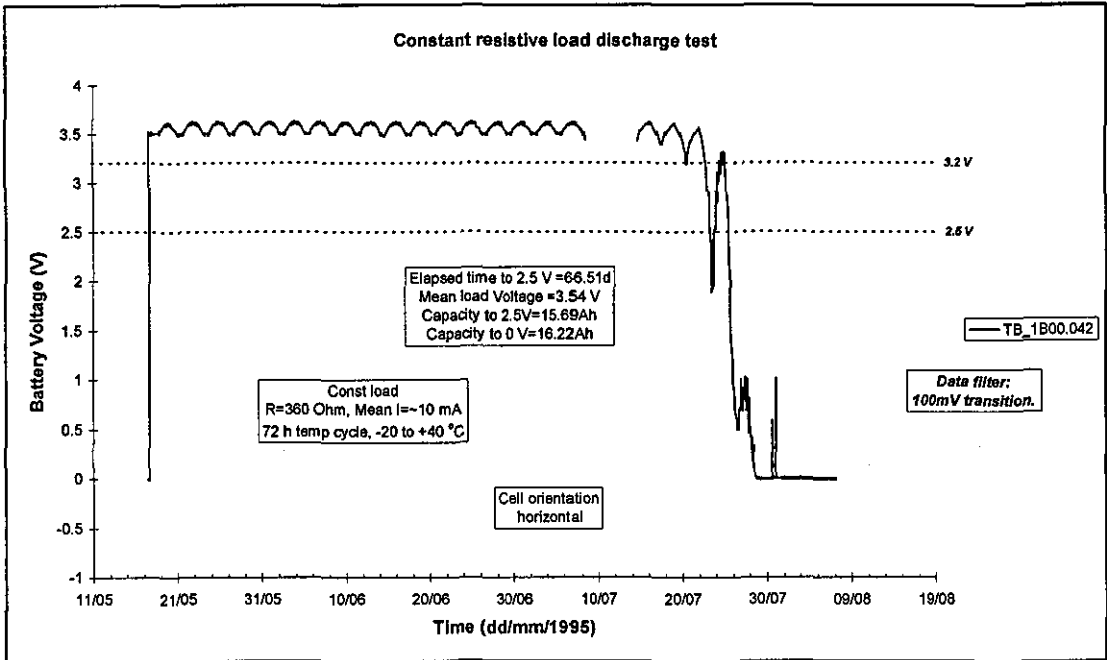


Figure 9.2 Typical ‘well-behaved’ battery discharge chart.

An example of a discharge chart for a cell discharging across a 360 Ω resistance under the standard (-20 to $+40$ $^{\circ}\text{C}$) thermal cycle is shown in Figure 9.2. The battery voltage (left hand y-axis) is plotted against time (x-axis). For ease of comparison, the y-axis scale of the discharge charts is standardised to give a range of -1 to $+4$ V. The negative part of the scale is included to provide a clear graphical distinction between any spurious negative voltage measurements caused by electrical noise or equipment malfunction, and battery voltage transients in the near zero range. Information regarding the test identification code, type of data reduction filter, discharge conditions, and the computed performance parameters (elapsed time to cut-off voltage, V_X , mean load voltage, and capacity) is given in text boxes. The periodic fluctuation of voltage is a significant feature of the discharge pattern, and is the voltage response to the thermal cycle.

The data reduction filter applied in Figure 9.2 is a 100 mV bandwidth, which defines the effective resolution of the voltage data and induces the ripples in the discharge profile that are particularly evident at the maximum and minimum inflexion points.

A discharge test normally comprises a batch of 10 nominally identical cells. Q_V is the capacity to a given voltage threshold V_X , e.g. 2.5 V, and the basic statistical capacity

parameters: mean, $\mu(Q_V)$; maximum, $^{\max}Q_V$; minimum, $^{\min}Q_V$; and standard deviation, $\sigma(Q_V)$, are calculated for each discharge test to provide a performance index for comparing different batteries. Two values of V_X are used in the present analyses, 2.5 and 0 V. The latter represents complete electrochemical exhaustion of the cells, and for a smaller number of selected test sets the capacity parameters to this threshold (Q_0), have been computed. Q_0 provides a measure of the total coulombic capacity of the given cell, and the difference, $(Q_0 - Q_V)$, is useful in determining the amount of capacity lost to polarisation. Assuming that Q_{SD} is negligible (i.e. relatively short storage and discharge periods), then the distribution of Q_0 for a given set of test cells also provides a measure of the variation associated with the stoichiometric capacity (Q_0), i.e. the amount of capacity limited reactant placed in the battery on manufacture. Apart from its obvious statistical interest, the maximum capacity parameter, $^{\max}Q_V$, defines the maximum electrical charge that a given battery can deliver under the specified discharge condition. It thus provides a benchmark for measuring the relative values of capacity losses associated with the other cells in the set that may be due to polarisation, self discharge and/or other failure processes.

The standard deviation, $\sigma(Q_V)$, of the capacity distribution obtained for a set of (10) cells in a specified test is calculated on the assumption that the set of Q_V data points are distributed normally. However, the upper bound of the distribution is defined by the stoichiometric capacity, Q_0 , which is a fixed rather than random variable; whereas the lower bound may be defined by a variety of random variables, e.g. electrochemical, mechanical or production. Thus, in practice the Q_V distribution will be skewed towards the low-capacity side, and it has been shown² that battery capacity is more accurately modelled by the Weibull distribution:

$$Q_V/Q_0 = \exp(-(I/b)^a) \quad \text{Equation 9.1}$$

As can be seen, the solution of this equation is complicated by the calculation of the shape factors, a and b . Here we simply require a measure of variance as an index for comparing the repeatability of the different types of cell. As any mathematical error associated with $\sigma(Q_V)$ should be relatively small and affect all of the sets by a similar amount, the normal distributions of battery capacity were assumed here.

9.4. Rig malfunctions

The rig was unmanned for periods of time during the testing, and suffered from

several types of malfunction, as listed below. For information, a discharge curve containing examples of these malfunctions is reproduced in Figure 9.3.

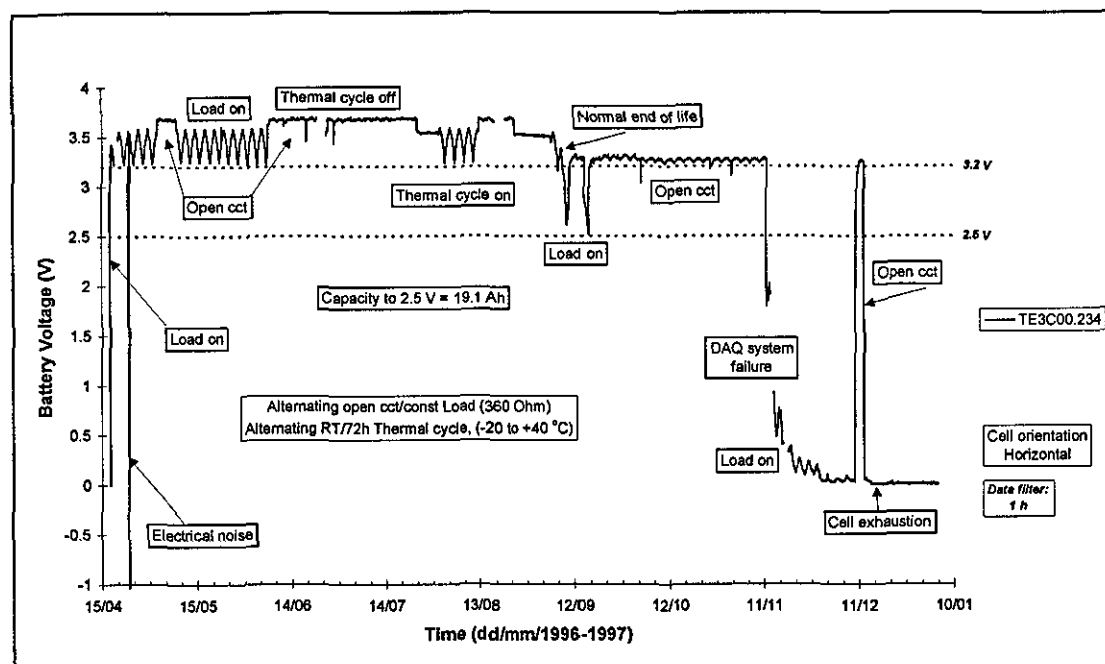


Figure 9.3 Discharge chart showing the effects of equipment malfunction.

1. PC or DAQ system failure and raw data loss - this is indicated by gaps in the voltage profile in the discharge charts.
2. Temporary failure of the environmental chamber temperature control, such that the thermal environment of test cells changes from the temperature cycle to room temperature, leading to a relatively uniform voltage profile.
3. Temporary dislodgement of low voltage signal and mains supply cables.
4. Temporary dislodgement of the environmental access port seal, allowing access of room temperature air and departure from the set thermal cycle for the cells in close proximity to the port.
5. Inadvertent switching of the battery from 'on-load' to 'off-load'.
6. A small number of spurious negative voltages caused by external electrical noise.
7. Failure of the 0-99 Channel A/D card in the Anville System (from 31/01 to 6/02/97).

Interpolation of the discharge capacity for periods where gaps in the data exist was based on voltage measurements from adjacent previous and subsequent periods, providing reasonable confidence existed that these data were representative of the missing data (i.e. by comparing trends).

9.5. Pre-discharge testing

The weights and open-circuit voltages of selected Li/SOCl₂ cells were measured before discharge. It was envisaged that in the event of any cells displaying unusual discharge behaviour, the data could be used to test for correlations between either of the parameters and the behaviour, as part of a diagnostic process.

It should be noted that (a) the accuracy of the weight measurements is reduced by inclusion of the external wrapper, etc., and (b) the open-circuit voltage of Li/SOCl₂ cells is subject to gradual changes (say 30 mV) over the months following filling; this is caused by side reactions involving impurities and/or proprietary 'additives'. For example, SO₂Cl₂ is a trace impurity in the catholyte mixture, it has an influence on cell voltage and open-circuit voltage reduces as it is chemically reduced.

CHAPTER 10

DISCHARGE TEST RESULTS FOR CELL TYPE TE

Six tests were carried out on this cell type, covering a range of R_L from 100 to 1200 Ω , and including a pulsed load test (Te6), and a room temperature discharge at 360 Ω with the cells mounted vertically (Te4).

Table 10.1 Te capacity parameters.

Capacity parameters to 2.5 V									
Battery Test Code	Load Res. R_L (Ohm)	Load Current I_L (mA)	Test Batch Size	Mean Cap. $\mu(Q_{2.5})$ (Ah)	Max. Cap. $^{max}Q_{2.5}$ (Ah)	Min. Cap. $^{min}Q_{2.5}$ (Ah)	Std Devn. $\sigma(Q_{2.5})$ (Ah)	Storage Duration (d)	Test Feature
1	2	3	4	5	6	7	8	9	11
Te6	100	36	10	13.78	15.84	11.88	1.13	962	Std.
Te7	200	16	5	18.65	18.86	18.41	0.17	962	Std.
Te1	360	10	10	19.95	20.17	19.49	0.26	494	Std.
Te4	360	10	10	19.40	19.72	19.07	0.21	879	RT,V
Te5p	400	9	10	19.65	20.15	19.49	0.24	962	Pulsed
Te2	1200	3	10	18.51	19.30	17.20	0.66	494	Std.
Capacity parameters to 0 V									
				$\mu(Q_0)$	$^{max}Q_0$	$^{min}Q_0$	$\sigma(Q_0)$		
Te6	100	36	10	20.54	20.94	20.04	0.32	962	Std.
Te4	360	10	10	20.21	20.61	19.84	0.24	879	RT,V
Te2	1200	3	10	19.91	20.15	19.76	0.14	494	Std.

RT = Room temperature, V = vertical mounting

The $Q_{2.5}$ and Q_0 capacity parameters for the battery are summarised in Table 10.1. The $Q_{2.5}$ parameters are also plotted against load resistance, R_L , in Figure 10.1, and it may be seen that discharge capacity varies with R_L and is maximised at approximately 360 Ω , at which load $\mu(Q_{2.5}) = 19.5$ Ah, which, as will be seen, is some 3 Ah higher than achieved by any other of the types of test cell. The values for $^{max}Q_{2.5}$ and $^{min}Q_{2.5}$ are similarly higher. $\mu(Q_{2.5})$ is minimised at low load resistances of R_L of 100 and 200 Ω , implying the (expected) effect of cathode polarisation, while at the other end of the load range, i.e. $R_L = 1200$ Ω , the value of $\mu(Q_{2.5})$ is also reduced below the maximum.

The relatively low values of $\sigma(Q_{2.5})$ for the 4 tests discharged in the range of R_L from 200 to 400 Ω indicate a high reproducibility of the discharge behaviour of this cell. The repeatability is the highest of any of the Li/SOCl₂ cells by a significant margin.

At both limits of the discharge range, i.e. at R_L of 100 and 1200 Ω , repeatability and capacity are reduced, implying variability due to the effects of polarisation and self-discharge respectively.

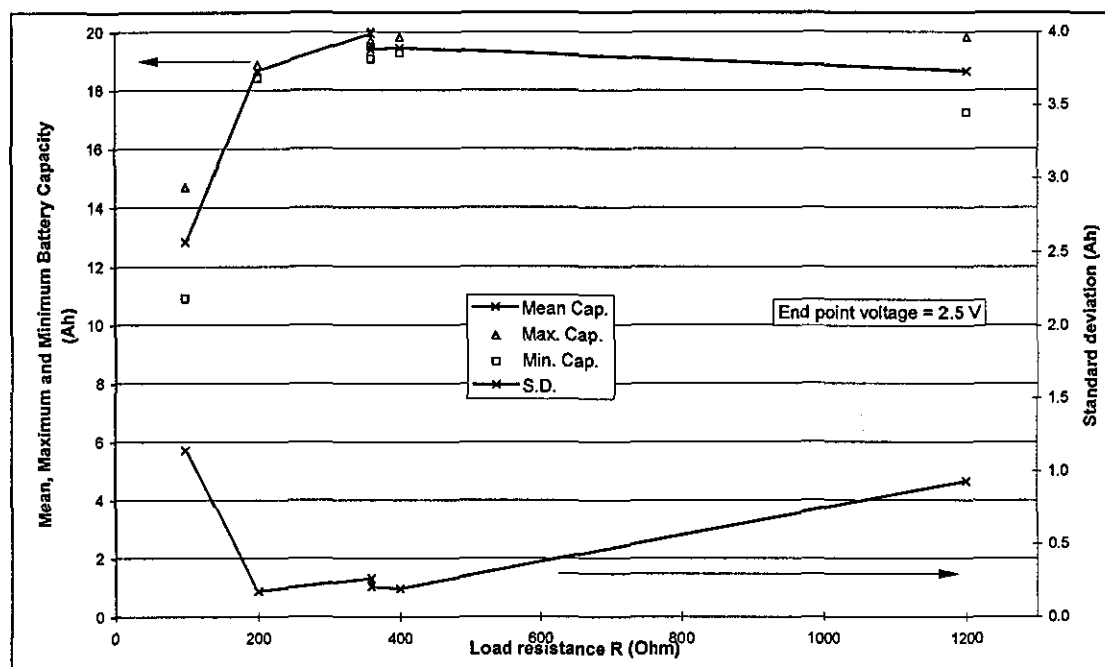


Figure 10.1 Capacity parameters as a function of resistance for Battery Type Te.

The capacity parameters for discharge to complete electrochemical exhaustion, Q_0 , were calculated for three discharge loads, namely: R_L of 100, 360 and 1200 mA, as given in the lower part of Table 10.1. An inverse relationship between R_L and Q_0 is evident, suggesting increasing capacity loss due to self-discharge as the test duration increases (this hypothesis is confirmed in Section 14.5). The difference, $[\mu(Q_0) - \mu(Q_{2.5})]$, gives the approximate value of the mean capacity loss due to polarisation, and at $R_L = 100 \Omega$ this amounts to 6.76 Ah. An estimate of the magnitude of self-discharge losses may be gained from the difference in Q_0 between short and long-term discharges; i.e. Te6 (2 months), and Te2 (13 months). The respective values of $\mu(Q_0)$ are 20.54 and 19.91 Ah, implying a loss due to self discharge of 0.63 Ah over the 11 month discharge period.

10.1. Characteristics of Discharge under Thermal cycle

A typical voltage profile of a cell (Te1-20) discharged through 360 Ω under thermal cycle is shown in Figure 10.2. A 1 h data filter was used to reduce the raw data, which causes the ripples on the voltage profile. The initial short-term high voltage of around 3.7 V is the open-circuit voltage; the drop to ~ 3.5 V at 05/12 marks the

connection of the load. The voltage 'spike' at around 02/02 is caused by the battery being switched 'off-load' (during the installation of further test cells in the environmental cabinet). The gaps in the data are due to computer malfunction.

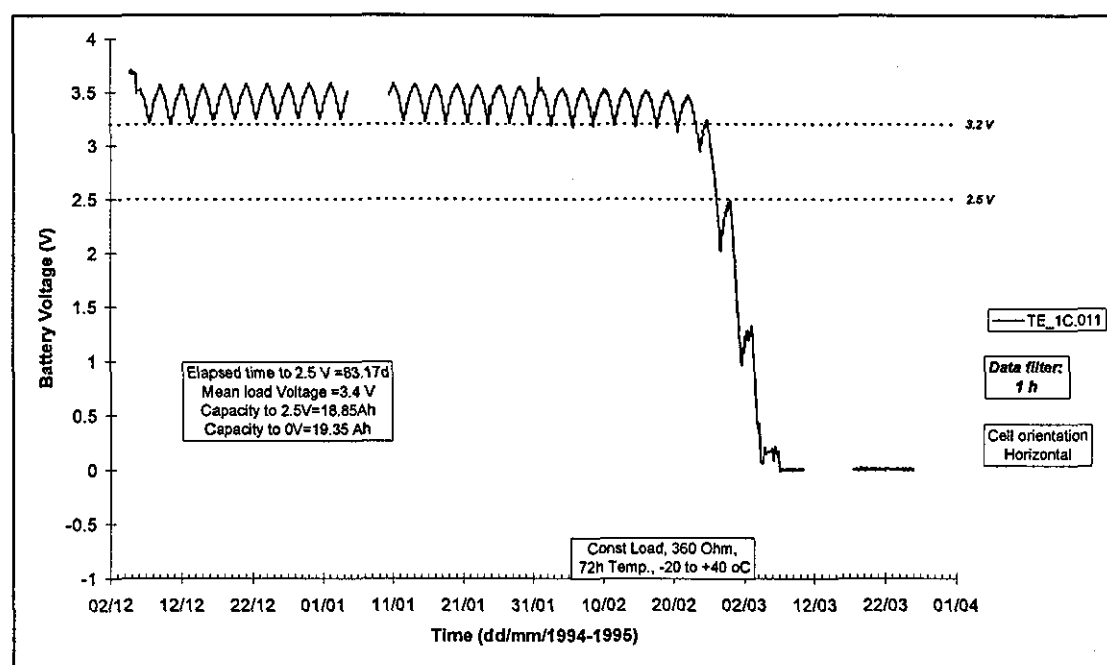


Figure 10.2 Chart of battery Te1-011 discharge through a $360\ \Omega$ resistor, 1 h data filter.

In general the discharge curves for the 10 Te cells discharged at $R_L \sim 360\ \Omega$ under a thermal cycling load are very repeatable, and follow similar voltage/temperature trends, with slight cell to cell variations during the early discharge period and towards end-of-life. The voltage cycle is very uniform for the main part of the discharge, and the final drop in voltage is relatively perpendicular. The voltage profile follows a periodic profile which is synchronous with the thermal cycle and which is smooth until the end-of-life phase.

10.1.1.1. High states of charge (C100% to C60%)

At high states of charge the cell behaviour is dominated by the anode; cathode limitations are undetectable. In the first discharge period, breakdown of the PL occurs, and the anode is reactivated, here observed as a slight but systematic increase of the cell voltage at the low temperature inflexion points. The reactivation process is short-lived, and by about C95%, its effect on load voltage vanishes.

The cyclic variation of load voltage, V_L through the -20 to $40\ ^\circ\text{C}$ temperature range is limited to some 200/300 mV, and is relatively uniform through this high state of charge.

10.1.2. Mid states of charge (C60% to C20%)

At mid states of charge, V_L at low temperature begins to drop slightly (~ 100 mV) at some point during this phase (from 11/01 in Figure 10.2) but otherwise the periodic discharge pattern continues unchanged. According to theory, precipitation of the LiAlCl_4 salt may begin during this phase. Reference to the low temperature inflexion points in Figure 10.2 shows that a marginal decrease in V_L occurs through the period 11/01 to the onset of the end-of-life phase. This pattern is in keeping with a slight increase in cell impedance as the precipitation of LiCl begins to impede the low temperature mass transfer process rates.

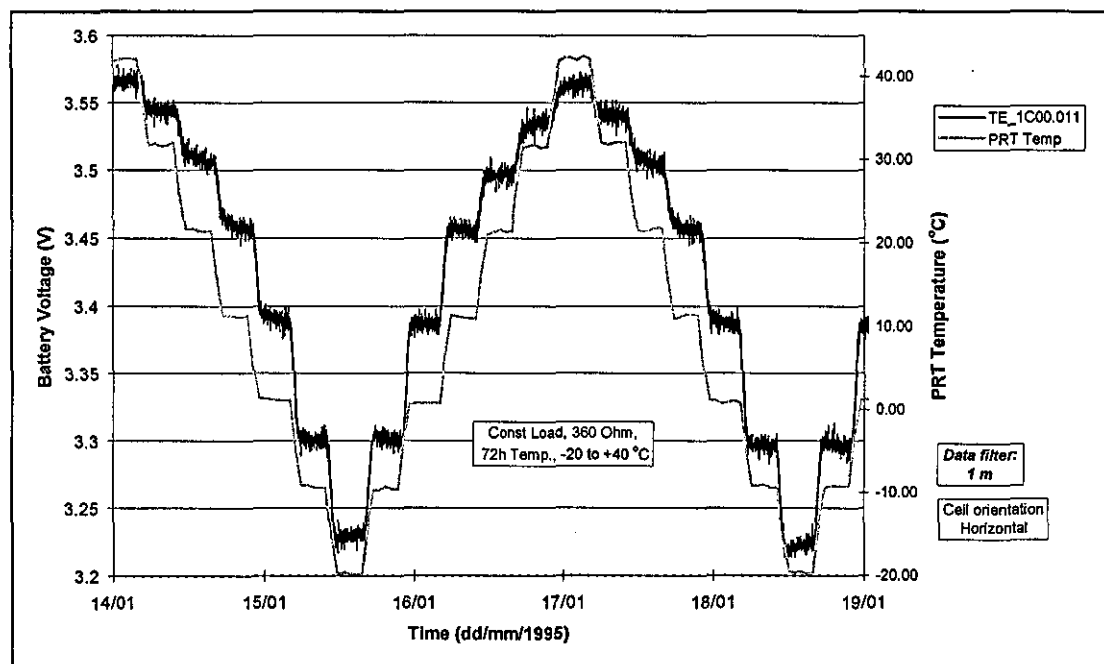


Figure 10.3 Expanded time scale (1 data point per min) and voltage scale, showing details of battery voltage detail at approximately Q90% (Te1-011)

Figure 10.3 expands the voltage and time scales to show that cell voltage is subject to 'noise', i.e. transient fluctuations of approximately 10 mV in amplitude, which may be attributed to baseline electrochemical noise reported by e.g. Farrington¹. The mean voltage changes synchronously with the 10 °C steps through the thermal cycle, and it may be seen that the magnitude of the voltage step reduces as temperature increases, implying that polarisation effects are greater at low temperature. At temperatures of -20 and +30 and 40 °C, cell voltage tends to rise slightly from the initial settled value, whereas at intermediate temperatures this trend is reversed. There is no obvious explanation for the effects.

10.1.3. Final states of charge (C20% to C0%)

The empirical model² predicts a significant increase in cell impedance from C20%. Very little effect is seen on load voltage until a state of charge of about C20%. At a state of charge of between C10% and C5%, the cell enters its 'end-of-life' phase, manifested by a progressive drop in voltage at a given temperature with each successive thermal cycle, and a significantly increased sensitivity of the cell voltage to load magnitude and to temperatures below 0 °C.

Reference to Figure 10.2 shows that polarisation effects increase more rapidly as the end-of-life phase evolves. The onset of the end-of-life phase at around 01/01/97 involves a relatively smooth but cyclic reduction in V_L . Figure 10.4 shows details of the end-of-life phase from 19/02. The voltage decrease follows a regular pattern, and following the first incursion of the 2.5 V threshold, V_L decreases comparatively sharply to 0 V over the next five thermal cycles. The interval associated with the change in voltage from 3 to 2.5 V is approximately 14 h, which is equivalent to 0.1 Ah, or 60 days operation at the 100 μ A meter rate.

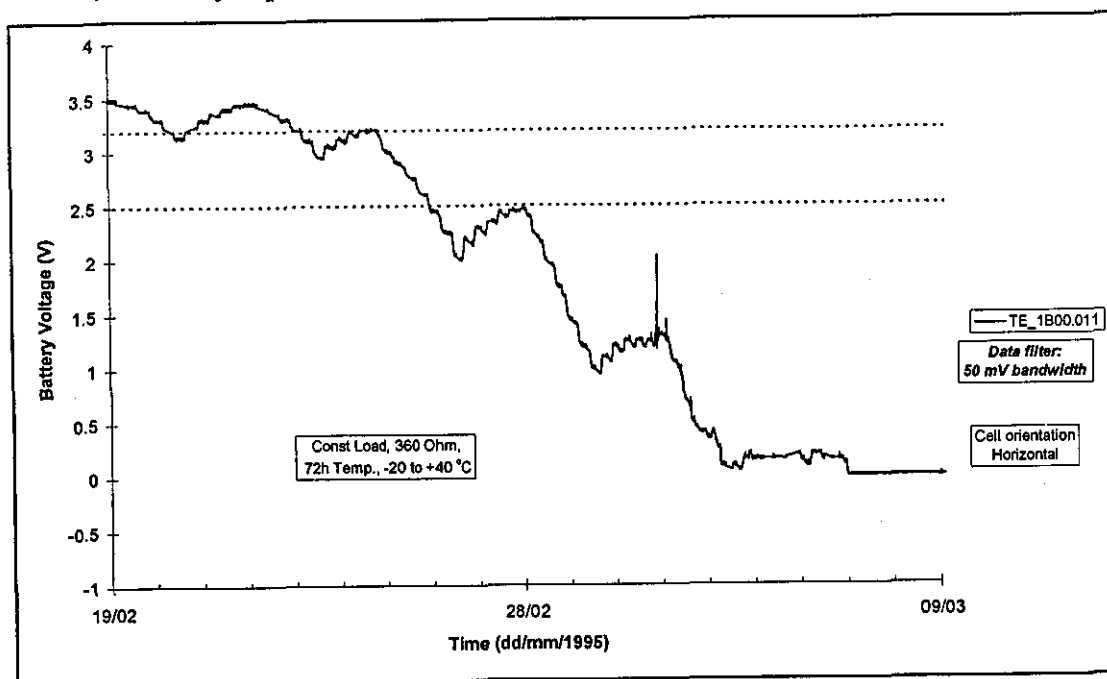


Figure 10.4 Expanded time scale of above battery Te1_b00.020 discharge showing the end-of-life phase.

Reference to the other nine cells in this test batch shows that the discharge behaviour described above is generally typical of the cell design, but that small cell to cell variations exist.

10.2. Room temperature discharge

Figure 10.5 gives an example of a Te cell discharged through a load resistance of R_L of $360\ \Omega$ at room temperature, and in a vertical orientation. The $Q_{2.5}$ and Q_0 capacity parameters of the 10 cells discharged at room temperature are included in Table 10.1 and Figure 10.1, and it can be seen that the results compare closely with those for cells discharged under the thermal cycle.

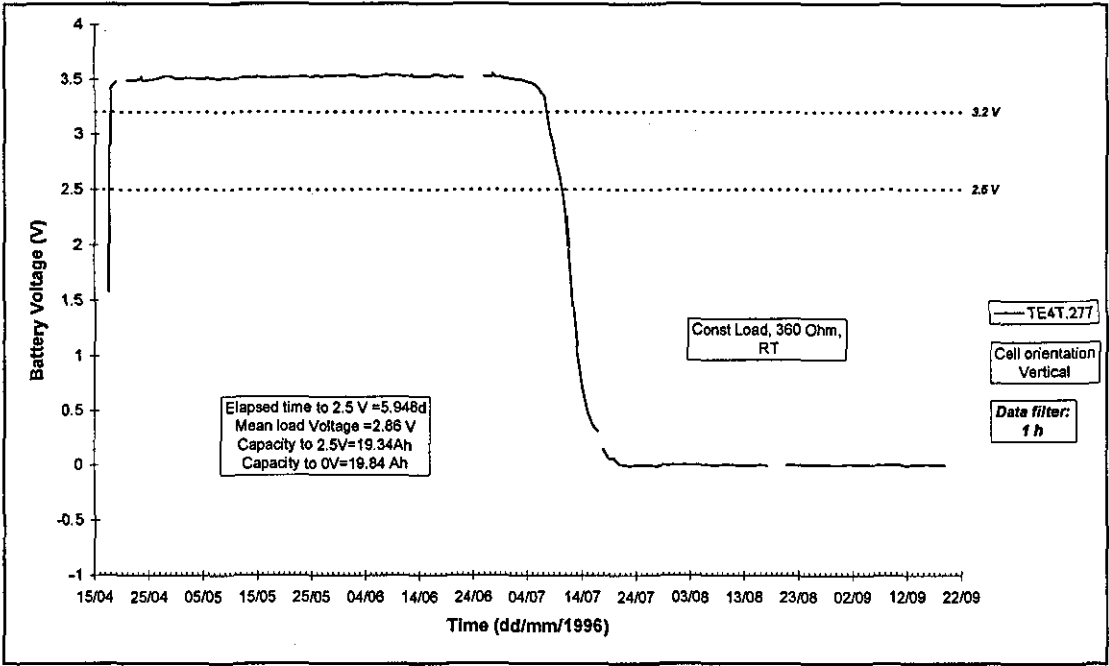


Figure 10.5 Room temperature discharge across a $360\ \Omega$ load (Te4c.277).

The voltage remains relatively uniform until the onset of the end-of-life phase, which is split into two sections. The first comprises a rapid drop to about 3 V, followed by a second more gradual fall to zero. This dual-phase end-of-life behaviour is common to all ten cells in the test batch. The manufacturer reports³ that the feature is engineered into the design to provide an ‘end-of-life’ predictor, and attributes the effect to a more gradual increase of pce impedance than occurs in its standard cell designs.

The first (constant voltage) stage covers the period 17/04 to 08/07, which corresponds to a discharge capacity of 19.1 Ah. The voltage drop from 3.2 to 2.5 V occurs in a period of 5 days, equivalent to a capacity of 0.9 Ah, 4.8% of 19 Ah.

10.3. Pulsed discharge

The capacity parameters for the pulsed load discharge test (50% duty cycle, 17 ms period, $400\ \Omega$ mean load) are included in Table 10.1 and Figure 10.1, and it can be seen that the results compare closely with those for the equivalent $360\ \Omega$ discharge tests.

10.4. Implications for the meter application

Of the four Li/SOCl₂ battery types tested here, type Te recorded the best performance figures, both in terms of repeatability and effective capacity. For this reason the cell discharge performance represents a useful benchmark for the Li/SOCl₂ battery type in general, and particularly for comparing the relative performances of the other three candidate designs investigated here.

The manufacturer's declared stoichiometric value of the Te cell is 19.6 Ah, based on the limiting amount of SOCl₂. Generally, the Q_0 values obtained here are significantly in excess of this value. The mean value, $\mu(Q_0)$, is in the region of 20.5 Ah, and the highest recorded value, $^{\max}Q_0$, achieves 20.94 Ah. This poses an interesting problem. The manufacturer's Research Manager, Dr Yamin, has stated⁴ that the main reaction products, SO₂ and S can be further reduced at 3.0 and 2.45 V versus lithium. However, these supplementary reactions would require that the electrochemical couples were in contact with an effective electrolyte. The exhaustion of the SOCl₂ would appear to remove this facility for effective ion exchange. Support for Yamin's argument is found in the changes of slope of the discharge curve at 3.0 and 2.45 V that are evident in the room temperature discharge profile (see Figure 10.5). It would appear that Yamin has quoted the stoichiometric capacity of the cell on the basis of an end-point voltage of 3.2 V, which is the end-point voltage of the Meter Type B (in which this cell type is fitted). Thus his declared value is not an absolute indicator of electrical capacity.

CHAPTER 11

DISCHARGE TEST RESULTS FOR BATTERY TYPE TD

Some 33 tests were carried out on different batches of Td cells from manufacturing dates covering the period 1993 to 1996, as given in Table 11.1. A range of test parameters was included in the test matrix, namely: load amplitude and type (continuous/pulsed), orientation, thermal environment (cycled, room temperature continuous), storage duration, and production lot (the batteries were selected from various production lots, selected to represent stages in the upgrading of the battery design and manufacturing process).

Table 11.1 Td test and capacity parameters to 2.5 V.

Battery Test Code	Load Res. R_L (Ohm)	Mean Cap. $\mu(Q_{2.5})$ (Ah)	Max. Cap. $Q_{2.5}^{max}$ (Ah)	Min. Cap. $Q_{2.5}^{min}$ (Ah)	Std. Devn. $\sigma(Q_{2.5})$ (Ah)	Test Details	Storage time (d)	Prod. Date (vv/ddd)
Td23	100	11.94	13.81	8.95	1.47	V, RT, 5cells	285	95/270
Td25	100	11.47	12.90	9.84	1.26		315	95/270
Td26	100	12.26	13.21	10.92	0.79		140	96/128
Td33	100	11.19	12.62	7.90	2.23		181	96/246
Td24	200	11.6	14.15	8.50	1.92	V	285	95/270
Td27	200	12.8	14.53	11.42	1.04		140	96/128
Td1	360	12.52	15.44	8.32	2.64	##	348	93/349
Td3	360	12.33	14.92	10.25	1.35		411	93/349
Td4	360	11.34	16.49	7.01	2.92		448	93/349
Td6	360	8.9	11.9	7.2	1.93		90	95/044
Td8	360	10.7	16.1	7.3	3.03		515	93/349
Td10	360	11.90	15.44	7.31	3.34		41	95/313
Td13	360	13.7	16.7	6.4	3.18	V V, RT	735	93/349
Td14	360	12.37	16.78	4.46	3.60		735	93/349
Td17	360	14.5	16.72	12.62	1.59		N/A	N/A
Td19	360	14.9	16.7	9.5	2.18	V Inverted*	256	95/270
Td31	360	12.0	15.7	5.4	2.92		187	96/128
Td32	360		11.8	5.5			187	96/128
Td22p	400	12.96	15.63	10.12	1.63	Pulsed	285	95/270
Td2	560	15.18	16.76	8.67	2.63		411	93/349
Td7	560	11.35	12.89	7.96	1.62		90	95/044
Td11	560	14.44	16.86	7.83	3.52		41	95/313
Td29	560	15.18	16.74	10.57	2.00		140	96/128
Td5	1200	15.71	16.24	14.78	0.52		468	93/349
Td12	1200	15.58	16.70	13.90	0.84		41	95/313
Td30	1200	15.63	16.35	14.40	0.68		141	96/128

V = vertically mounted, RT = room temperature

11.1. Capacity to 2.5 V

Table 11.1 gives details of the test conditions and storage durations, together with the capacity parameters to the 2.5 V cut-off voltage. The capacity parameters $\mu(Q_{2.5})$, $^{\max}Q_{2.5}$, $^{\min}Q_{2.5}$, and $\sigma(Q_{2.5})$ are plotted against load in Figure 11.1 to Figure 11.4 respectively. Regression lines have been fitted to these graphs to give clarity to the overlying trends. The index of determination (R^2 value) is also included to indicate the quality of fit (on a scale of 0 to 1, with 0 indicating a poor fit, and 1 a good fit and a meaningful regression line)¹. However, the trendlines are not necessarily mathematically accurate because (a) they are based on an unbalanced experimental design, and (b) the data includes more than one unrelated failure mode.

As will be seen, the discharge charts for this battery type disclosed a new and unexpected premature failure mode which affected a relatively high proportion of the 230 batteries discharged at values of R_L of 360 and 560 Ω . The results fall into three groups, defined by the load levels, namely: R_L of (a) 1200, (b) 360/560, and (c) 100/200 Ω . The equivalent values of I_L are 3, 6/10; and 18/36 mA, respectively.

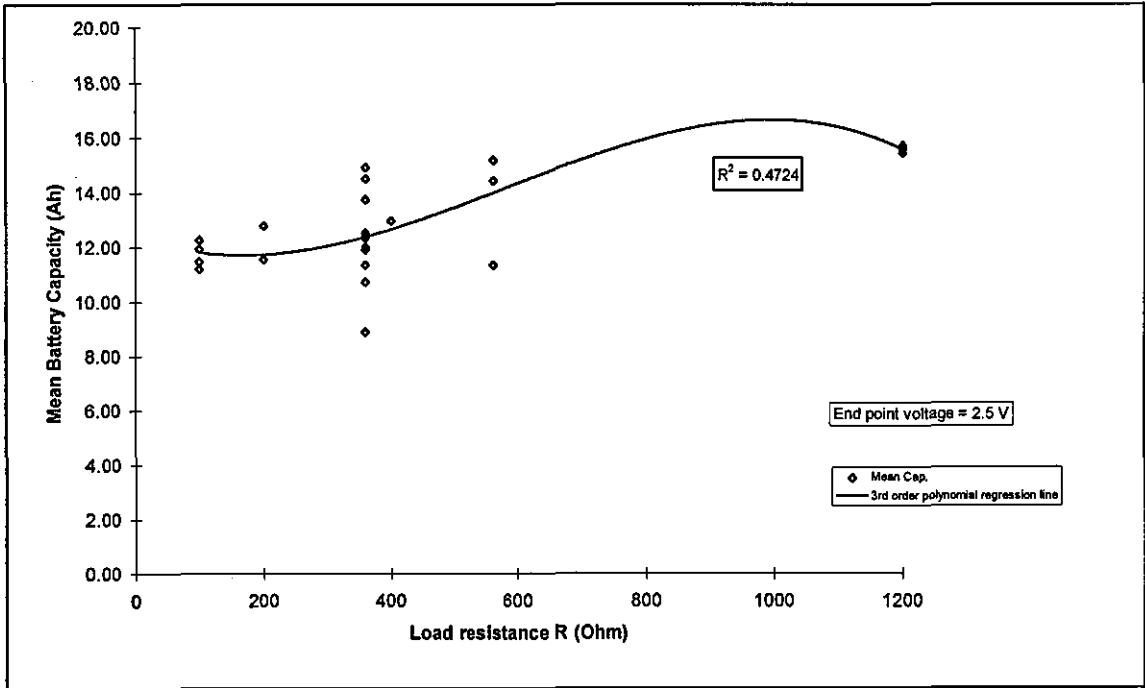


Figure 11.1 Mean capacity, $\mu(Q_{2.5})$, as a function of resistance for Battery Type Td. Figure 11.1 plots mean capacity, $\mu(Q_{2.5})$, for the various test batches against load resistance, R_L . The curve shows a maximum at approximately 800 Ω . The chart is complicated by the large scatter at 360 and 560 Ω , where a significant proportion of the values of $\mu(Q_{2.5})$ are unexpectedly lower than those for $R_L=100$ and 200 Ω . This

is a major difference from the trend of increasing polarisation as load current increases above 20 mA ($R_L < 360 \Omega$), which is predicted in the literature (Section 6.10), and observed for the Te type cells, where the $\mu(Q_{2.5})$ values of cells discharged at R_L of 100 and 200 Ω were significantly below those recorded for the 360, 560 and 1200 Ω .

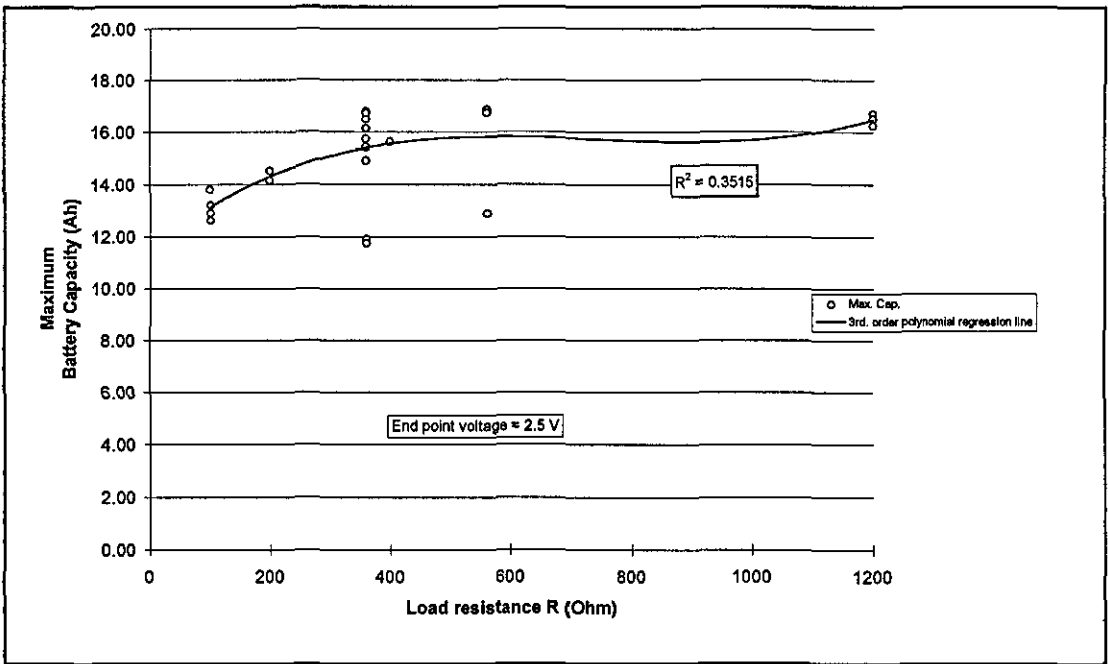


Figure 11.2 Td maximum capacity, $^{\max}Q_{2.5}$, parameter as a function of resistance. Figure 11.2 plots maximum capacity, $^{\max}Q_{2.5}$, against R_L . The $^{\max}Q_{2.5}$ values for all of the 100 and 200 Ω tests lie below 15 Ah, whereas all but 4 ‘outliers’ of the 16 results for cells discharged at 360 and 560 Ω are higher than 15 Ah. The 12 tests showing $^{\max}Q_{2.5} > 15$ Ah indicate that in general the cell type is capable of high coulombic efficiency, ε_C , where ε_C is as defined by Skarstad² in Equation 11.1:

$$\varepsilon_C = \mu(Q_{2.5})/\mu(Q_0) \qquad \text{Equation 11.1}$$

The 4 outliers are significant in that they indicate that the capacities of even the ‘best case’ cells in given test batches of 10 cells are widely distributed. They demonstrate that all of the cells in certain test batches achieve comparatively low values of ε_C even when discharged at the optimum load. The values of $^{\max}Q_{2.5}$ for the 30 cells discharged at 1200 Ω were all in excess of 16 Ah. Thus, the general trend is for $^{\max}Q_{2.5}$ to increase with increasing R_L to an asymptote of about 16.3 Ah.

Figure 11.3 plots minimum capacity, $^{\min}Q_{2.5}$, against R_L . The outstanding feature of the graph is the dip in the regression line with the minimum lying at roughly 360 Ω . The values of $^{\min}Q_{2.5}$ recorded by about half of the 360 Ω test sets are significantly lower than those for 100 and 200 Ω . The 560 Ω results show a slight improvement in

terms of dispersion and capacity. The $^{\min}Q_{2.5}$ values for the 1200 Ω tests are 13.9 Ah or greater. The $^{\min}Q_{2.5}$ results for R_L values of 360 Ω and 560 Ω indicate that at least one cell in each of these test sets records a capacity which is much lower than expected, and that the capacities of the set of 'worst case' cells are widely dispersed.

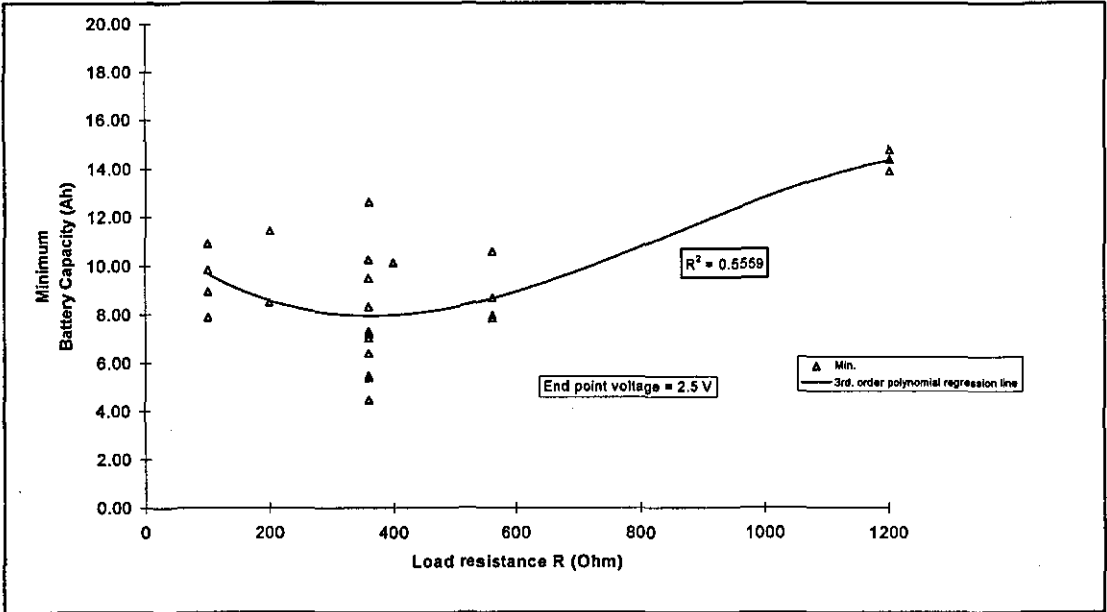


Figure 11.3 Td minimum capacity parameter, $^{\min}Q_{2.5}$, plotted as a function of resistance.

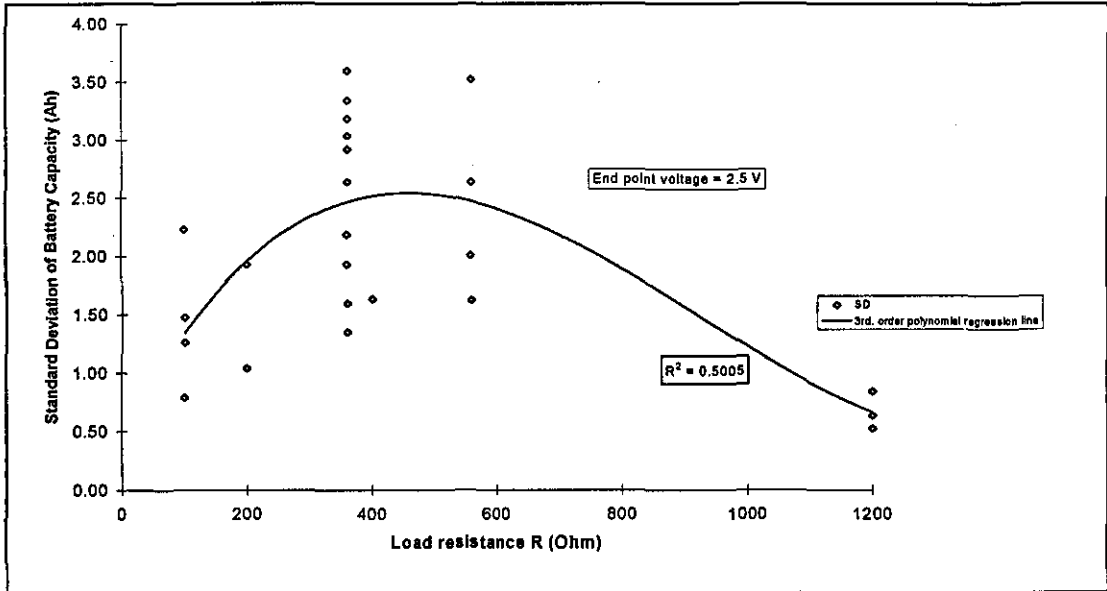


Figure 11.4 Td standard deviation of capacity, $\sigma(Q_{2.5})$, plotted as a function of resistance.

Figure 11.4 plots standard deviation, $\sigma(Q_{2.5})$, against R_L . The regression line is curved with a maximum at around 400 Ω . The $\sigma(Q_{2.5})$ results for R_L of 1200 Ω of ~0.6 Ah are both the lowest and the most tightly clustered; the R_L of 100 and 200 Ω test results are relatively higher and range from 0.8 to 2.2 Ah. The results at these loads compare

fairly closely with those recorded for the Te battery. However, the $\sigma(Q_{2.5})$ values for the R_L of 360 and 560 Ω tests are generally higher and range from 1.4 to 3.6 Ah. The relatively large values of $\sigma(Q_{2.5})$ imply that the $Q_{2.5}$ results for given test sets are widely dispersed, which in turn implies considerable differences in the quality of nominally identical cells.

11.2. Capacity to 0 V

Table 11.2 Td capacity parameters to 0 V.

Battery Test Code	Load Res. R_L (Ohm)	Load Current I_L (mA)	Mean Cap. $\mu(Q_0)$ (Ah)	Max. Cap. ${}^{\max}Q_0$ (Ah)	Min. Cap. ${}^{\min}Q_0$ (Ah)	Std. Devn. $\sigma(Q_0)$ (Ah)	Test Details	Storage time (d)	Prod. Date (yy/ddd)
Td26	100	36	17.12	17.28	16.97	0.10		140	96/128
Td10	360	10	16.99	17.14	16.65	0.15		41	95/313
Td14	360	10	16.97	17.26	16.67	0.18	V	735	93/349
Td17	360	10	16.96	17.23	16.37	0.26	RT,V		
Td5	1200	3	16.64	16.84	16.09	0.21		468	93/349

RT = room temperature, V = vertically mounted

Having observed a wide divergence of the $Q_{2.5}$ capacity parameters, it is of interest to examine the Q_0 results. In theory, these represent capacity under a vanishingly small load, and should discount failure due to polarisation. The Q_0 parameters for five selected tests are given in Table 11.2, and plotted in Figure 11.5. The five tests cover broad cross-sections of test conditions and discharge performances, i.e.: (a) cells drawn from different manufacturing lots and storage durations, (b) cells discharged over a wide range of loads, values of R_L of 100, 360 and 1200 Ω , (c) examples of both high and very low values of $Q_{2.5}$ (see Table 11.1), and (d) tests which yielded poor (high) values of $\sigma(Q_{2.5})$. The 1200 Ω test (Td5) is representative of an optimum set of $Q_{2.5}$ and $\sigma(Q_{2.5})$ performance parameters.

The capacity parameters for the Q_0 sets of results represent a very significant improvement over the $Q_{2.5}$ sets, both in terms of capacity magnitudes and the standard deviations. Figure 11.5 plots the $\mu(Q_0)$, ${}^{\max}Q_0$, and ${}^{\min}Q_0$ parameters (left hand y-axis) and $\sigma(Q_0)$, (right hand y-axis), against load. Third order polynomial regression lines have been plotted on the $\mu(Q_0)$ and $\sigma(Q_0)$ data. The dispersions of the data for all of the Q_0 capacity parameters are tightly bunched and yield capacities well in excess of 16 Ah (even the ${}^{\min}Q_0$ results). As observed for other battery types the trend is for a slight decrease in capacity with increasing R_L and discharge duration, suggesting the

impact of self discharge. The values of $\sigma(Q_0)$ for all of the tests lie within a range of 0.26 Ah down to 0.10 Ah. The trend is for a slight increase in value of $\sigma(Q_0)$ with increasing R_L , in line with the theory that predicts that the distributions of capacity loss through self-discharge tend to increase with time³.

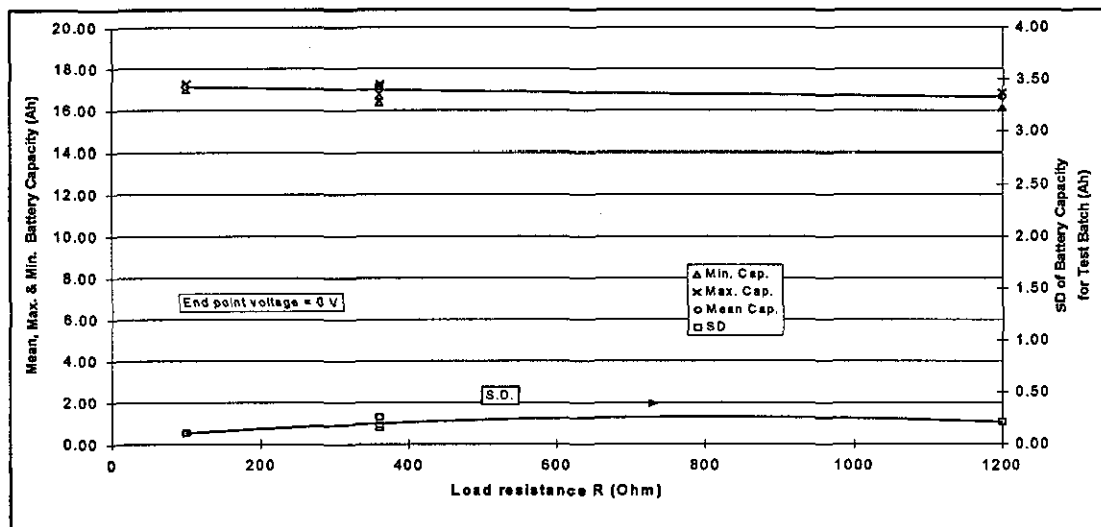


Figure 11.5 Td cell type - the Q_0 capacity parameters.

The recorded $\mu(Q_0)$ range of 16.6–17.1 Ah compares closely with the manufacturer's stated stoichiometric capacity, Q_0 , of 17.5 Ah, and demonstrates that the low $Q_{2.5}$ values observed for these test batches are not due to lack of reactants. The tight distributions implied by the $\sigma(Q_0)$ values of 0.26 Ah and below imply that there is little variation in the amounts of reactants incorporated at manufacture, and that the manufacturer is exercising close quality control over this production variable.

11.3. Discharge profiles

In this section we look at profiles considered to be typical of a 'well-behaved' discharge for each of the range of R_L settings. The raw data was reduced using a 50 mV bandwidth in order to trap all significant voltage perturbations. The 50 mV bandwidth effectively defines the voltage resolution, and accounts for the truncated and rippled nature of the some of the voltage profiles. The y-axis voltage scale in the charts is standardised to a range of -1 to +4 V, but the x-axis time scale range is scaled to fit the test duration.

11.3.1. R_L of 100 Ω

Figure 11.6 displays the discharge profile for a cell discharged across a load of R_L of 100 Ω . In this example, the $Q_{2.5}$ value of 12.8 Ah is close to the maximum for this test load. The cell voltage begins to decrease after 3 thermal cycles, and transition of

the 2.5 V threshold occurs after 16.7 days. The post 2.5 V transition profile is very spiky through to complete exhaustion of the cell. Q_0 for this cell is 17 Ah.

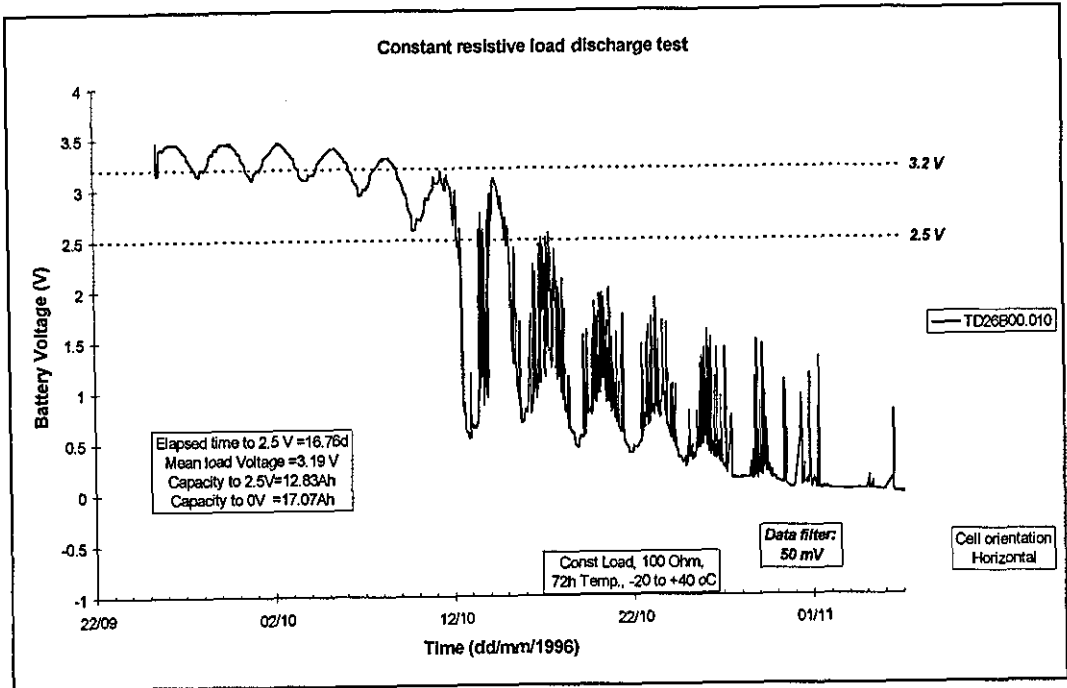


Figure 11.6 100 Ω discharge chart, an example of high capacity cell performance.

11.3.2. R_L of 200 Ω

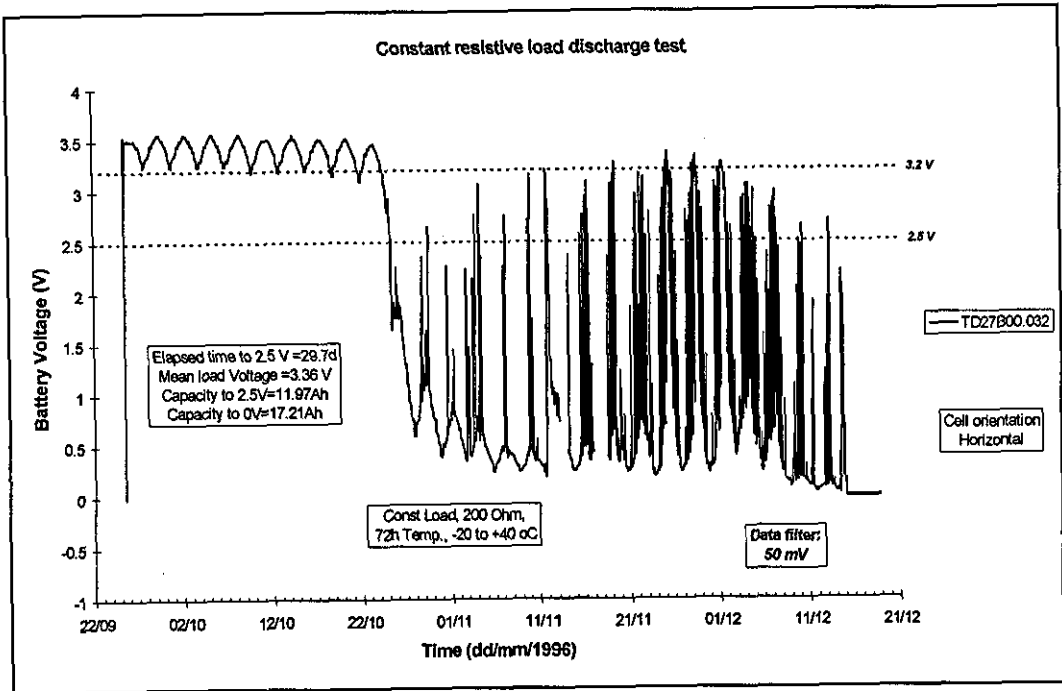


Figure 11.7 200 Ω discharge chart, an example of high capacity cell performance.

Figure 11.7 displays the discharge profile for a cell discharged across a load of R_L of 200. The value of $Q_{2.5}$ of 12 Ah is average for this test load. The cell voltage begins to decrease after about 6 thermal cycles, after which the voltage profile remains

constant for 3 more cycles until the final end-of-life phase begins. Transition of the 2.5 V threshold occurs after 29.7 days. Again, the post-transition voltage profile is very irregular, and intermittent recoveries to values above the threshold continue until complete exhaustion of the cell. The value of Q_0 for this cell is 17.2 Ah.

11.3.3. R_L of 360 Ω

Figure 11.8 displays the discharge profile for a cell discharged across a load of R_L of 360 Ω . The $Q_{2.5}$ of 16.7 Ah is near the maximum for this test condition, and it should be noted that the capacity of this cell is within the upper 10% of the capacity range for the Td cells discharged at this load. The mid-term discharge pattern is constant from cycle to cycle, and voltage decrease is only observed immediately prior to the end-of-life phase. The 2.5 V threshold transition occurs after 73.5 days. In this case the end-of-life phase is fairly orderly, and is relatively short in duration (2.6 d) and utilises a small amount of capacity (0.5 Ah). Q_0 for this cell is 16.72 Ah.

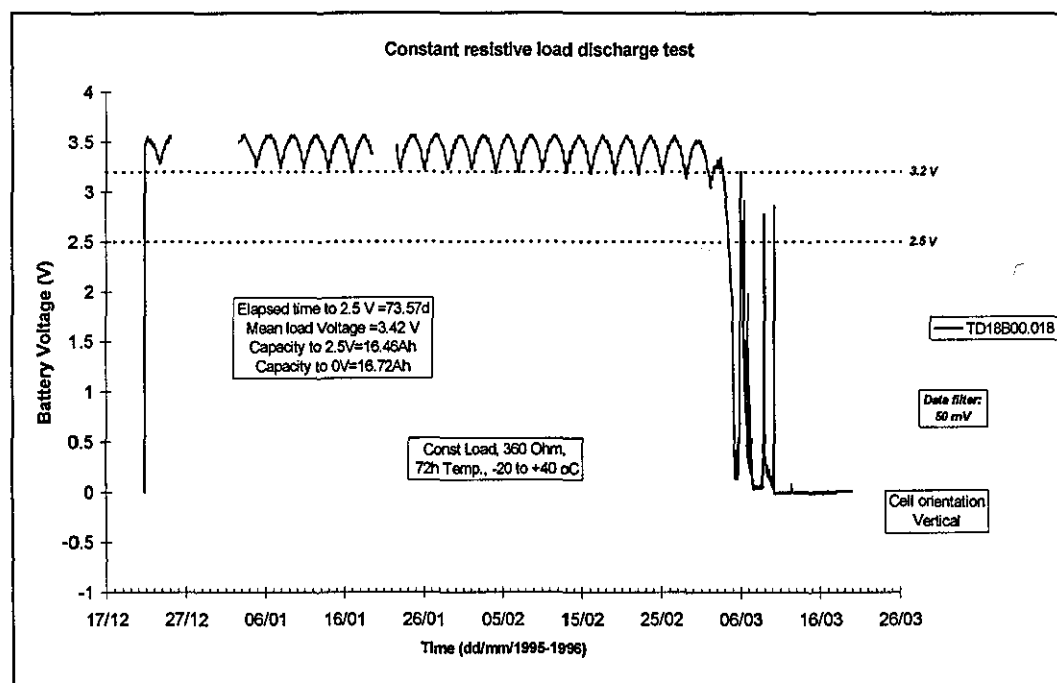


Figure 11.8 360 Ω discharge chart, an example of high capacity performance.

11.3.4. R_L of 560 Ω

Figure 11.9 displays the discharge profile for a cell discharged across a load of R_L of 560 Ω . The $Q_{2.5}$ value of 16.7 Ah is near the highest recorded for this test load. The increase in voltage that occurs at the beginning of discharge is evidence of depassivation of the anode. A slight reduction in voltage occurs mid-way through discharge, followed by a further change in pattern about 7 thermal cycles before transition of the 2.5 V threshold, which occurs after a duration of 112 days. Again,

the final end-of-life phase is fairly orderly, relatively short in duration (6 d), and low in terms of capacity dissipated (3.7 Ah). The value of Q_0 for this cell is 16.9 Ah.

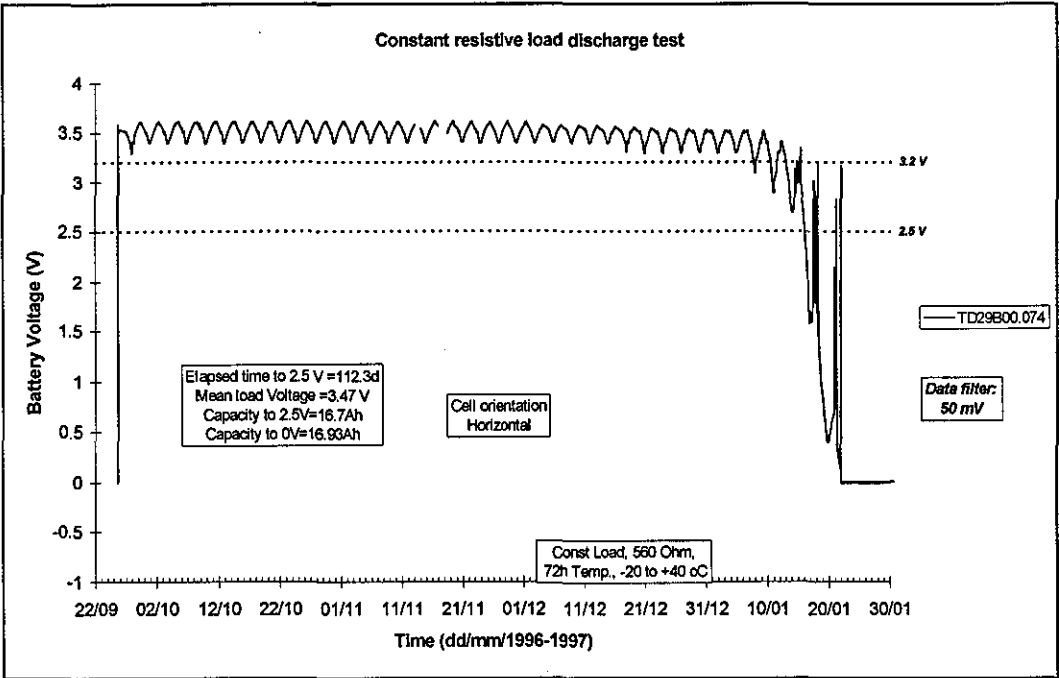


Figure 11.9 560 Ω discharge chart, an example of high capacity performance.

11.3.5. R_L of 1200 Ω

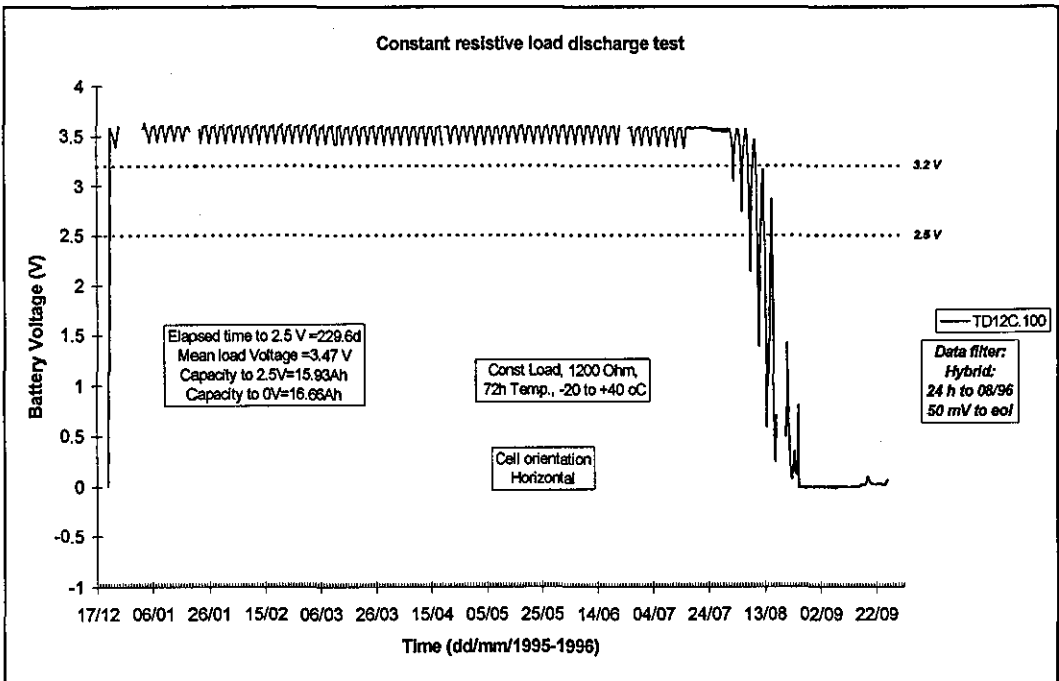


Figure 11.10 1200 Ω discharge chart, an example of high capacity performance.

Figure 11.10 displays the discharge profile for a cell discharged across $R_L = 1200 \Omega$. $Q_{2.5} = 15.93\text{Ah}$, which is a reasonably typical value for this test load. Transition of the 2.5 V threshold occurs after 229 days; no significant change in discharge pattern

occurs during mid-discharge. The period of uniform voltage immediately prior to the end-of-life phase is due to failure of the temperature control of the environmental chamber allowing the test batteries to settle at room temperature. The end-of-life phase is fairly orderly, and is relatively short in duration (18 days) and low in terms of capacity consumed (0.5 Ah). Q_0 for this cell is 16.66 Ah.

11.4. Capacity distributions

Figure 11.11 gives histograms of the ($Q_{2.5}$) capacity distributions of the results for the five levels of R_L , namely: 100, 200, 360, 560 and 1200 Ω (reading from top to bottom). The sample sizes vary from 20 to 118 cells, as indicated on the charts. The x-axis represents measured battery capacity and is scaled in intervals of 1 Ah. The y-axis represents the frequency density of measured capacity, and is normalised to give frequency as a percentage of the sample size. The scales of both axes have been standardised for ease of comparison between the different histograms. In each histogram, the data points have been linked to form a continuous frequency distribution profile.

Each frequency distribution has a defined maximum, and is skewed towards the low-capacity side as commonly observed with primary batteries. The 100 Ω distribution profile presents a well defined maximum at 13 Ah. The capacity values in the 200 to 560 Ω histograms are spread over comparatively large range, their maxima are less well defined and rise from 13 (200 Ω) to 17 Ah (560 Ω). The 1200 Ω distribution profile exhibits a well-defined maximum at 16 Ah.

Scanning the histograms from R_L of 100 through to 1200 Ω reveals a systematic peak shift from 13 to 17 Ah, and a trend from a unimodal distribution at 100 Ω , through the more complex distribution patterns exhibited by the 200 to 560 Ω load discharges, to a further unimodal distribution in the 1200 Ω histogram. A multiplicity of peaks may be seen in 560 Ω curve. The two located between 11 to 13 Ah relate to results from 5 and 6 cells respectively. The valley between them relates to 2 cells. The implication is that a larger sample would have resulted in a single peak located in the region of 11 to 13 Ah, corresponding to the existence of the premature failure mode. The significance of the curve is that it illustrates the diminishing effect of the premature failure mode as R_L is increased from 360 Ω where the effect is dominant, to 1200 Ω where it has disappeared.

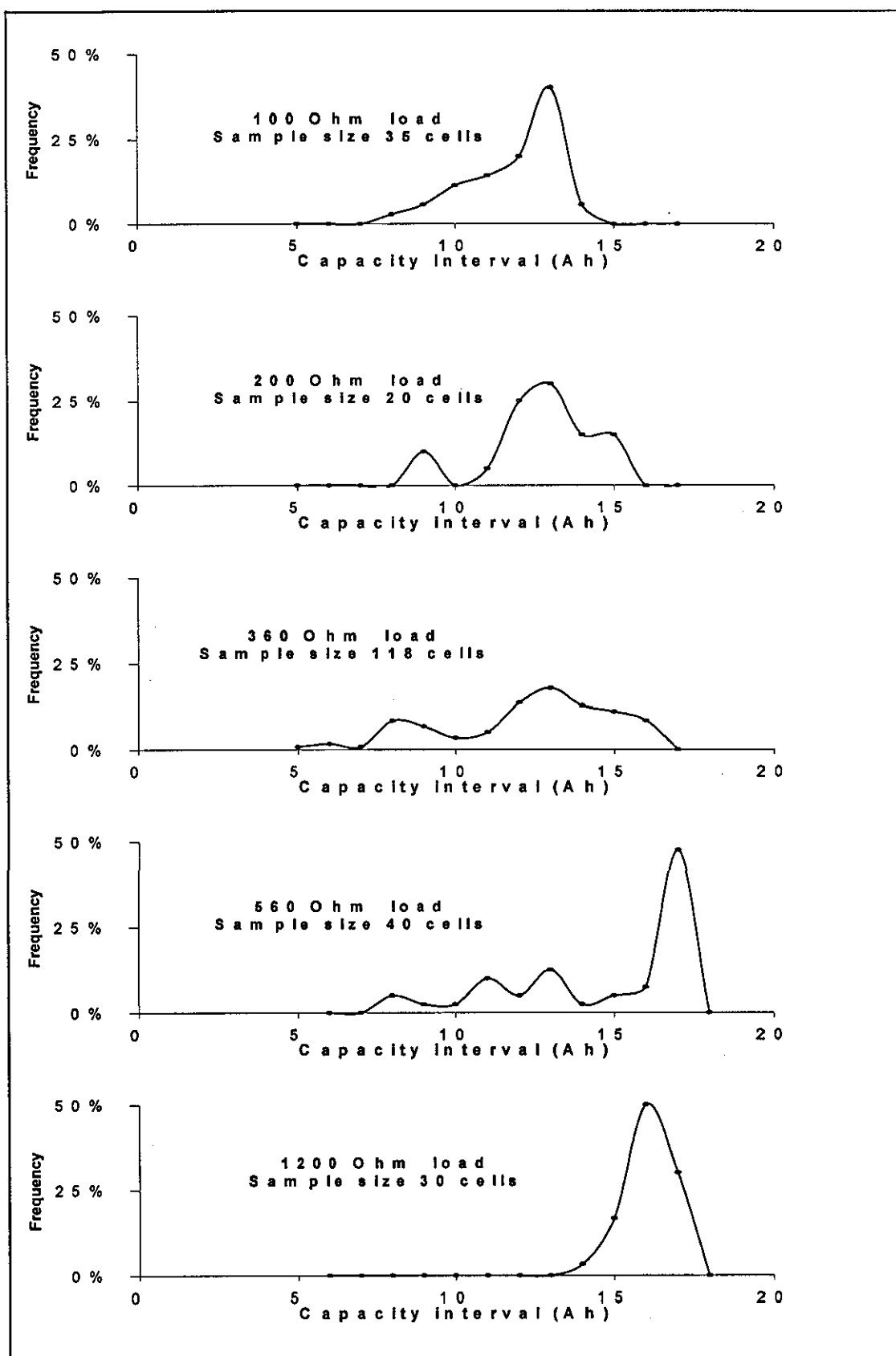


Figure 11.11 Histograms of Td cell capacity distributions for values of R_L from 100 to 1200 Ω .

The 200 to 560 Ω distribution profiles do not appear to be unimodal, and imply the existence of a new failure mode that limits the capacity of affected cells by a variable amount to a value in the range 5 to 13 Ah. The mode is labelled here as 'premature failure'. The premature failure mode is limited to the 200 to 560 Ω test loads, and occurs most frequently at a discharge load of 360 Ω . It was found to affect a variable proportion of each batch of cells, and the occurrence of the failure mode appears to be randomly dispersed within the test sample batches.

11.5. Effect of test parameter

In addition to load, the test variables included production lot, storage duration, load type (continuous/pulsed), orientation, and thermal environment (cycled, room temperature).

11.5.1. Production lot

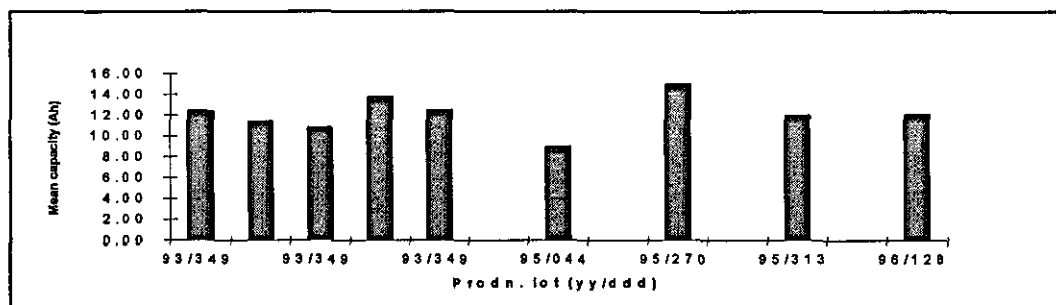


Figure 11.12 Histogram of production lot versus mean capacity, $\mu(Q_{2.5})$ - Td cells discharged through 360 Ω .

Five production lots spanning a period from 1993 to 1996 (as indicated in Column 10 of Table 11.1) were tested, corresponding to the period when the manufacturer moved from semi- to fully-automated production. The values $\mu(Q_{2.5})$ versus production lot time for cells discharged at 10 mA are plotted in Figure 11.12. As can be seen, no sustained improvement in the capacity statistics occurred as a result of changes in production method during this period.

11.5.2. Storage duration

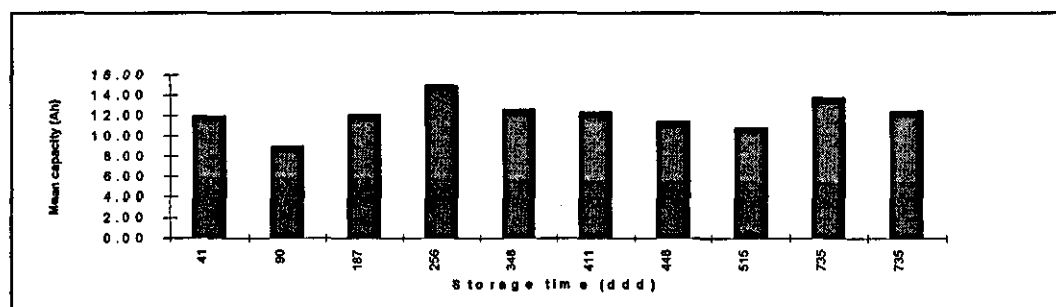


Figure 11.13 Histogram of storage time versus mean capacity, $\mu(Q_{2.5})$ - Td cells discharged through 360 Ω .

The histogram shown in Figure 11.13 plots $\mu(Q_{2.5})$ against storage time for cells discharged at 10 mA. Again there is no evident correlation.

11.5.3. Orientation

The change in cell orientation from horizontal to vertical appears both to increase the probability of the failure mode occurring and to accelerate its onset. Table 11.1 shows that the standard deviations of vertically mounted batteries, Td24 ($R_L=100\ \Omega$), and Td14, Td17 and Td31 ($R_L=360\ \Omega$) are among the highest recorded for any discharge regime, and the minimum capacity parameters lie at the low performance end of the range. Test set Td14 is particularly interesting as it includes cells which achieve both the highest and the lowest capacity recorded for the 120 cells discharged at 360 Ω . Discharging the battery in the upside-down position (Td32) induces the poorest overall set of capacity parameters. The reduction in performance may be associated with an unfavourable siting of the vapour bubble and restricted movement of the catholyte to the active electrode surfaces.

11.5.4. Room-temperature

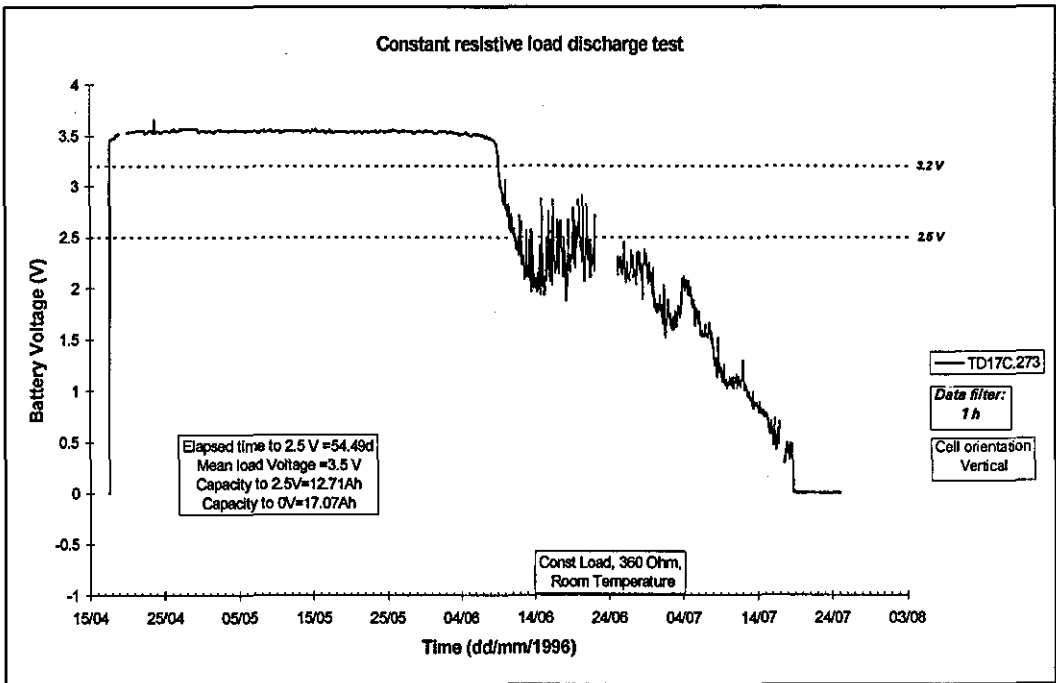


Figure 11.14 Room-temperature discharge at 360 Ω .

Figure 11.14 shows the voltage profile for test cell Td17-273, which was discharged at room temperature discharge. The $Q_{2.5}$ value of 12.7 Ah was the lowest recorded for this test condition. It is an important result because it demonstrates that premature failure can also occur for room temperature discharge. The dominant features of the

discharge profile are the abrupt fall in voltage from 3.5 V through the 2.5 V threshold, and the subsequent period of irregular voltage oscillations.

Figure 11.15 shows the voltage profile for the same test cell on day 10/06, in the middle of the region of relative voltage stability just after the 2.5 V transition. The time-scale has been expanded to a maximum resolution of 1 data point per minute. It may be seen that the cell voltage is subject to continuous oscillations having a peak to trough amplitude of up to approximately 0.5 V. Analysis shows that a typical single voltage spike has a width at half height of between 5 and 10 min.

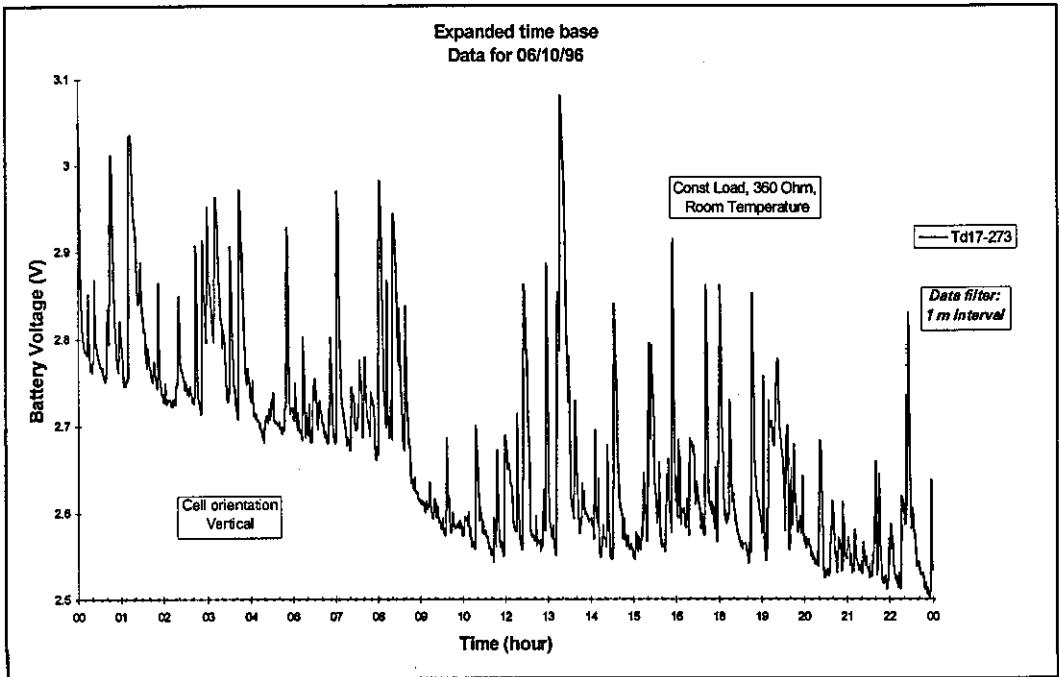


Figure 11.15 A section of a room-temperature discharge profile plotted on an expanded time scale.

11.5.5. Pulsed discharge

The capacity parameters recorded for the pulsed discharge test Td22p, (duty cycle of 50%, period of 16 ms, mean load of 400 Ω), are shown in Table 11.1, and are included in the plots of $Q_{2.5}$ versus R_L in Figure 11.1 through to Figure 11.4. It may be seen that the data points lie on the regression lines. This correspondence implies that there is no significant difference between performance under constant and pulsed loads. A key observation here is that the pulsing has no discernible effect on the premature failure mode; the different discharge profiles cover a range that is typical of that for an equivalent 360 Ω test.

11.6. The premature failure mode

Three types of end-of-life behaviour are observed with this cell type when discharged across resistances of 360 and 560 Ω , namely:

1. A short end-of-life phase that is characteristic of the well-behaved cell discharges discussed in the Section 11.3.
2. Premature failure followed by an extended end-of-life phase.
3. Premature failure followed by subsequent reactivation of the cell to a more or less normal end-of-life discharge pattern - because of its shape it is nicknamed the 'saddle-back' failure mode.

The premature failures would be of enormous significance if replicated in the field, and it is of great importance to determine the underlying cause, and to speculate on the implications for the application.

The two premature failure modes are distinguished by the early depth of discharge at which the 2.5 V transition occurs. The modes lead to low values of $Q_{2.5}$ and coulombic efficiency, ϵ_c . For clarity the premature failure mode is defined as occurring where ϵ_c is less than 0.7. This includes approximately 40% of Td cells discharged across 360 Ω . Considerable variations in the patterns of both failure modes are observed from cell-to-cell. The point of onset of the mode is highly unpredictable, and this feature is responsible for the large variance observed for the capacity of cells.

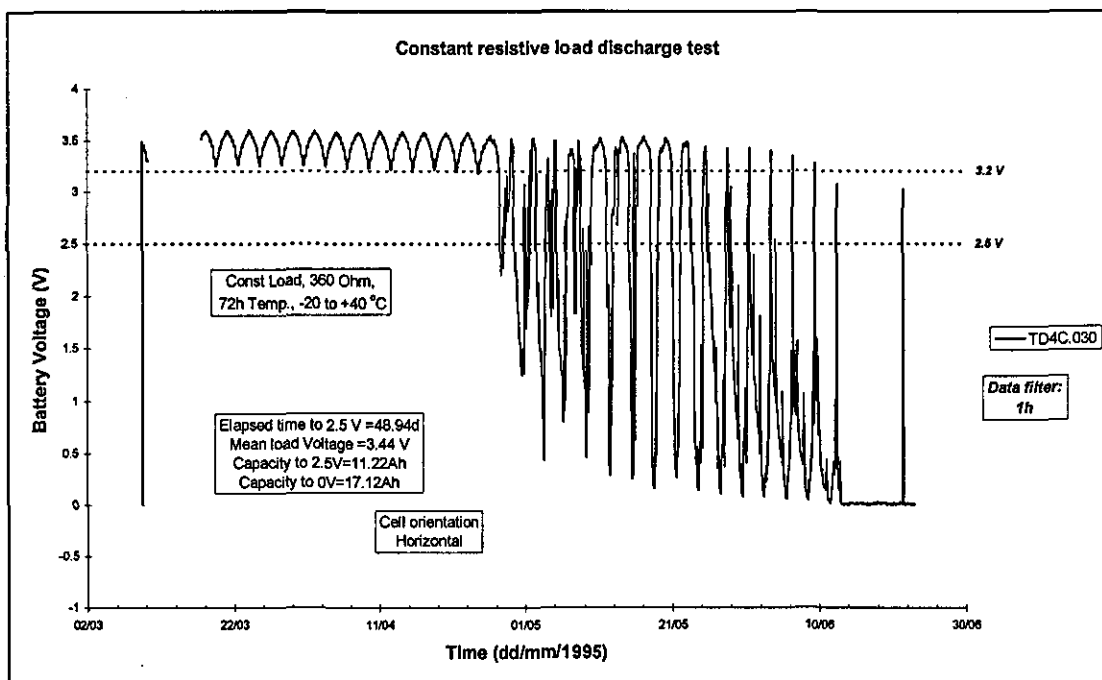


Figure 11.16 R_L of 360 Ω discharge chart, showing an example of extended end-of-life premature failure mode.

An example of an extended end-of-life premature failure mode is shown in Figure 11.16. In this case, the transition of the 2.5 V threshold is followed by a continuous cyclic pattern of low voltage incursions through to the point of complete exhaustion of cell reactants. Figure 11.17 gives an example of a cell displaying the 'saddle-back' failure mode from the evolution of the low-voltage phase, subsequent voltage recovery, and 'normal' discharge through to the end-of-life phase, the ultimate exhaustion of reactants and cessation of electrochemical activity. After the period of instability, the cell appears to recover to the more predictable pattern observed for high capacity cells. The voltage depression and recovery phases are generally associated with respective decreasing and increasing temperature phases of the thermal cycle, otherwise their timing is unpredictable and seemingly without external influence. No correlation was found between susceptibility to premature failure and either pre-discharge weight or open-circuit voltage, and no characteristic of the early discharge behaviour has been found to predict the effect. Thus premature failure cannot be linked to any obvious factor.

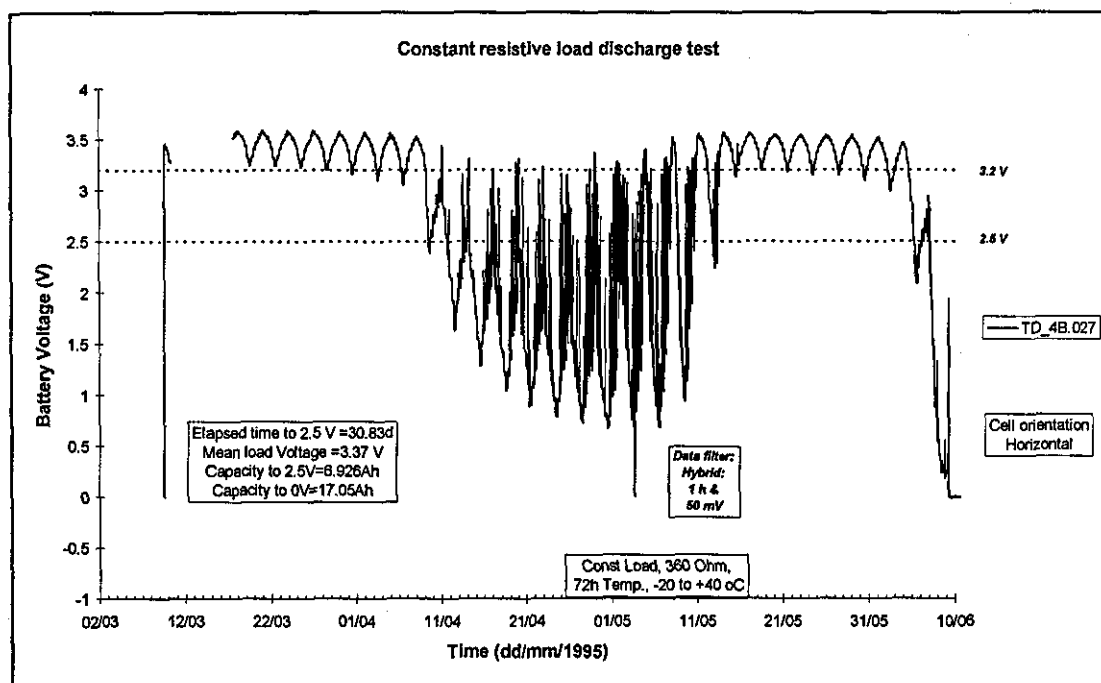


Figure 11.17 R_L of 360 Ω discharge chart, showing an example of the 'saddle-back' premature failure mode.

For the Td cell, premature failure is characterised by the onset of a period of large and irregular voltage perturbations. The onset of the failure mode is normally a progressive process, and significant deviations from the base-line voltage are only evident during the low temperature part of the thermal cycle, as can be seen in the

above Figures. After a relatively short period of normal discharge, the low temperature voltage inflection points begin to decrease almost linearly with successive temperature cycles. This trend evolves with succeeding cycles until voltage depression is evident at all temperature levels, although the effect at the high temperature phase of the cycle is restricted to a much smaller drop in the region of 200 to 300 mV.

11.7. The saddle-back failure mode

Thus the investigation is directed towards an understanding of the factors that could be responsible for the passivation processes. The key to understanding the premature failure problem is to identify mechanisms that can explain the observed 'saddle-back' and extended 'end-of-life' failure modes. Approximately half of the premature failures were of the saddle-back type. However, the forms of the voltage perturbations for both types of failure mode are essentially the same, and it would appear that the same general mechanisms can be used to account for both types, providing account is taken of the different end-of-life patterns. Several aspects of the discharge behaviour suggest that failure is due to an attenuation of cell kinetics, rather than physical malfunction of one of the cell components, namely:

1. Voltage instability at medium discharge rates would appear to be a characteristic of this battery type, and is also observed in the pulsed current and room-temperature discharge tests (some 50% of the 10 cells discharged at room temperature discharge curves give evidence of mid-range voltage instability, the lowest capacity being 75% of the Q_0 value). Figure 11.18 shows 3 of the unstable cells with 4 stable cells included for comparison.
2. Voltage never reduces to zero until complete exhaustion of the limiting active material, implying that the electrochemical reactions are not terminated, but merely proceed at reduced rates.
3. The Q_0 values recorded for all of the prematurely failed cells closely approach the manufacturer's declared stoichiometric value and are tightly dispersed about the mean. The capacity to zero volts, Q_0 , of all of the cells in a sample of 50 Td cells discharged across loads of 100, 360 and 1200 Ω , and which included cells which failed at capacities as low as 4.46 Ah, all yielded the Q_0 values close to the specified stoichiometric capacity; the values of $\mu(Q_0)$ and

$\sigma(Q_0)$ for the 50 cells were found to be approximately 17 and 0.2 Ah, respectively.

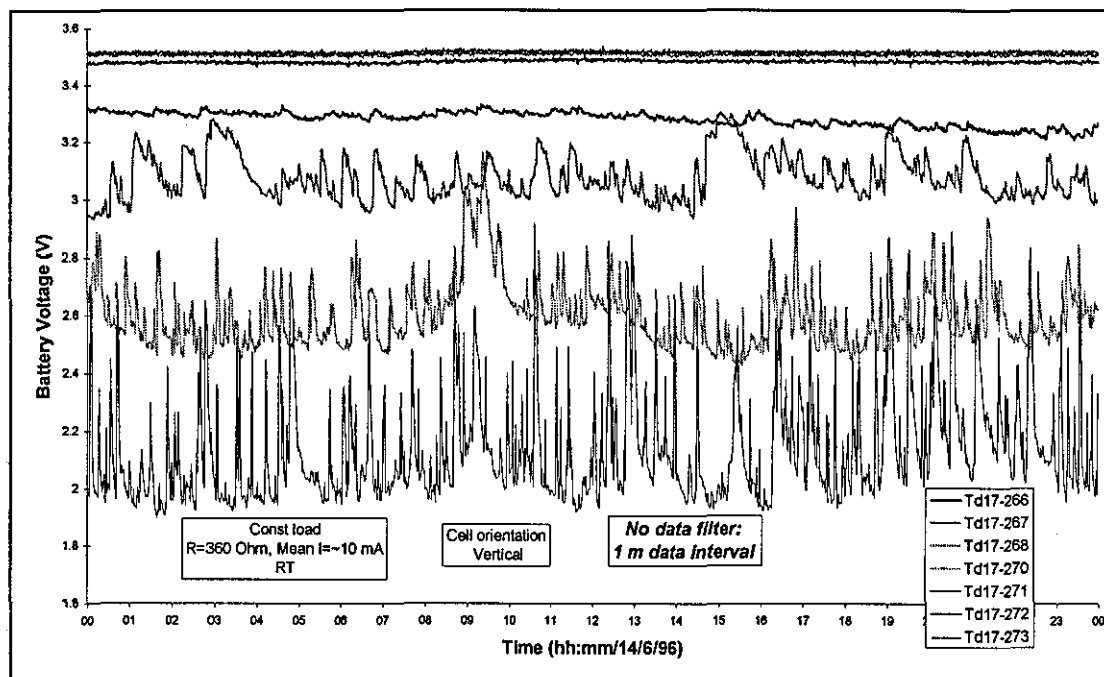


Figure 11.18 Extract of mid-term room-temperature discharge curve with expanded voltage and time-scale, showing 4 cells having well-behaved stable cell voltages and 3 cells exhibiting unstable voltage profiles.

The progressive nature of the onset of the failure mode is highly suggestive of a systematic growth of a 'barrier' layer between the positive and negative electrodes. This hypothesis implies that the problem is associated with a deficiency in the discharge process itself, rather than an engineering defect. Thus the mechanism for premature failure would appear to lie in some internal process that significantly retards cell kinetics, particularly at low temperature. The variability of discharge profiles exhibited during premature failure, suggests that the mode is predisposed towards cells that are affected by some defect in the control of manufacturing tolerances. It is interesting to note that a reduction in terminal voltage from 3.5 to 1.5 V corresponds to a change in cell internal resistance of 17 to 317 Ω for a 360 Ω load. Passivated cells sometimes revert to normal behaviour, and cell voltage is both unstable and subject to sudden rises that vary in interval and duration. Such a behaviour pattern is indicative of an unstable and quasi-random physical phenomenon.

11.7.1. Physical characteristics of the voltage perturbations

Details of the voltage perturbations are revealed by increasing the resolution of the time-base and focusing on specific sections of the discharge plots as shown in Figure

11.19 (x-axis time-scale range of 20 days, 50 mV bandwidth filter). The increasing frequency and magnitude of the voltage perturbations with depth of discharge are clearly evident. Figure 11.20 and Figure 11.21 increase the resolution of the time-base to the maximum of 1 point per minute, and the x-axis time-scales of the discharge plots are expanded to 4 and 1 day respectively.

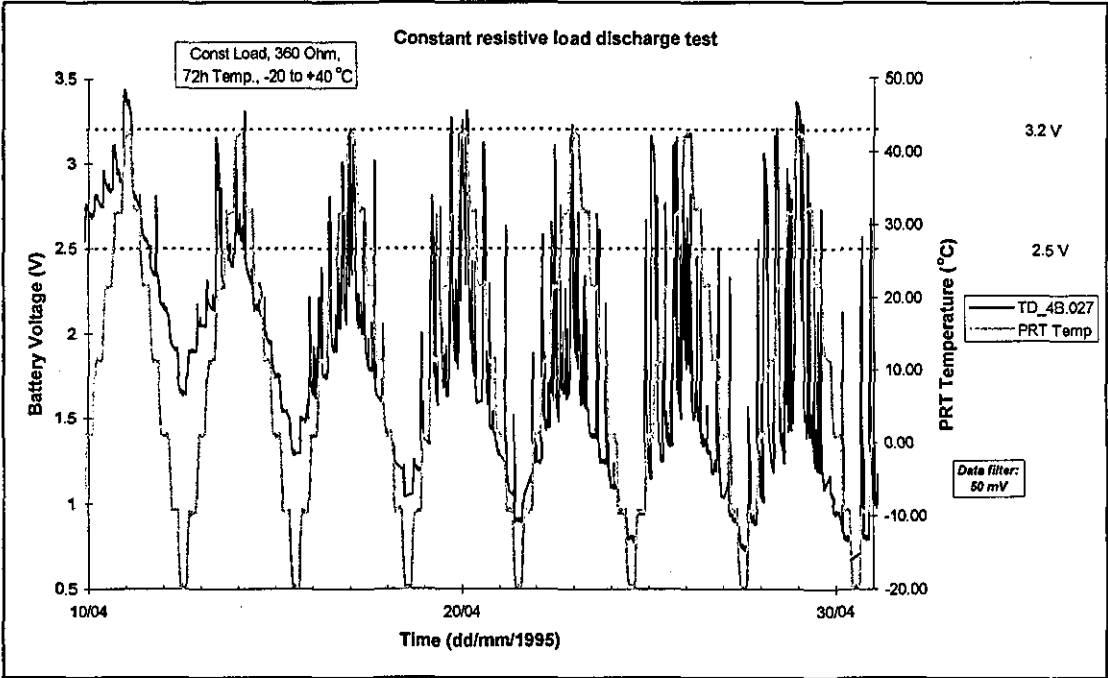


Figure 11.19 Expanded time scale discharge chart, showing details of the voltage

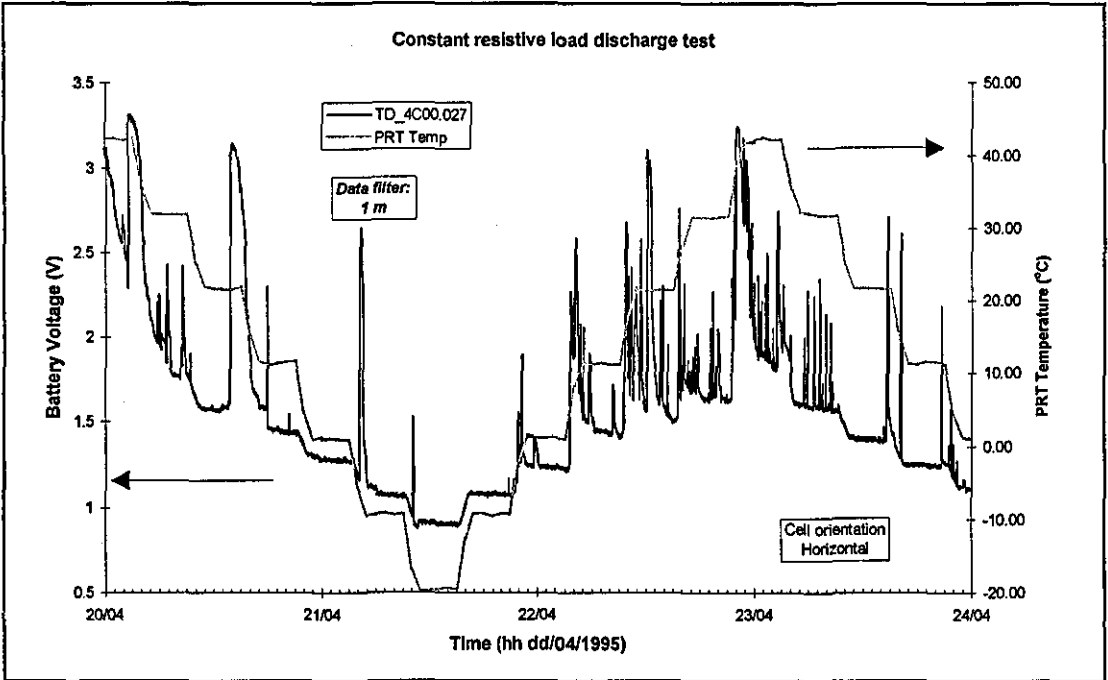


Figure 11.20 Maximum time-base resolution showing details of the voltage perturbations over one thermal cycle (72 h).

The base-line voltage profile moves in phase with the thermal cycle, and voltage spikes and longer term periods of voltage recovery are superimposed on the base-line voltage/temperature cycle. The peak to valley amplitude of the voltage spikes is highly variable, although the voltage typically recovers to >3 V during the high temperature phase of the thermal cycle. Both the intervals between of the voltage fluctuations and their durations are also variable.

There is a tendency for voltage reactivation to be associated with a dynamic change in test temperature. However, this conjunction is by no means exclusive, and voltage recovery can also occur intermittently, seemingly without external influence. Figure 11.21 shows that the rise-time of the leading edge of the positive voltage recovery spike is generally rapid. The slopes of the trailing edges are generally more gradual, although examples of a steep (rapid) fall in voltage do occur.

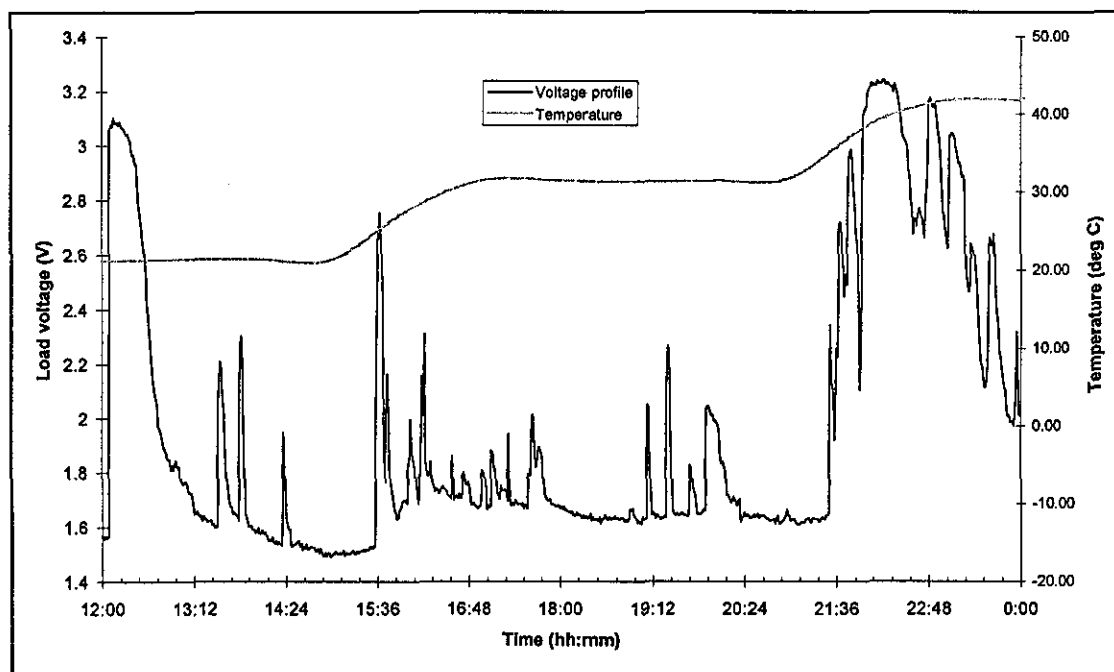


Figure 11.21 Expanded time scale plot of discharge profile of Td cell showing voltage perturbations, with temperature plotted against the secondary y-axis.

11.7.2. A speculative model for the saddle-back premature failure mode

As the discharge process proceeds, the build-up of reaction products will tend to reduce the active (porous) fraction of any LiCl barrier layer. If we assume the limiting case where cracks in the layer between the electrode surface and the bulk catholyte reduce to the stage where species transport becomes the rate determining process, then the layer acts as a membrane. Under these conditions Peled's model⁴ for describing

the processes involved in the voltage delay phenomenon at the anode would appear to provide a good explanation for the voltage perturbations observed here.

As active species are reacted at an electrode, so a concentration gradient of LiAlCl_4 builds up in the pores of the PL. The concentration of LiAlCl_4 will cause a significant increase in the viscosity of the electrolyte inside the cathode pores. As the viscosity increases, so solution conductivity decreases and the IR drop increases. (The conductivity of $\text{SOCl}_2:\text{LiAlCl}_4$ solutions at 20°C decreases from 21.2 mS/cm at 1.7 M to 17.5 mS/cm at 3.5 M, while at -30°C , it decreases from 9.7 mS/cm at 1.2 M to 4.0 mS/cm at 3.5 M LiAlCl_4). Chenebault et al.⁵ have proposed that the limiting case occurs where the LiAlCl_4 concentration at the bottom of the crack exceeds its maximum solubility, when precipitation of LiAlCl_4 can occur because of the lack of natural convection required to homogenise the concentration of the catholyte species at the bottom of cracks. Both of these models would lead to heavy blocking of the electrode surface and voltage reduction.

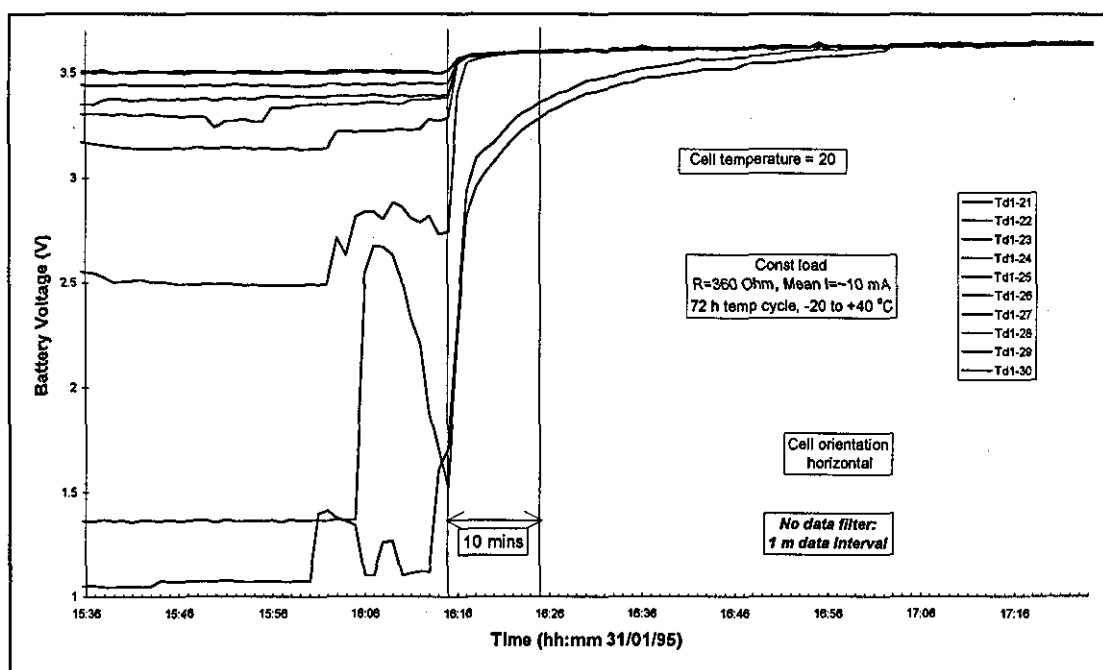


Figure 11.22 Voltage versus time chart showing voltage recovery from on-load polarisation to the equilibrium open-circuit voltage for 10 cells.

In order to validate this diffusion-based model, an experiment was conducted to measure the voltage dynamics of test cells switched from on-load to open-circuit. Details of the voltage recovery curves are shown in Figure 11.22, which plots cell voltage against time for 10 cells switched from $360\ \Omega$ load to open-circuit at 20°C . The time-base is at maximum resolution of 1 data point/minute. The chart includes

'normally' functioning cells, and two 'malfunctioning' cells operating at <1.5 V.

The removal of load is marked by the sudden increase in voltage at the time of 16:15 h. The higher voltage 'normally operating' cells respond quickly to the load change and recovery to the normal open-circuit voltage of 3.65 V takes only 2 to 3 minutes. However, the two 'prematurely-failed' cells take approximately 45 minutes to recover to 3.65 V from their on-load voltages of 1.1 and 1.4 V respectively. This extended voltage recovery time correlates with a gradual restoration of uniform species concentrations throughout the catholyte, and lends support to the theory that the low on-load voltage that occurs during premature failure is due to concentration polarisation occurring in a barrier layer situated at some point between the two electrodes.

With the present tests, terminal voltage typically recovers to >3 V during the >30 °C phase of the thermal cycle, implying that the threshold for effective mass transport (i.e. the limiting current density) for a prematurely failed cell occurs at some point in the 0 to $+20$ °C temperature range.

11.8. Explanation of 'saddle-back failure' mode

Four questions remain:

1. Where is the barrier layer situated?
2. How can we account for the variable incidence of the failure mode through the population of Td cells?
3. Why are only Td cells affected by this failure mode?
4. What are the implications for the long-term discharge duration of the meter application?

11.8.1. Positive electrode and separator

The characteristic processes which occur at the positive electrode do not fit the observed dynamic voltage fluctuations well. The glass transition point of the PTFE binder⁶ (160 K) is well below the temperature range utilised here. The elastic properties associated with the pce matrix over this temperature range should allow stresses associated with thermal and physical change to be absorbed by gradual expansion.

The normal cathodic processes are essentially passive; that is the sole active physical process is the deposition of the insoluble LiCl reaction product. There appears to be no obvious process in the pce/LiCl solid phase likely to trigger the frequent and high speed voltage changes, or longer term levels of regeneration. Yamin has stated⁷ that

the limiting current density for even precipitation of LiCl through the cathode structure is 0.5 mA/cm^2 . The present laboratory test results have shown that an increase in current density of 0.24 to 0.88 mA/cm^2 (resistance values of 360 and 100Ω , respectively) causes a significant reduction in cell capacity for both Td and Te battery types, which implies that the cathode is operating satisfactorily at R_L of 360Ω , and that the observed behaviour is generally consistent with Yamin's hypothesis.

It is known that LiCl crystals can be deposited on the separator (Section 6.4). However, as with the pce, such a process is entirely passive, and is not consistent with the dynamic nature of the voltage fluctuations observed with the failure mode.

11.8.2. Negative electrode

The intermittent and quasi-random nature of the observed voltage fluctuations are more consistent with active breakdown and repair processes that are known to occur at the negative electrode during discharge. These processes derive from: (a) the utilisation of the surface layers of lithium and periodic delamination of the PL, and (b) stress relief induced by thermal, mechanical or electrical shocks. Both effects can trigger physical changes in the structure of the PL, which can lead to the opening and closing of channels between the SEI and the bulk catholyte.

The fast rise-time of the leading edge of a voltage spike correlates well with a sudden fracturing of the friable secondary layer of the PL, and opening of access channels between the bulk catholyte and the inner layers of the PL adjacent to the lithium surface. The renewed availability of transport routes for active species added to the fast kinetics of the anodic processes would be compatible with the rapid reactivation of the electrode. The slower dynamics associated with the more sloping trailing edge of voltage spikes are consistent with the gradual closing of the channels due to the fresh deposition of LiCl. Voltage incursions having a fast trailing edge do take place, implying sudden attenuation of species transport. A rapid voltage incursion may occur in a case where a crack through the PL is very narrow and unstable. In such a case, the regenerated electrochemical processes can only be sustained momentarily, and quickly fail due either to further contractions between crystal layers which close the crack, or the onset of concentration polarisation at the bottom of the crack where exchange of species is restricted.

The fact that cells can recover to normal behaviour after extended periods of passivation can also be explained in terms of dynamic changes in the PL geometry. In

the case where the geometry of a new channel is relatively restrictive, then this reactivation may be relatively short-lived. If the crack is large and stable enough to provide permanent access for mass transport between the catholyte reservoir and the inner pore systems near the electrode, then a longer-term reactivation of the cell will occur.

The variability of the time intervals between voltage incursions will depend on the lithium usage rate, and the distributions of the physical properties of the Li/SEI/PL interfaces and the crystal structure within the PL. The naturally amorphous nature of the PL crystal structure, and the variable conditions under which it builds up will lead to non-uniform distributions of properties such as mechanical strength and thermal expansion coefficient within the crystal structure of the PL. Such non-uniformities can explain the unpredictability of the timing of the voltage dynamics.

11.8.3. Statistical distribution of the failure mode

The analysis suggests that the electrochemical 'barrier layer' is located on the anode, and that the source of the variable performance lies in some electrochemical impediment in the PL layer. The fact that 30% of the Td cells achieve high values of ϵ_c and discharge satisfactorily implies that the basic cell design is fit-for-purpose, and that the variable cell-to-cell performance is caused by one or more poorly controlled production variables, such as variations in the physical and chemical conditions of the lithium metal and or the catholyte.

Catholyte preparation is carried out in bulk, and the filling of cells is carried out under vacuum by an automatic process. A single batch of catholyte mix is used for many cells in a production lot. Thus catholyte impurity is not consistent with the cell-to-cell variations observed in the results. However, the manufacturing process involves manual preparation and fitting of the lithium anode in a relatively open dry-room environment. These operations may result in variations in the geometry and cleanliness of the anode assembly. Hagan et al.⁸ have observed significant variations in anode performance of lithium samples from different sources, which were attributed to differences in the electronic conductivity, permeability and mechanical strength of the PL, which in turn derived from the presence of impurities.

Some 500 papers were reviewed during the course of this study, and only two other reports of the 'saddle-back' failure pattern were found. In 1984, Buchman⁹ reported a similar failure for cells discharged at a current density of 0.25 mA/cm² at 37 °C, after

2 and 6 months of storage at 60 °C. Interestingly, this discharge rate corresponds to ~11 mA for a 'D' cell, broadly equivalent to discharge at the present 360 Ω load used here. Non heat-treated cells achieved close to the stoichiometric capacity. Impedance measurements showed that the voltage decay was linked to increases of internal cell resistance, and was further increased by higher current. Buchman could not explain the failure. Cieslak¹⁰ tested spiral-wound cells from a range of 6 (unidentified) manufacturers after ageing for 30 weeks at 50 °C and found two cell types that exhibited the saddle-back form of discharge pattern. Cells that had not been heat-treated performed satisfactorily, suggesting that the failure mode is related to some aspect of the heat treatment. Cieslak stated that she was unable to explain the variability in the results. The failure of these researchers to diagnose these failure phenomena satisfactorily suggests that the saddle-back mode has not previously been observed or analysed in such detail.

The generally accepted upper operating temperature limit for Li/SOCl₂ cells is well in excess of 60 °C, and in principle the temperature levels used in these laboratory tests should not affect the basic discharge performance. However, the combination of elevated temperatures and enhanced impurity levels will both serve to increase corrosion rates. Any variations in impurity level would tend to increase the distribution of the rates of the chemical processes that govern the growth of the PL. The impact of these distributions would be to increase the cell-to-cell variations in the morphology and mechanical properties of the PL, and hence the probability of variable discharge behaviour.

11.8.4. Susceptibility of the Td cell type to premature failure

The formulation of the catholyte of the Td cell has not been released, however the manufacturer has published a series of papers discussing the 'synergetic' effects of SO₂ and LiAl(SO₃Cl)₄ when added to the basic SOCl₂:LiAlCl₄ catholyte mixture^{11,12,13,14}. The given purposes of the additives are to alleviate voltage delay and improve start-up performance. Their function is to modify the internal morphology, external geometry and porosity of the PL. However, Cieslak¹⁵ carried out discharge tests and found that the addition of SO₂ to the standard 1 M SOCl₂:LiAlCl₄ catholyte causes a significant increase in the variability of capacity loss through self-discharge. (At a given test condition, self-discharge measurements varied over a range of 10:1). She was unable to explain these variations. Cieslak's baseline (non-SO₂) cell design gave

reproducible results, suggesting that the variable self-discharge behaviour may be due to modifications in the structure of the PL caused by the introduction of SO_2 .

The correlation of the saddle-back failure mode with the presence of additives in the standard catholyte would imply that the cell type has a heightened susceptibility to the failure mode, that is a reduced tolerance to production variations. The cell to cell performance variations would then be traced to small variations in some aspect of the manufacturing process, and it is suggested that these may include trace impurities. At present insufficient information exists to identify the relevant variables and the manner in which they affect cell performance.

11.9. Implications for the meter application

As may be seen in Table 11.1, the impact of the premature failure mode is minimal for low current (3 mA) discharge across a $1200\ \Omega$ resistance, suggesting that its effect in the meter application may be insignificant when the mean current is reduced further down to $\sim 100\ \mu\text{A}$. Nevertheless the results of the accelerated tests carried out at R_L of $360/560\ \Omega$ point to variations in quality control and variations in the morphology of the PL. Their long-term effects are not possible to predict at this stage, but they may be expected to result in variations in self-discharge rate and a wider dispersion of service life.

In terms of the laboratory evaluation of this battery type, the results have demonstrated that the premature failure mode casts uncertainty over the validity of using accelerated testing to predict longer-term cell performance, even at the manufacturer's recommended discharge rate of $\sim 10\ \text{mA}$. The $Q_{2.5}$ parameters yield misleading measurements of the electrical capacity of the battery. However, the Q_0 measurement would appear to offer a reasonably accurate value of the electrical capacity of the cell for longer term discharges. This is clearly contingent on the load current being low enough to avoid the impact of enhanced polarisation processes. Nevertheless, it is unclear whether the defective cell operating mechanisms which cause the premature failure modes observed in the accelerated tests will affect long-term performance and cell life in some other way, possibly through enhanced self-discharge.

CHAPTER 12

DISCHARGE TEST RESULTS FOR CELL TYPE TA AND TB

Battery types Ta and Tb are not being used in either of the meter applications at present, and because of the limited number of instrument channels, a total of only six discharge tests were carried out. Their use here is to provide experimental information to add to the performance database of manufactured Li/SOCl₂ cells.

12.1. Battery Type Ta

Table 12.1 Ta capacity parameters.

Capacity parameters to 2.5 V								
Test Code	R_L (Ω)	I_L (mA)	Batch Size	$\mu(Q_{2.5})$ (Ah)	$^{max}Q_{2.5}$ (Ah)	$^{min}Q_{2.5}$ (Ah)	$\sigma(Q_{2.5})$ (Ah)	Test conditions
1	2	3	4	5	6	7	8	11
Ta3	360	10	10	12.60	14.76	11.32	1.57	Standard
Ta2	560	6.4	10	12.37	14.07	11.42	0.77	Standard
Capacity parameters to 0 V								
				$\mu(Q_0)$	$^{max}Q_0$	$^{min}Q_0$	$\sigma(Q_0)$	
Ta3	360	10	10	15.96	16.34	15.32	0.30	Standard
Ta2	560	6.4	10	16.34	16.67	16.10	0.23	Standard

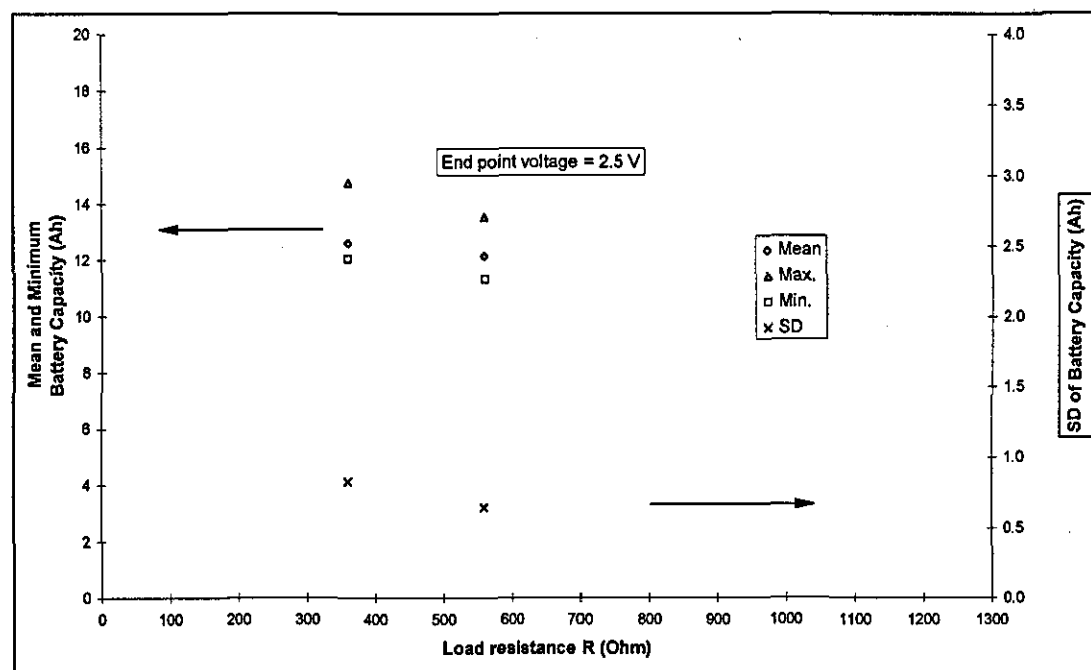


Figure 12.1 $Q_{2.5}$ capacity parameters as a function of resistance for battery type Ta.

Three tests were carried out on battery type Ta, however data was lost during the critical end-of-life phases of the first Ta1 (360 Ω) discharge test, which precluded capacity measurement.

The available $Q_{2.5}$ and Q_0 capacity parameters are given in Table 12.1, and those for

$Q_{2.5}$ are plotted against load resistance in Figure 12.1. The values 12.37 and 12.60 Ah for $\mu(Q_{2.5})$ are approximately 7 Ah less than those recorded in equivalent tests for cell type Te. The $\sigma(Q_{2.5})$ values of approximately 1.5 and 0.8 Ah (360 and 560 Ω respectively) also compare unfavourably with type Te.

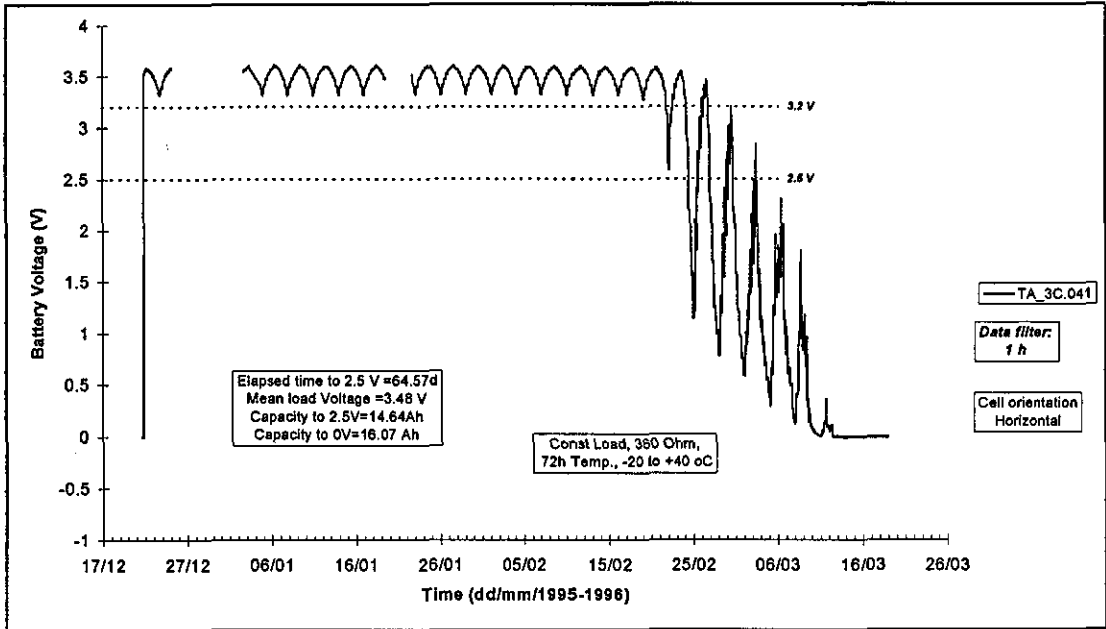


Figure 12.2 Ta 'maximum capacity' cell 360 Ω discharge chart (Ta3-041).

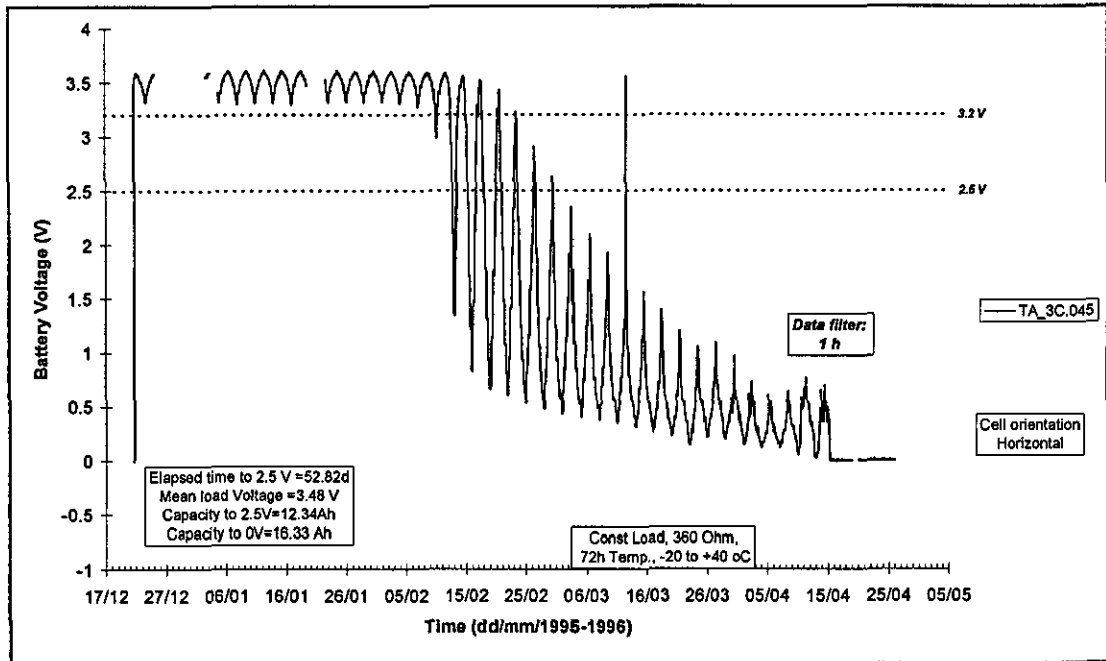


Figure 12.3 Ta 'minimum capacity' cell (Ta3-045) 360 Ω discharge chart.

For this cell type, variation in capacity appears to be dependent on the length of the end-of-life phase. This may be seen by comparing the discharge profiles for the maximum and minimum capacity cells recorded in test Ta3, which are shown in

Figure 12.2 and Figure 12.3, respectively. The initial discharge patterns are very similar, however their end-of-life phases are differentiated both by their point of onset and subsequent duration. The end-of-life phase of the high capacity cell lasts for only 5 temperature cycles, whilst that for the low capacity cell is extended through some 20 cycles. The respective values of Q_0 of 16.07 and 16.33 Ah for the two cells are similar and indicate that the cells were provided with similar amounts of reactant on manufacture. However, variations in the impact of the polarisation processes in the cells cause a significant difference in discharge performance and in the respective $Q_{2.5}$ capacities.

The $\sigma(Q_0)$ values are low and compare well with those for the type Te results and imply tight manufacturing control of the amounts of reactants.

12.2. Battery Type Tb

Three tests were carried out on this battery type, the capacity parameters for the Tb cell are tabulated in Table 12.2 below, and plotted in Figure 12.4. It is important to note that the lithium surface area of this cell type is 145 cm^2 , thus the current density for a given value of R_L is approximately one third of that for an equivalent test on battery types Ta, Td and Te.

Having a $Q_{2.5}$ of approximately 16 Ah, this battery type delivers the second highest capacity of the 4 types tested. The repeatability of the cell type was second to that of type Te. Two 360Ω tests were carried out, and the respective values of $\mu(Q_{2.5})$ and $\sigma(Q_{2.5})$ compare closely with one another, and are about 16 Ah and 0.2 Ah respectively.

Table 12.2 Tb capacity parameters.

Capacity parameters to 2.5 V								
Test Code	R_L (Ohm)	I_L (mA)	Batch Size	$\mu(Q_{2.5})$ (Ah)	$^{\max}Q_{2.5}$ (Ah)	$^{\min}Q_{2.5}$ (Ah)	$\sigma(Q_{2.5})$ (Ah)	Test condition
1	2	3	4	5	6	7	8	11
Tb1	360	10	10	15.75	16.14	15.59	0.15	Std.
Tb3	360	10	10	16.08	16.32	15.60	0.24	Vertical
Tb2	560	6.4	10	15.41	15.90	13.60	0.67	Std.
Capacity parameters to 0 V								
				$\mu(Q_0)$	$^{\max}Q_0$	$^{\min}Q_0$	$\sigma(Q_0)$	
Tb1	360	10	6	16.20	16.36	16	0.12	Std.
Tb2	560	6.4	10	16.00	16.23	14.67	0.47	Std.

The values of $\mu(Q_{2.5})$ and $\sigma(Q_{2.5})$ for the 560Ω tests are approximately 15.4 Ah and 0.7 Ah respectively. The mean capacity is lower than that achieved by the 360Ω

tests, which is unexpected given that the discharge rate is lower. The two $\mu(Q_0)$ values decrease slightly with increasing load current, possibly implying the impact of self-discharge.

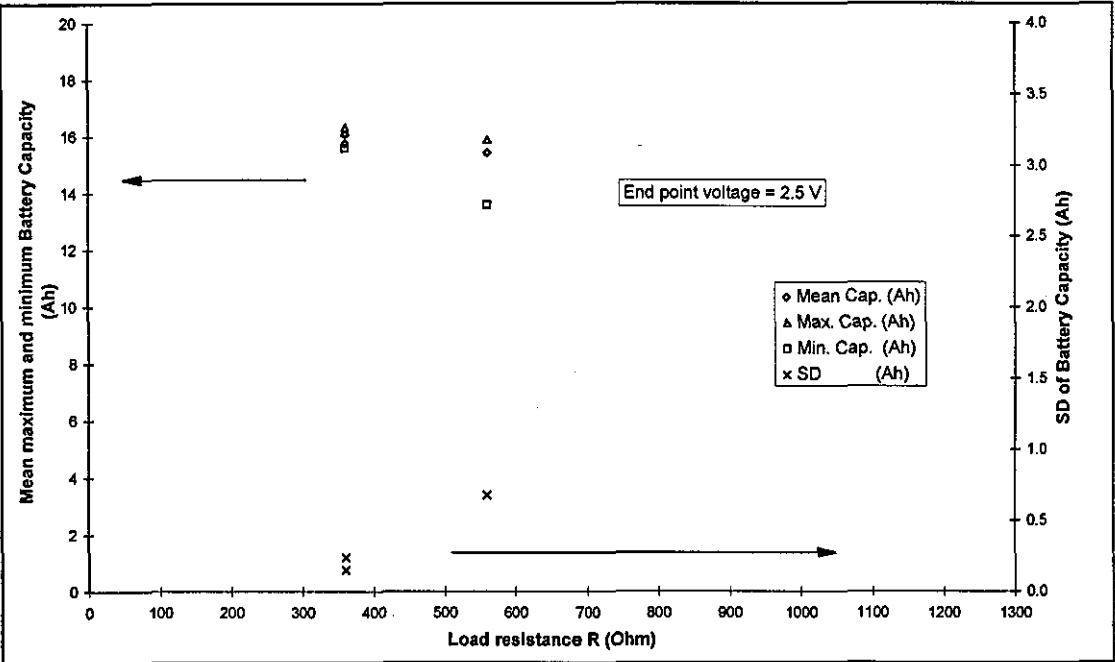


Figure 12.4 $Q_{2.5}$ capacity parameters as a function of resistance for Battery Type Tb. The higher than normal standard deviation recorded for test Tb2 (R_L of 560 Ω), is caused by a single outlier (Tb2-92), whose value of $Q_{2.5}$ of 13.60 Ah is significantly below the mean. Removing this outlier reduces the value of $\sigma(Q_{2.5})$ from 0.7 to 0.2 Ah, which is in line with the 360 Ω results, and increases the value of $\mu(Q_{2.5})$ to 15.6 Ah.

The discharge profiles for the maximum capacity and the outlier (minimum) capacity cells are reproduced in Figure 12.5 and Figure 12.6 respectively, and it may be seen that the profile is generally smooth and predictable. Both batteries reach 0 V after approximately the same discharge duration. The capacity difference may be traced to the points of onset and the durations of the end-of-life phases. The onset is approximately 10 days earlier for the low capacity cell, and the respective end-of-life phases endure for 6 and 2 thermal cycles. The value of Q_0 recorded for the outlier was found to be significantly lower than that for the other 29 test cells, i.e. 14.67 Ah rather than the mean of 16 Ah. The $(Q_0 - Q_{2.5})$ difference of 4.86 Ah (ϵ_c of 70%) indicates that the end-of-life phase sets in well before exhaustion of the active components of the cell.

With the exception of the outlier, the pattern of the discharge profile is repeatable for all 30 Tb cells.

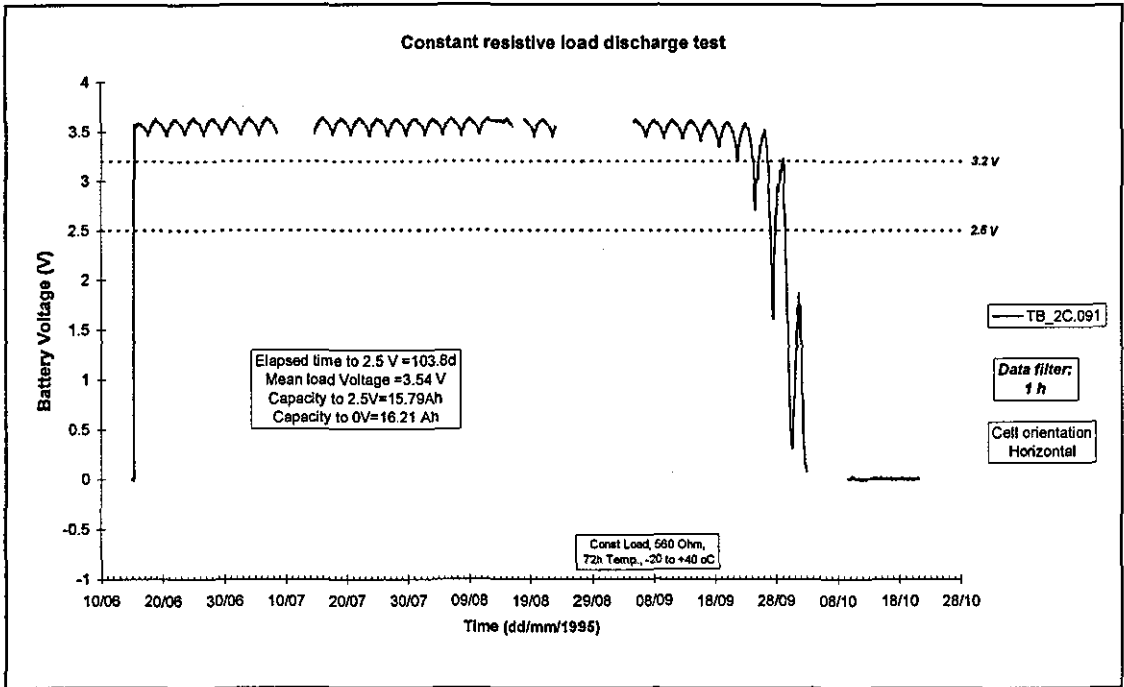


Figure 12.5 Tb 'maximum capacity' cell (Tb2-91) 560 Ω discharge chart.

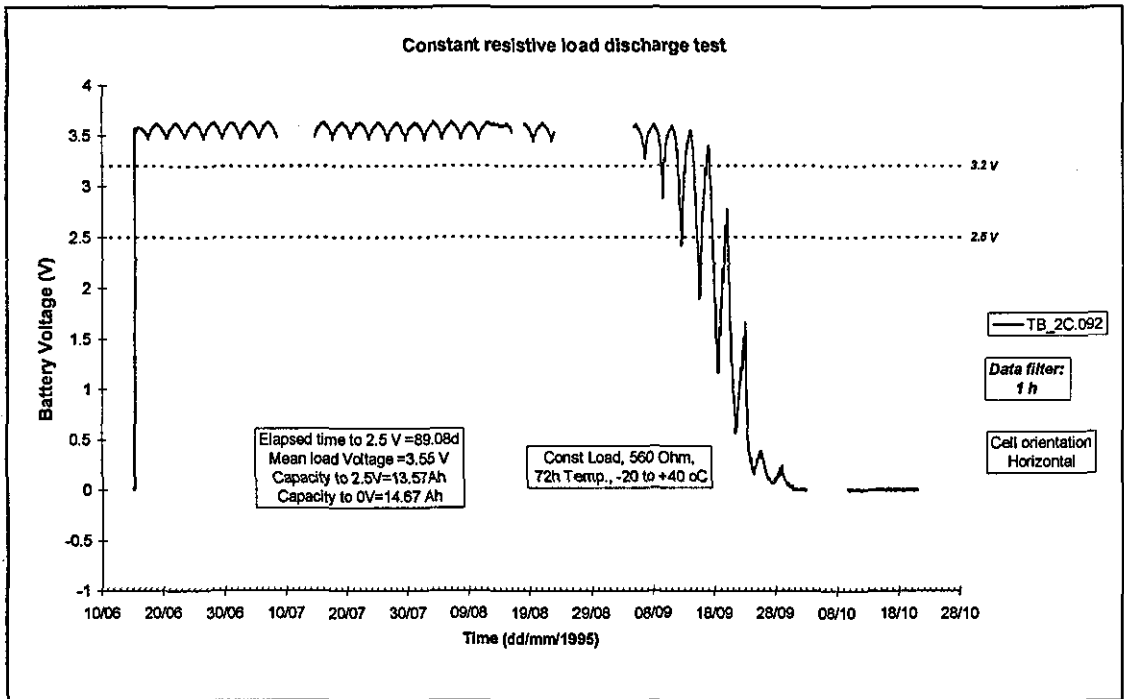


Figure 12.6 Tb 'minimum capacity' cell (Tb2-92) 560 Ω discharge chart.

12.3. Interpretation of the Ta and Tb test results

The Ta and Tb cell types were not initially considered for the application, due mainly to commercial considerations. The restricted number of test channels in the test rig limited the number of levels of stress that could be applied to these cell types, and it is

not possible to draw meaningful correlations of performance with test load from only two levels of stress. Nevertheless the Ta and Tb cell type performance results help to define 'typical' and 'non-typical' discharge behaviour and as such are an important additions to the data base. In this respect, these data demonstrate that the predictable discharge behaviour observed for the Te cells is representative of best performance for a Li/SOCl₂ cell, and that the incidence and type of premature failure recorded for the Td cells is non-typical.

The results identify two further failure modes. The low Q_0 outlier recorded for the Tb is unique amongst the results for cell types, and implies a deviation in manufacturing quality, such as an insufficiency of one of the reactants, or an internal engineering defect, rather than an electrochemical malfunction. The Q_0 values observed for the Ta cell type were all tightly dispersed around the mean, suggesting that the low $Q_{2.5}$ values are due to the premature advent of some enhanced polarisation process, leading to reductions of cell kinetics and on-load voltage.

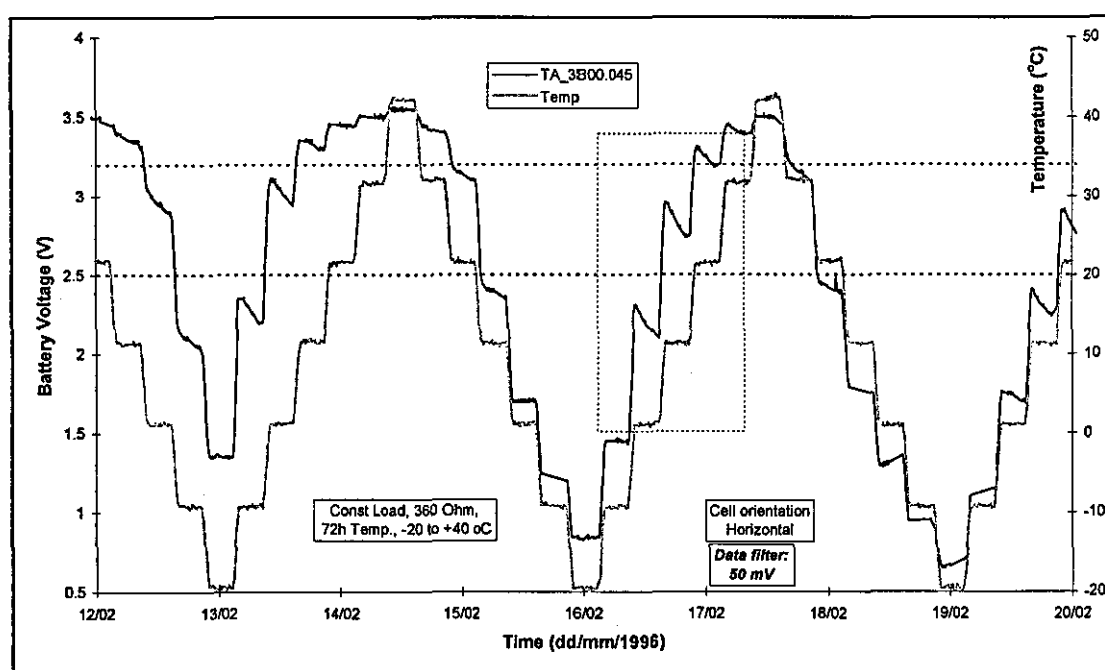


Figure 12.7 Expanded voltage- and time-scales discharge curve for a Ta cell at the inception of the premature failure mode.

Figure 12.7 shows the inception of the end-of-life phase for a prematurely failed Ta cell. The voltage and time-scales are expanded to show details of the voltage patterns, and the test temperature profile is plotted against the secondary y-axis. The voltage and time scales have been expanded in order to show details of the voltage profile at

the inception of the premature failure mode. The cell voltage shows a significant increase in sensitivity to change as temperature reduces below 0 °C.

Unlike the spiky voltage profiles observed for the prematurely failed Td cells, the discharge profile is smooth, and no permanent recovery occurs once the voltage begins to decrease. With the Ta cell, a further pattern of voltage relaxation is superimposed on top of the base line voltage cycle at a given equilibrium temperature. For example, the voltage profile within the dashed-edged rectangle is subject to a decay phase following certain of the 10 °C temperature change steps, and this phase can persist for most of the subsequent 5 hour constant-temperature period. Such a voltage pattern would appear to be consistent with a diffusion controlled activation and relaxation process.

As discussed in Section 11.8.1, normal cathodic processes are essentially passive. The insolubility and permanence of the LiCl precipitate does not lend itself to significant reactivation of the cell, either temporary or permanent. Thus the gradual and smooth end-of-life behaviour of a prematurely failed Ta cell would appear to be related to a progressive reduction of accessible and active reaction sites, and is compatible with a gradual decrease of the active fraction of the catholyte phase in the pce matrix, and a transition to increasing diffusion control and enhanced sensitivity to imposed thermal and resistive loads.

However, as discussed in Section 6.8.5, the cathode capacity at such relatively low discharge rate should not be susceptible to blocking. Marincic¹ has identified two types of pce failure mechanism: (a) restricted catholyte supply to the electroactive pores, and (b) a lack of active sites in the pore. It is commonly accepted that the physical (e.g. packing pressure) and geometric properties affect pce performance (see Section 6.8.3), and these are factors that could stray out of tolerance on manufacture.

As with the Td cells, a reasonable proportion of the Ta cells achieve a high value of ϵ_c , and the root of the problem would appear to be variable quality control. The catholyte of the two battery types both utilise SO₂ as an additive, and it is conceivable that the LiCl crystal layer which forms in the pce may be more susceptible to evolving as a closed-channel structure, with resulting attenuation of the mass transfer processes between the inner pores of the pce and the bulk catholyte, and a reduction in pce utilisation efficiency. Again the admission of impurities during manufacture may induce such an adverse change in channel structure.

CHAPTER 13

REVIEW OF DISCHARGE TEST RESULTS

The main aims of this study are to predict the service lives of battery candidates for the two meter applications, and to identify the best design options. The discharge data provide key indicators of capacity and performance. However, the results fall into complex patterns that do not easily function as predictors for long-term discharge. Here we present the collective discharge test results for the four candidate batteries with a view to comparing performance and extracting the information required to determine service life and suitability for the meter applications.

13.1. $R_L = 360 \Omega$ results

The discharge load resistance R_L , of 360Ω , was recommended by the battery manufacturers as being benign, i.e. polarisation and self-discharge effects should be minimal, and compatible with providing an accurate quick measure of capacity. The end-point voltage of 2.5 V was originally selected to correspond with the low voltage operating threshold of the Meter Type A, and to conform with conventional battery evaluation methods. The majority of tests were carried out at the 360Ω load level, thus providing the largest base of directly comparable data. In practice, the $Q_{2.5}$ results form complex distributions, but provide essential information regarding: (a) susceptibility to elevated levels of polarisation, (b) available electrical capacity, (c) quality control of physical parameters and amounts of reactants and (d) ranking orders of the performance parameters.

The $Q_{2.5}$ and Q_0 capacity parameters for the four types of cell under 360Ω discharge load are summarised in the two parts of Table 13.1. The values in square brackets in columns (3), (4) and (7) give the rankings in terms of the given performance parameter, where [1] is best and [4] worst. Column 7 gives the coulombic efficiency, ε_C .

We can summarise the data by discussing the batteries in order of decreasing performance. With respect to the $Q_{2.5}$ test results, Type Te records the highest mean capacity when the end-point voltage is 2.5 V, $\mu(Q_{2.5})$, and also the lowest standard deviation, $\sigma(Q_{2.5})$, implying the highest quality of design and production standards. The value of ε_C is 0.98, the highest registered for any of the test cell types.

Tb possesses the next best capacity and standard deviation figures. $\sigma(Q_{2.5})$ is greater than that of the Te cell, this is mainly due to one low capacity outlier of value 13.59 Ah, otherwise the value would be 0.28 Ah, comparable with the Te cell. The value of ε_c is 0.96, which is also high and close to that of the Te cell type.

Table 13.1 Capacity parameters to 2.5 V for the four types of test cell.

Capacity parameters to 2.5 V, ($Q_{2.5}$)						
Battery Test Code	Load Res. R_L (Ω)	Mean Cap. $\mu(Q_{2.5})$ (Ah)	Max. Cap. $\max Q_{2.5}$ (Ah)	Min. Cap. $\min Q_{2.5}$ (Ah)	Std Devn. $\sigma(Q_{2.5})$ (Ah)	Coulombic Efficiency ε_c
(1)	(2)	(3)	(4)	(5)	(6)	(7)
Ta	360/560	12.38 [3]	14.76	11.32	0.76 [3]	0.77 [3]
Tb	360	15.75 [2]	16.32	13.59	0.49 [2]	0.96 [2]
Td	360	12.22 [4]	16.78	4.46	2.91 [4]	0.72 [4]
Te	360	19.95 [1]	20.17	19.49	0.26 [1]	0.99 [1]
Capacity parameters to 0 V, (Q_0)						
	R_L	$\mu(Q_0)$	$\max Q_0$	$\min Q_0$	$\sigma(Q_0)$	
Ta	360/560	16.15 (4)	16.67	15.32	0.32 (3)	
Tb	360/560	16.36 (3)	14.67	16.08	0.38 (4)	
Td	360	16.97 (2)	17.26	16.67	0.18 (1)	
Te	360	20.21 (1)	20.61	19.84	0.24 (2)	

The value of ε_c of 77% for cell type Ta is significantly lower than that for both Tb and Te. The relatively low $\mu(Q_{2.5})$ of only 12.38 Ah and the relatively high value of $\sigma(Q_{2.5})$ of 0.77 Ah reflects a relatively high variation in performance caused by the higher susceptibility to premature failure.

The averaged performance parameters for the type Td cell are the poorest of the set. The value of ε_c of 0.72 is 0.22 lower than that for both Tb and Te, and 0.05 lower than that for the Ta cell. The low $\mu(Q_{2.5})$ of only 12.22 Ah, and the very high value of $\sigma(Q_{2.5})$ of 2.22 Ah reflects the very high susceptibility to significant polarisation and the high proportion of 'prematurely failed' cells. The $Q_{2.5}$ capacity range of 4.46 to 16.78 Ah is by far the widest recorded for any cell type, and demonstrates the high variability of the cell performance at this test load.

The Q_0 data for all four battery types are all tightly dispersed, and are extremely repeatable. The $\mu(Q_0)$ results show that the available electrical energy capacity of 20.2 Ah for cell Te is the highest of the test cell types. Those for the other three cell types fall into a group approximately 3 Ah lower, namely: 16.2, 16.4 and 17.0 Ah, for cell types Ta, Tb, and Td respectively. Changing the end-point voltage from 2.5 to

0 V results in a change in Td cell ranking from fourth to second for the $\mu(Q_x)$ parameter, and from fourth to first for the $\sigma(Q_x)$ parameter! The $\sigma(Q_0)$ and $\sigma(Q_{2.5})$ values for the Tb cell are similar, as they are for the Te cell. However, the value of the $\sigma(Q_0)$ parameter for the Ta cell is 50% of that of the $\sigma(Q_{2.5})$ value, whilst the equivalent parameters for the Td cell register an improvement of greater than an order of magnitude, implying very significant improvements in repeatability.

13.2. The $Q_{2.5}$ results

Direct comparisons of the $Q_{2.5}$ results for the Td and Te cells at all load levels illustrate the underlying trends. Unfortunately the Ta and Tb cell tests were restricted to R_L values of 360 and 560 Ω . Although they are of use in defining the load versus $Q_{2.5}$ capacity trends for the Li/SOCl₂ cell type generally, a load range of two levels is too restricted to allow the development of individual trends for the two battery types.

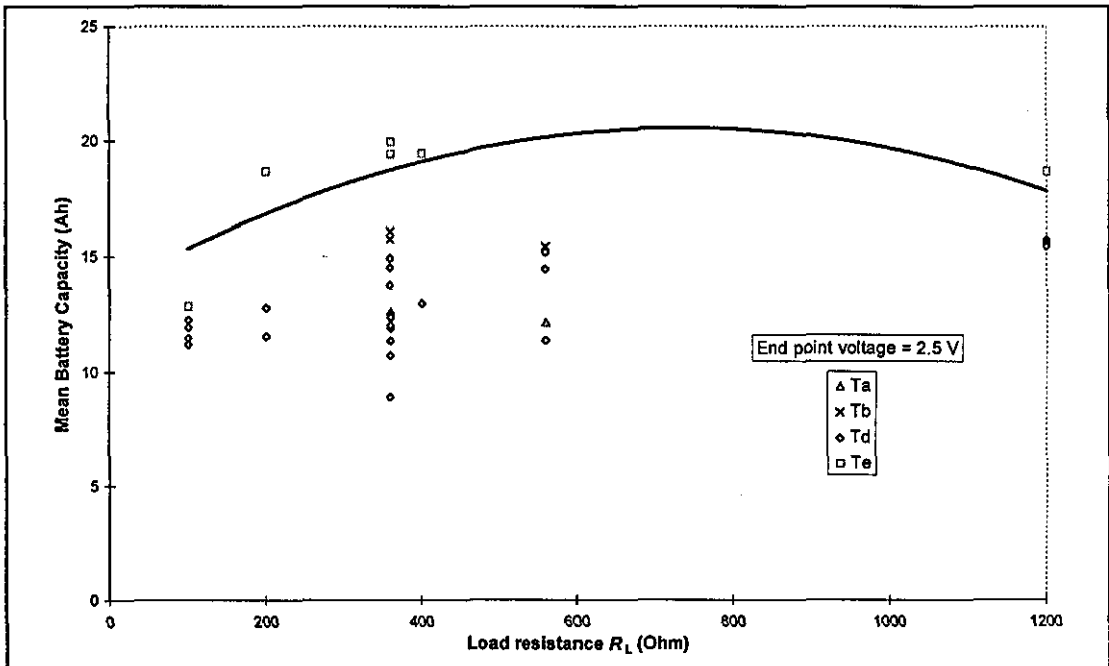


Figure 13.1 Mean capacity to 2.5 V, $\mu(Q_{2.5})$, versus load resistance R_L for the four candidate cells.

The mean capacity values to 2.5 V, $\mu(Q_{2.5})$, versus load resistance, R_L , for 37 tests carried out on the four battery types are plotted in Figure 13.1. Each point represents the mean of 10 individual batteries of a given battery type and test condition, and the data summarises a total of 370 battery discharges.

A second order regression line has been overlaid over the Te results (diamonds). This follows the classic curved profile of the capacity/load curve, with reductions in capacity at the low and high extremes of R_L , due to polarisation effects and self-

discharge respectively. The maximum occurs at approximately 500 Ω , where these effects are minimised. By contrast, the distributions of the Td cell results (squares) are complex, and do not lend themselves to regression analysis. Although the capacity trends at the low and high extremes of R_L conform to type, the wide dispersion of the 360 and 560 Ω data implies a very broad mix of both high capacity and prematurely failed cells.

The Ta results (crosses), lie close to the lowest $\mu(Q_{2.5})$ values for the 360 and 560 Ω Td cell results (diamonds), and also indicate a high proportion of premature failures. The Tb results (triangles), lie close to the highest $\mu(Q_{2.5})$ values for the 360 and 560 Ω Td cell results, in this case indicative of high coulombic efficiency.

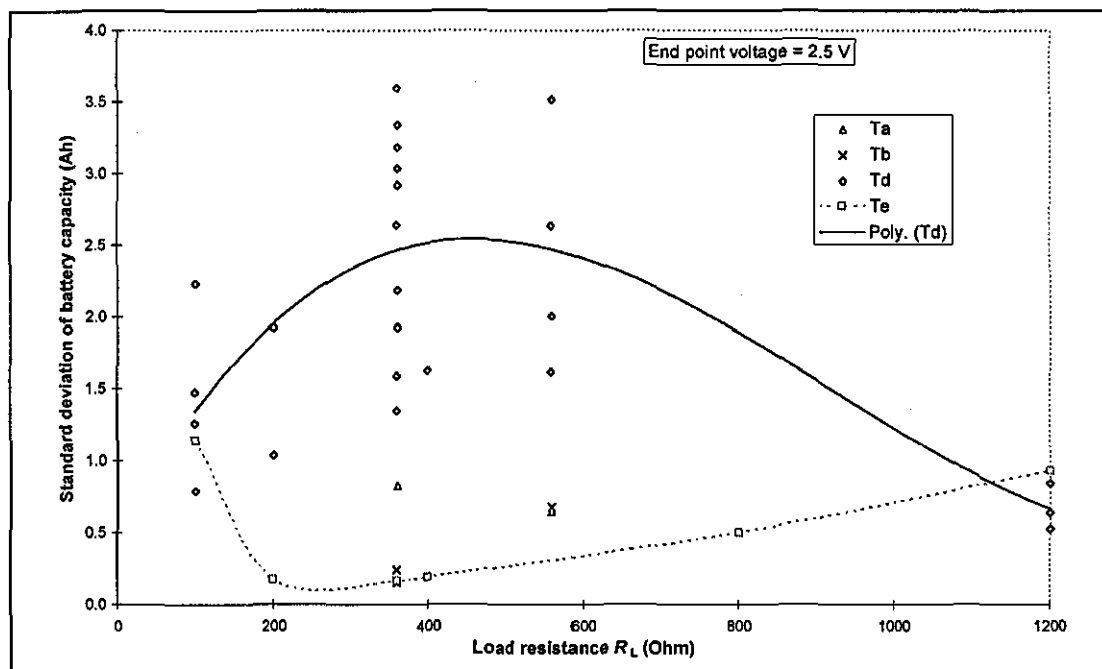


Figure 13.2 Standard deviation of capacity to 2.5 V, $\sigma(Q_{2.5})$, versus load resistance R_L for the four candidate cells.

The standard deviations of capacity to 2.5 V, $\sigma(Q_{2.5})$, versus load resistance R_L for the four candidate cells are given in Figure 13.2. A second order regression line has been fitted to the Td data. The trend-line for the Te data is simply a 'smoothed' curve linking the actual data points. The shape of the $\sigma(Q_{2.5})$ profile for cell type Te indicates that repeatability is maximised at R_L values of 360-560 Ω , and that the twin effects of polarisation and self-discharge increase the variability of the effective discharge capacity at the extreme values of R_L . The $\sigma(Q_{2.5})$ results for cell types Td and Te at values of R_L of 100 and 1200 Ω are similar, but the maximum in the regression line of the Td cell at 360-560 Ω emphasises the dominant effect of the

prematurely failed cells. The three $\sigma(Q_{2.5})$ values for cell type Tb lie close to those of cell type Te again, and those for Ta lie between the lowest of the Td values and the Te values.

The $Q_{2.5}$ graphs provide visual confirmation of the ranking order for both $\mu(Q_{2.5})$ and $\sigma(Q_{2.5})$ parameters for R_L of 360 Ω , and show that the premature failure problem exhibited by the Td type cell is restricted to a fairly narrow load range. Figure 13.1 shows that there is little difference between the $\mu(Q_{2.5})$ values of the Td and Te cells at the extremes of R_L of 100 and 1200 Ω . The value of $\mu(Q_{2.5})$ for the Te cell for R_L of 1200 Ω is ~ 3 Ah higher than the Td value, accurately reflecting their respective declared stoichiometric capacities. There is little difference in $\mu(Q_{2.5})$ values for the two cell types at R_L of 100 Ω .

13.3. Q_0 results

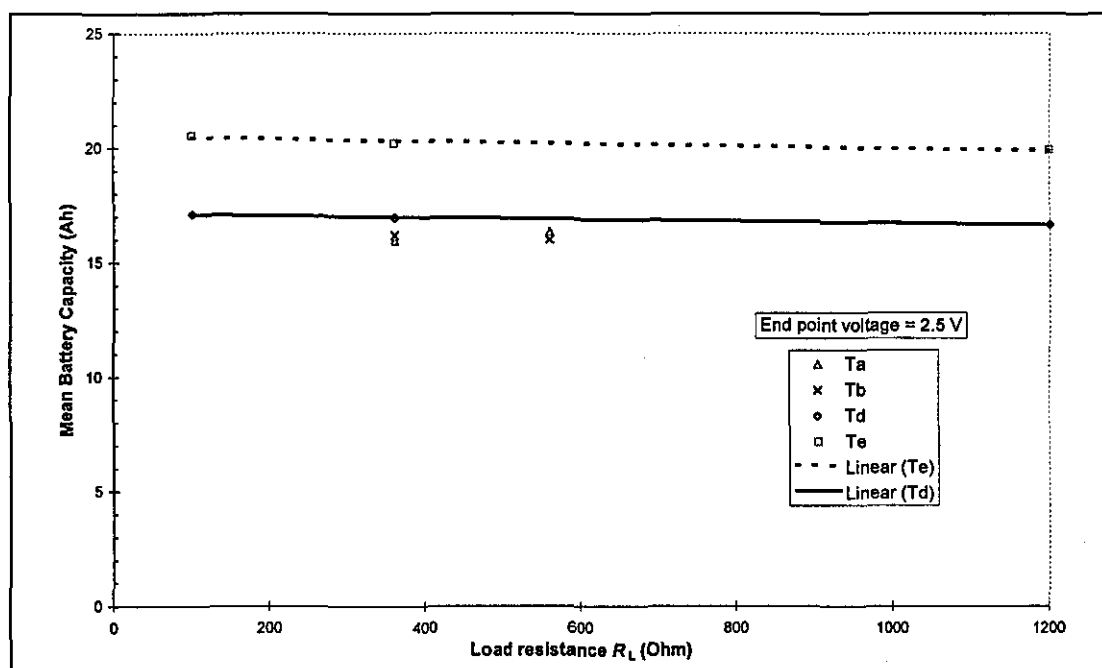


Figure 13.3 Mean capacity to 0 V, $\mu(Q_0)$, versus load resistance R_L for the four candidate cells.

The problem is to translate the complex dispersions of the accelerated discharge data into predictions of the long-term low-current discharge service life. The mean meter load impedance is approximately 35 k Ω , and the trend of increasing capacity and performance reliability as R_L increases through 1200 Ω is a reasonable indication that the performance of battery type Td in the meter should be free of the prominent polarisation effects observed at 360 and 560 Ω . Measuring capacity to 0 V, Q_0 , gives an unambiguous measure of the available electrical capacity of the cell, and as such a

reasonable approximation of the available capacity for the meter, providing that we take account of (a) self-discharge, and (b) that the meter capacity is measured to end point voltages of 3.2 and 2.5 V respectively.

Figure 13.3 plots the mean capacity to 0 V, $\mu(Q_0)$, versus load resistance R_L for the available data for the four candidate cells. The difference between the distributions of these and the $\mu(Q_{2.5})$ data is immediately evident. It may be seen that the $\mu(Q_0)$ values for the Ta, Tb and Td cell types all lie on essentially the same (horizontal) regression line, implying that the stoichiometric capacities of these battery types are similar, and that this test method gives reproducible results. The high degree of polarisation which limits capacity at R_L of 100 Ω , which is an evident feature of all of the $\mu(Q_{2.5})$ results, has disappeared. The regression lines slope slightly downwards with increasing value of R_L , suggesting an increasing effect of self-discharge with discharge duration.

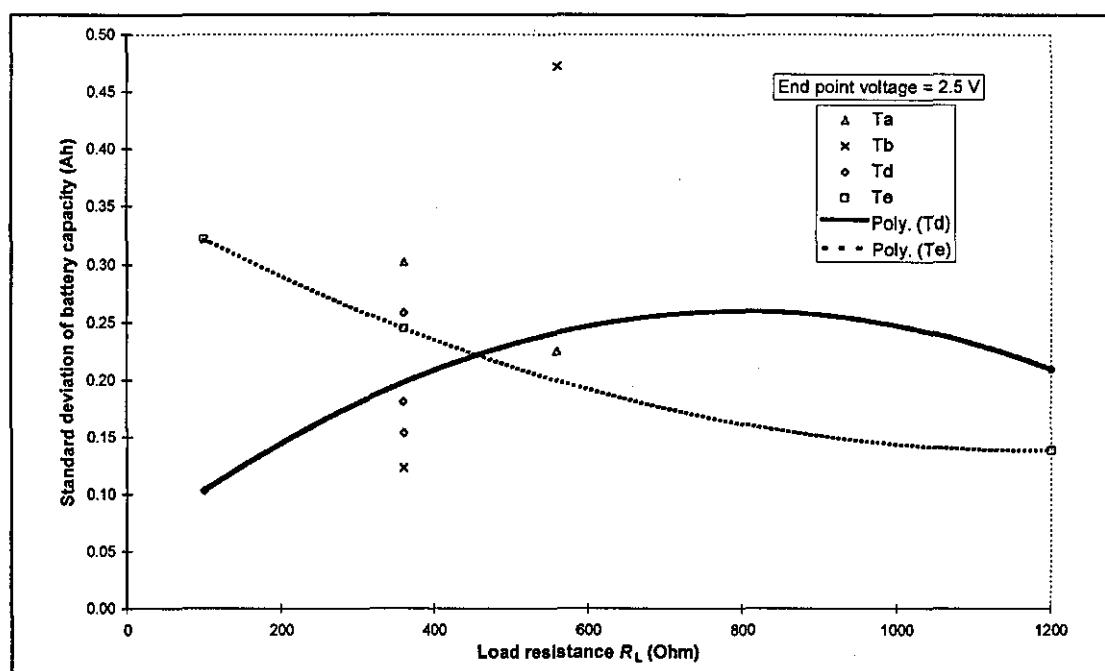


Figure 13.4 Standard deviation of capacity to 0 V, $\sigma(Q_0)$, versus load resistance R_L for the four candidate cells.

Figure 13.4 plots the standard deviation of capacity to 0 V, $\sigma(Q_0)$, versus load resistance R_L for the four candidate cells. Comparisons with the $\sigma(Q_{2.5})$ data given in Figure 13.3 reveals a very significant reduction in the dispersions of the data at all values of R_L (note that the maximum value of $\sigma(Q_0)$ is lower by almost an order of magnitude than that for the $\sigma(Q_{2.5})$ results, i.e. compare Figure 13.2 with Figure 13.4). Second order regression lines have been over-plotted to highlight the placement of the Td and Te data, but again are not to be taken as accurate predictors.

13.4. Implications for the meter application.

The analysis of the $Q_{2.5}$ results has identified a wide divergence between the discharge performance and available electrical capacity of different cell types at certain values of load resistance. It also illustrates that it is impossible to gain a reliable measure of electrical capacity from accelerated discharge tests when the conventional approach of using an end-point voltage in the range 1.5 to 2.5 V is employed. Nevertheless the $\mu(Q_{2.5})$ results provide useful information regarding the susceptibility of a given cell type to polarisation, whilst the $\sigma(Q_{2.5})$ values give data regarding the influence of production tolerances on the failure mode.

The Q_0 measurements provide repeatable information regarding the available amount of electrical energy under vanishingly small discharge currents. The $\sigma(Q_0)$ data gives information regarding the quality of control of the reactants and production tolerances under low load, and their eventual effect on service life. To use the $\mu(Q_0)$ data to estimate service life, it is useful to consider the effect of polarisation when operating under the pulsed meter load which averages to 100 μA .

Table 13.2 gives mean values of capacity to end point voltages of 2.5 and 0 V, $\mu(Q_0)$ and $\mu(Q_{2.5})$ respectively, together with the arithmetic difference, $[\mu(Q_0) - \mu(Q_{2.5})]$ which provides a measure of the effect of polarisation at the d.c. current of 3 mA, (load resistance of R_L of 1200 Ω). The differences are relatively low, 0.9 and 1.4 respectively for the Td and Te cells, which approximates to 6% of available capacity.

Table 13.2 Difference between the values of the $\mu(Q_0)$ and $\mu(Q_{2.5})$ parameter values at R_L of 1200 Ω .

Battery test code	R_L	$\mu(Q_0)$	$\mu(Q_{2.5})$	$\mu(Q_0) - \mu(Q_{2.5})$
	Ω	(Ah)	(Ah)	(Ah)
Td5	1200	16.64	15.71	0.93
Te2	1200	19.91	18.51	1.40

In practice, the effect of polarisation at the low discharge rate of 3 mA can be very small. Figure 13.5 and Figure 13.6 respectively show the end-of-life discharge patterns of a Td and Te cell discharged through a load resistance of R_L of 1200 Ω . In both cases cells which display extended end-of-life phases have been selected to represent reasonable 'worst case' examples. The Q_0 and $Q_{2.5}$ values are given in the text box for each chart, and the arithmetic differences between the values for the two parameters are 0.07 and 0.1 Ah respectively. These amounts of charge are small, and

amount to less than 1% of the Q_0 values. For the purpose of determining the meter battery service life it seems reasonable to discount the effects of polarisation.

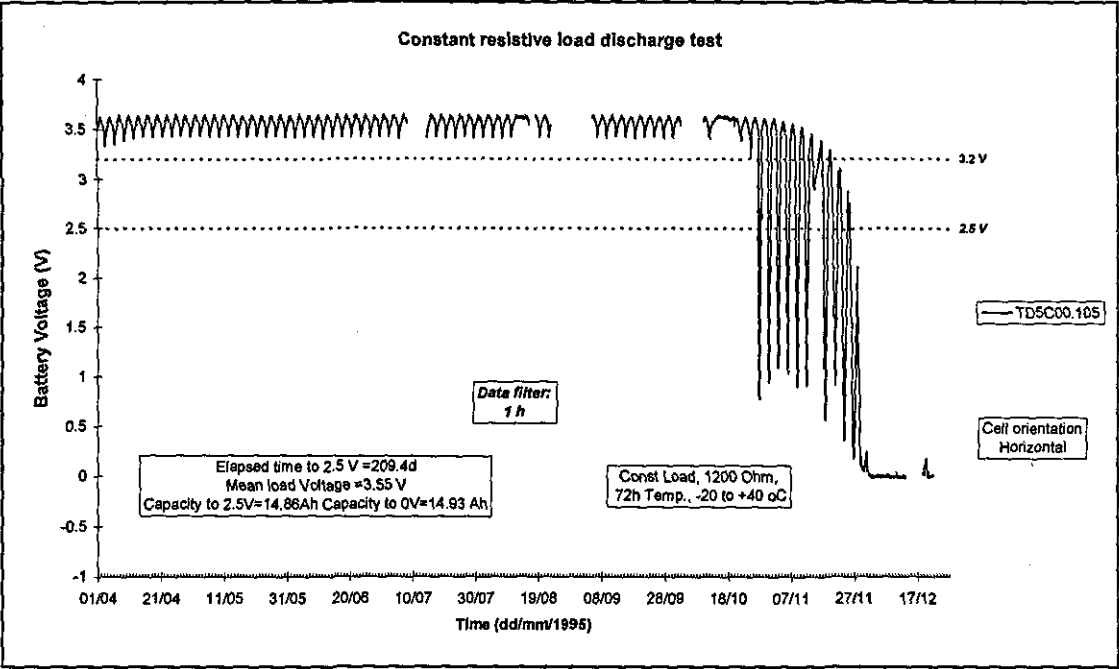


Figure 13.5 End-of-life discharge patterns of a ‘worst case’ Td cell discharged through a load resistance of R_L of 1200 Ω .

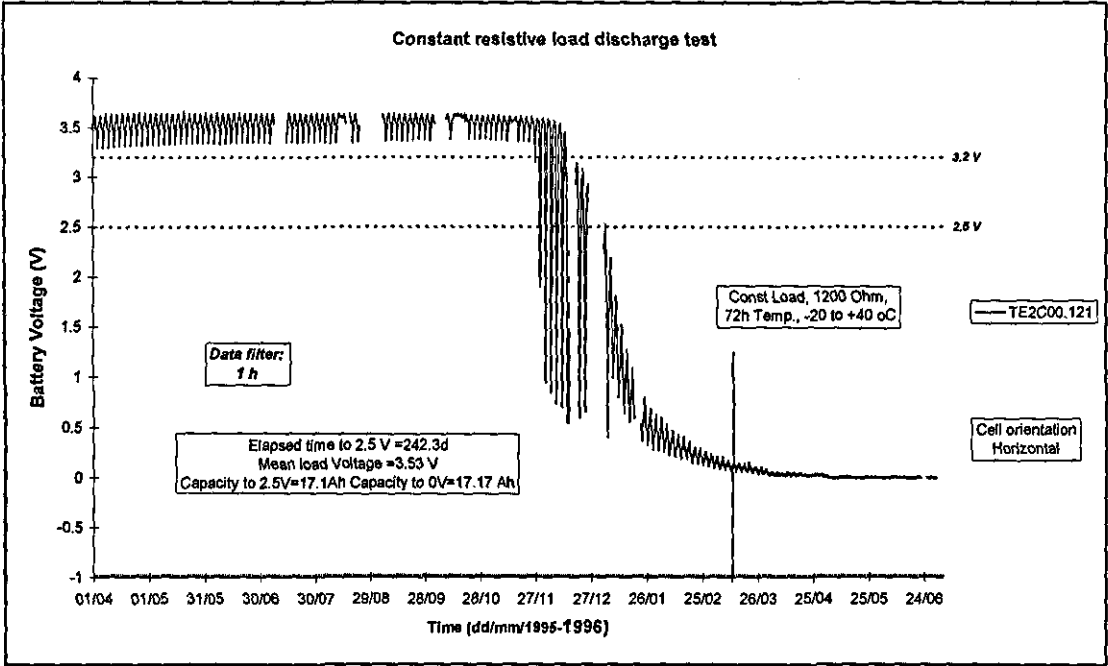


Figure 13.6 End-of-life discharge patterns of a ‘worst case’ Te cell discharged through a load resistance of R_L of 1200 Ω .

In fact, the mean impedance of the meter load is of the order of 35 k Ω , giving a mean pulsed load current of approximately 100 μ A, i.e. a factor of ten less than the 3 mA accelerated load. If we assume a negligible polarisation effect at this low load, then it

is reasonable to use the $\mu(Q_0)$ values of given in Table 13.2. This approach contains two provisos. Firstly, it is unclear whether the manufacturing variations implied in the premature failures exhibited by the Td battery type will have any effect during long-term discharge. Secondly, we do not have data on the voltage response to the transducer firing pulse, whose amplitude is between 10 and 20 mA. Such a high amplitude may induce enhanced polarisation and reduce cell capacity. We can introduce a safety factor to allow for these two provisos, by rounding down the $\mu(Q_0)$ values to 16.5 and 20 Ah for the Td and Te cell types. These are the values used in service life calculations in Section 15.5 and Section 15.8.

13.5. General comments on the experimental techniques

Laboratory based capacity and performance measurements conventionally utilise either a fixed end-point voltage in the range 0.5-3 V for Li/SOCl₂ cells^{2,3}, or as in the classical electrochemical research techniques, constant current or voltage. The strategy used here of discharging cells through a passive load resistance and allowing the load current to move in proportion to changes in cell impedance has proved to be a very useful and flexible method of determining maximum available electrical capacity and observing end-of-life behaviour under low discharge currents. The method does not appear to have been used on a systemic basis previously.

The systematic evaluation of battery discharge performance under the range of loads in a thermally cycling environment has generated a novel set of data. It has also identified and characterised a failure mechanism that does not appear to have been reported in detail previously. It is noteworthy that the 'saddle-back' failure mode would almost certainly take a different form and may possibly not be observed at all if the cell potential or the current was controlled at set levels. This is due to the fact that controlling the voltage or current at a constant level would almost certainly perturb the discharge profile from the form taken under passive load. It is also likely that the automatic safety shut-off conventionally employed in such a circuit design to enhance safety would actuate experimental shut-down as voltage reduces below a set lower threshold (to avoid the possibility of driving the cell into reverse and triggering an explosion). Such a device would occlude the observation of subsequent cell discharge behaviour.

The Td cell manufacturer routinely discharges samples of cells taken from each production lot at a relatively high rate (R_L of 100 Ω) in their 'qualification tests',

under a thermal cycle varying between -40 to +70 °C, creating dynamic conditions. This quality test does not appear to trigger premature failure. The present results would suggest that this is due to two of the features of the qualification test. First, the continuous and high rate of temperature change may act to continuously reactivate the cell. Secondly, the high discharge current will lead to normal cathodic polarisation, and an expected (lower) cell capacity of 10-12 Ah. The premature failure mode normally only starts to occur at around this capacity value and would thus be occluded by cathode failure.

Thus the discharge charts would appear to form a unique database of battery performance under relatively low rates and under a temperature cycle. It would appear that associated voltage dynamics have not been recorded at such a high time-base resolution and over the complete discharge process at medium load levels.

CHAPTER 14

SELF DISCHARGE MEASUREMENTS

Very little self-discharge data is available in the literature that can be applied to the present application, possibly because self-discharge measurement is costly in terms of equipment, resources and time. The approach taken here is to collect data from several sources and to build a model from a broad spread of data. Self discharge measurements were obtained from several sources: Sandia National Laboratories (SNL), the literature, the battery manufacturers, and estimates of self-discharge from the discharge tests. SNL were tasked to carry out microcalorimetric measurements on Te battery samples to a test specification supplied by the author. The specification called for tests over a range of pulse loads, and included pulse trains similar to those employed by the electronic meter. The battery manufacturers also supplied test results based on average drain rates designed to be similar to the meter. The aims here are as follows; (a) to determine whether the results from the different sources correlate with one another; (b) to determine whether the disparities between the Q_0 values recorded for the accelerated discharge test loads of R_L of 100, 360 and 1200 Ω can be explained in terms of self-discharge, and (c) to assess the implications for the application.

14.1. SNL tests

Table 14.1 SNL measurements of Te cell self-discharge microcalorimeter data

Test Code	Pulse On onsec s	Pulse Off offsec s	Duty cycle P	Pulse Amptde. I_p mA	Pulse Charge mC	Mean load I_L mA	Current density j $\mu\text{A}/\text{cm}^2$	Heat O/p Q_c mW	F ratio ϕ_F	S.D. Rate j_{SD} μA
(1)	(2)	(3)	(4)	(5)	(6)	(7)	(8)	(9)	(10)	(11)
1	0.005	2.000	0.002	8.020	0.040	0.020	0.444	0.158	0.323	0.301
2	2.000	0.000	1.000	0.100	0.200	0.100	2.222	0.230	0.621	0.842
3	0.030	2.000	0.015	8.120	0.244	0.120	2.667	0.158	0.741	0.691
4	0.200	2.000	0.091	8.800	1.760	0.800	17.778	0.300	0.910	1.600
5	0.500	2.000	0.200	8.000	4.000	1.600	35.556	0.490	0.925	2.667
6	1.000	1.000	0.500	5.480	5.480	2.740	60.889	0.750	0.932	4.140
7	1.000	1.000	0.500	8.400	8.400	4.200	93.333	1.150	0.932	6.347
8	1.000	0.500	0.667	8.250	8.250	5.500	122.222	1.440	0.935	7.944
9	2.000	0.000	1.000	8.000		8.000	177.778	2.400	0.926	13.156
bg2	0.060	2.000	0.029	8.068	0.484	0.235	5.222	0.220	0.801	1.039
bg1	0.013	2.000	0.006	13.477	0.175	0.087	1.934	0.180	0.646	0.685
bg1a	0.006	2.000	0.003	13.546	0.081	0.041	0.900	0.160	0.488	0.461
bg1b	0.003	2.000	0.001	13.410	0.040	0.020	0.446	0.162	0.319	0.304

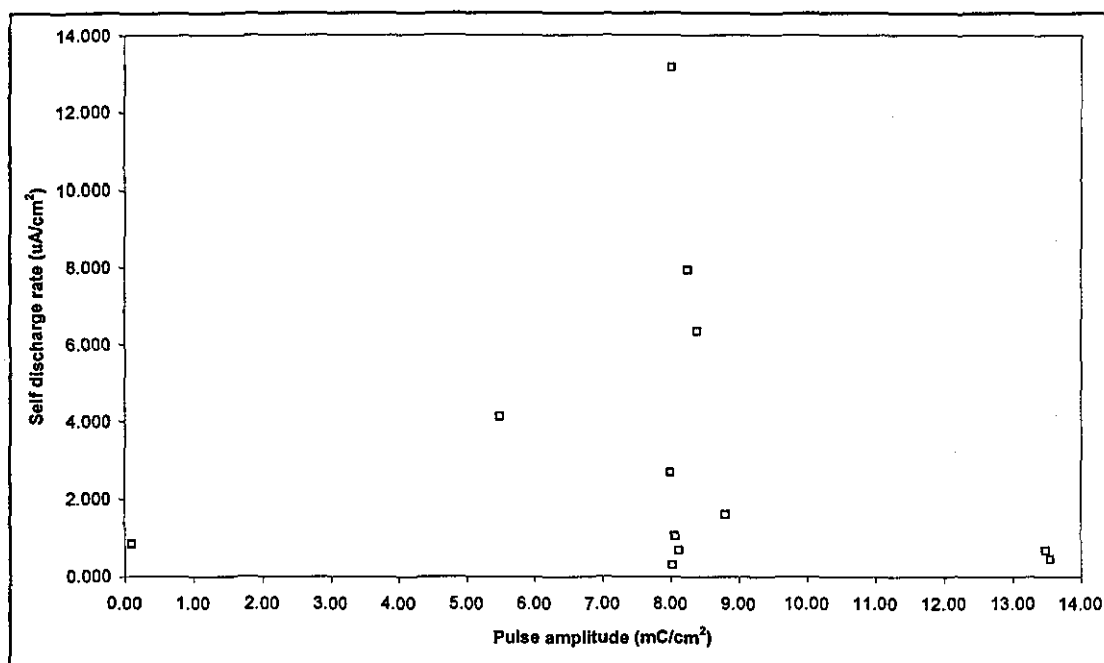


Figure 14.1 Self discharge rate versus pulse amplitude (SNL data).

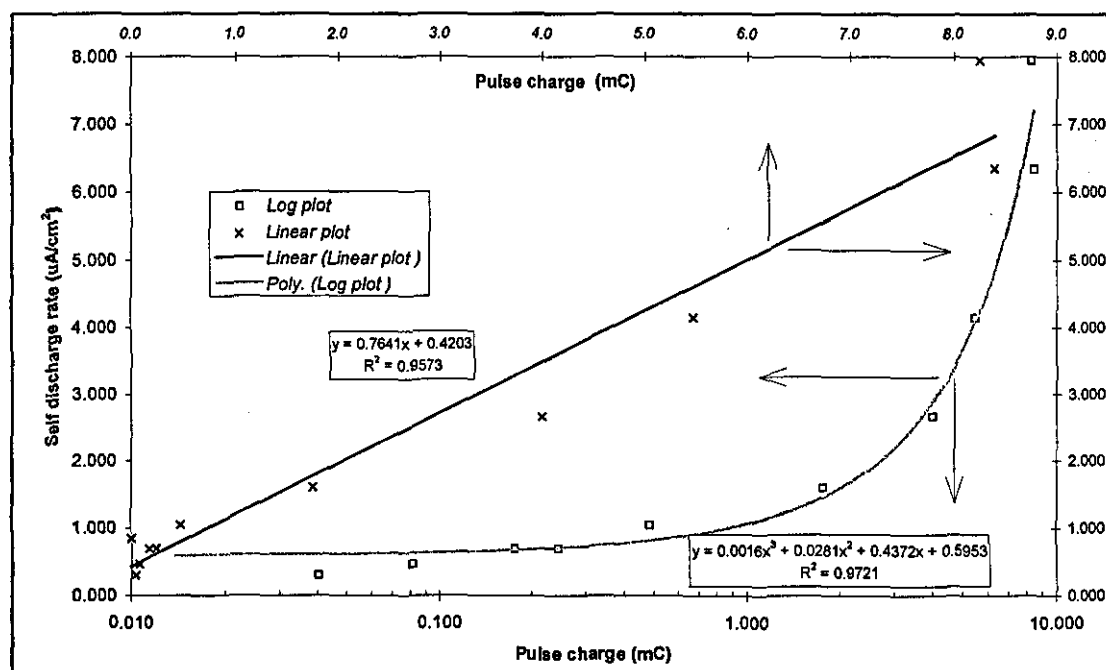


Figure 14.2 Self discharge rate versus pulse charge (SNL data). Logarithmic scale for pulse charge on the primary x-axis, linear pulse charge on the secondary axis.

The SNL tests were carried out using a microcalorimetric method that has been described in some detail by Hoier et al.^{1,2}. A 'D' size Te cell was used, and the measurements were conducted on a partially discharged cell (C90%) at 30 °C. The current density, pulse width and interval (onsec, offsec), charge, amplitude and duty cycle (P) parameters were varied in order to identify the pulse elements which influence self-discharge rates. The test conditions and results are given in Table 14.1.

The self-discharge measurements tests given in the bottom four rows of the Table relate to a battery supplying representative meter pulse trains, and are labelled bgxx.

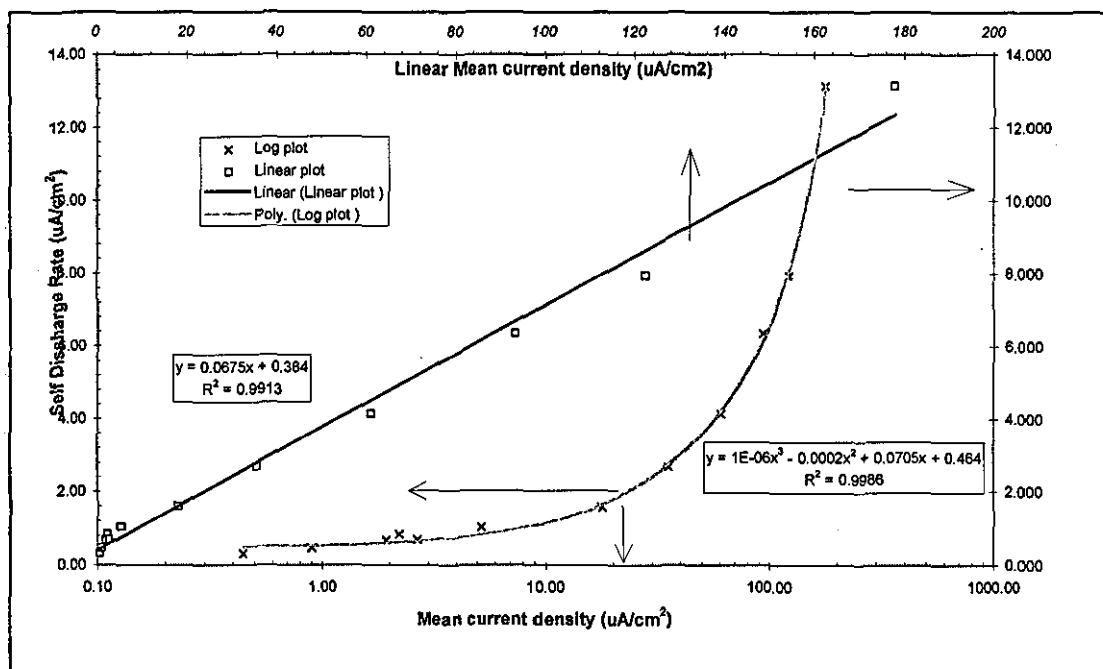


Figure 14.3 Self discharge rate versus mean current density, including all duty cycle types (SNL data). Logarithmic scale for current density on the primary x-axis, linear current density on the secondary axis.

For reference purposes, the measured self-discharge results are given in Columns (10) and (11) of the Table, and are expressed in terms of the F Ratio, Hoier's abbreviation for calculated Faradaic efficiency, ϵ_F , where³:

$$\epsilon_F = (Q_L)/(Q_L + Q_{SD}) \quad \text{Equation 14.1}$$

and self-discharge rate per unit surface area of the lithium electrode, j_{SD} , respectively, i.e. I_{SD}/A_a , where I_{SD} and A_a are the self-discharge rate and surface area of the anode, respectively. ϵ_F is a useful measure for designers who need to know the amount of capacity lost at a given discharge condition in order to determine the stoichiometric quantities of the reactants required for a specific service life. However, j_{SD} presents a direct measure of corrosion rate and is utilised in this analysis.

To detect correlations between self-discharge and the test variables, j_{SD} is plotted against different pulse parameters in Figure 14.1 to Figure 14.3, respectively: pulse amplitude, pulse charge, and mean current density.

Pulse amplitude is plotted against self-discharge in Figure 14.1; no correlation is evident.

Figure 14.2 and Figure 14.3 respectively plot self-discharge rate against the pulse charge and mean current density, the latter assuming a value of A_a of 45 cm². The

parameters are plotted against log (primary axes) and linear scales (secondary axes), together with least squares fit regression lines, and their equations and R^2 values, which are also given in Table 14.2. Curve fits were attempted with five types of analytic expression, namely: linear, logarithmic, polynomial, power, and exponential. The R^2 values provided unambiguous evidence that the best fits are given by linear and polynomial expressions. Visually, the linear plots offer better fits at discharge rates above about 0.1 C/cm^2 and $1 \mu\text{A/cm}^2$, whereas the polynomial plots offers a better correlation when the low discharge rates are included. The high R^2 values for both load parameters infer very good fits with the data, marginally favouring the polynomial model. This is probably due to the change in slope at a transition point located at approximately $0.01 \mu\text{A/cm}^2$, implying a changing relationship between j_{SD} and j .

Table 14.2 Regression parameters for correlations of charge and current density with self-discharge for SNL microcalorimeter results.

Parameter	Plot	R^2 value	Equation
Charge	Linear	0.9589	$y = 0.7682x + 0.3955$
	Polynomial	0.9727	$y = 0.0034x^3 + 0.0048x^2 + 0.5156x + 0.5595$
Current density	Linear	0.9913	$y = 0.0675x + 0.384$
	Polynomial	0.9988	$y = 1\text{E-}06x^3 - 0.0002x^2 + 0.0685x + 0.5014$

where $x = j$, and $y = j_{\text{SD}}$.

Of the two load parameters, the R^2 values are slightly lower for pulse charge, implying that self-discharge rate is more closely correlated with mean current density, although there is little difference between the two. Equation 14.2 given below provides a reasonable 'first approximation' model at discharge rates in this range should allow the simple interpolations where required.

$$j_{\text{SD}} = 0.0675j + 0.384 \mu\text{A/cm}^2 \text{ (provisional model)} \quad \text{Equation 14.2}$$

14.2. Results in the literature

A recent study by Hoier and Eisenmann¹ of SNL reviewed self-discharge data in the literature, and presented their own microcalorimetric measurements. Interestingly, only two external sources^{4,5} were found with data in a format suitable for analysis. The results were normalised and plotted as α_f against anode discharge current density with duty cycle, P , as parameter, where:

$$P = \text{onsec}/(\text{onsec} + \text{offsec}) \quad \text{Equation 14.3}$$

The effect of P is of particular concern in the long-life pulsed-mode applications such as the ultrasonic meter, where a pulsed technique is employed to minimise mean drain

rates.

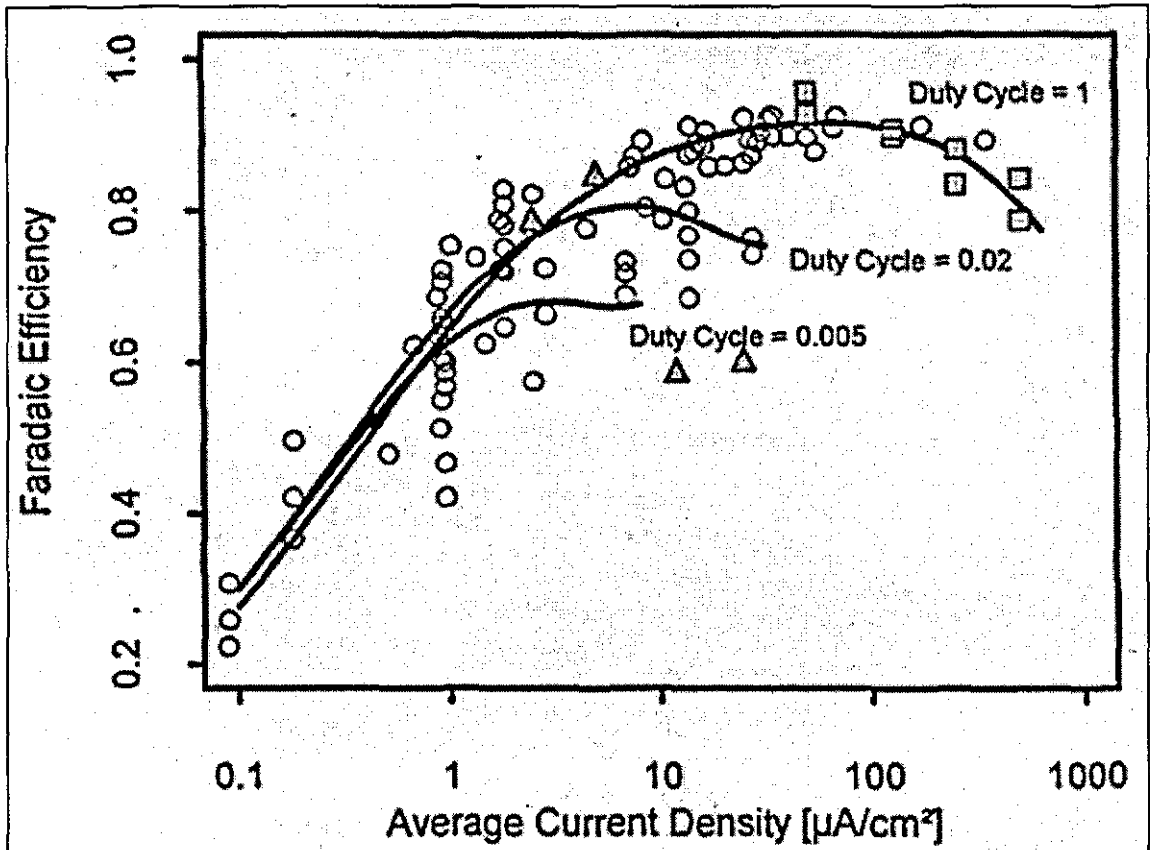


Figure 14.4 Eisenmann and Hoier's plot of Faradaic efficiency versus log mean current density, with duty cycle as parameter, data taken from published literature.

Hoier's graph plots ϵ_F against j and is reproduced in Figure 14.4. Eight data points come from Bro's paper⁴ (squares) and four from Takeuchi et al.⁵ (triangles). Three features stand out.

1. P has little effect at values of j below $\sim 1 \mu\text{A}/\text{cm}^2$.
2. Above $1 \mu\text{A}/\text{cm}^2$ the effect of P becomes evident and ϵ_F becomes inversely proportional to P . At a given value of j a reduction in P is counterbalanced by an increase in the magnitude of the pulse charge, this would be expected to increase j_{SD} by virtue of an increase in the rates of breakdown of the PL.
3. All of the curves show a peak, a feature which is in agreement with Yamin's empirical rule that the effect of current density on self-discharge is linear up to a threshold, when it becomes non-linear (see Section 7.12). The peak marks the threshold, and the same effect causes the changes of slope in transformed curves plotted in Figure 14.5.

From her analysis, Hoier concluded that ϵ_F ranged from 30 to 90%, and that its effect

is 'far more persuasive than previously acknowledged'. This conclusion is misleading: an ε_F of 0.5 applies to a cell discharged at a value of j of $0.9 \mu\text{A}/\text{cm}^2$, which equates to a discharge duration of about 28 years for a 'D' cell, which is well in excess of the manufacturers' claimed operating life. At the lowest current density of $0.089 \mu\text{A}/\text{cm}^2$ in the figure, the cell would take 567 years to discharge completely!

Using Equation 14.1 to transpose ε_F into units of j_{SD} , we can compare these results with the present measurements of self-discharge rate. Hoier's transformed data is plotted in Figure 14.5 as j_{SD} versus j with P as parameter. The data from Table 14.1 is also included. Correlation between the data sets is reasonably good, giving confidence in the Te cell results.

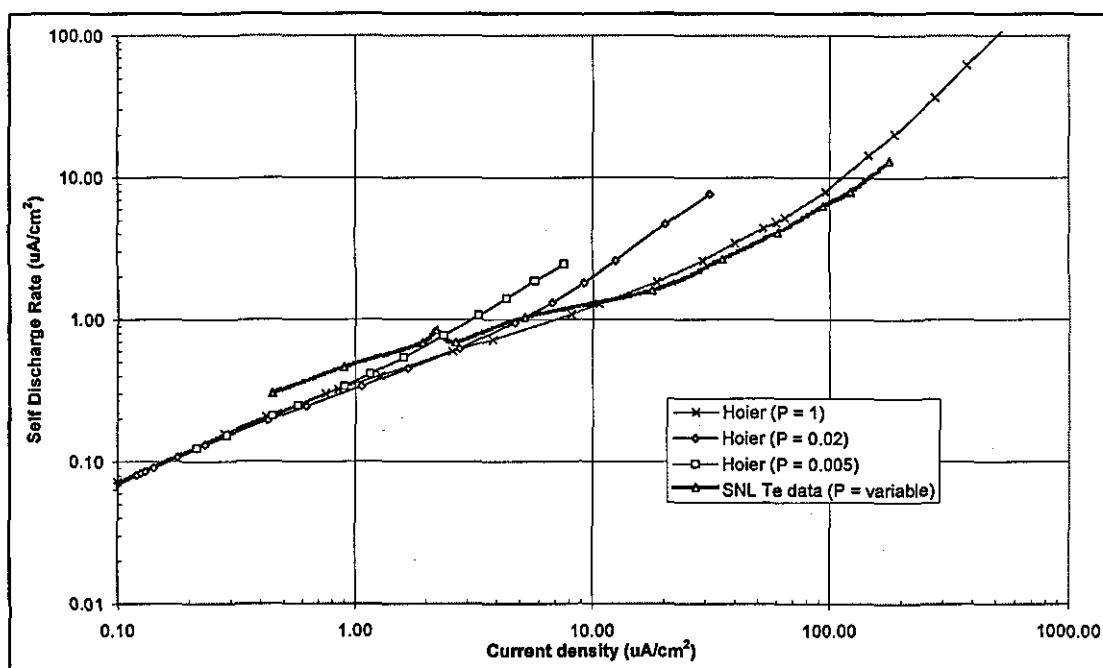


Figure 14.5 Figure 14.4 translated into a plot of log self-discharge versus log current density, with the data from Table 14.1 overlaid.

Each of the four curves appears to exhibit an inflection point, above which the gradient of $\Delta j_{SD}/\Delta j$ increases. The point shifts to the right with increasing value of P ; it occurs at $j \approx 1, 5, \text{ and } 80 \mu\text{A}/\text{cm}^2$ for $P = 0.005, 0.02, \text{ and } 1$ respectively. The Te curve flexes at approximately $20 \mu\text{A}/\text{cm}^2$.

It should be noted that P for the Te data is variable, but approaches a value of 1 at values of $j > 30 \mu\text{A}/\text{cm}$ which explains why this region of the curve lies close to Hoier's $P=1$ curve. $P \approx 0.01$ at values of $j < 3 \mu\text{A}/\text{cm}$, and the curve lies close to Hoier's $P=0.005$ curve.

14.3. Self-discharge measurements from the manufacturers

The manufacturers of candidate battery types Ta, Td and Te, also carried out self-discharge measurements. These are overlaid on Hoier's data in Figure 14.6, which plots j versus j_{SD} on logarithmic scales. The cell types are identified in the legend included in the graph.

The Te data derive from two tests: (a) actual measurements with the battery powering Meters A and B, and (b) a set of measurements carried out on ten cells discharging at a fixed d.c. current of $119\ \mu\text{A}$, midway between the mean drain rates employed by the two meters. For (a), close correlations with the data for P of 0.02 and 0.005 are evident (P for the pulsed meter load approximates to 0.005). For (b), the Te measurements lie on and below the $P=1$ curve in Figure 14.6. The 10 measurements of j_{SD} have a mean and standard deviation of 0.48 and $0.12\ \mu\text{A}/\text{cm}^2$ respectively, implying that a large dispersion may be expected even with a population of nominally identical cells discharged under the same stable conditions.

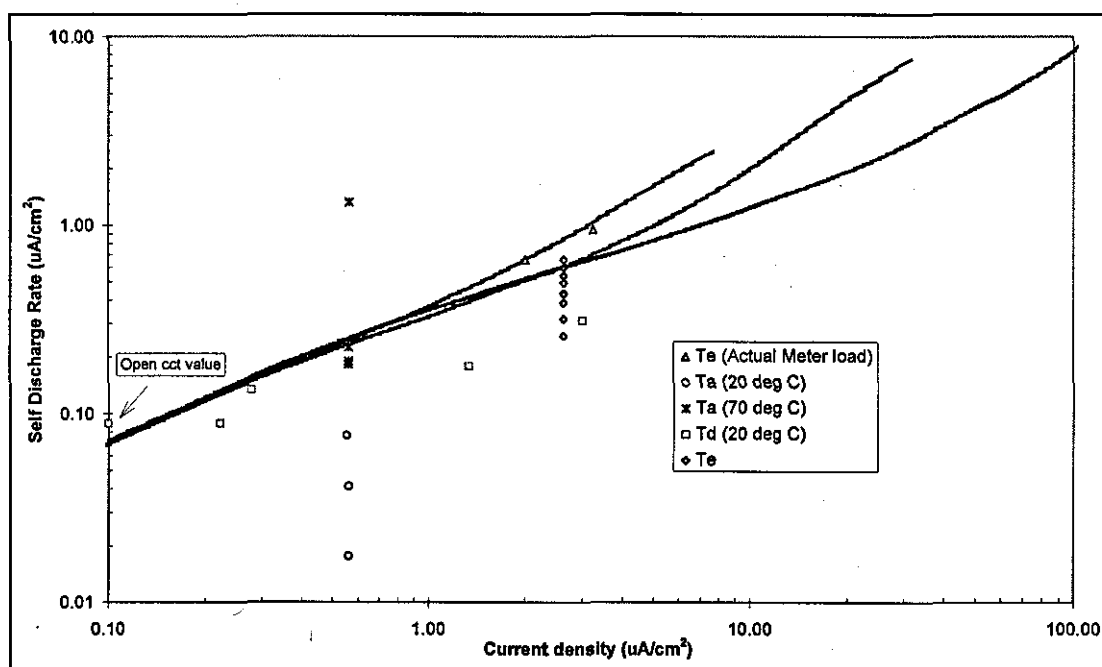


Figure 14.6 Self-discharge rate data from the battery manufacturers.

The Td results are based on measurements of the self-discharge of a single cell loaded incrementally with the various components of the meter load, namely: open-circuit, microprocessor sleep mode ($10\ \mu\text{A}$), on which pulses of 1, 20 and $50\ \text{mA}$ were superimposed, giving mean current densities of 0.22 , 0.28 , 1.33 and $3.00\ \mu\text{A}/\text{cm}^2$, respectively. The cell was stabilised at a temperature of $30\ ^\circ\text{C}$ over a six month period. The data points (squares) lie somewhat below the established trends; this may

be due to the decay in self-discharge rate that develops over a long period at equilibrium temperature and load.

The Ta results were not generated specifically for this study but have been included for comparison. They derive from two sets of cells discharged under a d.c. load of $0.55 \mu\text{A}/\text{cm}^2$ at 20 and 70 °C; 4 cells at each temperature. The 20 °C results are low by comparison with the Hoier's data; 3 of the 70 °C cells sit astride the curve, while one outlier lies an order of magnitude above the other members of the set at a value of j_{SD} in excess of $1 \mu\text{A}/\text{cm}^2$. In this instance it is thought that the passivation layer may have suffered damage, and that the high self-discharge rate is due to the onset of the repair phase.

14.4. Correlation of discharge-test capacity losses

The Q_0 values for the accelerated discharge tests showed a trend of decreasing magnitude for increasing discharge time, t , (increasing load resistance, R_L). The trend was consistent across the range of battery types, with the very minor exception of the Ta trend which was based on a relatively small number of samples. It is of interest to determine whether the Q_0/t trend can be correlated with self-discharge. There is no direct means of testing this hypothesis. However, by comparing measured capacity losses with those computed from theoretical principles we can determine whether a reasonable correlation is possible.

Table 14.3 Comparison of self discharge estimated from the discharge tests and calculated from the microcalorimeter generated self discharge model.

Test Code	Load res. R_L Ω	Mean cap. $\mu(Q_0)$ Ah	Cap. Diff Ah	Current density j $\mu\text{A}/\text{cm}^2$	Test Duration t d	SD rate j_{SD} $\mu\text{A}/\text{cm}^2$	SD rate I_{SD} μA	SD Cap loss Q_{SD} Ah	SD Cap loss diff. Ah
(1)	(2)	(3)	(4)	(5)	(6)	(7)	(8)	(9)	(10)
Te6	100	20.54	-	711.11	19.00	48.38	2177.28	0.99	-
Te4	360	20.21	0.33	209.88	83.00	14.55	654.78	1.30	0.31
Te2	1200	19.91	0.63	64.26	276.00	4.72	212.47	1.41	0.41
Td26	100	17.12	-	711.11	20	48.38	2177.28	1.05	-
Td10	360	16.99	0.12	203.70	80	14.13	636.03	1.22	0.18
Td5	1200	16.64	0.48	65.74	247	4.82	216.97	1.29	0.24

Table 14.3 presents the computed and calculated self-discharge capacity losses and test parameters for six accelerated discharge tests covering R_L values of 100, 360 and 1200 Ω , for Td and Te cells. The self-discharge rates were obtained from (a) calculated self-discharge capacity losses using Equation 14.2, and (b) losses derived

from the different Q_0 values recorded for the six tests. The relative effects of capacity loss were calculated by taking the arithmetic differences between the $\mu(Q_0)$ value for R_L of 100 Ω and those for 360 and 1200 Ω , which are given in Column (4).

The mean values of j for the three loads are given in (5), and Equation 14.2 is used to calculate j_{SD} for these loads (7). The self-discharge rates calculated for an anode of A_a of 45 cm² are given in (8). By taking account of the elapsed time for the discharge tests, (6), the cumulative capacity loss due to self-discharge, Q_{SD} , is calculated (9). Column (10) gives the Q_{SD} capacity losses for 360 and 1200 Ω tests relative to the 100 Ω value.

Comparison of the Q_{SD} and Q_0 losses for the given loads in Columns (4) and (10) shows a close match for both batteries, although the predicted capacity losses for the R_L of 1200 Ω tests are lower than achieved in the discharge tests. This is probably due to the fact that Equation 14.2 is being used to define values of j_{SD} in a zone well above the change in slope at $j = 80 \mu A/cm^2$, and would thus be expected to be subject to error.

The fact that these Q_0 ratios correlate with the calculated Q_{SD} ratios is significant and adds confidence to the utilisation of the Q_0 measurement as an indicator of the total available electrical capacity.

14.5. Self discharge model for the accelerated test range

The qualitative correlation between Q_0 and self discharge in the accelerated test range suggests that the present data can be used to modify Equation 14.2 to produce a model that can predict self-discharge rates for the accelerated tests. In principle, and providing polarisation effects are negligible, it is possible to calculate the capacity loss due to self-discharge, $^LQ_{SD}$, during a given accelerated discharge test from Equation 14.4:

$$^LQ_{SD} = Q_\theta - Q_0 - ^{OC}Q_{SD} \quad \text{Equation 14.4}$$

where $^{OC}Q_{SD}$ denotes the capacity losses during at open-circuit storage, Q_θ is the stoichiometric capacity, and Q_0 the measured discharge capacity to complete electrochemical exhaustion. In practice, (a) Q_θ is not known accurately (see Section 10.4), and (b) discharge is subject to inefficiency and Q_0 of a cell cannot be measured accurately. As Q_0 reflects capacity down to zero load current, polarisation effects will be negligible, and Q_P may be discounted here. In addition, $^LQ_{SD}$ is minimised for

short-term discharges, i.e. R_L of 100 Ω , and the value of Q_0 may be substituted as an approximation of Q_0 . Here this value is termed Q_{Ref} , and Equation 14.4 can be rewritten, as follows:

$$Q_{Ref} = {}^L Q_{SD} + {}^{OC} Q_{SD} + Q_L \quad \text{Equation 14.5}$$

Q_L is the electrical charge discharged across the load. This can be measured using the test rig. The self-discharge during open-circuit storage, ${}^{OC} Q_{SD}$, is the product $I_{SD} \times t_S$, where t_S is the duration of the storage period, and I_{SD} is given by Equation 14.6:

$$I_{SD} = j_{SD} \times A_a, \quad \text{Equation 14.6}$$

As found in Section 7.13, j_{SD} is sensitive to battery history, but for the purpose of this exercise, we assume the steady-state open-circuit value of $j_{SD} = 0.2 \mu A/cm^2$ derived in Section 7.12.

Table 14.4 Discharge test and calculated self-discharge parameters.

Test code	t_S	${}^{OC} Q_{SD}$	Q^0	R_L	\bar{V}_L	$\mu(Q_0)$	Q_{SD}	\bar{j}	t_L	I_{SD}	j_{SD}	${}^L Q_{SD}$	Cap loss
	d	Ah	Ah	Ohm	V	Ah	Ah	$\mu A/cm^2$	d	μA	$\mu A/cm^2$	Ah	Ah
1	2	3	4	5	6	7	8	9	10	11	12	13	14
Ta3	178	0.04	17.4	360	2.01	15.96	1.40	124.07	80	709	16.14	1.40	
Ta2	387	0.08	17.4	560	1.80	16.34	0.98	71.43	152	248	5.97	0.98	- 0.42
Tb1	178	0.17	17.6	360	3.44	16.20	1.23	65.82	72	672	4.90	1.23	
Tb2	207	0.20	17.6	560	3.37	16.00	1.40	41.52	117	485	3.44	1.40	0.16
Td26	140	0.03	17.5	100	1.53	17.12	0.35	339.19	41	332	7.99	0.35	
Td10	41	0.01	17.5	360	2.90	16.99	0.50	179.01	85	241	5.45	0.50	0.15
Td5	468	0.10	17.5	1200	2.45	16.64	0.76	45.37	250	112	2.81	0.76	0.41
Te6	962	0.21	21.1	100	1.50	20.54	0.35	333.33	50	141	6.56	0.35	
Te4	879	0.19	21.1	360	1.95	20.21	0.70	120.29	83	268	7.83	0.70	0.35
Te2	494	0.11	21.1	1200	2.61	19.91	1.08	48.31	276	149	3.64	1.08	0.73

The aim here is to develop a model that relates j to j_{SD} . However during discharge, the battery load current, I_L , and hence j 'floats' according to the battery voltage, and decreases through discharge (and at low temperature). For these calculations an averaged value of I_L is used, which is given by $\bar{I}_L = \bar{V}_L / R_L$, where \bar{V}_L is calculated by means of Equation 14.7.

$$\bar{V}_L = 1/n \sum_{i=0}^{i=n-1} V_i \quad \text{Equation 14.7}$$

Where n is the number of incremental voltage measurements, and V_i the voltage of the i^{th} measurement. The mean current density, \bar{j} , is then \bar{I}_L / A_a . For reference, Table 14.4 gives the values of the discharge test parameters and the worked values of the

test variables on which the calculated values of j and j_{SD} are based. The analysis is summarised in Figure 14.7, which plots j_{SD} against j .

Except for one outlier, the values of j_{SD} for the different tests form a reasonably consistent trend with j . The outlier is associated with test Ta3, a 360 Ω discharge; no explanation for the divergence of the point from the other data sets is available other than either (a) the standard deviation $\sigma(Q_0)$ of 0.3 Ah for the 10 cells is relatively large suggesting that the cells in this test batch are not very representative of the normal population, or (b) quality control of the amounts of reactants is variable, or that (c) one of the reactants has become electrochemically isolated during discharge.

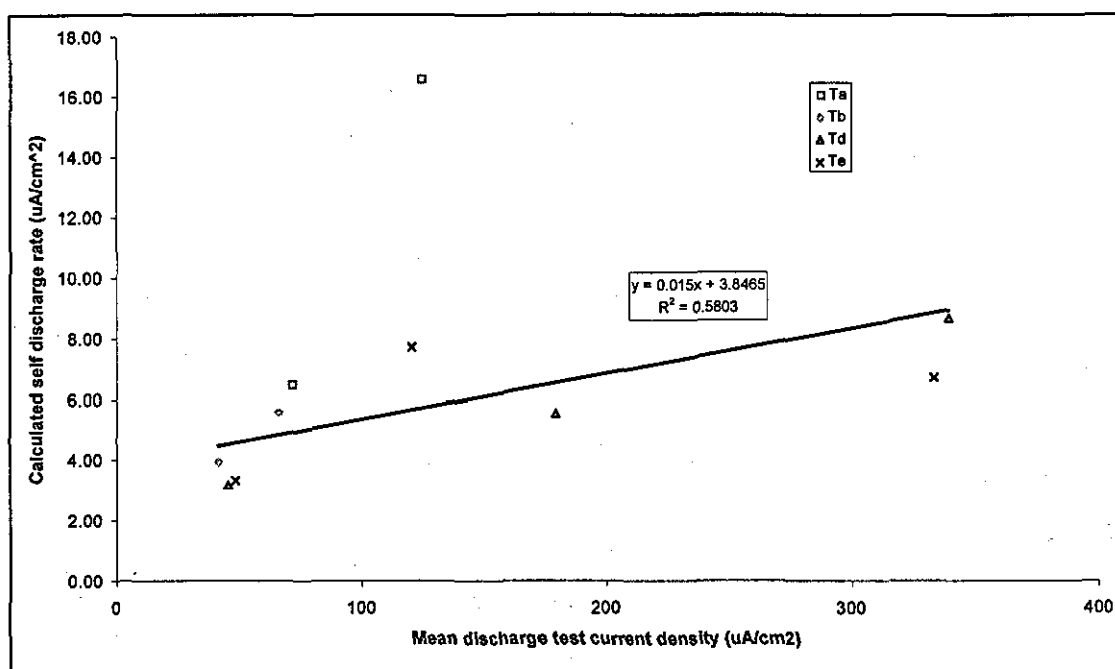


Figure 14.7 Self discharge rate versus mean discharge test current density for candidate Li/SOCl₂ 'D' Cells (calculations based on $(Q_0 - Q_0)$ data from the laboratory discharge tests).

The linear regression line and equation in Figure 14.7 ignores the outlier. The R^2 value of 0.97 indicates a reasonable fit, and the relationship between j and j_{SD} at current densities in the range above approximately 40 $\mu A/cm^2$ is given by Equation 14.8.

$$j_{SD} = 0.015j + 3.8465 \mu A/cm^2 \quad (\text{Accelerated discharge rates}) \quad \text{Equation 14.8}$$

14.6. Battery manufacturers' self-discharge data

To provide a visual comparison of the self-discharge data from the different sources, Figure 14.8 combines the manufacturers' self-discharge results with thresholds of

practical interest, as indicated in the text boxes. The $P=0.005$ and $P=1$ regression lines have been superimposed on Hoier's data.

The horizontal dashed lines are for reference. They indicate self-discharge rates which would lead to losses of 2 and 3 Ah over the required meter battery service life duration of 11.5 y ($j_{SD} = 0.44$ and $0.66 \mu A/cm^2$ respectively). The left hand vertical dashed line represents the maximum load quoted in the literature at which the impedance of the passivation layer remains unchanged; this line also represents the drain rate of Meter type A. The right hand dashed line represents the maximum meter drain rate of $3.22 \mu A/cm^2$.

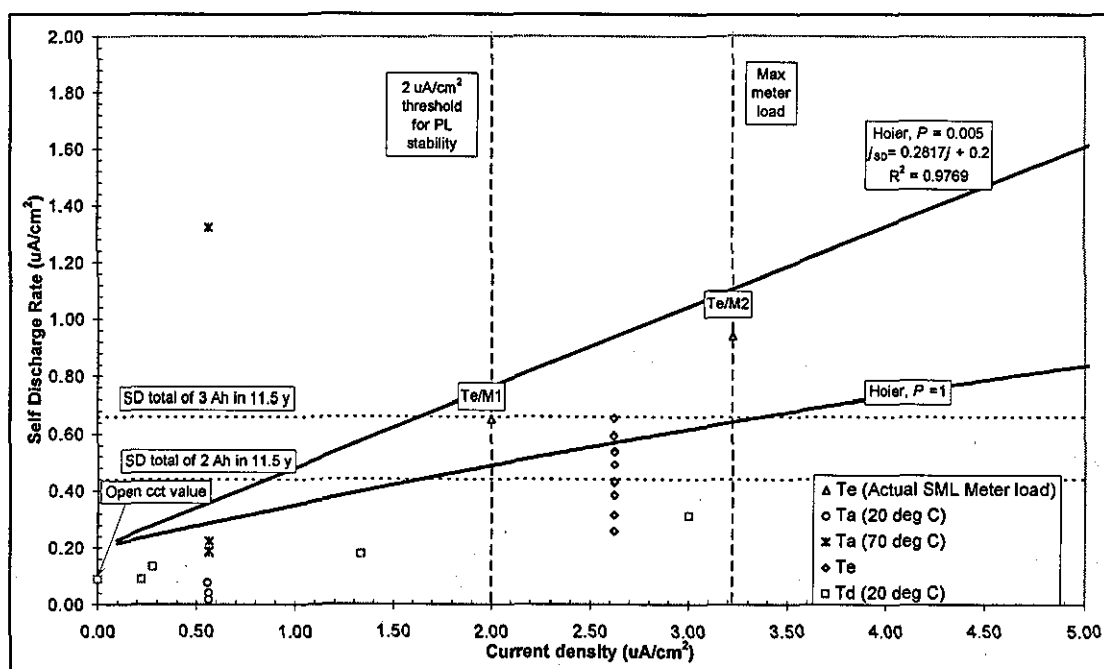


Figure 14.8 Graph of manufacturer's self-discharge measurements with operating thresholds overlaid.

The zone of principal interest lies between the two vertical meter load indication lines. The text boxes Te/M1 and Te/M2 indicate the self-discharge rates of 0.66 and $0.9 \mu A/cm^2$ respectively recorded for Te cells discharging through the two meters; the two results lie close to Hoier's $P=0.005$ line. Other results in the zone include the batch of Te cells discharged under a d.c. load, and a Td measurement, which both lie astride the $P=1$ line. Measurements at current densities lower than the zone of interest here are included in the figure, and a Ta cell outlier of j_{SD} of $1.3 \mu A/cm^2$ supports the theory that self-discharge rate can vary significantly. Further support is given by the set of 10 Te data points, which represent nominally identical cells and measurement conditions whose normalised standard deviation lies at a value of 25% of the mean.

The results suggest that (a) the $P=0.005$ line is a reasonable predictor of self discharge in the meters, and (b) self-discharge will account for a capacity loss of ≥ 3 Ah or more during an 11.5 y discharge at ultrasonic meter drain rates. The results from the different sources are in general agreement, although it is important to note that the range for a given value of j can span an order of magnitude.

14.7. Implications for the meter application

The timing parameters of the pulse train employed in the electronic meters are approximately 5 ms on, and 2000 ms off, a value of P of approximately 0.0025, close to the $P=0.005$ regression line given in Figure 14.9, and represented by Equation 14.9

$$j_{SD} = 0.2817j + 0.2 \mu\text{A}/\text{cm}^2 \quad (P=0.005) \quad \text{Equation 14.9}$$

The results of the range of self-discharge rate measurements made in the current density zone employed by the meters and given in Figure 14.8 imply that this equation should give a reasonable prediction of self-discharge losses associated with the operation of the electronic meter. (As such, it is used to estimate the self-discharge losses associated with meter loads in Section 15.7 of the next Chapter 15). It is important to note that the value of $0.2 \mu\text{A}/\text{cm}^2$, represents the y-axis intercept value i.e. the open-circuit self-discharge current, and is the mean of the values found in the literature as described in Section 7.12. The value is dependent on the elapsed time since the PL was formed or disrupted and can clearly vary. However, it would appear to represent a reasonable indicator, and is used as the open-circuit value for the purpose of the calculations carried out in Chapter 15.

The mean drain of the meters is $\sim 2 \mu\text{A}/\text{cm}^2$. From Equation 14.9 the associated self-discharge rate would work out to $34 \mu\text{A}$ for the Ta, Td and Te cells having a value of A_a of 45 cm^2 , and $110 \mu\text{A}$ for the Tb of A_a of 145 cm^2 . On open-circuit where $j = 0$, j_{SD} is $0.2 \mu\text{A}/\text{cm}^2$, equivalent to $9 \mu\text{A}$ for the Ta, Td and Te cells, and $29 \mu\text{A}$ for the Tb cell. The equation predicts a self-discharge rate of $37 \mu\text{A}$ for a mean meter drain rate of $100 \mu\text{A}$, which approximates to nearly 30% of the electrical discharge rate.

The data given above show that the self-discharge for a given battery design can span a range of up to an order of magnitude even under a controlled stable laboratory condition. This value would be expected to vary more widely under field operating conditions. Thus, the regression line must be treated as a best estimate. Clearly, the implied wide dispersions of self-discharge rate in service would have a very

significant impact on the meter/battery life distributions, and care must be taken in estimating such capacity losses.

The self-discharge losses calculated in Section 14.4 from the accelerated test Q_0 results include the integrated effects of battery discharge over a period of some months and under the representative thermal cycle. In principle, this approach offers a useful alternative to the microcalorimetric method, which suffers by contrast in that it provides a 'snapshot' measurement of self-discharge at a single temperature, load condition and depth of discharge.

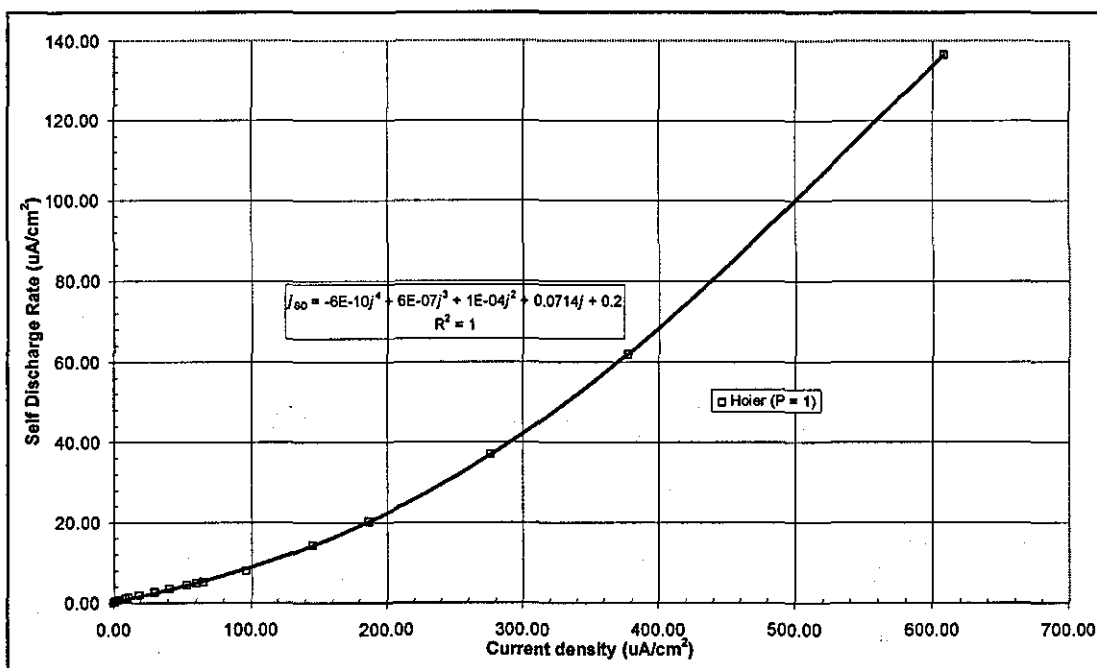


Figure 14.9 Hoier's $P=1$ data plotted on linear scales to show the trend.

Finally, Figure 14.9 plots Hoier's data for $P=1$ on linear scales of j versus j_{SD} . The trend shows reasonable agreement with Yamin's hypothesis of a non-linear increase in self-discharge rate as the discharge current density increases beyond a certain threshold, in this case a value of j of about $100 \mu\text{A}/\text{cm}^2$. Below the threshold, the curve is approximately linear.

CHAPTER 15

OPERATIONAL CAPACITY LOSSES OF THE METER BATTERY

The regular monitoring of batteries in service provides real-time capacity usage rates on which to base service life predictions, and information regarding any 'unforeseen' operational variables. To this end, 5000 of each of the two types of the first installed populations of production meters were selected for observation as part of an ongoing national Monitoring Exercise.

Meter Types A and B are fitted with battery types Td and Te respectively. Random samples of 28 and 30 of these meter/battery units were removed from the field in 1996 after periods of up to 800 days in service as the first stage of this exercise. Because of the major restructuring within BG at the time, it proved difficult to implement the monitoring exercise and the number of meter and battery samples tested fell short of the original plan. The two main aims of the measurements reported here are: (a) to determine the rate of capacity utilisation for a battery in normal operation, and (b) to test the goodness of fit of operational data with the laboratory based models derived in earlier Chapters.

15.1. Operational capacity loss measurement principles

The following nomenclature is used in this Chapter to qualify the capacity loss, Q :

1. The lower case letters m, c and p, identify the battery discharge type: meter, control and predicted, i.e. Q_m , Q_c and Q_p .
2. The superscripts M, OC and 360 are used in this section to denote the relevant electrical load, i.e. meter load, open-circuit and 360 Ω .
3. The subscripts indicate the capacity loss process, i.e. DEP, L, R and SD respectively denote depassivation, electrical discharge, residual capacity measurement and self-discharge processes, and Σ denotes the combination of the electrical and self-discharge processes during discharge.

We wish to determine the mean rate of capacity loss of the meter batteries dQ_m/dt_m in normal operation in order to predict service life. We let:

$$dQ_m/dt_m = ({}^M Q_{m\Sigma})/(tm_{OP}) \quad \text{Equation 15.1}$$

where tm_{OP} is defined as the period of battery operation powering the meter, and ${}^M Q_{m\Sigma}$ represents the combined losses due to powering the meter and associated self discharge during meter operation:

$${}^M Q_{m\Sigma} = {}^M Q_{mL} + {}^M Q_{mSD} \quad \text{Equation 15.2}$$

t_{mOP} is known from the battery history records, and the first task is to find a means to determine ${}^M Q_{m\Sigma}$.

After a given period of service, the cumulative battery capacity loss, Q_{mTotal} , due to the sum of ${}^M Q_{m\Sigma}$, and other processes occurring outside the service period, Q_{mOther} , is given by:

$$Q_{mTotal} = {}^M Q_{m\Sigma} + {}^M Q_{mOther} \quad \text{Equation 15.3}$$

and

$${}^M Q_{m\Sigma} = Q_{mTotal} - {}^M Q_{mOther} \quad \text{Equation 15.4}$$

Providing the stoichiometric capacity of the battery type, Q_0 , is known, ${}^M Q_{mTotal}$ may be ascertained by calculating the difference between Q_0 and the residual capacity of the battery, Q_{mR} , i.e.:

$$Q_{mTotal} = Q_0 - Q_{mR} \quad \text{Equation 15.5}$$

In principle, Q_{mR} may be measured quite quickly in the laboratory by means of an accelerated discharge through a resistive load. Conventionally, Q_{mR} is measured to a finite end-point voltage, often 2 V. However, as discussed in Section 13.2, such an end-point can lead to error, and here the capacity across a load of R_L of 360 Ω to electrochemical exhaustion is utilised, as described in Section 15.2, below.

This capacity is defined as ${}^{360}Q_{mL}$ and is equivalent to Q_{mR} . However, as shown in the previous Section 14.3, a significant capacity loss due to self-discharge occurs during a 360 Ω discharge, ${}^{360}Q_{mSD}$. Thus the total capacity dissipated during the accelerated discharge, ${}^{360}Q_{m\Sigma}$, actually comprises two parts, as described in Equation 15.6:

$${}^{360}Q_{m\Sigma} = [{}^{360}Q_{mL} + {}^{360}Q_{mSD}] \quad \text{Equation 15.6}$$

Equation 15.5 expands to become:

$$Q_{mTotal} = Q_0 - [{}^{360}Q_{mL} + {}^{360}Q_{mSD}] \quad \text{Equation 15.7}$$

Unfortunately, as determined in Section 10.4, the declared value of Q_0 may be subject to error, and a substitute parameter whose accuracy is known with reasonable confidence is required. This may be achieved by measuring the Q_0 capacity of a control group of representative fresh cells whose discharge history is known with accuracy. This quantity can be substituted for Q_0 , and here it is defined as Q_{Ref} , i.e.

$$Q_0 = Q_{Ref} \quad \text{Equation 15.8}$$

where:

$$Q_{\text{Ref}} = {}^{360}Q_{\text{C}\Sigma} + Q_{\text{COther}} \quad \text{Equation 15.9}$$

and:

$${}^{360}Q_{\text{C}\Sigma} = [{}^{360}Q_{\text{CL}} + {}^{360}Q_{\text{CSD}}] \quad \text{Equation 15.10}$$

then:

$$Q_{\text{Ref}} = [{}^{360}Q_{\text{CL}} + {}^{360}Q_{\text{CSD}}] + Q_{\text{COther}} \quad \text{Equation 15.11}$$

We can now substitute measurable or known parameters in Equation 15.4 to obtain a value of ${}^M Q_{\text{m}\Sigma}$:

$${}^M Q_{\text{m}\Sigma} = [{}^{360}Q_{\text{CL}} + {}^{360}Q_{\text{CSD}} + Q_{\text{COther}}] - [{}^{360}Q_{\text{mL}} + {}^{360}Q_{\text{mSD}} + Q_{\text{mOther}}] \quad \text{Equation 15.12}$$

It is not possible to measure ${}^{360}Q_{\text{CSD}}$ and ${}^{360}Q_{\text{mSD}}$ directly, however both are relatively small, and similar in magnitude, i.e. ${}^{360}Q_{\text{CSD}} \approx {}^{360}Q_{\text{mSD}}$, due to the fact that the 360 Ω discharge periods for both the meter and control cells are similar (as yet the service durations are relatively short and little capacity has been removed from the meter batteries). Thus, the error implied in the equivalence is not significant, and the two factors cancel one another out, leading to Equation 15.13.

$${}^M Q_{\text{m}\Sigma} = [{}^{360}Q_{\text{CL}} + Q_{\text{COther}}] - [{}^{360}Q_{\text{mL}} + Q_{\text{mOther}}] \quad \text{Equation 15.13}$$

The batteries in the control groups are fresh, and here Q_{COther} is simply the self-discharge on storage:

$$Q_{\text{COther}} = {}^{\text{OC}}Q_{\text{CSD}} \quad \text{Equation 15.14}$$

${}^{\text{OC}}Q_{\text{CSD}}$ is the product of the off-load self discharge rate, ${}^{\text{OC}}I_{\text{SD}}$, for that type of battery, and the duration of the open-circuit storage period, t_{mSt} , as shown in Equation 15.15:

$${}^{\text{OC}}Q_{\text{CSD}} = {}^{\text{OC}}I_{\text{SD}} \times t_{\text{CSt}} \quad \text{Equation 15.15}$$

t_{CSt} is known from the battery history records, and a value of ${}^{\text{OC}}I_{\text{SD}}$ of 17 μA was deduced in Section 14.7.

Q_{mOther} comprises a number of factors:

$$Q_{\text{mOther}} = [{}^{\text{OC}}Q_{\text{mSD}} + Q_{\text{mDEP}} + Q_{\text{mREAD}}] \quad \text{Equation 15.16}$$

${}^{\text{OC}}Q_{\text{mSD}}$ may be calculated using Equation 15.15. Q_{mDEP} arises because the Te battery installed in Meter A is also subjected to the following depassivation process prior to installation in the meter, (76 Ω for 20 m, 1 k Ω for 1 h following which the battery is continuously discharged through a 22 k Ω 'Keeper' resistance pending installation), which adds a further capacity loss, Q_{mDEP} , a magnitude of 0.04 Ah assuming 1 week on the keeper. $Q_{\text{mDEP}} = 0$ for battery type Td. Q_{mREAD} is the

capacity lost due to the downloading of meter data through the optical port that was carried out prior to the meter being removed from the field (in order to provide performance records for the Monitoring Exercise). Although it is very small, $\sim 1 \mu\text{Ah}$, it is included in the analysis for completeness.

The duration of the period of battery discharge through the meter, t_{mOP} , may be derived from meter manufacturers' and BG records. $^M Q_{\text{m}\Sigma}$ may be calculated by solving Equation 15.13, and the capacity loss rate dQ_m/dt_m may be determined.

15.2. Meter and control battery capacity measurements

The $^{360}Q_{\text{mL}}$ and $^{360}Q_{\text{cL}}$ battery capacity measurements were carried out in the laboratory using the discharge test rig. The control groups of batteries and the sampled meter batteries were mounted in a vertical orientation at room temperature in a purpose-designed test cabinet and discharged through 360Ω to a zero volt cut-off. The Q_0 parameters were computed as described in Section 8.7.

15.3. Control cells - capacity measurements

The control groups of batteries comprised two sets each of 10 'fresh' Td and Te cells, nominally identical to those used in the meters, but from different manufacturing lots. These were discharged through a resistor of R_L of 360Ω concurrently with the sampled meter cells, and under the same discharge conditions. The history and measured capacity parameters of the control sets of cells are given in Table 15.1.

Table 15.1 Td and Te 'control' battery history and capacity parameters.

Cell Test Code	Load Res. R_L Ω	Storage Time t_{cSt} d	SD rate on store I_{SD} μA	Total SD on store $^{OC}Q_{\text{cSD}}$ Ah	Mean Cap. $\mu(^{360}Q_0)$ Ah	Max. Cap. $^{max}Q_0$ Ah	Min. Cap. $^{min}Q_0$ Ah	Std. Devn. $\sigma(Q_0)$ Ah	Total cap. (6+7) Q_{Ref} Ah
(1)	(3)	(4)	(5)	(6)	(7)	(8)	(9)	(10)	(11)
Td17	360	853	0.9	0.18	16.96	17.23	16.37	0.26	17.14
Te4	360	879	0.9	0.19	20.21	20.61	19.84	0.24	20.40

In the case of battery type Td, the spread of Q_0 results covers a range 16.96 to 17.23 Ah, and the standard deviation, $\sigma(Q_0)$, is 0.26 Ah. For type Te, the equivalent values are 20.61, 19.84 and 0.24 Ah. In addition to defining the value of the required parameter, Q_{Ref} , the values of $\sigma(Q_0)$ are of interest because they define the minimum dispersions to be expected of results from the field batteries.

Column 11 gives the maximum calculable capacity, Q_{Ref} , of the Td and Te cells as calculated according to Equation 15.11 and Equation 15.14. Their respective values are 17.14 and 20.40 Ah for the Td and Te cells. They are the sums of columns 6 and 7

in the Table, and are the values used for calculating the residual capacity values in Section 15.4, below.

15.4. Meter batteries - capacity measurements

The main history and capacity loss parameters for the two sets of meter batteries returned from the field are summarised in Table 15.2. Complete history records were available for 19 Td and 25 Te type batteries.

Table 15.2 Summary of storage and service durations and in-service capacity losses for meter batteries type Td and Te.

Meter battery parameter	Battery type Td (n=19)				Battery type Te (n=25)			
	Durations		Cap losses		Durations		Cap losses	
	Storage t_{mSt} d	Service t_{mOP} d	Storage $^{OC}Q_{mSD}$ Ah	Service $^M Q_{m\Sigma}$ Ah	Storage t_{mSt} d	Service t_{mOP} d	Storage $^{OC}Q_{mSD}$ Ah	Service $^M Q_{m\Sigma}$ Ah
(1)	(2)	(3)	(4)	(5)	(6)	(7)	(8)	(9)
Minimum	48	5	0.01	0.29	304	307	0.07	1.35
Maximum	504	386	0.11	2.02	822	765	0.18	5.52
Mean	178	299	0.04	1.10	389	400	0.08	2.43
Std Devn.	101	128	0.02	0.44	93	109	0.02	1.17

The storage durations vary widely from 48 to 822 days (Columns 2 and 6). The associated values of capacity loss due to self-discharge during storage, $^{OC}Q_{mSD}$, were calculated using Equation 15.15, and are given in Columns 4 and 8. The mean values of $^{OC}Q_{mSD}$ are comparatively low at 0.04 and 0.08 Ah (battery types Td and Te respectively), and represent approximately 3% of the capacity loss measured after about 400 days of service operation for each of the two battery types.

The battery service durations are given in Columns 3 and 7 and these vary widely over a range from 5 to 765 days. However, the majority of the battery samples were in service for periods of between 300 and 400 days.

The evaluation of $^M Q_{m\Sigma}$ was based on laboratory measurement of the residual capacity and using Equation 15.13; the basic statistical parameters of $^M Q_{m\Sigma}$ are given in Columns 5 and 9, and the individual values for each meter battery type are plotted as operational capacity loss against service duration in Figure 15.1. The origin of the graph is located at a value of $^M Q_{m\Sigma}=0$, which represents the start point of the discharge in the meter.

Each battery type is associated with a meter type, which has its own characteristic specific drain rate. In principle, the data points for a given battery type should pass through the origin of the graph and be distributed about a regression line characteristic

of that meter drain rate. The results for both types of battery fall into two groups: (a) outliers that consistently fall on the high capacity loss side of (b) a more compact cluster of data points.

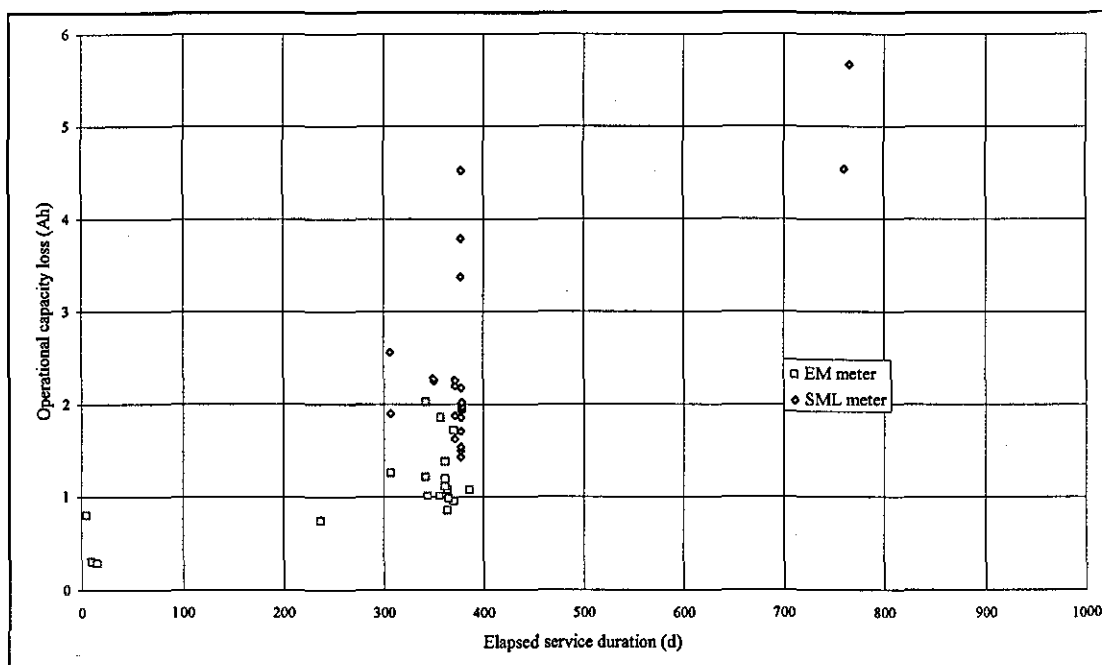


Figure 15.1 Capacity losses ($^M Q_{m\Sigma}$) during meter operation versus service duration of Td and Te batteries removed from the field.

Any meaningful statistical analysis of these capacity loss data is precluded by both the large scatter and the comparatively short meter battery discharge durations. A clearer identification of the underlying trends is achieved by considering the capacity loss rate, which effectively normalises capacity loss by defining it as a function of time.

15.5. In-service capacity loss rates

The in-service capacity loss rates, (dQ_m/dt_m) , for the available batteries were calculated using Equation 15.1, and are plotted against service duration in Figure 15.2. In theory, the results should fall slightly higher than the mean drain rate for each meter type (which is represented by the dashed lines), the difference should relate to the self-discharge losses.

The graph shows that the dQ_m/dt_m values for each meter/battery pair fall into two groups: a fairly tight clustering of points, and a number of outliers. The Meter A/Td data contain five outliers: 11.07, 7.07 and 58.72 Ah/y, which relate to very short in-service durations of 10, 15 and 5 days respectively, and two measuring 2.16 and 1.90 Ah/y at approximately 350 days which are situated marginally above the upper dashed line. The Meter B/Te data set also contain five outliers, whose values of

dQ_m/dt_m exceed 2.5 Ah/y. The outliers are all positively dispersed above the clustered values.

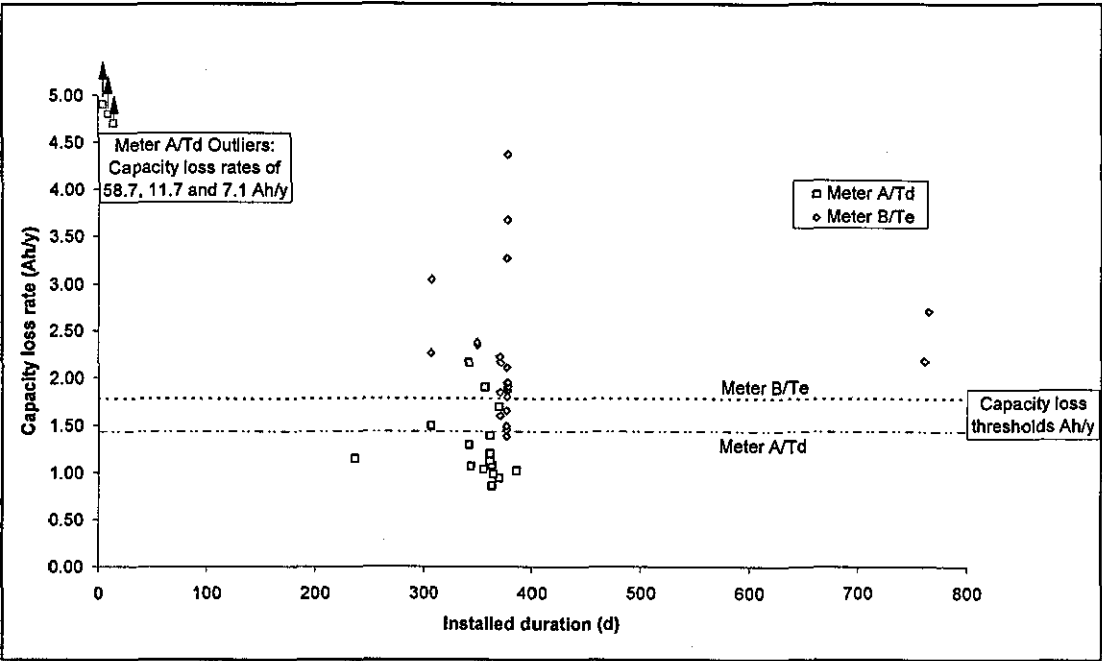


Figure 15.2 In-service capacity loss rates (dQ_m/dt_m) recorded for battery types Td and Te.

For simplicity, let us first consider only the clustered results. The measured capacity loss rate parameters for the clustered data for two types of meter battery are given in Table 15.3 (Columns 1 and 2). The extrapolated 11.5 year predictions of capacity loss based on the 1 year maximum, minimum and mean values for the Td and Te batteries are presented in Columns 3 and 4 respectively.

Table 15.3 Measured 1 year in-service capacity loss rates and extrapolated 11.5 year capacity losses for the ‘clustered’ data for the two types of meter battery.

Parameter	Measured in-service capacity loss rate, (dQ_m/dt_m)		Extrapolated capacity loss for 11.5 years operation	
	1	2	3	4
	Td (n=14) Ah/y	Te (n=19) Ah/y	Td Ah	Te Ah
Min	0.86	1.38	9.85	15.90
Max	1.69	2.37	19.47	27.29
Mean	1.16	1.92	13.39	22.03
Std Devn.	0.23	0.29		

The rounded-down values of Q_{Ref} of 16.5 and 20 Ah determined in Section 13.4 are used for the capacity life analyses. In the case of the Td battery type, the extrapolated 11.5 year mean capacity loss value falls just inside the 16.5 Ah stoichiometric

capacity. However, the equivalent extrapolation for the Te cell exceeds the 20 Ah stoichiometric capacity. The standard deviations in the bottom row of Table 15.3 show that operational capacity loss rates are dispersed over a comparatively wide range, and imply that significant proportions of both of the cell types will fail within the 11.5 year target service life.

15.6. Meter drain rate measurements

In principle, battery capacity loss rate should correlate with the characteristic drain rate of the host meter, and comparisons between the two parameters should enable the difference between real and predicted capacity loss rates to be determined. Meter drain rates and pulse parameters were measured using the purpose designed rig shown schematically in Figure 15.3.

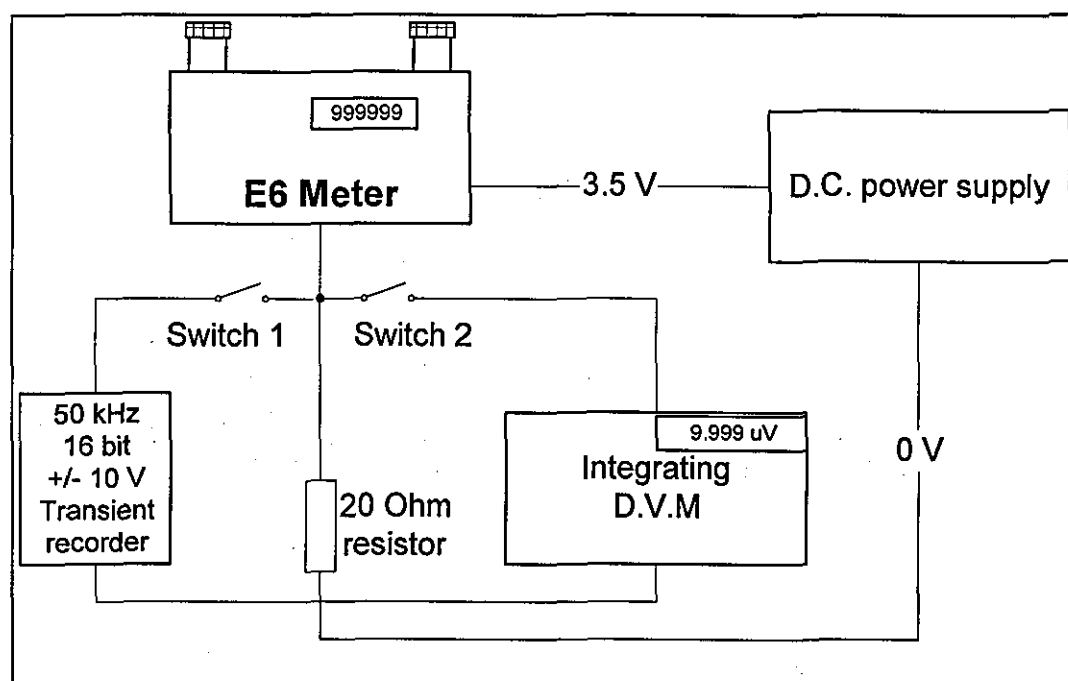


Figure 15.3 Meter load measurement equipment

In order to control the supply voltage and ensure stable conditions, the meter battery was removed and replaced by a mains connected d.c. power supply. The output was set to 3.5 V, in order to be representative of the load voltage of a Li/SOCl₂ cell. A 20 Ω resistor was connected in series with meter in order to provide a voltage signal that would allow the meter load current characteristics to be measured. Switches 1 and 2 enable independent selection of either a high resolution digital voltmeter to measure the meter background current of ~10 μA, or a logging system to record the transients associated with the high amplitude flow measurement pulse. The logger comprised a high speed (50 kHz) transient recorder which was installed in a PC. The

data acquisition and analysis processes were managed by a National Instruments 'Labview' software utility. The software provided the signal processing tools to extract measurements of the pulse amplitude, duration and shape, and to integrate the pulsed load voltage profile with respect to time, and thus quantify the electrical charge associated with the pulse. Screen dumps of the pulse profiles recorded for each meter type are given in Figure 2.1 and Figure 2.2 (pages 10 and 11). The mean load was calculated by time-averaging the background and pulse load measurements.

Table 15.4 gives the measured meter drain rates and the predicted 1 and 11.5 year electrical capacity requirements. The mean drain rate of Meter B is greater than that of Meter A by a factor of 1.7. The individual drain rates for each meter type are dispersed relatively closely about the means (i.e. high magnitude outliers are absent), and the upper values limited to relatively low values of 100 and 150 μA respectively.

Table 15.4 Measured meter load current parameters for Meters A and B

Meter load parameter	Meter A (n=8)	Meter B (n=23)
Minimum drain rate	65.75 μA	123.10 μA
Maximum drain rate	99.90 μA	148.80 μA
Average drain rate	79.18 μA	136.67 μA
Standard deviation of drain rate	10.43 μA	5.54 μA
Predicted mean capacity requirement for 1y	0.69 Ah	1.2 Ah
Predicted mean capacity requirement for 11.5 y	8 Ah	14 Ah

15.7. Comparison of the measured and predicted models

In principle, a measured battery capacity loss rate for a given meter battery should equal the predicted loss rate, which is the sum of the meter drain rate (measured in 15.6), and the self-discharge rate. The self-discharge rate may be calculated using the $P=0.005$ model developed in Section 14.7.

The predicted capacity loss for a meter for a given duration, $^M Q_{p\Sigma}$, is given by the sum of the integrated electrical load, $^M Q_{pL}$, and the estimated self-discharge loss, $^M Q_{pSD}$, as given in Equation 15.17:

$$^M Q_{p\Sigma} = ^M Q_{pL} + ^M Q_{pSD}, \quad \text{Equation 15.17}$$

$^M Q_{pL}$ is calculated by means of Equation 15.18:

$$^M Q_{pL} = I_m \times t_m \quad \text{Equation 15.18}$$

where I_m is the mean meter drain rate, and t_m is the required is the service duration.

The self discharge rate associated with a given meter load, I_{mSD} , may be determined by means of Equation 15.19, which was developed as Equation 14.9 in Section 14.7:

$$I_{mSD} = 0.2817 I_m + 0.2 \text{ (}\mu\text{A)} \tag{Equation 15.19}$$

and ${}^M Q_{PSD}$ is calculated by means of Equation 15.20:

$${}^M Q_{PSD} = I_{mSD} \times tm \tag{Equation 15.20}$$

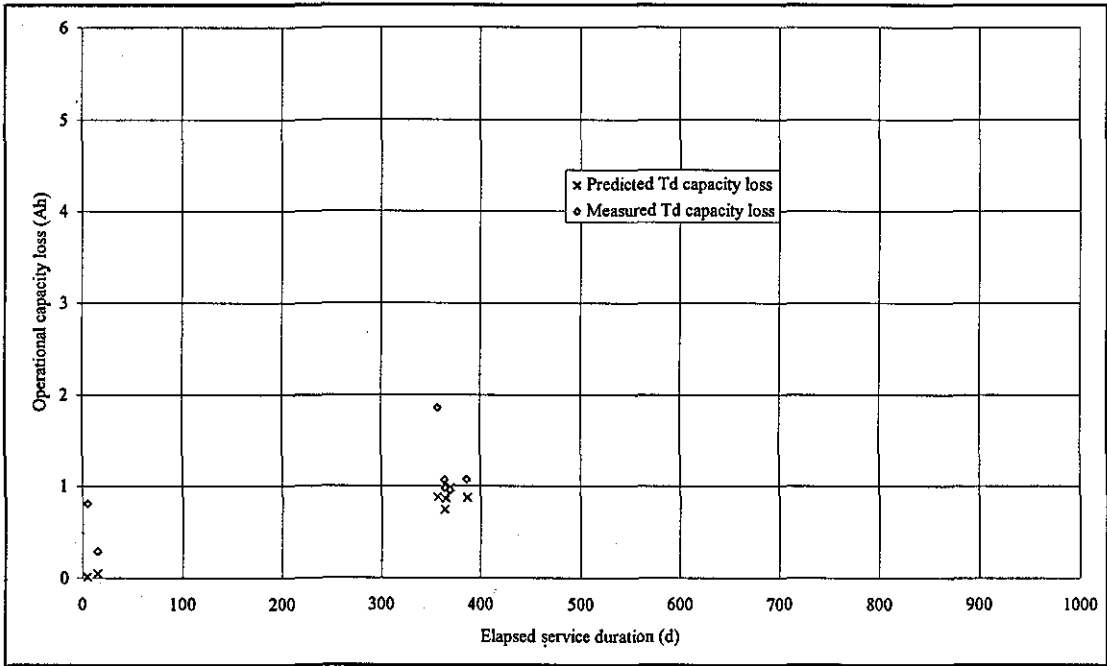


Figure 15.4 Comparison of real and predicted service capacity losses for battery type Td.

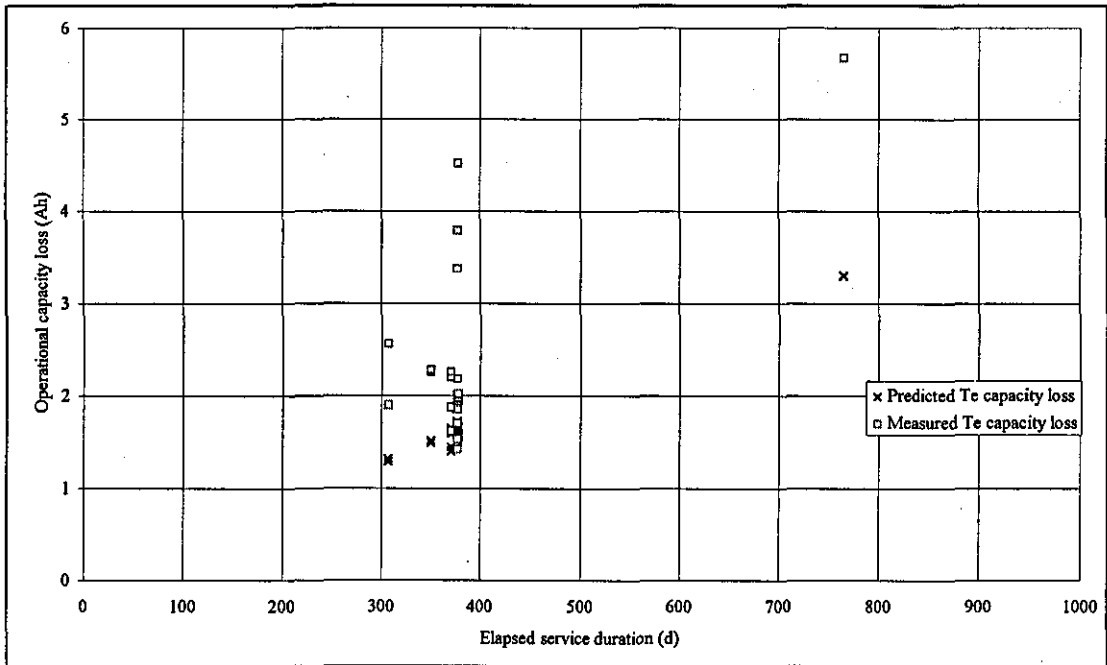


Figure 15.5 Comparison of real and predicted service capacity losses for battery type Te

Figures 15.4 and 15.5 plot both the measured operational and the predicted capacity losses against service duration for battery types Td and Te respectively. The number of data points is small because the required combination of in-service capacity loss and measured meter drain rate data is only available for 7 Meter A/Td and 23 Meter B/Te meter/battery pairs.

Each measured capacity loss data point for a given meter battery, ${}^M Q_{m\Sigma}$, is accompanied by the predicted capacity loss point, ${}^M Q_{p\Sigma}$. Only meter/battery pairs for which a complete set of capacity and meter load measurements is available are included in the graphs. An example of this pairing is observed at a duration of 760 days in Figure 15.5, where the values of ${}^M Q_{m\Sigma}$ and ${}^M Q_{p\Sigma}$ are 5.7 and 2.8 Ah respectively. Identical x- and y-axis scale lengths are used in the two graphs in order to provide easy visual comparisons between the two meter/battery types.

The graphs for both meter/battery pairs show that the measured values generally exceed the predicted values, although there is some overlap of the two distributions.

The means of the measured, $\mu({}^M Q_{m\Sigma})$, and the predicted, $\mu({}^M Q_{p\Sigma})$, capacity loss values, and the respective ratios $({}^M Q_{m\Sigma})/({}^M Q_{p\Sigma})$ for the 'clustered' Meter/battery data are given in Table 15.5. The ratios give a measure of the agreement between the predicted and measured value where 1 is an exact match. The ratios of 1.32 and 1.24 (Td and Te cell respectively) are in reasonable agreement with one another, suggesting that the divergence of the measured from the predicted value is due to a disparity whose magnitude is common to both meter/battery pairs.

Table 15.5 Mean measured and calculated capacity losses and their ratios for Meter A/Td and Meter B/Te

Meter A/Td (n=5)			Meter B/Te (n=18)		
Measured capacity loss rate $\mu({}^M Q_{m\Sigma})$ Ah/y	Calculated capacity loss rate $\mu({}^M Q_{p\Sigma})$ Ah/y	Ratio $({}^M Q_{m\Sigma})/({}^M Q_{p\Sigma})$	Measured capacity loss rate $\mu({}^M Q_{m\Sigma})$ Ah/y	Calculated capacity loss rate $\mu({}^M Q_{p\Sigma})$ Ah/y	Ratio $({}^M Q_{m\Sigma})/({}^M Q_{p\Sigma})$
1.16	0.88	1.32	1.92	1.54	1.24

The capacity losses represented by the high magnitude outliers were also compared with the theoretical values based on the measured meter drain rates. No obvious correlation is evident.

15.8. Predicted service life distributions

We wish to estimate the proportions of batteries that may be expected to become exhausted by the 11.5 year target lifetime. The limiting values of available electrical capacity for the Td and Te batteries are taken to be 16.5 and 20 Ah respectively as determined in Section 13.4. For the purpose of this preliminary analysis a normal distribution for the 'clustered' capacity loss rates is assumed.

Columns 3 and 4 of Table 15.3 give extrapolated capacity losses based on the measured capacity rate loss of the Td and Te batteries in service. These are calculated simply by multiplying the readings in columns 1 and 2 by 11.5. The 11.5 y standard deviations, σ , may be estimated from the ranges as given by Chatfield¹:

$$\sigma \cong \text{range}/\sqrt{n} \text{ for } n < \text{about } 12, \text{ and } \sigma \cong \text{range}/4 \text{ for } 20 < n < 40.$$

For the Td batteries, the range is $19.47 - 9.85 = 9.62$ Ah, and $n = 14$, giving $\sigma_{Td} = 2.67$ Ah. For the Te batteries, the range is $27.29 - 15.90 = 11.38$ Ah, and $n = 19$, giving $\sigma_{Te} = 2.89$ Ah.

By determining the standard normal variate, z , the proportion of batteries that will become exhausted prior to the 11.5 year target service life, $\Phi(z)$, can be extracted from the Normal Probability Distribution table², using the symmetrical properties of the normal distribution. For the Td batteries, the extrapolated mean at 11.5 y, $11.5\mu(MQ_{m\Sigma})$, is 13.39 Ah and:

$$z_{Td} = [Q_{Ref} - 11.5\mu(MQ_{m\Sigma})]/\sigma_{Td} \quad \text{Equation 15.21}$$

Thus:

$$z_{Td} = (16.50 - 13.39)/2.67 = 0.38, \text{ giving } \Phi(z_{Td}) = 1.00 - 0.65 = 35\%.$$

For the Te batteries, $11.5\mu(MQ_{m\Sigma}) = 22.03$ Ah, which is greater than Q_{Ref} (20.5 Ah) and:

$$z_{Te} = [11.5\mu(MQ_{m\Sigma}) - Q_0 + 11.5\mu(MQ_{m\Sigma})]/\sigma_{Te} \quad \text{Equation 15.22}$$

Thus:

$$z_{Te} = (23.56 - 22.03)/2.89 = 0.53, \text{ giving } \Phi(z_{Te}) = 1 - (1.00 - 0.70) = 70\%.$$

15.9. Practical implications

The main implications of the results are

1. The measured battery capacity loss rates exceed the predicted values by a considerable margin: a factor of 1.32 and 1.24 for the Meter A/Td and Meter B/Te units respectively.

2. The measured battery capacity loss rates for both meter/battery units are very widely distributed with outliers positively dispersed above the means for the data sets.

First, we consider the tight clustered grouping of capacity loss data, the implications of the outliers are considered at the end of the section.

15.9.1. Clustered capacity loss data

The statistical analysis predicts that 35% of the Td and 70% of the Te batteries will fail prior to the intended 11.5 year target life, which will impact significantly on the commercial and technical viability of the application. Thus it is important to identify possible sources of error in the analytical approaches utilised here.

The field and laboratory data appear to be at variance with one another. The disparities of 1.32 and 1.24 between predicted and actual capacity loss for the two meter/battery pairs are similar, suggesting that the variance is due to a systematic rather than random error. In addition, the measured in-service discharge data points are consistently greater than those predicted from the electrical load and estimated self-discharge rates. This consistency between two unconnected sets of data tends to suggest that the data trends are accurate in qualitative terms. Thus, we are looking for a source of error in one or more of the factors influencing either the measured or predicted capacity loss rates. The variability and influence of the error factor must be great enough to account for (a) the large variance observed for the values of $^M Q_{m\Sigma}$ recorded for both meter/battery pairs, and (b) the levels of disparity between measured or predicted results.

The measured capacity losses were estimated by means of Equation 15.13

$$^M Q_{m\Sigma} = [^{360} Q_{CL} + Q_{COther}] - [^{360} Q_{mL} + Q_{mOther}] \quad \text{Equation 15.13}$$

and the predicted capacity losses are based on Equation 15.17

$$^M Q_{p\Sigma} = ^M Q_{pL} + ^M Q_{pSD} \quad \text{Equation 15.17}$$

The factors Q_{COther} and Q_{mOther} are relatively small, their sum being only 8% of the measured capacity loss. They will tend to cancel each other out, and are unlikely to contribute to the discrepancies significantly. Theoretically, $^M Q_{pSD}$ should be of minor significance (but see below).

Of the remaining factors, $^{360} Q_{mL}$, $^{360} Q_{CL}$, and $^M Q_{pL}$ are dominant and derive from measured data whose normalised standard deviations can be compared. Normalisation is achieved by dividing the standard deviation by the mean, σ/μ . Table

15.6 gives the σ/μ values for $^{360}Q_{CL}$, $^MQ_{PL}$, and $^MQ_{m\Sigma}$; those of $^{360}Q_{CL}$ and $^MQ_{PL}$ are considerably smaller in magnitude than $^MQ_{m\Sigma}$, implying that these two factors are not responsible for the wide dispersions of observed for $^MQ_{m\Sigma}$. Thus the analysis strongly suggests that source of the disparity lies with the measure of $^MQ_{m\Sigma}$ itself. In the meter, $^MQ_{m\Sigma}$ is the sum of the electrical load and the associated self-discharge as given by Equation 15.2:

$$^MQ_{m\Sigma} = ^MQ_{mL} + ^MQ_{mSD} \quad \text{Equation 15.2}$$

Table 15.6 Normalised distributions of the measured capacity loss and meter drain factors.

Meter/Cell	$\sigma(^{360}Q_{CL})/\mu(^{360}Q_{CL})$	$\sigma(^MQ_{PL})/\mu(^MQ_{PL})$	$\sigma(^MQ_{m\Sigma})/\mu(^MQ_{m\Sigma})$
(1)	(2)	(3)	(4)
Meter A/Td	0.01	0.11	0.25
Meter B/Te	0.01	0.04	0.15

$^MQ_{PL}$ was derived in the laboratory using calibrated equipment, and the magnitudes of the present results match those supplied independently by the two meter manufacturers. However, $^MQ_{PSD}$ is estimated from a simple model of self-discharge based on a regression line through measurements that were made under closely controlled equilibrium conditions in the laboratory. These may be unrepresentative of the dynamic conditions in the field, implying that the disparity lies in the predicted value of $^MQ_{PSD}$ being an underestimate of the actual value of $^MQ_{mSD}$ that occurs in service.

Table 15.7 Self-discharge rate measurements of battery type Te at Meter A and B rates under steady-state conditions. Column 10 of the Table gives the predicted loss rates assuming that the laboratory 'steady state' self-discharge rates are increased by a multiplication factor (MF).

Steady-state measurements (Te cell)					Assume* I_{SD} of [MF] \times [d Q_P /dt]				Ratio
Meter type	I_m μA	I_{mSD} μA	ε_F (%)	d(Q_{PE})/dt μA	MF(I_{mSD})	$I_{mSD} \times MF$ μA	ε_F (%)	d($^{MF}Q_{PE}$)/dt μA	$^{MF}Q_{PE}/Q_{PE}$ (8)/(4)
(1)	(2)	(3)	(4)	(5)	(6)	(7)	(8)	(9)	(10)
Meter A	90	25.55	78	115.55	2.10	53.66	0.63	143.66	1.24
Meter B	145	41.05	78	186.05	2.45	100.56	0.59	245.56	1.32

*MF denotes multiplication factor.

It is possible to determine the increase in self-discharge rate that is required to match the predicted capacity loss rate with the mean measured value. Table 15.7 gives the respective original values of I_m , I_{mSD} , and d Q_{PE} /dt values for the Td and Te batteries in their respective meter types. By adjusting the original values of the steady-state

self-discharge rate by a multiplication factor (MF) given in Column (6), we can produce recalculated values, $(I_{msD} \times MF \text{ and } MF dQ_{pZ}/dt)$, (7) and (9), which enable the disparities of 1.32 and 1.24 between predicted and actual capacity loss rates to be reconciled. The required ratios, $MF Q_{pZ}/Q_{pZ}$, are in (10), and it may be seen that the required MFs are 2.1 and 2.45. As observed in the literature survey (Section 7.15) and in the laboratory (Section 14.7), such levels of self-discharge rate are within the tolerance band for self-discharge where the battery is subject to external stresses. The adoption of these MFs does, however, significantly reduce the value of α_F for the two cells, from around 76% to 60% (see columns 4 and 8).

15.9.2. Outlier capacity loss data

Several possibilities are available to account for the outliers. However, it is important to note that they all consistently lie on the high side of the clustered groups of capacity loss data points, giving confidence in their qualitative accuracy.

Firstly, the three outliers observed for the short service duration batteries may be the result of mechanical shocks generated during transportation and installation and ensuing disruption to the PL. This could generate high self-discharge rates for a short-term, and imply capacity loss rates which are not representative of longer-term operation when mounted in a fixed installation. Clearly from the statistical viewpoint the data sets would be improved by a greater number of meter/battery samples, and longer service durations. This would increase both the confidence in the distribution curve, and the accuracy of the time-averaging process. However, there is no ready explanation to account for the longer service duration outliers. These require MFs of 6.5 and 9 for the Meter A/Td and Meter B/Te meter batteries to account for the discrepancies between predicted and measured capacity loss rates.

Secondly, it is possible that the outliers represent a different set of operating conditions from those in the clustered groups. For example, external as opposed to internal installations, or meters that have been subjected to a large number of optical read operations - however the relevant data is not available³.

Thirdly, Yamin⁴ found that the capacity of Li/SOCl₂ cells is dependent on the type of discharge. He states that the capacity of a low-current long-term discharge was found to be higher than that for a two-phase discharge comprising low-current followed by high current. His analysis showed that the transition from low to high discharge rate leads to non-uniform utilisation of the lithium surface in the second phase, and the

greatly enhanced possibility of electrical isolation of parts of the electrode. This effect will lead to a lower measured (residual) capacity, and an overestimate of the capacity usage rates.

Fourthly, a major restructuring of BG involving significant manpower losses was occurring during periods of the monitoring exercise, and it proved difficult to administer the programme as originally planned. The number of meter and batteries removed as test samples fell short of the numbers required to achieve a statistically meaningful sample size, and because the work was carried out in an ad hoc manner it is possible that some of the individual meter/battery history records include errors.

Finally, the (remote) possibility exists that field operation triggers some new or greatly enhanced corrosion mechanism.

15.10. Comment on elevated self-discharge

The MFs of up 9 discussed in Sections 15.9.1 and 15.9.2 are significantly greater than those predicted by measurements carried out in the laboratory and derived in Section 7.14. Nevertheless, the literature survey of self-discharge in Section 7.15 provided evidence to suggest that such disparities are not unrealistic. The analysis also tends to agree with Eisenmann's contention that the effect of environment on self-discharge is greater than generally reported in the literature, which tends to assume that the steady-state measurements carried out in the laboratory can be translated into external working environments⁵.

CHAPTER 16

PREDICTED BATTERY SERVICE LIFE DISTRIBUTIONS

A main purpose of this study was to provide estimates of the meter battery service lives, and hence formulate replacement schedules for meter batteries in the field. Initially, it had been hoped that a mathematical model could be developed which could predict changes within either the Li/SOCl₂ bobbin cell as a whole, or elements of the cell such as the anode/PL and the pce, and hence their eventual effects on cell operation. Several papers^{1,2,3,4,5} were identified which presented mathematical models of the Li/SOCl₂ cell, based on idealised one dimensional cell designs, for high rate discharges lasting only several minutes, and under isothermal conditions. Tsaur and Pollard^{6,7} considered the mathematical aspects of precipitation of solids in the Li/SOCl₂ cell, and work has been carried out to model porous electrodes.

In 1982, Hughes et al.⁸ found that the concept of a simple model being accurately applied to the discharge of a Li/SOCl₂ 'D' cell through all of the different states of charge is not feasible. Temperature and solution composition vary continuously, the volume of catholyte decreases and new phases appear. In addition, design details such as the structure of the carbon pce, separator, catholyte composition and purity are not available and differ from manufacturer to manufacturer. In 1996 Eisenmann⁹ reported that after nearly thirty years of research on lithium primary batteries, no unified model has been produced which is able to collate the range of material contained in the scientific literature. He reported two major problems. Firstly, the authors of technical disclosures usually provide processed and not raw data, and omit significant design and test details that would enable a general model to be formulated. Secondly, very few studies focus on long operating life applications under varying temperature conditions, and there is mounting evidence that the environment controls the self-discharge of Li/SOCl₂ cells.

The results generally support the view of Hughes et al., in that the discharge performance of certain cell types cannot be predicted even under optimised discharge conditions. No simple mathematical model will be capable of predicting the variable processes such as the significant polarisation effects observed with the Ta and Td cell types. Much work is required before we are able to present a general model that

translates the results of accelerated discharges into predictions that are representative of the meter operating environment.

16.1. Battery service life

In the absence of a general model, measurements of battery capacity, self-discharge capacity loss rates, capacity losses due to polarisation, time-averaged meter load and operational capacity loss rates have been undertaken. Service life may be calculated by simply dividing the initial electrical capacity of the battery by the capacity loss rate, where capacity loss rate is the sum of self-discharge and electrical discharge loss rates. In principle, it is necessary to take account of polarisation, however as shown in Section 13.4, this amounts to less than 1% of the Q_0 value at 3 mA. It should be even lower at the meter operating load of 100 μ A, and may be discounted for the purpose of this analysis.

As has been observed, the data distributions associated with several of the measured performance parameters are complex, the field and laboratory loss rates do not agree, and thus the results do not lend themselves easily to the formulation of a battery life model. The strategy adopted here is to formulate first approximations of expected service life and associated distribution statistics on the basis of the clustered operational capacity loss data. The outliers are used to define a worst case battery life. Thus, service life of a given battery in the application, t_P , may be calculated by means of Equation 16.1.

$$t_P = Q_0 / (dQ_m / dt_m) \quad \text{Equation 16.1}$$

where dQ_m / dt_m is the measured operational capacity loss rate, and Q_0 is the available electrical capacity of a given battery type. Values of these parameters and their standard deviations and the calculated t_P , are given in Table 16.1. The measured values of Q_0 and dQ_m / dt_m were derived in Section 15.5.

Table 16.1 In-service measured capacity loss rates, Q_0 parameters and calculated mean service life, μt_P , and standard deviation, σt_P , for battery types Td and Te in Meter type A and B respectively.

dQ_m / dt_m Parameter	Td			Te		
	dQ_m / dt_m	Q_0	t_P	dQ_m / dt_m m	Q_0	t_P
1	2	3	4	5	6	7
	Ah/y	Ah	y	Ah/y	Ah	y
Mean	1.16	16.97	14.63	1.92	20.21	10.53
Standard Deviation, σt_P	0.23	0.18	2.6	0.29	0.24	1.5
$\mu t_P - 3 \sigma t_P$			5.9			5.8

The respective calculated mean values of t_p for battery types Td and Te in Meter A and B work out to 14.6 and 10.5 years. The second row of the Table gives values of the standard deviations, σ , of the measured and calculated parameters, assuming normal distributions. The 3σ value is the boundary outside of which 0.26% of a population of a normal distribution will lie, and is conventionally used by engineers as a notional failure limit. Here we are interested only in the low capacity tail of the probability distribution function, and by subtracting the mean from the 3σ value, as given in Equation 16.2, we derive the service life that 99.87% of the batteries will exceed, $t_{p3\sigma}$

$$t_{p3\sigma} = [\mu_t - 3\sigma_t]$$

Equation 16.2

The values of $t_{p3\sigma}$ correspond to 5.9 and 5.8 years for the Td and Te battery types in their respective meters.

The capacity loss rate outliers for the two Meter A/Td and Meter B/Te battery pairs registered 2.2 and 4.5 Ah/y respectively, which implies respective service lives of 7 and 4.5 years, respectively.

It may be seen from these estimates that the service life of battery type Te is the lower of the two, giving the impression that the battery type offers an inferior performance. This is not the case, and is caused by the fact that the load current of its host meter is 50% greater than that of the meter in which the Td battery is installed.

16.2. Implications for the meter application

The service life predictions imply that the first Te batteries will fail at 4.5 years and the Td batteries at 5.9 years. However, it is important to note that the results are based on capacity loss rates measured as the first phase of the battery monitoring exercise. Significant improvements in the data validation, statistical and measurement procedures are possible, particularly in terms of the number of battery samples extracted and in their history records. As the duration of batteries in the field is extended so the time averaging processes should give an improved measurement of the capacity loss rate. This may serve to reduce the scale of the discrepancy between predicted and measured loss rates, and will certainly improve confidence in the predictions.

As discussed in Section 9.3, the service life distribution will be skewed towards the low-capacity side, and is more accurately modelled by the Weibull distribution. It will be interesting to observe the actual distributions as further records become available. Finally, it is important to note that these calculations are based on a 0 V end-point voltage, whereas the electronic systems of the meters cease to operate at 3.2V (Meter A), and 2.5 V (Meter B). Unfortunately, no information exists regarding the shape of the discharge curve at end-of-life under a very low pulsed load. Thus the above service life predictions are over-estimate, and the magnitude of error is uncertain.

CHAPTER 17

FINAL SUMMARY AND CONCLUSIONS

- 17.1 A research project been carried out to provide BG with scientific and technical support in its evaluation of lithium primary battery technologies to meet a novel, long life (11.5 year), low power drain electronic meter application.
- 17.2. A status review of the development history and general performance characteristics of lithium primary cell technologies, and a literature survey of test methods, self-discharge and electrical processes that apply to the Li/SOCl₂ cell technology has been carried out (500 publications).
- 17.3. A dedicated 1032 channel combined battery load and data acquisition and control test rig has been designed, built and commissioned. The modular design allows independent connection and selection of batteries and test loads. Control of the test temperature is by environmental chamber; a thermal cycle was developed to determine the battery voltage/temperature/state of charge relationships under both dynamic and equilibrium conditions over the range -20 to +40 °C. Voltage measurements of 1000 channels are taken at 1 minute intervals. The raw data is logged to PC hard disk and archived to CD ROM.
- 17.4. The battery test load is simply a resistor. However, by employing a passive load, battery discharge current, I_L , floats according to Ohm's law: an increase in cell impedance, Z , causes a reduction in load voltage which is balanced by a decrease in I_L . The reduction in I_L leads to a reduction in Z , and the electrochemical processes continue through to depletion of the cell reactants. By measuring the capacity to zero volts, Q_0 , it is possible to measure the total available electrical capacity of the cell. This experimental approach has yielded a novel method of determining total available electrical capacity of a lithium primary battery.
- 17.5. Data acquisition, data-processing and analysis tasks are managed by means of a suite of purpose-designed software modules. Analysis of the discharge profiles yields voltage relationships with temperature, state of charge, load, and integrated capacity to the end-of-life.
- 17.6. Accelerated discharge tests have been carried out on a total of ~400 cells from 4 Li/SOCl₂ low/medium rate candidate battery types. The batteries were tested

in batches of 10 units, over a range of loads from 100 to 1200 Ω , involving discharge periods of up to 15 months.

- 17.7. The results were analysed assuming end-point voltages of both 2.5 and 0 V. The basic statistical parameters (mean, maximum, minimum and standard deviation) of the distributions of performance have been determined as a function of load (pulsed and continuous), state of charge, temperature and manufacturing lot of batches of test cells. The analysed results provide a unique data set of high resolution voltage/temperature relationships and capacity.
- 17.8. The discharge tests produced a clear ranking of battery capacity to an end-point-voltage of 2.5 V: Type Te provides >19 Ah of capacity, and is highly repeatable, Type Tb provides ~16.5 Ah of capacity, and is also highly repeatable. However, although Types Ta and Type Td can yield capacities of ~16.5 Ah, the discharge performance of the two cell types is unreliable, and both are susceptible to premature failure.
- 17.9. The discharge tests have been subjected to a detailed analysis, and by correlating behaviour patterns with available published information on discharge processes, mechanisms for the premature failures of Types Td and Ta have been proposed. The former is linked to blocking of the anode by modified crystal morphology of the PL. The latter is linked to blocking of the cathode by LiCl discharge product.
- 17.10. One of the premature failure modes exhibited by the Td battery type is characterised by an early load voltage transition through the 2.5 V threshold, followed by a period of voltage instability and subsequent reactivation of the cell to a more or less normal end-of-life discharge pattern. Because of the double 'humped' shape of the discharge profile it is nick-named the 'saddle-back' failure mode. A qualitative model has been derived to account for the deviations from normal behaviour.
- 17.11. The standard deviations of the capacity test results imply that the quality control of the Te cells is excellent, that of Tb is good, but that of the Ta and Td cells varies significantly, and is the partial cause of the premature failures.
- 17.12. Self discharge measurements were tasked to and obtained from several sources to build a model from a broad spread of data. The quantitative analysis of

self-discharge rate measurements has provided models of the relationship between self-discharge rate and continuous and pulsed load. It has also shown that the self-discharge rate for a given cell type may vary by a factor of up to 7 for a given laboratory condition.

- 17.13. Capacity losses observed during long-term (12 month) accelerated discharge tests in the laboratory have been positively correlated with self-discharge.
- 17.14. The analysis implies that self-discharge rate, j_{SD} , is dependent on (a) d.c. current density, j , and (b) the pulsed load duty cycle, P , pulse charge magnitude and mean current density, j . For steady-state laboratory conditions, the relations between j_{SD} and j are given by: $j_{SD} = 0.2817j + 0.2 \mu A/cm^2$ (for a pulsed load of $P=0.005$, j in the range of the meter applications, i.e. $100 \mu A$); and for accelerated discharges, $j_{SD} = 0.015j + 3.8465 \mu A/cm^2$ ($P=1$).
- 17.15. The literature and laboratory tests give qualitative evidence that j_{SD} can increase by up to an order of magnitude above the steady-state value when subject to stresses. Disruption of the PL leads to a peak in self-discharge rate, followed by a decay. Neither the peak amplitude nor the time constant is known with any accuracy. Because of the complex and largely unknown nature of the relationship between stress and j_{SD} , it is not possible to predict cumulative self-discharge capacity losses in the normal field operation in the meter.
- 17.16. As the first stage of an on-going monitoring exercise to determine capacity loss rates of batteries in operation in the field, random samples of about 30 of each type of meter/battery unit were removed from the field in 1996 after service periods of up to 800 days.
- 17.17. The respective predicted mean values of service life for battery types Td and Te in Meter A and B are 14.6 and 10.5 years.
- 17.18. The measured operating loss rates are significantly greater (by a factor of ~ 1.3) than those predicted from laboratory tests.
- 17.19. To resolve the discrepancy between predicted and actual capacity loss rates, the time-averaged drain rates of the two types of electronic meter were measured by means of a purpose-designed test rig, comprising a high speed (50 kHz) a/d card and data analysis software to measure meter pulse charge, and a high resolution voltmeter to measure background load.

- 17.20. Capacity loss predictions based on the sum of meter drain rate and the self-discharge model given in Conclusion 17.14 and the actual capacity losses of batteries retrieved from the field do now agree. A detailed survey of published information regarding self-discharge mechanisms offers reasonable evidence that the discrepancy between predicted and actual field capacity loss rates is due to enhancement of self-discharge rates under dynamic thermal and physical stresses imposed by field operation. Mathematically it was shown that multiplication factors of up to 8 are required to reconcile the discrepancy.
- 17.21. The operational capacity loss measurements form complex distributions that fall into two groups: clustered and outliers. Assuming a normal distribution for the clustered data, a service life that 99.87% of the batteries will exceed was derived. These correspond to 5.9 and 5.8 years for the Td and Te battery types in their respective meters. The capacity loss rate outliers for the two Meter A/Td and Meter B/Te battery pairs registered 2.2 and 4.5 Ah/y respectively, which imply respective service lives of 7 and 4.5 years, respectively.
- 17.22. Recommendations for future work have been made to improve the accuracy of the service life predictions and the scientific understanding of Li/SOCl₂ cell processes and failure modes.

CHAPTER 18

FUTURE WORK

The analysis of results signifies that several areas of research exist which would lead to significant improvements in the service life predictions. One aim would be to extend the range of scientific knowledge of the various polarisation and self-discharge processes that occur during discharge by systematic research. Secondly, the project would benefit from the development of measurement techniques to enhance the resolution and accuracy of both the accelerated tests, and an improved knowledge of performance characteristics in the operating domains of the meter application. Specific areas of research towards these objectives are outlined below.

18.1. Monitoring Exercise

An exhaustive assessment of battery capacity losses under field operation requires the continuous monitoring of battery capacity loss rates at regular intervals, say on an annual cycle. This approach should provide sufficient information to develop self-discharge and electrical capacity usage rate trends. Improvement of the statistical analysis of cells returned from field operation requires:

1. A greater number of meter/battery samples.
2. Accurate battery history records.
3. Sampling at frequent time intervals until good confidence in the capacity loss trends is obtained.

A further investigation to determine the implications behind Yamin's suggestion in Section 15.9.2 that the Q_0 results are distorted by contact loss with parts of the anode when discharge rate is increased from low to relatively high rate. This would provide the information needed to explain the 'greater-than expected' operational capacity loss rates, and would enable the residual capacity measurement process to be refined. Validation of Yamin's theory could be achieved by quantitative elemental analysis of residual lithium after discharge to electrochemical exhaustion. This would involve dismantling the cell.

18.2. Self-discharge

More knowledge is required regarding the actual self-discharge rates at the stress levels encountered in the field in order to resolve the discrepancy between predicted and measured capacity loss rates. This would imply the systematic investigation of

capacity losses under pre-selected and controlled levels of electrical, thermal, and mechanical stresses. By measuring the integrated electrical discharge, and the effect of different stress levels on the 'on-load' self-discharge rates, the accuracy of the battery life prediction model would be greatly improved.

18.3. End-of-life polarisation and discharge profile

The present service life predictions are based on an interpolation of the end-of-life discharge curve, under accelerated d.c. load discharge. It is necessary to determine the amount of capacity that is lost due to polarisation under pulsed load where 3.2 and 2.5 V end-point voltages apply, and to determine the limits of battery performance, particularly of prematurely failed cells. Two 'accelerated' methods of achieving this are suggested below:

1. Load switching from a 'high' accelerated load, to a 'real' meter. The switch would be triggered on transition of a series of thresholds, say 3.2, 3, 2.75 and 2.5 V, etc. In principle, the reduced load level should cause a recovery of the cell voltage and satisfactory meter operation. Repeating this procedure until the battery meter fails should provide the correction factor necessary to adjust the service life predictions based on the Q_0 measurements. Other approaches to the programmed stepping down the load current on steps triggered by the transition of battery voltage are given by Fester and Levy¹.
2. By means of a signal generator to load the battery(s) with pulsed load whose pulse interval is systematically increased to reduce the time-averaged load. The reduction would be triggered by transitions of the battery terminal voltage through pre-selected voltage thresholds. By appropriate selection of the pulse parameter values, this test would comprise a stepped load which would move from an 'accelerated' towards the actual meter load.

18.4. Premature failure

Analysis of the premature failure modes and verification of the qualitative models which were postulated in Sections 11.8 and 12.3 to account for deviations from normal behaviour exhibited by the Ta and Td cell types. presented above. This would appear to be a complicated task. Initially, confirmation of the site of the breakdown in electrochemical process rates, i.e. anode/cathode, would be required. A definitive diagnostic test could be achieved by inserting a third terminal in the inter-electrode space. However, as it is presently impossible to predict which battery will fail out of a

sample, this would be a costly and time consuming approach. A second approach would be to dissect both failed cells at the point of failure and a control cell which achieves high coulombic efficiency, to audit the differences exist between the two. The fact that some prematurely failed cells subsequently recover emphasises the possible complexity of this project.

18.5. Noise

As discussed briefly in Section 10.1.2, cell voltage is subject to 'noise', i.e. transient fluctuations of approximately 10 mV in amplitude. It is likely that these noise patterns differ from cell design to cell design, and that they represent signatures. They may also give information as to the cause of premature failure. Techniques for carrying out noise analysis have been developed in a series of papers published by Farrington and Lockwood and Co^{2,3,4}. A simple analysis would search for patterns in the voltage noise. Voltage noise also lends itself to quantifying by Fourier transforms of the time-domain noise records to compute the power spectral density.

THE END

CHAPTER 19

REFERENCES

The first digit of reference number gives the chapter number; the number after the point gives the number of the reference within the chapter.

- 0.1. Brennen K.R., Fester K.E. Owens B.B. and Untereker D.F., *J. Power Sources*, 5 (1980) 25.
- 0.2. Sutton J.B. *The Statistician*, 39 (1990) 461.
- 0.3. Yamin H., Tadiran Ltd., Israel, Personal communication, 1996.
- 0.4. Skarstad P., in *Batteries for Implantable Biomedical Devices*, (Ed. B.B. Owens), Plenum (1986) 230.
- 0.5. Hoier S.N. and Eisenmann E.T. *The Faradaic Efficiency of the Lithium-Thionyl Chloride battery*, Sandia Report SAND96-0956 (1996).
- 1.1. Chapman N.R., Etheridge D.W. and Sussex A.D., *I.G.E. Communication 1527*, Institution of Gas Engineers 130th Annual General Meeting, London (1993).
- 1.2. Saunders T.G., *Watson House Bulletin* (1994).
- 1.3. Patraboy T.J., Farrington M.D. and Donaldson G.J., *J. Power Sources*, 65 (1997) 94.
- 1.4. HSE - Health and Safety Executive, *Lithium Batteries*, Guidance Note GS 43 from the Health and Safety Executive, HMSO (1987).
- 1.5. Saunders T.G., *Power Sources 15*, (Ed. A. Attewell and T. Keily), International Power Sources Symposium Committee, Crowborough, UK (1995) 317.
- 1.6. Karunathilika S.A.G., Hampson, N.A., Leek R. and Sinclair T.J., *J. Appl. Electrochem.*, 10 (1980) 357.
- 1.7. Karunathilika S.A.G., Hampson, N.A., Hughes M., Marshall W.G., Leek R. and Sinclair T.J., *J. Appl. Electrochem.*, 13 (1983) 577.
- 1.8. Hughes. M., Hampson, N.A. and Karunathilika S.A.G., *J. Power Sources*, 12 (1984) 84.
- 1.9. Hagan W.P., Hampson N.A. and Packer R.K., *Electrochim. Acta*, 31 (1986) 699.
- 1.10. Hills A.J. and Hampson N.A., *J. Power Sources*, 24 (1988) 253.
- 1.11. Hagan W.P., Hampson N.A. and Packer R.K., *Power Sources 11*, (Ed. L.J. Pearce), International Power Sources Symposium Committee, Leatherhead, England (1986) 413.
- 1.12. Bro P. and Levy S.C., *Quality and Reliability Methods for Primary Batteries*, The Electrochemical Science Series, John Wiley & Sons, Inc., NY (1990) 15.
- 2.1. *Ibid.*

- 3.1. *Ibid.* p.31.
- 3.2. *Ibid.* p.16.
- 4.1. Linden David, *Handbook of Batteries and Fuel Cells*, McGraw-Hill Book Company, (1984) Table 11.2.
- 4.2. Gabano J.P., in *Lithium batteries*, Academic Press Ltd., (1984) 3.
- 4.3. Chenebault P., in *Lithium Batteries, New Materials, Developments and Perspectives*, Industrial Chemistry Library, Vol. 5, Elsevier (1994) 347.
- 4.4. Gabano J.P. *Lithium batteries*, Academic Press Ltd., (1984) Table 1.
- 4.5. Fukuda M. and Iijima T., *Lithium-Carbon Monofluoride Cells*, in *Lithium batteries*, (Ed. J-P. Gabano), Academic Press Ltd. (1984) 216.
- 4.6. Linden David (Ed.), *Handbook of Batteries and Fuel Cells*, McGraw-Hill Book Co., (1984) Fig. 4.2.
- 4.7. Schlaiker C.R., *Lithium-Oxyhalide Cells*, in *Lithium batteries*, (Ed. J-P. Gabano) Academic Press Ltd. (1984) 305.
- 4.8. Linden David (Ed.) , *Handbook of Batteries and Fuel Cells*, McGraw Hill Book Co. (1984) Table 4.3.
- 4.9. Dey A.N., *Thin Solid Films*, 43, (1977) 131.
- 4.10. Harris W.S., *PhD. Thesis*, University of California, Berkeley, (1958).
- 4.11. Linden David (Ed.), *Handbook of Batteries and Fuel Cells*, McGraw Hill Book Co. (1984) 11-1.
- 4.12. Gabano J-P., French Patents, 1,583,804 (1969), 2,079,744 (1972).
- 4.13. Auborn J.J. and French K.W., *J. Electrochem. Soc.*, 120 (1973) 1613.
- 4.14. Behl W.K., Christopulos J.A., Ramirez M. and Gilman S., *J. Electrochem. Soc.*, 120 (1973) 1619.
- 4.15. Kawauci S., Iijima T. and Kawase T., *New Battery Technologies*, Matsushita Battery Industrial Co. Ltd., (1994).
- 4.16. Saunders T.G., in *Power Sources 15*, (Ed. A. Attewell and T. Keily), International Power Sources Symposium Committee, Crowborough, UK (1995) 317.
- 4.17. Narukawa S. and Furukawa N., *Lithium Manganese-Dioxide Batteries*, in *Modern Battery Technology*, (Ed. C.D.S. Tuck), Ellis Horwood Ltd. (1991) 348.
- 4.18. Eyre D. and Tuck C.D.S., *Lithium Carbon-Fluoride Batteries*, in *Modern Battery Technology*, (Ed. C.D.S. Tuck), Elliss Horwood Ltd. (1991) 336.
- 4.19. Bro P. and Levy S.C., *Quality and Reliability Methods for Primary Batteries*, The Electrochemical Science Series, John Wiley & Sons, Inc. (1990) 3.
- 4.20. Patraboy T.J., Farrington M.D. and Donaldson G.J., *J. Power Sources*, 65 (1997) 93.

- 4.21. Fester K. and Levy S.C., *Evaluation Methods*, in Batteries for Biomedical Devices, (Ed. Boone B. Owens), Plenum, 8, (1986) 85.
- 4.22. Brennan K.R. and Kim J.S., *Battery Performance Modelling*, in Batteries for Implantable Biomedical Devices, (Ed. Boone B. Owens), Plenum, 8, (1986) 113.
- 4.23. Patrabooy T.J., Farrington M.D. and Donaldson G.J., *J. Power Sources*, 65 (1997).
- 4.24. Personal communications with Mr Tony Rogers of Electrodetectors Ltd, (March 1996).
- 5.1. Tuck C.D.S. (Ed.), *Modern Battery Technology*, Ellis Horwood Ltd., (1991) 287.
- 5.2. Cieslak W.R., *Proc. 36th. Power Sources Symp.*, Cherry Hill, NJ (1994) 347.
- 5.3. Marincic N., *J. Appl. Electrochem.*, 6 (1976) 463.
- 5.4. Eichinger G. and Gabriel W., *Practical Lithium Batteries*, (Ed. Y. Matsuda and C. Schlaiker), JEC Press, USA, (1988) 47.
- 5.5. Eyre D., Hawker Eternacell, Personal communication, (May 1997).
- 5.6. Peled E., *Proc. 32nd. Power Sources Symp.*, Cherry Hill, (1986) 448.
- 5.7. Dey A.N., *J. Electrochem. Soc.*, 123 (1976) 1262.
- 5.8. Dey A.N. and Bro P., in *Power Sources 6* (Ed. D.H. Collins), Academic Press, London (1976) 493.
- 5.9. Hagan W.P., Hampson N.A. and Packer K.A., *Electrochim. Acta*, 31 (1986) 699.
- 5.10. Abraham K.M., *J. Power Sources*, 34 (1991) 87.
- 5.11. Hills A.J. and Hampson N.A., *J. Power Sources*, 24 (1988) 259.
- 5.12. Seager N.J. and Waghorne T., *Proc. 36th. Power Sources Symp.*, Cherry Hill, NJ (1988) 252.
- 5.13. Gibbard H.F. and Reddy T.B., *Modern Battery Technology*, (Ed. C.D.S. Tuck), Ellis Horwood Limited, (1991) 291.
- 5.14. O'Hara III T.J., *Proc. 36th. Power Sources Symp.*, Cherry Hill, NJ (1988) 262.
- 6.1. Iwamaru T. and Uetani Y., *J. Power Sources*, 20 (1987) 47.
- 6.2. Linden D., *Handbook of Batteries and Fuel Cells*, McGraw Hill Book Co., (1984) 11.
- 6.3. Hill I.R., Sibbald A.M., Donepudi V.S., Adams W.A. and Donaldson G.J., *J. Power Sources*, 39 (1992) 93.
- 6.4. Gibbard H.F. and Reddy T.B., *Modern Battery Technology*, (Ed. C.D.S. Tuck), Ellis Horwood Limited, (1991) 288.
- 6.5. Hagan W.P., Hampson N.A. and Packer R.K., *Electrochim. Acta*, 31 (1986) 703.

- 6.6. P.M. Skarstad, in *Batteries for Implantable Biomedical Devices*, (Ed. Boone B. Owens), Plenum, 8, (1986) 215.
- 6.7. Atkins P.W., *Physical Chemistry*, 5th Edition, Oxford University Press (1995) 1016.
- 6.8. Hagan W.P., Hampson N.A. and Packer R.K., in *Power Sources 11* (Ed. L.J. Pearce) International Power Sources Symposium Committee, Leatherhead, England, (1987) 420.
- 6.9. Atkins P.W., *Physical Chemistry*, 5th Edition, Oxford University Press (1995) 850.
- 6.10. Tsaur K-C. and Pollard R., *J. Electrochem. Soc.*, 131 (1984) 983.
- 6.11. Chenebault P., Vallin D., Thevenin J. and Wiart R., *J. Appl. Electrochem.*, 18 (1988) 631.
- 6.12. Popov B.N., Zhang W., Darcy E.C. and White R.E., *Proc. Symp. of Batteries and Fuel Cells for Stationary and Electric Vehicle Applications*, (Ed. A.R. Landgrebe and Z-I Takehora), 118th Mtg. of the Electrochem. Soc., Hawaii, Publication 93-8, Electrochem. Soc. (1993) 79.
- 6.13. Mogensen M., *Proc. Electrochem. Soc. Meeting on Primary and Secondary Ambient Temperature Lithium Batteries*, Publication 88-6, Electrochem. Soc. (1988) 229.
- 6.14. Mogensen M., *Kinetics of LiCl Film Formation on Lithium Anodes in SOCl₂*, Riso-M-2619, Riso National Laboratory, DK-4000, Roskilde, Denmark, (1987).
- 6.15. Hagan W.P., Hampson N.A. and Packer R.K., *Electrochim. Acta*, 31 (1986) 700.
- 6.16. Yamin H., Tadiran Ltd., Israel, Personal communication, 1996.
- 6.17. Dhamelincourt M.C., Wallart F., Barbier P., Mairesse G. and Descroix P., *J. Power Sources*, 14 (1985) 77.
- 6.18. Bedfer Y., Corset J., Dhamelincourt M.C., Wallart F. and Barbier P., *J. Power Sources*, 9 (1983) 267.
- 6.19. Hill I.R., Sibbald A.M., Donepudi V.S. Adams W.A. and Donaldson G.J., *J. Power Sources*, 39 (1992) 92.
- 6.20. Hagan W.P. and Sargeant D.G., *J. Power Sources*, 34 (1991) 1.
- 6.21. Dey A.N., *J. Electrochem. Soc.*, 123 (1976) 1263.
- 6.22. Demakhin A.G. and Kuznetsov N.N., *J. Applied Electrochem. of the USSR*, 65 Part 2 (1992) 229.
- 6.23. Deligiannis F., Ratnakumar B.V., Frank H., Davies E. and Surampudi S., *Proc. 36th Power Sources Conf.*, Cherry Hill, NJ, (1996) 374.
- 6.24. Klinedinst K.A., *J. Electrochem. Soc.*, 128 (1981) 2511.
- 6.25. Shlepakov M., Tadiran Ltd., Personal communication, 16 September, 1997.

- 6.26. Evans T.I., Nguyen T.V. and White R.E., *J. Electrochem. Soc.*, 136 (1989) 332.
- 6.27. Tsaur K-C. and Pollard R., *J. Electrochem. Soc.*, 131 (1984) 976.
- 6.28. Yamin H., Tadiran Ltd., Israel, Personal communication (1996).
- 6.29. Chenebault P., Vallin D., Thevenin J. and Wiart R., *J. Appl. Electrochem.*, 19 (1989) 419.
- 6.30. Chenebault P., Vallin D. Thevenin J. and Wiart R., *J. Appl. Electrochem.*, 18 (1988) 631.
- 6.31. Hu H-Y and Ko H-K., *J. Power Sources*, 26 (1989) 419.
- 6.32. Chakov N.I., Povarov Y.M. and Pleskov Y.V., *Elektrokhimiya*, 16 (1980) 1445.
- 6.33. Madou M.J., Smith J.J. and Szpak S., *J. Electrochem. Soc.*, 131 (1987) 2794.
- 6.34. Hansen L.D. and Frank H., *J. Electrochem. Soc.*, 134 (1987) 1.
- 6.35. Mogensen M., *J. Power Sources*, 14 (1985) 125.
- 6.36. Cieslak W.R and Street H.K., *Proc. 34th. Power Sources Symp.*, Cherry Hill, (1990) 255.
- 6.37. M. Hughes, S.A.G.R. Karunathilika, N.A. Hampson, *J. Appl. Electrochem.*, 13 (1983) 669.
- 6.38. Zhang Y and Cha C-S., *Electrochim. Acta*, 37 (1992) 1207.
- 6.39. Zhang Y and Cha C-S., *Electrochim. Acta*, 38 (1993) 822.
- 6.40. Hagan W.P and Sargeant D.G., *J. Power Sources*, 34 (1991) 1.
- 6.41. Bagostky V.S. Volkovich Y.M., Kanevsky L.S. and Skundin A.M., in *Power Sources 15*, (Ed. A. Attewell and T. Keily), International Power Sources Symposium Committee, Crowborough, England (1995) 369.
- 6.42. Evans T.I., Nguyen T.V. and White R.E., *J. Electrochem. Soc.*, 136 (1989) 335.
- 6.43. Szpak S. and Venkasetty H.V., *Power Sources 9* (Ed. J. Thompson), Academic Press, London, (1983) 403.
- 6.44. Dey A.N., *J. Electrochem. Soc.*, 128 (1978) 1574.
- 6.45. Sun H-W. and Chen S-C., *Proc. Electrochem. Soc. - Extended Abstracts, Abstract No.6*, Electrochem. Soc., Publication 89-1 (1989) 9.
- 6.46. Chenebault P., in *Lithium Batteries, New Materials, Developments, and Perspectives*, (Ed. G. Pistoia) Elsevier, London (1994) 353.
- 6.47. Szpak S. and Venkasetty H.V., *Power Sources 9* (Ed. J. Thompson), Academic Press, London, (1983) 410.
- 6.48. Bagostky V.S. Volkovich Y.M., Kanevsky L.S. and Skundin A.M., in *Power Sources 15*, (Ed. A. Attewell and T. Keily), International Power Sources Symposium Committee, Crowborough, England (1995) 364.

- 6.49. Szpak S. and Driscoll J.R., *J. Power Sources*, 10 (1983) 351.
- 6.50. Chiu J.G., Wang Y.Y. and Wan C.C., *J. Power Sources*, 21 (1987) 122.
- 6.51. Bagotsky V.S. Volkovich Y.M., Kanevsky L.S. and Skundin A.M., in *Power Sources 15*, (Ed. A. Attewell and T. Keily), International Power Sources Symposium Committee, Crowborough, England (1995) 362.
- 6.52. Bagotsky V.S., Kazarinov V.E., Yu M., Volkovich Y.M, Kanevsky L.S. and Beketayeva L.A., *J. Power Sources*, 26 (1989), 432.
- 6.53. Marincic N., *J. Appl. Electrochem.* 5 (1975) 313.
- 6.54. Dey A.N. and Bro P., *J. Electrochem. Soc.*, 125 (1978) 1574.
- 6.55. Dey A.N., *J. Electrochem. Soc.*, 123 (1976) 1262.
- 6.56. Hagan W.P., Hampson N.A. and Packer R.K., *Electrochim. Acta*, 31 (1986) 699.
- 6.57. Klinedinst K.A., *J. Electrochem. Soc.*, 132 (1985), 2044.
- 6.58. Bagotsky V.S., Kazarinov V.E., Yu M., Volkovich Y.M, Kanevsky L.S. and Beketayeva L.A., *J. Power Sources*, 26 (1989), 427.
- 6.59. Danel V., Descroix J-P. and Petit A., *Proceedings of the Symposium on Lithium Batteries* (Ed. A.N. Dey), Electrochem. Soc., (1984) 136.
- 6.60. Bagotsky V.S. Volkovich Y.M., Kanevsky L.S. and Skundin A.M., in *Power Sources 15*, (Ed. A. Attewell and T. Keily), International Power Sources Symposium Committee, Crowborough, England (1995) 360.
- 6.61. Klinedinst K.A., *J. Electrochem. Soc.*, 128 (1981) 2508.
- 6.62. Yamin H., Tadiran Ltd., Israel, Personal communication (1996).
- 6.63. Deligiannis F., Ratnakumar B.V. Frank H., Davies E. and Surampudi S., *Proc. 36th Power Sources Conf.*, Cherry Hill, NJ, (1996) 373.
- 6.64. Yamin H. and Pallivathikal M., *6th Int. Seminar on Lithium Battery Technology and Applications*, Deerfield Beach, Florida, (1993).
- 6.65. *Inorganic Lithium Batteries* Sonnenschein Lithium Technical Brochure, Sonnenschein Lithium GmbH, 110 1150 01, 2/5/795/Hell. (1995) 14.
- 6.66. Dr. Chenebault P., SAFT, Poitiers, France, Personal communication, 1995.
- 6.67. Doddepaneni N., Chua D.L. and Eppley W.J. *Proc. Symposium on Lithium Batteries*, Electrochem. Soc., Publication 84-1, (1984) 132.
- 6.68. Prof. V. Bagotsky, Frumkin Institute, Moscow, Personal communication (April 1995).
- 6.69. Marincic N., *Practical Lithium Batteries*, (Ed. Matsuda Y. and Schlaiker C.), JEC Press, USA, (1988) 9.
- 6.70. *Inorganic Lithium Batteries* Sonnenschein Lithium Technical Brochure, Sonnenschein Lithium GmbH, 110 1150 01, 2/5/795/Hell. (1995) 13.

- 6.71. Eichinger G. and Gabriel W., *Practical Lithium Batteries*, (Ed. Matsuda Y. and Schlaiker C.), JEC Press, USA, (1988) 42.
- 7.1. James Sullivan, Power Conversion Inc., USA, Personal communication (Oct. 6th 1995).
- 7.2. Dr. H Yamin, Tadiran Ltd, Israel, Personal communication (November 1997).
- 7.3. Phillips J. and Gibbard H.F., *Proceedings on the Symposium on Lithium Batteries*, Publication 81-4, Electrochem. Soc. (1981) 54.
- 7.4. Buchman R., Fester K., Patel B., Skarstad P.M. and Untereker D., *Proc Symp. on Lithium Batteries*, Publication 84-1, Electrochem. Soc., (1984) 212.
- 7.5. Patel B., Skarstad P.M. and Untereker D., *Proc Symp. on Lithium Batteries*, Electrochem. Soc., 84-1 (1984) 221.
- 7.6. Mogensen M., *Kinetics of LiCl Film Formation on Li Anodes in SOCl₂*, Riso-M-2619, Riso National Laboratory, DK-4000 Roskilde, Denmark (1987).
- 7.7. Gabrielli C., *Identification of Electrochemical Processes by Frequency Response Analysis*, Technical Report Number 004/83, Solartron Instruments, Farnborough, England (1984).
- 7.8. Gabrielli C., *Use and Applications of Electrochemical Impedance Techniques*, Technical Report Part No.12860013, Solartron Instruments, Farnborough, England (1990).
- 7.9. Shih H. and Lo T-C., *Electrochemical Impedance Spectroscopy for Battery Research and Development*, Technical Report 31, Solartron Instruments, Farnborough, England (1996).
- 7.10. Popov B.N., Zhang W., Darcy E.C. and White R.E., *Proc. Symp. on Batteries and Fuel Cells for Stationary and Electric Vehicle Applications*, (Ed. A.R. Landgrebe), Publication 93-8, Electrochem. Soc., (1993) 74.
- 7.11. Delnick F.M., *Proc. Symp. on Primary and Secondary Ambient Temperature Lithium Batteries*, Publication 88-6, Electrochem. Soc., (1988) 215.
- 7.12. Mogensen M., *J. Power Sources*, 20 (1987) 255.
- 7.13. Yamin H., Pallivathikal M. and Zak U., *5th Int. Seminar on Lithium Battery Technology and Applications*, Deerfield Beach, Florida, (1991) 4.
- 7.14. Cieslak W. R., *Proc. 36th. Power Sources Symp.*, Cherry Hill, NJ (1994) 347.
- 7.15. Kronenburg M.L., Baker J.W., Rissmiller P. and Bytella J., *Proc 35th. Power Sources Conf.*, Cherry Hill, NJ (1992) 60.
- 7.16. Hansen L.D. and Hart R.M., *J. Electrochem. Soc.*, 125 (1978) 842.
- 7.17. Untereker D.F., *J. Electrochem. Soc.*, 125 (1978) 1907.
- 7.18. Hansen L.D. and Frank H., *J. Electrochem. Soc.*, 134 (1987) 5.
- 7.19. Kalu E.E., White R.E. and Darcy E.C., *J. Electrochem. Soc.*, 139 (1992) 2378.
- 7.20. Kalu E.E., White R.E. and Darcy E.C., *J. Electrochem. Soc.*, 139 (1992) 2755.

- 7.21. Bittner H.F., Carter B.J., Donley S.W. and Quinzio M.V., *J. Power Sources*, 26 (1989) 441.
- 7.22. Godshall N.A. and Driscoll J.R., *J. Electrochem. Soc.*, 131 (1984) 2221.
- 7.23. Godshall N.A. and Driscoll J.R., *Proc Symp. on Lithium Batteries*, Electrochem Soc., 84-1 (1984) 171.
- 7.24. Mogensen M., *Proc. Symp. on Primary and Secondary Ambient Temperature Lithium Batteries*, Publication 88-6, Electrochem. Soc., (1988) 234.
- 7.25. Zhang Y. and Cha C-S., *Electrochim. Acta*, 37 (1992) 1211.
- 7.26. Peled E. and Yamin H., *Proc. 28th Power Sources Symp.* (1978) 237.
- 7.27. Moshtev R.V., Geronev Y. and Puresheva B., *J. Electrochem. Soc.*, 128 (1981) 1851.
- 7.28. Kazarinov V.E. and Bagotsky V.S., *J. Power Sources*, 20 (1987) 259.
- 7.29. Moshtev R.V., Geronev Y. and Puresheva B., *J. Electrochem. Soc.*, 128 (1981) 1851.
- 7.30. Dey A.N., *Li anode film & organic & inorganic electrolyte batteries*, Thin Solid Films, 43 (1977) 131.
- 7.31. Peled E. and Yamin H., *Proc. 28th. Power Sources Symp.* (1978) 237.
- 7.32. Peled E. and Yamin H., *Israel J. Chem.*, 18 (1979) 131.
- 7.33. Peled E., in *Lithium Batteries*, (Ed. J-P. Gabano), Academic Press, London (1983), 43.
- 7.34. Peled E., in *Lithium Batteries*, (Ed. J-P Gabano), Academic Press, 1983, 46.
- 7.35. Delnick F.M., *J. Power Sources*, 26 (1989) 129.
- 7.36. Peled E. and Yamin H., *Proc. 28th Power Sources Symp.* (1978) 238.
- 7.37. Mogensen M., *About the Properties of the LiCl-films on Lithium Anodes in Liquid Cathodes*, unpublished draft report, Riso National Laboratory, DK-4000, Roskilde, Denmark (1996) 19.
- 7.38. Blomgren G.E., *J. Power Sources*, 26 (1989) 51.
- 7.39. Peled E., in *Lithium Batteries*, (Ed. J-P. Gabano), Academic Press, London (1983) 65.
- 7.40. Mogensen M., *Kinetics of LiCl Film Formation on Li Anodes in SOCl₂*, Riso-M-2619, Riso National Laboratory, DK-4000, Roskilde, Denmark (1987) 8.
- 7.41. Peled E. and Yamin H., *Proc. 28th Power Sources Symp.* (1978) 239.
- 7.42. Dr. M. Mogensen, Riso National Laboratory, DK-4000, Roskilde, Personal communication (1996).
- 7.43. Delnick F.M., Cieslak W.R., Peebles D.E. and Rogers J.W., *Proc. 172nd Electrochem. Soc. Meeting*, Honolulu, Publication 87-2, Electrochem. Soc., (1987) 204.
- 7.44. Bailey J.C., *Proc. 31st Int. Power Sources Symp.*, (1984) 546.

- 7.45. Chenebault P., Vallin D., Thevenin J. and Wiart R., *J. Appl. Electrochem.*, 18 (1988) 631.
- 7.46. Moshtev R.V., Geronev Y. and Puresheva B., *J. Electrochem. Soc.*, 128 (1981) 1851.
- 7.47. Boyd J.W., *J. Electrochem. Soc.*, 134 (1987) 18.
- 7.48. Holleck G.L. and Brady K.D., *Proc. Symp. On Lithium Batteries*, Publication 84-1, Electrochem. Soc. (1984) 48.
- 7.49. Chenebault P., Vallin D., Thevenin J. and Wiart R., *J. Appl. Electrochem.*, 18 (1988) 625.
- 7.50. Chenebault P., SAFT, Personal communication, (September 1996).
- 7.51. Gaberscek M., Jamnik J. and Pejnovik S., *J. Electrochem. Soc.*, 140 (1993) 308.
- 7.52. Chenebault P., Vallin D., Thevenin J. and Wiart R., *J. Appl. Electrochem.*, 19 (1989) 413.
- 7.53. Jamnik J., Gaberscek M., Meden A. and Pejnovik S., *J. Electrochem. Soc.*, 138 (1991) 1582.
- 7.54. Shlepakov M., Tadiran Ltd., Israel, Personal communication (16 September, 1997).
- 7.55. Klinedinst K.A., *J. Electrochem. Soc.* 131 (1984) 492.
- 7.56. Dey A.N., *Thin Solid Films*, 43 (1977) 166.
- 7.57. Mogensen M., *Proc. Electrochem. Society Symp. On Primary and Secondary Ambient Temperature Lithium Batteries*, Publication 88-6, Electrochem. Soc. (1988) 236.
- 7.58. Dey A.N., *Thin Solid Films*, 43 (1977) 131.
- 7.59. Dey A.N., *Thin Solid Films*, 43 (1977) 164.
- 7.60. Chua D.L. and Merz W.C., *Proc. 27th Int. Power Sources Symp.* (1976) 33.
- 7.61. Chenebault P., Thevenin J., Vallin D. and Wiart R., *Abstract No. 35, Proc. 172nd Electrochem. Soc. Meeting*, Honolulu, Publication 87-2, Electrochem. Soc. (1987).
- 7.62. Chenebault P. and Vallin D., *Proc. Electrochem. Soc. Symp. On Primary and Secondary Ambient Temperature Lithium Batteries*, Electrochem. Soc. (1988) 201.
- 7.63. Chenebault P., Vallin D. Thevenin J. and Wiart R., *J. Appl. Electrochem.*, 18 (1988) 625.
- 7.64. Chenebault P., Vallin D. Thevenin J. and Wiart R., *J. Appl. Electrochem.*, 19 (1989) 413.
- 7.65. Yamin H., Pallivathikal M. and Zak U., *5th Int. Seminar on Lithium Battery Technology and Applications*, Deerfield Beach, Florida, (1991).

- 7.66. Yamin H., Pallivathikal M. and Elster M., *Proc. 35th Power Sources Symp.*, Cherry Hill (1992), 68.
- 7.67. Yamin H. and Pallivathikal M., *6th Int. Seminar on Lithium Battery Technology and Applications*, Deerfield Beach, Florida (1993).
- 7.68. Yamin H., Shlepakov M., Elster M. and Shapira D., *7th Int. Seminar on Lithium Battery Technology and Applications*, Deerfield Beach, Florida (1995).
- 7.69. Yamin H., Shlepakov M., Elster M. and Shapira D., *7th Int. Seminar on Lithium Battery Applications*, Deerfield Beach, Florida (1995) 7.
- 7.70. Hagan W.P., Hampson N.A. and Packer R.K., *J. Power Sources*, 24 (1988) 95.
- 7.71. Cieslak W. R. *Proc. 36th Power Sources Symp.*, Cherry Hill, NJ (1994).
- 7.72. Dey A.N., *Thin Solid Films*, 43 (1977) 161.
- 7.73. Peled E., in *Lithium Batteries*, (Ed. J-P. Gabano), Academic Press, London (1983) 52.
- 7.74. Yamin H., Tadiran Ltd., Israel, Personal communication (11/1997).
- 7.75. M. Babai and Y. Gal, *Proc. Electrochem. Soc.*, 80-4 (1980) 536.
- 7.76. Iwamaru T. and Uetani Y., *J. Power Sources*, 20 (1987) 50.
- 7.77. Marincic N. in *Practical Lithium Batteries*, (Ed. Y. Matsuda and C. Schlaiker), JEC Press, USA, (1988) 9.
- 7.78. Kronenburg M.L. and Bro P., *Proc Symp. on Power Sources for Biomedical Implantable Applications and Ambient Temperature Lithium Batteries*, Electrochem. Soc., 80-4 (1980).
- 7.79. Eichinger G., in *Materials for Advanced Batteries* (Ed., D.W. Murphy, J. Broadhead and B.C.H. Steele), *Proc. NATO Symp. On Materials for Advanced Batteries*, Aussois, France, Plenum Press, NY and London (1979).
- 7.80. Yamin H., Shlepakov M., Elster M. and Shapira D., *11th International Seminar on Lithium Battery Applications*, Deerfield Beach, Florida, (1995).
- 7.81. Deligiannis F., Ratnakumar B.V. Frank H., Davies E. and Surampudi S., *Proc. 36th Power Sources Conf.*, Cherry Hill, NJ, (1996) 373.
- 7.82. Hoier S.N. and Eisenmann E.T., *The Faradaic Efficiency of the Lithium-Thionyl Chloride Battery*. Sandia Report SAND96-0956, Sandia National Laboratories Albuquerque, New Mexico 87185, USA, (1996) 10.
- 7.83. Mogensen M., *Kinetics of LiCl Film Formation on Li Anodes in SOCl₂*, Riso-M-2619, Riso National Laboratory, DK-4000 Roskilde, Denmark (1987).
- 7.84. Leef A. and Gilmour A., *J. Appl. Electrochem.*, 9 (1979) 664.
- 7.85. Dey A.N., *Electrochim. Acta* 21 (1976) 377.
- 7.86. Kronenberg M.L., Baker J.W., Rissmiller P. and Bytella J., *Proc 35th. Power Sources Symp.*, Cherry Hill, NJ, (1992) 63.

- 7.87. Mogensen M., *Proc. Electrochem. Soc. Symp. On Primary and Secondary Ambient Temperature Lithium Batteries*, Publication 88-6, Electrochem. Soc. (1988) 232.
- 7.88. Mogensen M., *Extended Abstracts of the Electrochemistry Society Mtg.*, Las Vegas, 13-18th Oct., 1985, Electrochem. Soc., Abstract No. 99.
- 7.89. *Inorganic Lithium Batteries* Sonnenschein Lithium Technical Brochure, Sonnenschein Lithium GmbH, 110 1150 01, 2/5/795/Hell. (1995) 15.
- 7.90. Frank H., Carter B. and Hansen L.D., Abstract 31, *The Electrochemical Society Extended Abstracts*, Vol. 82-2, Detroit (1982).
- 7.91. Skarstadt P., in *Batteries for Implantable Biomedical Devices* (Ed. Boone B Owens), Plenum (1986) 246.
- 7.92. Iwamaru T. and Uetani Y., *J. Power Sources*, 20 (1987) 50.
- 7.93. Hansen L.D. and Frank H., *J. Electrochem. Soc.*, 134 (1987) 1.
- 7.94. Sutton J.B. *The Statistician*, 39 (1990) 461.
- 7.95. Pallivathikal M, Yamin H. and Zak U., Abstract 82, *The Electrochemical Society Extended Abstracts*, Florida (1989).
- 7.96. Hoier S.N., Schlaiker C., Johnson A. and Riley S., *Proc 37th. Power Sources Conf.*, Cherry Hill, NJ., (1996).
- 7.97. Babai M., *Progress in Batteries and Solar Cells*, 3 (1980) 114.
- 7.98. Babai M. and Gal Y., *Proc. Electrochem. Soc.*, 80-4 (1980) 539.
- 7.99. Patel B., Skarstad P.M. and Untereker D., *Proc Symp. on Lithium Batteries*, Electrochem Soc., 84-1 (1984) 226.
- 7.100. Bro P. and Levy, S.C., *Quality and Reliability Methods for Primary Batteries*, The Electrochemical Science Series, John Wiley & Sons, Inc. (1990) 127.
- 7.101. Eisenmann E.T., *Lithium Thionyl Chloride Battery - State-of-the-Art Assessment*, Sandia Report SAND96-0839, Sandia National Laboratories Albuquerque, New Mexico 87185, USA (1996), 18.
- 7.102. Yamin H., Pallivathikal M. and Zak U., *5th Int. Seminar on Lithium Battery Technology and Applications*, Deerfield Beach, Florida, (1993) 9.
- 7.103. Dr. H. Yamin, Tadiran Ltd., Israel, Personal communication, (June 1996).
- 7.104. Hoier S. and Eisenmann E.T., Sandia Report SAND96-0956, Sandia National Laboratories Albuquerque, New Mexico 87185, USA (1996), 14.
- 7.105. Hansen L.D. and Frank H., *J. Electrochem. Soc.*, 134 (1987) 6.
- 7.106. Skarstadt P., in *Batteries for Implantable Biomedical Devices* (Ed. Boone B Owens), Plenum (1986) 242.
- 7.107. Takeuchi E.S., Meyer S.M. and Holmes C.F., *J. Electrochem. Soc.*, 137, (1990) 1667.
- 7.108. Patel B., Skarstad P.M. and Untereker D., *Proc Symp. on Lithium Batteries*, Electrochem. Soc., 84-1 (1984) 221.

- 7.109. Buchman R., Fester K., Patel B., Skarstad P.M. and Untereker D., *Proc Symp. on Lithium Batteries*, Publication Vol. 84-1, Electrochem. Soc. (1984) 212.
- 7.110. Untereker D., *Lithium Primary Cells for Power Sources*, in *Batteries for Implantable Biomedical Devices*, (Ed. Boone B. Owens), Plenum, (1986) 71.
- 7.111. Bro P., *Proc Symp. on Power Sources for Biomedical Implantable Applications and Ambient Temperature Lithium Batteries*, Electrochem Soc., Vol. 80-4, (1980) 570.
- 7.112. McLean R.L. and Brookman M.J., *Proc Symp. on Advances in Battery Materials and Processes*, Electrochem. Soc., 84-4 (1984) 212.
- 7.113. Dr. Sally Hoier, Sandia National Laboratories, USA, Memo to author *Tadiran Cells 4* (19/4/96).
- 7.114. Dr. Sally Hoier, Sandia National Laboratories, USA, *Tadiran Cells*, Memo to author (29/4/96).
- 7.115. *Inorganic Lithium Batteries* Sonnenschein Lithium Technical Brochure, Sonnenschein Lithium GmbH, 110 1150 01, 2/5/795/Hell. (1995) 14.
- 8.1. Brennen K.R. and Kim J.S., *Battery Performance Modelling*, in *Batteries for Biomedical Devices*, (Ed. Boone B. Owens), Plenum, 8, (1986) 114.
- 8.2. Bro P. and Levy S.C., *Quality and Reliability Methods for Primary Batteries*, The Electrochemical Science Series, John. Wiley & Sons, Inc. (1990).
- 8.3. Fester K. and Levy S.C., *Evaluation Methods*, in *Batteries for Implantable Biomedical Devices*, (Ed. Boone B. Owens) Plenum. (1986) 83.
- 8.4. Size P.J. & Takeuchi E.S., *Proc. 36th Int. Power Sources Conf.*, Cherry Hills (1994).
- 8.5. Fester K. and Levy S.C., *Evaluation Methods*, in *Batteries for Implantable Biomedical Devices*, (Ed. Boone B. Owens) Plenum (1986) 84.
- 8.6. Farrington Lockwood Company Ltd., *Study on the Improved Reliability and Safety of Lithium Batteries by the Use of Electrochemical Noise Measurement*, Vols. 1 and 2, Report FL-D-22, (1992).
- 8.7. RS Catalogue, (July - October 1996) 1-36.
- 8.8. Howard W.G., Buchman R.C., Owens B.B. and Skarstad P.M., in *Power Sources 10* (Ed. L.J. Poole), International Power Sources Symposium Committee, Leatherhead, England (1985).
- 8.9. Buchman R.C., Fester K., Patel B., Skarstad P.M and Untereker D., *Proc. Symp. on Lithium Batteries*, (Ed. A.N. Dey), Publication 84-1, Electrochem. Soc., (1984) 212.
- 8.10. Saunders T.G., in *Power Sources 15*, (Ed. A. Attewell and T. Keily), International Power Sources Symposium Committee, Crowborough, England (1995) 317.
- 8.11. UL1642, *Standard for lithium batteries*, Underwriters Laboratories Inc., 2nd Edition, (1992).

- 9.1. Walsh F., *A First Course in Electrochemical Engineering*, ISBN 0 9517307 1 1, The Electrochemical Consultancy (Romsey) Ltd., (1993) 84.
- 9.2. Eisenmann E.T., *Lithium-Thionyl Chloride Battery - State of the Art Assessment*, Sandia Report SAND96-0839, (March 1996) 8.
- 10.1. Donaldson G.J., Nip W.S., Patraboy T.J., Anderson J.S. and Farrington M.D., in *Power Sources 14*, (Ed. A. Attewell and T. Keily), International Power Sources Symposium Committee, Crowborough, England (1993) 131.
- 10.2. *Inorganic Lithium Batteries* Sonnenschein Lithium Technical Brochure, Sonnenschein Lithium GmbH, 110 1150 01, 2/5/795/Hell. (1995) 14.
- 10.3. Yamin H. and Pallivthikal M., *Very High Energy Density Lithium Thionyl Chloride Batteries*, Wolsky Seminar, Florida, March 1993 (Oral presentation, not paper).
- 10.4. Yamin H., Tadiran Ltd., Israel, Personal communication (December, 1987).
- 11.1. Sutton J.B. *The Statistician*, 39 (1990) 461.
- 11.2. Skarstad P., *Lithium-Liquid Oxidant Batteries*, in *Batteries for Implantable Biomedical Devices*, (Ed. B.B. Owens), Plenum, (1986) 230.
- 11.3. Bro P. and Levy S.C., *Quality and Reliability Methods for Primary Batteries*, The Electrochemical Science Series, John Wiley & Sons, Inc., (1990).
- 11.4. Peled E. *Film Formation*, Lithium Batteries, (Ed. by J-P. Gabano), Academic Press, (1983) 68.
- 11.5. Chenebault P., Vallin D., Thevenin J. and Wiart R., *J. Appl. Electrochem.*, 19 (1989) 419.
- 11.6. *CRC Handbook of Chemistry and Physics*, 74th edition (Ed. David R. Lide), (1994), 13-7.
- 11.7. Yamin H., Tadiran Ltd., Israel, Personal communication (1996).
- 11.8. Hagan W.P, Hampson N.A. and Packer R.K., *J. Power Sources*, 24 (1988) 112.
- 11.9. Buchman R., Fester K., Patel B., Skarstadt P and Untereker D., *Proc. Symp. On Lithium Batteries*, J. Electrochem Soc., 84-1 (1984) 214.
- 11.10. Dr Wendy Cieslak, Sandia National Laboratories, Albuquerque, New Mexico, Personal communication, (1995).
- 11.11. Chenebault P. Thevenin J., Vallin D. and Wiart R., Abstract No. 35, *Proc. 172nd Electrochem. Soc. Meeting*, Honolulu, Publication 87-2, Electrochem. Soc. (1987).
- 11.12. Chenebault P., Vallin D. Thevenin J. and Wiart R., *J. Appl. Electrochem.*, 18 (1988) 625.
- 11.13. Chenebault P. and Vallin D., *Proc. Electrochem. Soc. Symp. on Primary and Secondary Ambient Temperature Lithium Batteries*, Publication 88-6, Electrochem. Soc. (1988) 201.

- 11.14. Chenebault P., Vallin D. Thevenin J. and Wiart R., *J. Appl. Electrochem.* 19 (1989) 413.
- 11.15. Cieslak W. R., *Proc. 36th. Power Sources Symp.*, Cherry Hill, NJ, (1994) 348.
- 12.1. Marincic N., *J. Appl. Electrochem.*, 5 (1975) 313.
- 13.2. Howard W.G., Buchman R.C., Owens B.B. and Skarstad P.M., in *Power Sources 10* (Ed. L.J. Poole) International Power Sources Symposium Committee, Leatherhead, England (1984).
- 13.3. Buchman R.C., Fester K., Patel B., Skarstad P.M and Untereker D., *Proc. Symp. on Lithium Batteries*, (Ed. A.N. Dey), Publication 84-1, Electrochem. Soc. (1984) 212.
- 14.1. Hoier S.N. and Eisenmann E.T., *The Faradaic Efficiency of the Lithium Thionyl Chloride Battery*, Sandia Report SAND96-0956, Sandia National Laboratories, Albuquerque, NM 8715, (1996).
- 14.2. Hoier S.N., Schlaiker C., Johnson A. and Riley S., *Proc. 32nd Power Sources Symp.*, Cherry Hill, NJ (1996).
- 14.3. Dr Sally Hoier, Sandia National Laboratories, Albuquerque, NM, USA, Personal communication, (29/4/96).
- 14.4. Bro P., in *Power Sources 7*, (Ed. J. Thompson), Academic Press, London (1979).
- 14.5. Takeuchi E.S., Meyer S.M. and Holmes C.F., *J. Electrochem. Soc.*, 137 (1990) 1665.
- 15.1. Chatfield C., *Statistics for Technology*, (3rd Edition), Chapman and Hall, (1973) 355.
- 15.2. *CRC Handbook of Chemistry and Physics*, 74th edition (Ed. David R. Lide), (1994) A-104.
- 15.3. Ullathorne D.P., Project Leader, Gas Research Centre, BG plc, Personal communication (1997).
- 15.4. Yamin H., Tadiran Ltd., Israel, Personal communication, (January 1998).
- 15.5. Eisenmann E.T., *Lithium Thionyl Chloride Battery State-of-the-Art Assessment*, Sandia Report SAND96-0839, (1996) 18.
- 16.1. Tsaur K-C., Pollard R., *J. Electrochem. Soc.*, 131 (1984) 975.
- 16.2. Evans T.I. and White R.E., *J. Electrochem. Soc.*, 136 (1989) 328.
- 16.3. Evans T.I. and White R.E., *J. Electrochem. Soc.*, 136 (1989) 2798.
- 16.4. Driscoll J.R., Pollard, Smith J.J. and Szpak S., *Power Sources 10*, (Ed. L.J. Pearce), International Power Sources Symposium Committee, Leatherhead, England (1985) 145.
- 16.5. Szpak S. and Venkasetty H.V., in *Power Sources 9*, (Ed. L.J. Pearce), International Power Sources Symposium Committee, Leatherhead, England (1985) 403.

- 16.6. De Levie R., *Electrochemical response of porous and rough electrodes*, in *Advances in Electrochemistry and Electrochemical Engineering*, Vol. 6, (Ed. Paul Delahay and C.W. Tobias) Interscience Publishers, John Wiley and Sons, New York, (1967) 329.
- 16.7. Dunning J.S. and Bennion D.N., *J. Electrochem. Soc.*, 120 (1973) 906.
- 16.8. Hughes M., Karunathilika S.A.G.R., Hampson N.A. and Sinclair T.J., *J. Appl. Electrochem.*, (1983), 669.
- 16.9. Eisenmann E.T., *Lithium-Thionyl Chloride Battery - State of the Art Assessment.*, Sandia Report, SAND96-0839, (March 1996).
- 18.1. Fester K. and Levy S.C., *Evaluation Methods*, in *Batteries for Biomedical Devices*, (Ed. Boone B. Owens), Plenum, 8, (1986) 94.
- 18.2. Roberge P.R., Beaudoin R., Verville G. and Smit J., *J. Power Sources*, 27 (1989) 177.
- 18.3. Roberge P.R., Halliop E. and Farrington M.D., *J. Power Sources*, 27 (1991) 233.
- 18.4. Donaldson G.J., Nip W.S., Patraboy T.J. Anderson M.D. and Farrington M.D., in *Power Sources 14* (Ed. T. Keily) International Power Sources Symposium Committee, Crowborough, England (1993) 131.

